学位論文

Numerical and Observational Studies of

Flux Emergence in the Sun

(太陽の浮上磁場に関する数値的・観測的研究)

平成２５年１２月博士（理学）申請

東京大学大学院理学系研究科

地球惑星科学専攻

鳥海　森

Numerical and Observational Studies of Flux Emergence in the Sun

(太陽の浮上磁場に関する数値的・観測的研究)

by

Shin Toriumi

鳥海　森

A dissertation submitted to the Department of Earth and Planetary Science,
Graduate School of Science, The University of Tokyo
in partial fulfillment of the requirement for the degree of
Doctor of Philosophy (Science)

December, 2013

Abstract

The birth of active regions (ARs) in the Sun, or, the flux emergence, is one of the most important scientific targets in solar physics. It is widely believed that the ARs are created by rising magnetic fields from the deeper interior below the visible surface, i.e., the convection zone, although we cannot investigate such subsurface magnetic flux from direct optical observations. In this thesis, motivated by a scientific curiosity to understand the dynamics of the magnetic flux, particularly when the flux rises through the top convection zone and approaches the surface layer, we carried out numerical and observational studies of flux emergence.

First, in Part II, we performed three-dimensional magnetohydrodynamic simulations of magnetic flux tubes rising from a depth of -20 Mm in the convection zone. In Chapter 3, as a result of the simulation, we found that the rising flux expands and slows down as it approaches the solar surface. Here, the expansion is due to the decrease in the pressure and density of the surrounding material. The deceleration of the rising flux tube occurs because unmagnetized plasma is trapped between the flux tube and the solar surface, which is an isothermally-stratified (i.e., convectively-stable) layer. Then, the trapped plasma escapes around the surface as a horizontal divergent flow (HDF). When the field strength of the flux tube increases enough, the flux restarts its ascent from the surface to the upper atmosphere. Based on the numerical results, we suggested a theoretical "two-step emergence" model of the rising magnetic flux.

We also conducted a parametric study of the numerical simulation in Chapter 4 by varying

the field strength, the twist, and the perturbation wavelength of the initial tubes, aiming to investigate the relation between these parameters and the properties of the flux emergence. Consequently, we succeeded in obtaining the parameter dependencies of the flux evolution and of the HDF. It is also found that the HDF is driven by the lateral pressure gradient. Furthermore, the numerical results were explained by taking an analytical approach.

Second, in Part III, in order to examine the theoretical "two-step emergence" model, we carried out two observational studies by developing our original methods. In this study, we exploited observational data obtained by *SOHO* and *SDO*. Thanks to their continuous full-disk observations, now we are able to analyze the very moment of, or even before the start of flux emergence.

The first observation target is the HDF of the unmagnetized plasma, which is expected to appear at the visible surface just before the flux itself emerges. In Chapter 7, we investigated the temporal evolution of the Dopplergram and the line-of-sight (LoS) magnetogram of NOAA AR 11081 taken by *SDO*/HMI, and detected the HDF about 100 minutes earlier than the start of the LoS magnetic flux emergence. The HDF duration and its speed were found to be comparable to the numerical results. By analyzing Hα images, we also investigated the chromospheric response to the flux emergence at the surface.

For a statistical analysis of the HDF, in Chapter 8, we repeated our detection in another 23 flux emergence events. As a result, we found HDFs in more than half of the entire data set. If we exclude the emergence events in the central region of the solar disk, which are supposed to have less LoS velocity components, the detection rate increases up to more than 80%. Therefore, we can conclude that the HDF is rather a common feature in the earliest phase of the AR appearance. The HDF duration and the maximum HDF speed were, on average, consistent with the event study and our numerical results.

The second target of the observational study is the rising magnetic flux in the uppermost convection zone. In Chapter 9, for detecting the subsurface flux, we used helioseismology, the unique way to probe the solar interior. We newly developed a helioseismic technique that

measures acoustic oscillation signals, and applied this method to the *SOHO*/MDI Dopplergram of NOAA AR 10488. The obtained oscillation powers showed reductions, indicating that a magnetic flux rises through the top convection zone with a gradual deceleration. The estimated rise velocity of the flux and its decelerating nature were well accorded with the numerical results.

In Part IV, the obtained results are summarized and discussed. The clear consistencies between the numerical and the observational studies strongly support the "two-step emergence" model that the rising magnetic flux slows down in the top convection zone before the flux evolves further into the upper atmosphere. Our results demonstrate that the surface layer plays an important role in the large-scale transportation of magnetic flux from the deeper convection zone to the higher atmosphere, changing the structure, velocity, and plasma-β of the emerging flux. Moreover, our study provides the means to investigate the physical state of subsurface magnetic flux, even before the flux appears at the visible surface. We believe that, by developing our numerical and observational methods, the transportation mechanism of the magnetic flux in the Sun will be revealed further in the future.

Acknowledgments

I would like to express my sincere gratitude to my supervisor, Takaaki Yokoyama, for his continuous guidance, constant encouragement, and endless patience during my PhD work. I owe it to him that I finish my dissertation. He introduced me to the world of solar physics and, through valuable discussions, I learned much from his attitude towards science. I cannot thank him enough.

I am also deeply grateful to my collaborators, K. Hayashi, S. Ilonidis, and T. Sekii, for their kind supports, suggestion of ideas, and useful advice. Without their help, the completion of this dissertation would not be possible. My distinguished colleagues of Yokoyama lab helped me in various ways. Valuable, stimulating, and sometimes tough discussions in the lab seminar inspired me very much. It was a huge privilege to be a member of this lab.

During the years, I had a lot of useful discussions with professors, researchers, and students of NAOJ, ISAS/JAXA, Kyoto University, Nagoya University, Chiba University, High Altitude Observatory (HAO), Stanford University, Lockheed-Martin Solar and Astrophysics Laboratory (LMSAL), Observatoire de Paris, and many other institutes. They gave me numerous helpful comments and I would like to acknowledge all of them.

I have been supported by the Research Fellowship for Young Scientists of the Japan Society for the Promotion of Science (JSPS). I am grateful to the JSPS Institutional Program for Young Researcher Overseas Visits for supporting my visits to the HAO in 2010 and to Stanford University in 2011 and 2012. The JSPS Global COE Program supported me to visit Observatoire de Paris in 2013.

Numerical computations were carried out on NEC SX-9, Cray XT4, and Cray XC30 at the Center for Computational Astrophysics, CfCA, of NAOJ. This work also depends on observational data. I am thankful to the *SOHO* and *SDO* team for distributing MDI and HMI data.

Finally, I would like to express my special appreciation to my family and my beloved fiancée Rieko for their continuous supports.

Contents

Part I

General Introduction

Chapter 1

General Introduction

We have long been observing the Sun, the only star we can observe with high spatial resolution. Since Galilei started to observe the Sun using his telescope in the beginning of the 17th century, vast amounts of observational data have been collected. Theories on the Sun have also been constructed for a long time. In this chapter, we introduce some observational aspects and theoretical works of the Sun.

1.1 The Sun and its Activity

1.1.1 The Sun

The Sun is a G-type main-sequence star and is a central star of the Solar System. It is composed of hot plasma (mainly hydrogen and helium), having a radius of about 700 Mm (1 Mm = 1000 km). From the center, the core extends to 20–25% of its radius, then the radiative zone to $\sim$ 70%. The Sun's outer layer, extending from 70% to the surface (the thickness $\sim$ 200 Mm), is the convection zone, in which the energy transportation is primarily done by thermal convection. The visible surface is called the photosphere. Above that are the chromosphere and the hot corona, which are connected by the transition region.

Figure 1.1 is the Sun observed in multiple wavelengths by the *SDO* spacecraft. In the

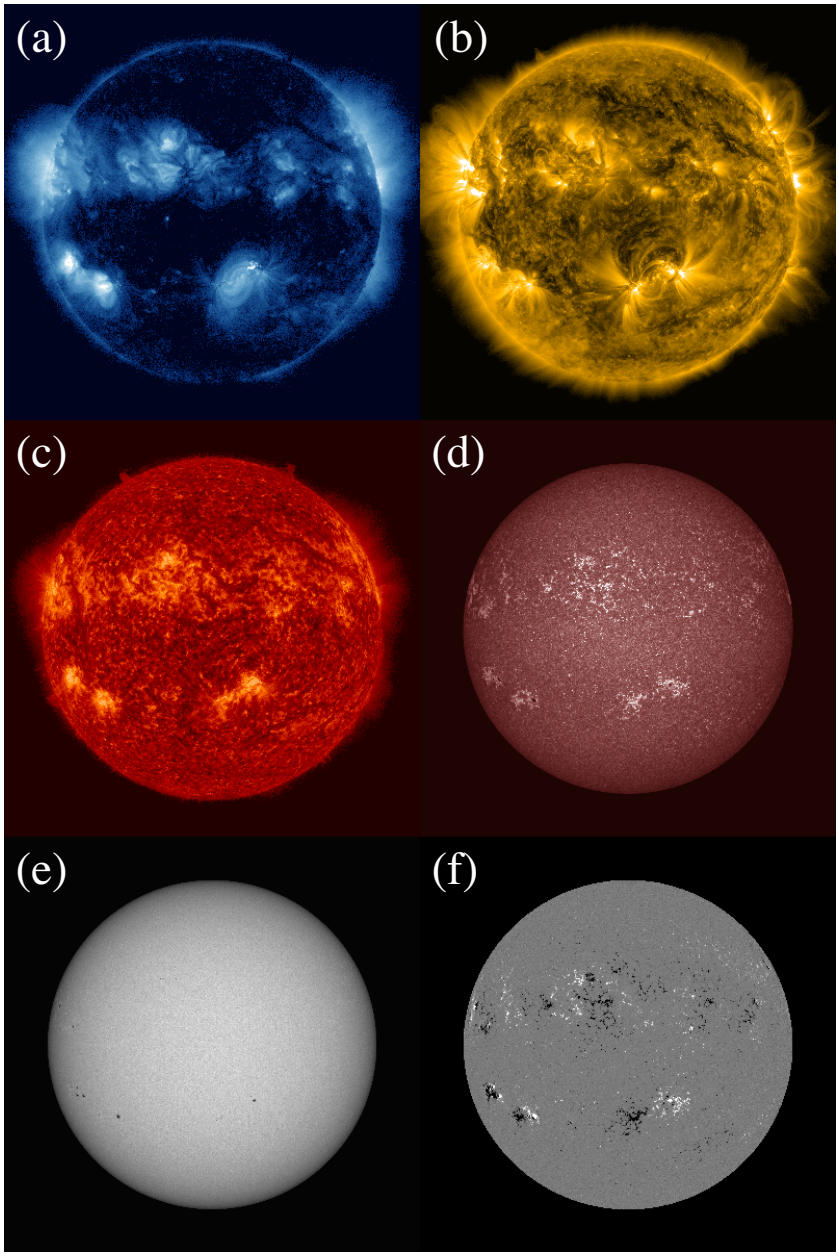

Figure 1.1: The Sun observed in multiple wavelengths by the *SDO* spacecraft. (a) 335 Å, (b) 171 Å, (c) 304 Å, and (d) 1700 Å taken by *SDO*/AIA, and (e) continuum and (f) line-of-sight magnetic field strength by *SDO*/HMI.

coronal images as in panels (a) and (b), one may find some alignments of bright features, particularly just above and below the equator. These regions are called active regions (ARs), which are also seen as bright features in lower temperature lines as in panels (c) and (d). The most important point about the AR is that AR is highly related to the magnetic fields. In the surface magnetogram, we can find that each AR consists of positive and negative magnetic elements (panel f). Areas where the field strengths are strong enough can be seen as sunspots in the continuum image (panel e). Through magnetic reconnection, some strongest ARs may cause catastrophic eruptions into the heliosphere, which are known as flares and coronal mass ejections (CMEs). They may have violent impacts on the interplanetary space around the Earth.

1.1.2 Flux Emergence and Active Region Formation

It is widely accepted that AR is the product of magnetic flux emergence, i.e., dynamo-generated flux transported from the deep convection zone (Parker, 1955). In most dynamo models, a toroidal flux wrapping around the core is generated in the subadiabatically-stratified overshoot layer at the bottom of the convection zone. Then, the toroidal flux locally rises through the interior to the visible surface (photosphere) to make an alignment of ARs (see Figure 1.1).

Figure 1.2 shows the model of the flux emergence and the AR formation suggested by Zwaan (1985). Here, the magnetic flux rising from the convection zone penetrates the surface layers (photosphere and chromosphere) and expands into the higher atmosphere (corona), forming an AR. Here, the coronal loops are the continuation of the magnetic flux from the deep convection zone and the cross-sections of the magnetic flux at the surface can be seen as sunspots. Therefore, the entire process of the flux emergence should be understood in a self-consistent manner as a coherent mechanism from the deep interior to the upper atmosphere through the surface layer.

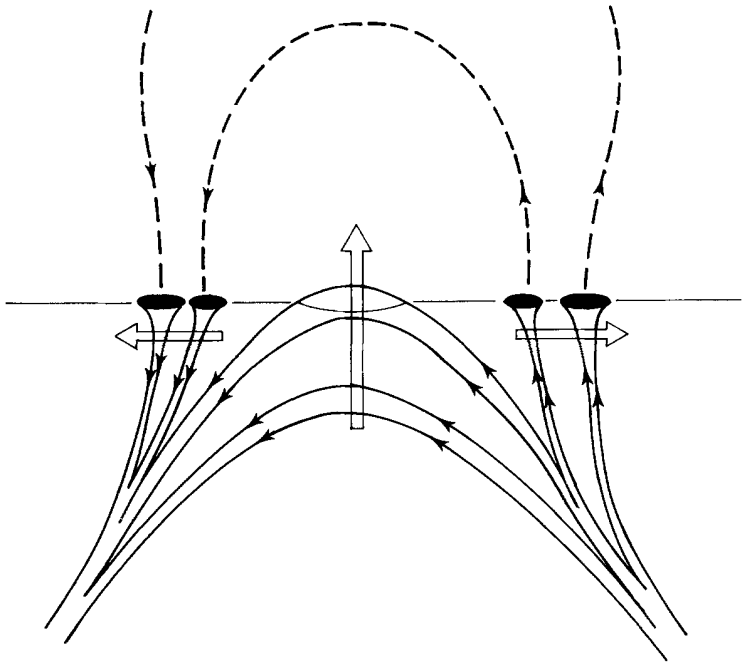

Figure 1.2: Model of flux emergence and active region formation. The horizontal line indicates the photosphere. Figure reproduced from Zwaan (1985).

1.2 Observation of Flux Emergence

1.2.1 Birth of Active Region

Observationally, newly emerging flux appears as small and bright bipolar plages in the chromospheric Ca II H and K lines (Fox, 1908; Sheeley, 1969). Soon, arch filament system (AFS) composed of parallel dark fibrils appears in the Hα line core (Bruzek, 1967, 1969; see Figure 1.3). The fibrils are thought to be the magnetic fields connecting the faculae of opposite polarities. They are 20–30 Mm in length with a maximum height of 5 Mm. The apex of a loop rises upward at a speed of up to 5 km s^{-1}, while, in both legs, the redshifts up to 50 km s^{-1} are observed, namely, the plasma flows down with a velocity faster than a local sound speed. Also, in the photosphere, small pores are formed at the roots of the chromospheric filaments with downflows up to about 1 km s^{-1}. Ellerman bombs (Ellerman, 1917), also known as moustaches by their shape of the Hα spectral profile, are found under the growing AFSs.

The faculae of opposite polarities separate from each other, initially at a rate of $>$ 2 km s^{-1}, and then the rate drops to 1.3–0.7 km s^{-1} during the next 6 hours (Harvey & Martin, 1973). The magnetic flux emerges continuously within the opposite polarities. If the emerged flux is sufficient, pores are formed, and finally sunspots are created near the plages; Zirin (1972) named this area as emerging flux region (EFR). Figure 1.4 shows the observation of a sunspot with a highest resolution. Here, a darkest spot at the center is the umbra, which is surrounded by a brighter region, the penumbra.

Zwaan (1978, 1987) introduced the hierarchy of magnetic elements of EFR. According to observations, sunspots with a flux of 5×10^{20}–3×10^{22} Mx have penumbrae. In this group, the umbral field is 2900–3300 G, sometimes exceeding 4000 G. The flux of pores (small spots without penumbra) is 2.5×10^{19}–5×10^{20} Mx with a field strength of $\sim$ 2000 G. If the flux is less than 10^{20} Mx, EFRs do not develop beyond ephemeral ARs (Harvey & Martin, 1973).

Strous et al. (1996) and Strous & Zwaan (1999) observed NOAA AR 5617 and found a hierarchy of motions of magnetic elements (faculae, pores, and sunspots). Figure 1.5 shows

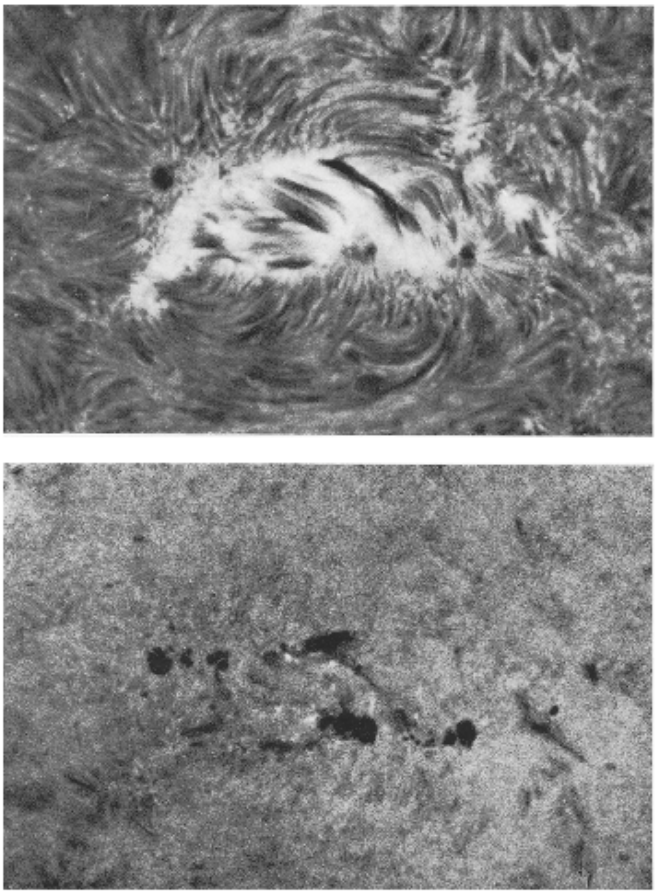

Figure 1.3: Arch filament system (AFS) and plages. (Top) Filtergram in the Hα line core shows AFS connecting plages of opposite polarities. (Bottom) Filtergram at Hα $\pm$ 1 Å shows pores with bright points (Ellerman bombs). Figure reproduced from Bruzek (1967).

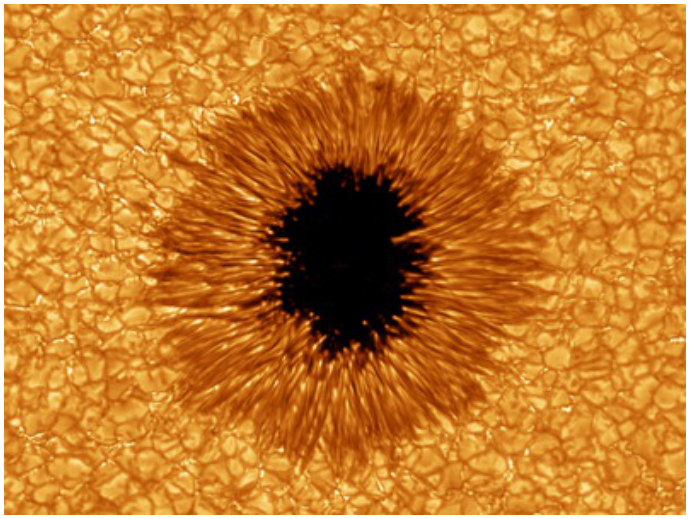

Figure 1.4: Newest observation of a sunspot: NOAA AR 11084 on 2010 July 2 observed with the New Solar Telescope (TiO filter). Image courtesy of Big Bear Solar Observatory.

the motion of these elements; faculae of either polarity scatter throughout the AR and move obliquely toward the edges of the region, which are defined by strings of pores of the same polarity. Faculae move faster (0.84 km s^{-1}: yellow arrow) than the pores (0.73 km s^{-1}: orange arrows). The pores move along the edges toward the major sunspots of their polarities, and the major sunspots also move apart from each other (0.50 km s^{-1}: red arrows). Strous & Zwaan (1999) found that flux emergence occurs recurrently in the middle of an AR to form a pattern with a wavelength of about 8 Mm as in Figure 1.5(a), which is comparable to the typical wavelength of the Parker instability (Parker, 1979; see also Appendix A). From these findings, Strous & Zwaan (1999) suggested a model of a hierarchical evolution in EFR (Figure 1.6). Here, each emergence occurs within a set of slightly curved, nearly parallel vertical sheets. Each field line undulates at the surface and emerges at multiple locations, whose spatial distribution is determined by the wavelength of the Parker instability.

The undulation of emerging flux at the surface was also studied by Bernasconi et al. (2002) and Georgoulis et al. (2002). They found that, in nearly-horizontal photospheric fields, Ellerman bombs occur in the dipped parts (where the field lines are submerged)

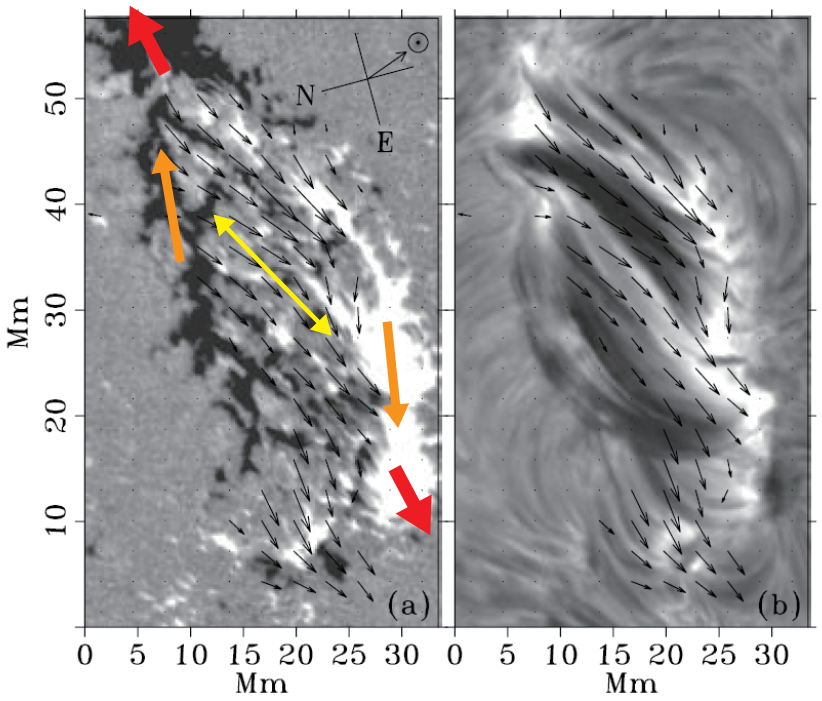

Figure 1.5: Motion of faculae, pores, and sunspots. (a) Photospheric magnetogram and (b) chromospheric arch filament system (AFS) of NOAA AR 5617. Figure reproduced from Strous & Zwaan (1999) by permission of the AAS. Color arrows are overlaid.

and are caused by magnetic reconnection between the dipped fields. Pariat et al. (2004) suggested a resistive model for the emergence of undulating magnetic fields (Figure 1.7). Here, at the photosphere, field lines are undulating, whose wavelength is determined by the Parker instability. At the dips of the undulating fields, magnetic reconnections take place to make longer coronal loops. Through the reconnection, the trapped plasma in the dipped part is ejected downward, which is observed as an Ellerman bomb.

Thanks to the *Hinode* satellite (Kosugi et al., 2007), now we are able to observe the Sun with much higher resolution. Among others, Otsuji et al. (2010) observed the birth of a small-scale AR using the Solar Optical Telescope (SOT: Tsuneta et al., 2008) and found that the emerging flux first expands laterally with a speed of 2.9 km s^{-1} at the surface. Then, as time goes on, the flux gradually move upward at a rate of 2.1 km s^{-1}.

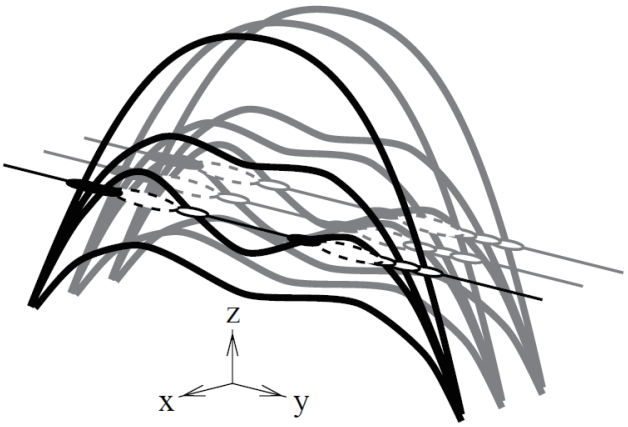

Figure 1.6: Model of flux emergence. Each emergence event occurs in a vertical sheet, while sheets are aligned in a parallel fashion. White and black patches represent positive and negative polarities, respectively, which drift into magnetic alignments at the edge of the AR. Figure reproduced from Strous & Zwaan (1999) by permission of the AAS.

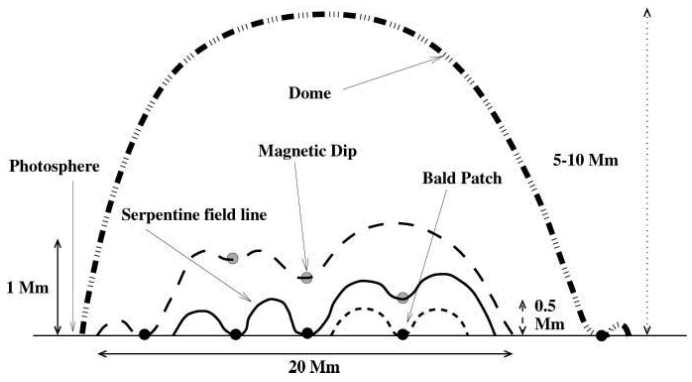

Figure 1.7: Model for the resistive emergence of undulating magnetic fields. Through magnetic reconnection, undulating (serpentine) fields reconnect to form longer coronal loops that cover the entire AR. Figure reproduced from Pariat et al. (2004) by permission of the AAS.

1.2.2 Flux Emergence in the Convection Zone

Helioseismology is perhaps the only way to probe the solar interior. Recent progress in local helioseismology opens a new door into the investigation of emerging magnetic flux in the convection zone, even before the flux itself appears at the visible surface of the Sun.

Kosovichev (2009) studied, using the time-distance helioseismology (Duvall et al., 1993), the emergence of NOAA AR 10488 which appeared in October, 2003. According to him, it was difficult to detect any significant seismic signatures associated with the emerging flux because of the fast emergence and low signal-to-noise ratio (S/N). Recent observation by Ilonidis et al. (2011), however, detected strong seismic anomalies, one to two days before the photospheric flux attained its peak flux emergence rate. Figure 1.8 shows that the seismic anomaly (mean travel-time perturbation) is detected in AR 10488 (panel a), even when the flux is not evident at the surface of the Sun (panel b). They estimated the flux rising speed from -65 Mm to the surface to be 0.3–0.6 km s^{-1}. Zharkov & Thompson (2008) estimated the rising speed from ~ -20 Mm to the surface to be about 1 km s^{-1}.

Komm et al. (2008) studied the emerging flux region, using an independent technique called ring-diagram analysis (Hill, 1988), and found that five out of 13 ARs show upflow at a depth of 2–10 Mm before flux emergence. Also, the vertical flow showed a transition into downflows after the emergence. Hartlep et al. (2011) focused on the acoustic oscillation power (time-averaged squared velocity) measured at the solar surface and found that a reduction in acoustic power in the frequency range of 3–4 mHz can be seen about 1 hr before the start of the flux appearance (see Figure 1.9). Their interpretation was that the acoustic power is reduced by the subsurface magnetic field. A statistical analysis of a large amount of data sets with another method, helioseismic holography, was done by Birch et al. (2013). They found that there were statistically significant signatures in the average subsurface flows before the visible emergence.

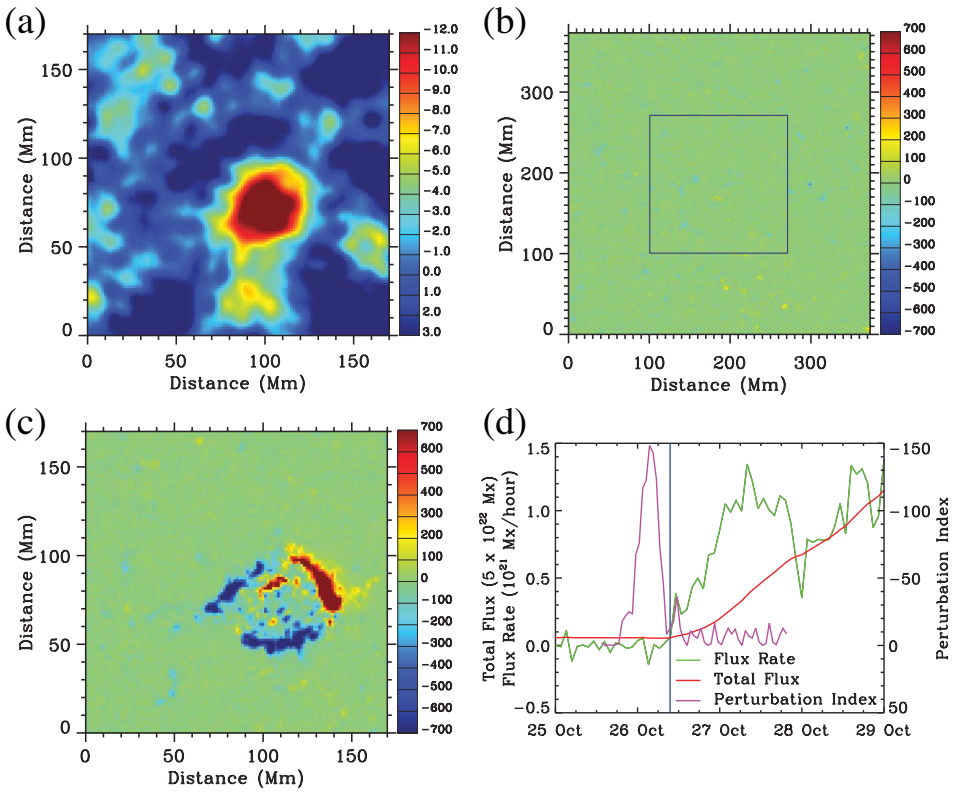

Figure 1.8: Seismic anomaly detected in NOAA AR 10488. (a) Anomaly (mean travel-time perturbation) at a depth of 42 to 75 Mm, obtained from an 8 hr data centered at 03:30 UT, 2003 October 26, while panel (b) is the photospheric magnetogram at the same time as (a). The central square indicates the field-of-view of panels (a) and (c). (c) Same as (b) but for 24 hr later. (d) Total unsigned magnetic flux (red) and magnetic flux rate (green). The vertical blue line indicates the start of emergence, while the pink line shows the perturbation index. Figure reproduced from Ilonidis et al. (2011).

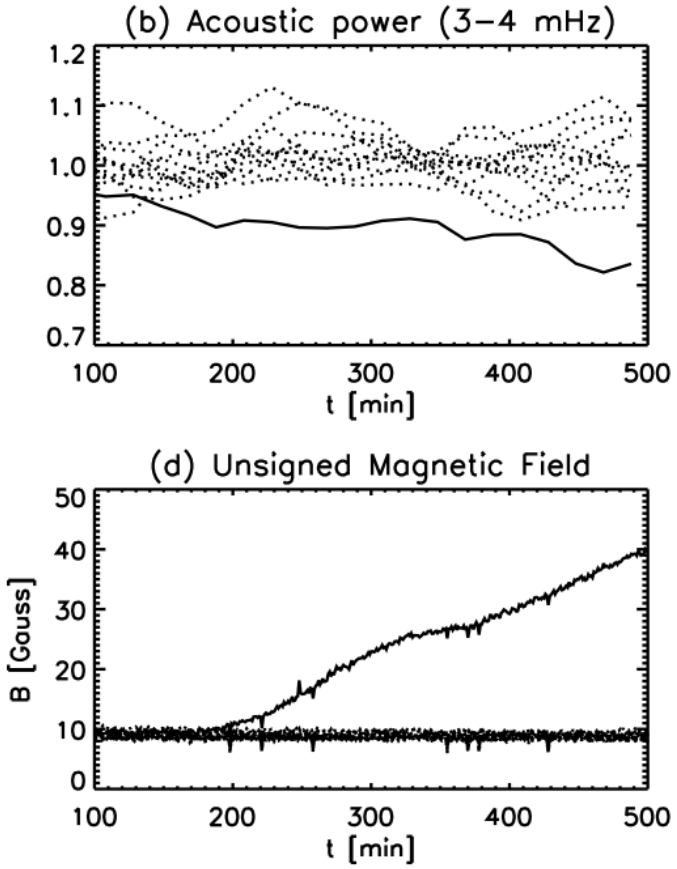

Figure 1.9: Reduction of acoustic oscillation power in NOAA AR 10488. (b) Normalized acoustic power in the frequency range of 3–4 mHz for the emergent area (solid line) and surrounding quiet regions (dotted lines). (d) Unsigned magnetic flux densities of the emergent and surrounding regions. The acoustic power in the emergent location starts deviation from $t \sim 130$ min, while the flux increases from $t \sim 190$ min. Figure reproduced from Hartlep et al. (2011).

1.2.3 Summary of this Section

The birth of an AR is characterized by the separation of magnetic elements (faculae) of both polarities and the chromospheric arch filament system (AFS) rising into a higher altitude with strong downdrafts at its footpoints. In the center of the emerging flux region (EFR), the flux continuously emerges and magnetic elements gather to make pores. If the flux is sufficient, the pores stream into sunspots of the same polarity, which also separate from each other.

At the photosphere, each emerging magnetic field has undulating (serpentine) structure and the typical wavelength of this structure is comparable to that of Parker instability. The undulating fields may reconnect with each other to make longer coronal loops that cover the entire AR. Emergence events occur in a series of vertical sheets, which are aligned in a parallel fashion.

The development of local helioseismology may allow us to investigate the flux emergence in the solar interior even before the flux appears at the visible surface. Time-distance technique detected a seismic anomaly in the deep convection zone, up to two days before the peak emergence at the photosphere. The rising speed of an emerging flux was estimated to be 0.3–0.6 km s^{-1}. Other observations also indicate the existence of rising flux in the convection zone.

1.3 Numerical and Theoretical Approach

1.3.1 Buoyant Emergence of a Flux Tube

It is now widely accepted that active regions (ARs) are the consequence of the emerging magnetic flux transported from the deep convection zone. Therefore, the flux emergence is one part of a global dynamo mechanism in the Sun. Theoretical works on the flux emergence in early days were done in the context of dynamo theories.

Parker (1955) showed that a horizontal magnetic flux tube is buoyant and tends to rise (magnetic buoyancy). Here, we assume the pressure balance between inside and outside of the flux tube,

$$p_{\rm e} = p_{\rm i} + \frac{B^2}{8\pi}, \tag{1.1}$$

where $p_{\rm i}$ and $p_{\rm e}$ denotes the pressure inside and outside the flux tube, of which the field strength is B. When the plasma is in thermal equilibrium, namely, $T_{\rm e} = T_{\rm i} = T$, the above equation can be rewritten as

$$\rho_{\rm e} = \rho_{\rm i} + \frac{B^2}{8\pi}\frac{m}{k_{\rm B}T}, \tag{1.2}$$

where ρ is density, m mean molecular mass, and $k_{\rm B}$ the Boltzmann constant. Thus, we can see that the flux tube is buoyant ($\rho_{\rm i} < \rho_{\rm e}$), and the buoyancy per unit cross-sectional area is

$$f_{\rm B} = (\rho_{\rm e} - \rho_{\rm i})g = \frac{B^2}{8\pi}\frac{mg}{k_{\rm B}T} = \frac{B^2}{8\pi H_{\rm p}}, \tag{1.3}$$

where $H_{\rm p} = k_{\rm B}T/(mg)$ is a local pressure scale height.

Parker (1975) calculated the rising time of the flux tube in the convection zone. He assumed that only aerodynamic drag resists the magnetic buoyancy of the flux tube. For a flux tube with a radius $R_{\rm tube}$, the aerodynamic drag per unit cross-sectional area is

$$f_{\rm D} = C_{\rm D}\frac{\rho_{\rm e}V_z^2}{\pi R_{\rm tube}}, \tag{1.4}$$

while V_z is the vertical velocity of the tube and $C_{\rm D}$ is the drag coefficient of order unity. From Equations (1.3) and (1.4), one can calculate the tube's rising speed when it reaches

the terminal velocity:

$$V_z = \left[\frac{B^2}{8\pi H_\mathrm{p}}\frac{\pi R_\mathrm{tube}}{\rho C_\mathrm{D}}\right]^{1/2} = V_\mathrm{A}\left(\frac{\pi R_\mathrm{tube}}{2C_\mathrm{D}H_\mathrm{p}}\right)^{1/2}. \tag{1.5}$$

That is, the rising velocity V_z is of the order of the Alfvén speed $V_\mathrm{A} = B/\sqrt{4\pi\rho}$. According to Parker (1975), the rising time is down to less than a year, which is much shorter than the expected time of 10 years, i.e., the solar cycle. Schüssler (1977) introduced the conservation of mass and flux and assumed that the tube's radius is not a constant but a function of height. Then he got a rising time of $\sim$ 10 years, which is consistent with the solar cycle. Schüssler (1979) revisited this issue by conducting numerical simulations. He calculated the cross-sectional evolution of the rising flux tubes and found that, as the tube rises, it expands due to the decreasing external density. He concluded that the rising speed is consistent with the analytical velocity in Schüssler (1977) as long as the tube keeps its coherency.

1.3.2 Thin-flux-tube Approximation

The magnetic field at the base of the convection zone has at least B_eq, where B_eq is the field strength that is in equipartition with the kinetic energy density of the convective motions:

$$\frac{B_\mathrm{eq}^2}{8\pi} = \frac{\rho V_\mathrm{c}^2}{2}. \tag{1.6}$$

According to the mixing length model at the bottom (Stix, 1989), the convective velocity V_c is of the order of 10 m s^{-1} and the density ρ is about 0.2 g cm^{-3}, and thus B_eq is estimated to be 10^4 G. Considering the total flux of the active region (AR) is 10^{20}–10^{22} Mx (see Section 1.2), the cross-sectional size of the flux tube at the bottom is about 1000 km, which is much shorter than the local pressure scale height (a few 10,000 km). It should be noted that this approximation is not applicable in the top convection zone (shallower than -30 Mm) where the tube's cross-section exceeds the local pressure scale height (Fan, 2009).

Under the above-mentioned assumption, Spruit (1981) introduced the thin-flux-tube

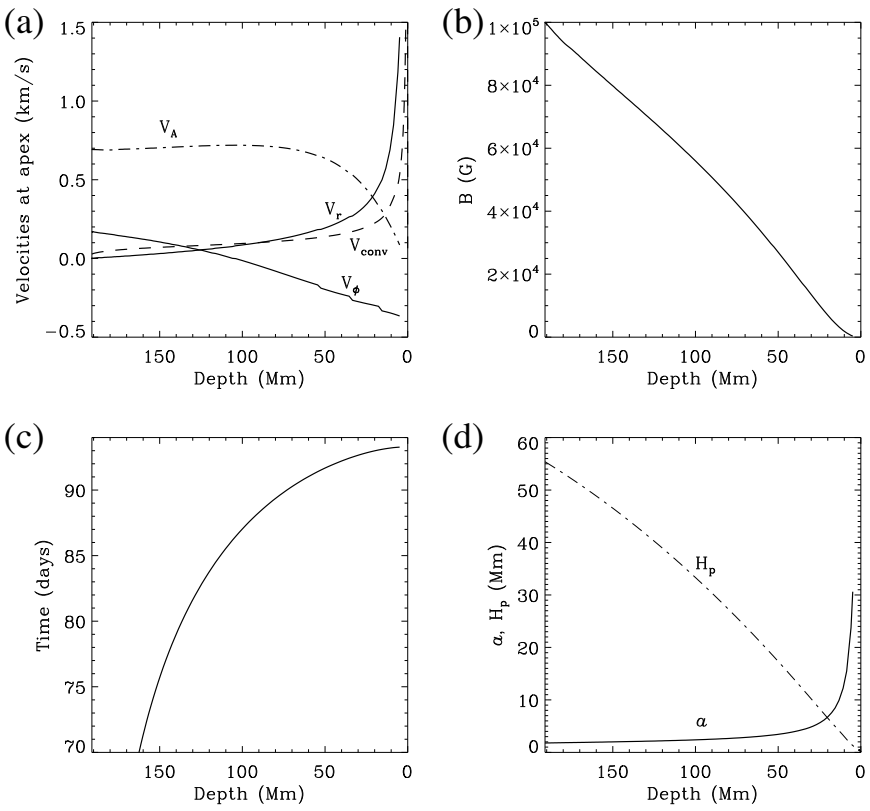

Figure 1.10: Thin-flux-tube (TFT) simulation of a rising flux tube with an initial field strength of 10^5 G. (a) The Alfén speed $V_{\rm A}$, rise velocity V_r, convective velocity $V_{\rm conv}$, and the azimuthal velocity V_ϕ, (b) the magnetic field strength B, (c) the rising time, and (d) the tube radius a and the local pressure scale height $H_{\rm p}$. Figure reproduced from Fan (2009).

(TFT) approximation that the cross-sectional variation of physical quantities is negligible (see also Longcope & Klapper, 1997). Figure 1.10 is the results of the TFT simulation (Fan, 2009), which shows the evolution of a flux tube as it rises through the convection zone. One can see that the rising speed gradually accelerates and the tube's radius also expands during its ascent. At a depth of ~ -20 Mm, the tube's radius exceeds the local pressure scale height and the assumption breaks down.

Numerical calculations using this model have revealed many observational aspects. Choudhuri & Gilman (1987) found that the Coriolis force drifts the rising tube of 10^4 G poleward. To overcome this poleward drift, the initial tube needs a field strength of 10^5 G at the bottom of the convection zone (Caligari et al., 1995), which is ten times stronger than the local equipartition field strength. D'Silva & Choudhuri (1993) showed that the Coriolis effect can explain the AR tilt described by Joy's low (Hale et al., 1919), while Fan et al. (1993) found that the Coriolis force causes asymmetries of leading and following spots of bipolar ARs. One of the important conclusions obtained from the various TFT simulations may be that rising tubes with small magnetic flux (less than 10^{21} Mx for 10^4 G at the base) cannot reach the photosphere because the apexes of the loops lose magnetic field and subsequently "explode" (Moreno-Insertis et al., 1995).

1.3.3 Anelastic Approximation

Another approach in the numerical experiments is the anelastic approximation. In order to calculate the cross-sectional evolution of the rising flux tube and its interaction with the external material, we need to use the direct magnetohydrodynamic (MHD) equations. In the anelastic MHD, equation of continuity is approximated by $\boldsymbol{\nabla} \cdot (\rho \boldsymbol{V}) = 0$ (Gough, 1969). The most important characteristic of this approximation is that the sound waves are filtered out and thus the computation is not limited by the sound speed, which is much faster than the flow velocity and the Alfvén speed in the deep interior.

Fan (2008) carried out 3D anelastic MHD simulation of buoyant twisted flux tubes in a rotating spherical shell mimicking the solar interior without convection. They found that, for strongly twisted tubes, the tilt caused by the twist dominates that caused by the Coriolis force and deviates from the observed Joy's law. In order to fit the Joy's law, the initial twist needs to be smaller than half of that required for a cohesive emergence. They also found that, because of the Coriolis force, the retrograde flow is induced, which results in the greater stretching and stronger field strength in the leading leg of the rising flux. Jouve & Brun (2009) calculated the evolutions of flux tubes rising in a turbulent rotating convection zone. They recovered many important findings obtained by previous simulations, e.g., the distortion of an untwisted flux tube and the poleward drift of a weak field tube.

1.3.4 Twist Component of a Flux Tube

The thin-flux-tube (TFT) approximation (Section 1.3.2) does not consider the cross-sectional distortion during the emergence. In other words, the cross-section of the tube is assumed to be perfectly circular, whose radius is determined by mass and flux conservations. Parker (1979) insisted that, if the tube has its azimuthal component, i.e., if the tube is twisted, the tube keeps its coherency by the inward magnetic tension of the azimuthal field. Based on the stability analysis and the laboratory experiment of rising gas bubbles in liquids, Tsinganos (1980) speculated that the twist reduces hydrodynamic instabilities at the interface between the flux tube and the surrounding plasma.

Longcope et al. (1996) returned to Schüssler (1979)'s situation and calculated cross-sectional evolution of rising flux tubes using Boussinesq magnetohydrodynamic (MHD) equations. He found that, when the tube has no or slight twist, it is fragmented into two counter-rotating elements moving apart horizontally from each other. Eventually, the tube stops rising. Moreno-Insertis & Emonet (1996) and Emonet & Moreno-Insertis (1998) confirmed that the azimuthal component of the flux tube keeps its shape and that the tube approaches the terminal velocity when the aerodynamic drag counteracts the buoyancy (see also Section

1.3.1). They also did a parametric study on the twist strength; the tube becomes more fragmented as the twist decreases.

1.3.5 Flux Emergence from the Photospheric Layer

Regarding the flux emergence from the photospheric layer to the corona, the pioneering work was done by Shibata et al. (1989, see Figure 1.11), who performed two-dimensional hydrodynamic (2D MHD) simulations of the flux emergence through the Parker instability (Parker, 1979): the undular mode of the magnetic buoyancy instability ($\boldsymbol{k} \parallel \boldsymbol{B}$, where $\boldsymbol{k}$ and $\boldsymbol{B}$ denote the wavenumber and the initial magnetic field vector, respectively); see also Appendix A. Shibata et al. (1989) successfully reproduced dynamical features observed in the emerging active region (AR) such as the rising motion of arch filament system (AFS) and the supersonic downflow along the magnetic fields (see also Section 1.2.1).

Since then, the flux emergence and its interaction with a pre-existing coronal field have widely been studied in 2D and 3D simulations. Nozawa et al. (1992) simulated the emergence from the convectively-unstable solar interior (convective Parker instability), while Yokoyama & Shibata (1995, 1996) studied the reconnection between the expanding loop and a pre-existing coronal field and a subsequent formation of X-ray jets. 3D simulations by Matsumoto & Shibata (1992) and Matsumoto et al. (1993) were carried out for studying the interchange ($\boldsymbol{k} \perp \boldsymbol{B}$), undular ($\boldsymbol{k} \parallel \boldsymbol{B}$), and mixed mode instabilities. Magara (2001) studied the cross-sectional evolutions of emerging flux tubes from the top convection zone. He found a deceleration of the flux tube when it enters the convectively-stable photosphere. Matsumoto et al. (1998) performed 3D simulations of the buoyant emergence of strongly-twisted flux tubes (Figure 1.12). Through the kink instability, their tube deformed into a helical shape, which is consistent with the observed sigmoidal AR.

Fan (2001) compared her 3D simulation results with observed features of a newly emerged AR by Strous et al. (1996); see Figure 1.13. Using the criterion by Acheson (1979), Archontis et al. (2004) analyzed the magnetic buoyancy instability of the rising flux tube at the

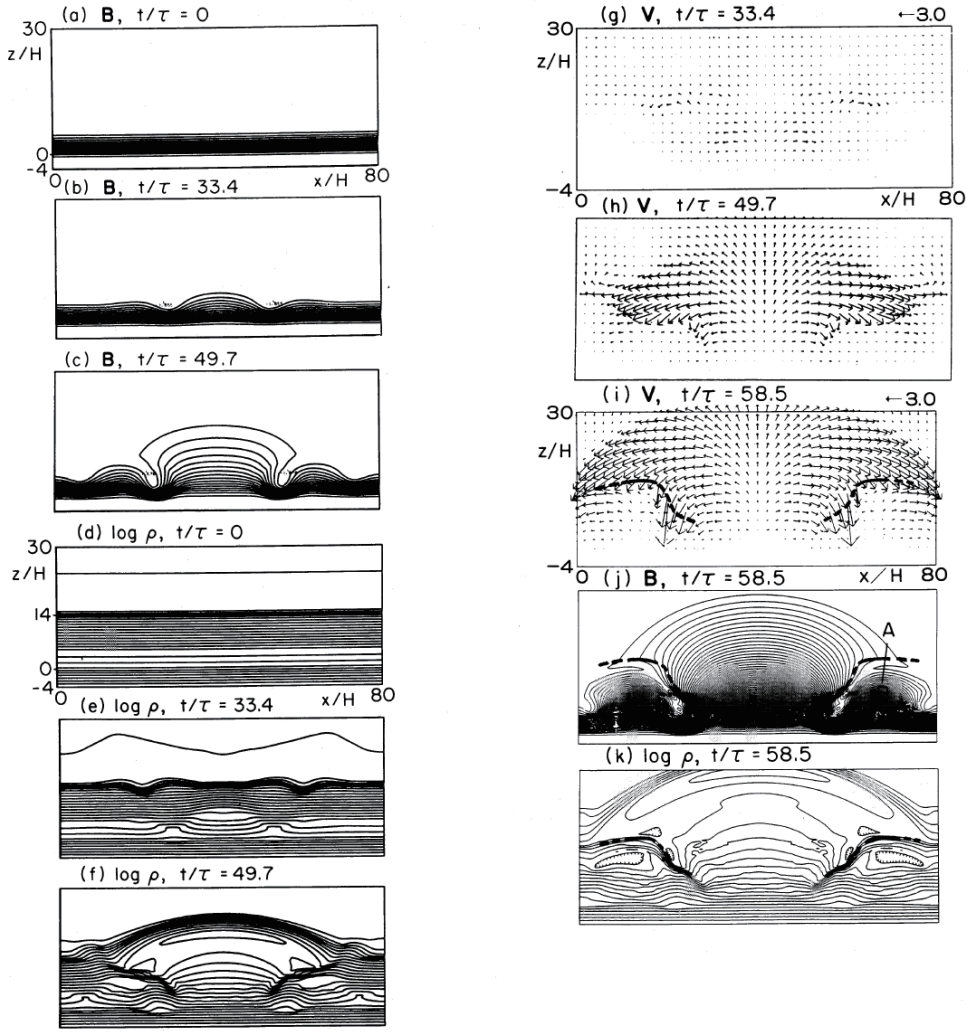

Figure 1.11: Two-dimensional simulation of the flux emergence due to the Parker instability. Panels show the magnetic field $\boldsymbol{B}$, the density ρ, and the velocity vector $\boldsymbol{V}$. The initial flux sheet at the photosphere shows a self-similar expansion into the atmosphere, forming arch filament system (AFS) with strong downflows along the field lines. Figure reproduced from Shibata et al. (1989) by permission of the AAS.

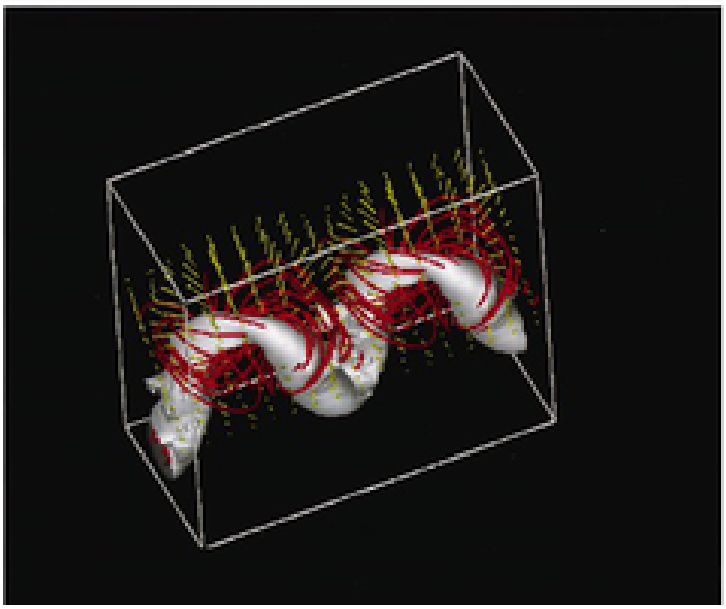

Figure 1.12: 3D view of a kink-unstable flux tube. Red curves show magnetic field lines, while gray surface indicates isosurface of the field strength. Green arrows show the velocity field. Figure reproduced from Matsumoto et al. (1998) by permission of the AAS.

photosphere in their 3D simulations, while Murray et al. (2006) performed parameter studies of the dependence of the tube's evolution on the initial field strength and the twist, finding that the instability at the photosphere (further emergence into the corona) does not occur when the field or the twist is too weak.

Linear stability analysis of the magnetic buoyancy instability in a sheared magnetic layer was conducted by Hanawa et al. (1992), while the nonlinear process was studied in 2D by Kusano et al. (1998) and in 3D by Nozawa (2005).

Isobe et al. (2007) focused on the resistive process of flux emergence and its relation to the Ellerman bombs, which is suggested by Pariat et al. (2004, see also Figure 1.7). Due to the Parker instability, the photospheric fields have an undulatory shape, which gradually reconnect with each other to form longer coronal loops that cover the entire AR. Archontis & Hood (2009) conducted 3D calculation of this issue.

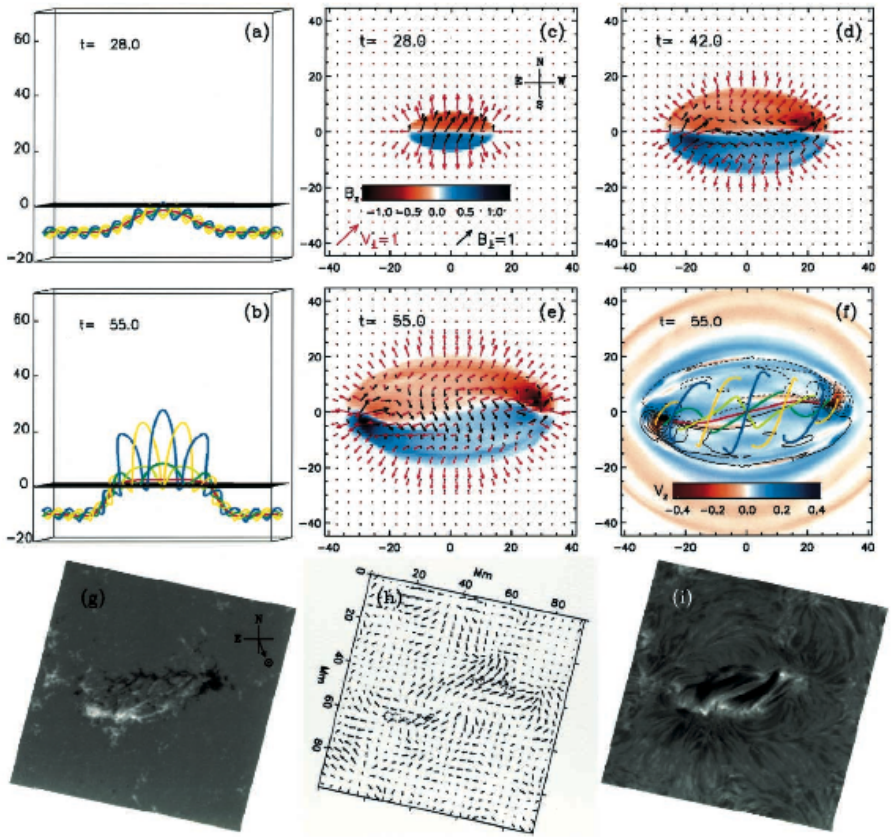

Figure 1.13: Numerical results of a 3D emergence simulation. (a, b) Snapshots of the evolution of selected field lines. (c–e) Evolution of the vertical magnetic field B_z, the horizontal field (black arrows), and the horizontal velocity field (red arrows) on the photosphere, respectively. (f) Same set of field lines as shown in (b), but projected onto the photosphere, overlying the vertical velocity field V_z and the contours of B_z (solid contours represent positive B_z). (g–i) Line-of-sight magnetogram, the horizontal velocity field, and the Hα image of NOAA AR 5617 (Strous et al., 1996). Figure reproduced from Fan (2001) by permission of the AAS.

1.3.6 Coupling with Thermal Convection

With the growing availability of computational resources, simulations are now able to take into account the interaction between emerging magnetic flux and thermal convection. For instance, Cheung et al. (2008) found that a numerical modeling of the emerging flux by 3D radiative MHD simulations shows photospheric characteristics that are well consistent with

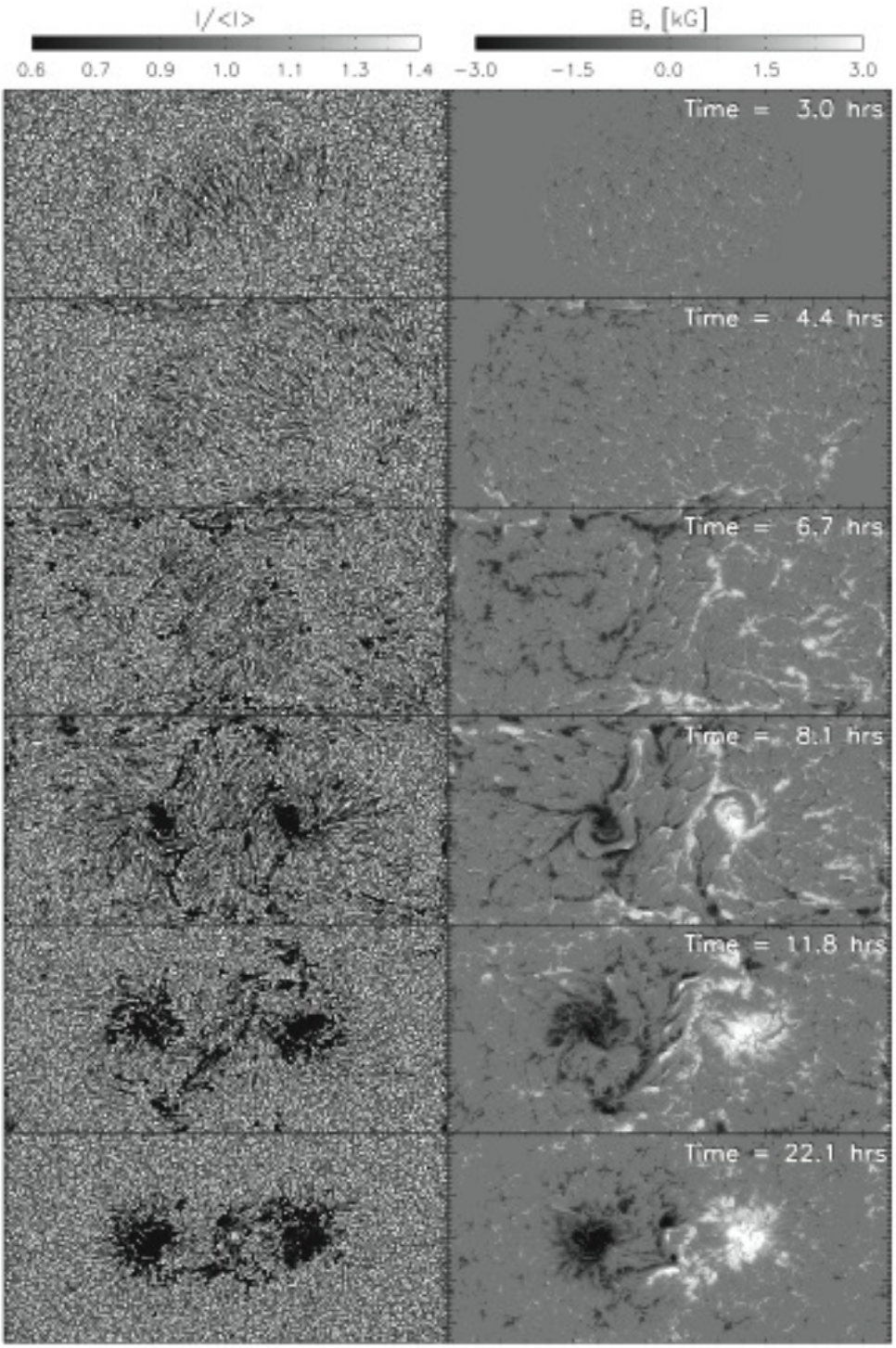

Figure 1.14: Flux emergence by 3D radiative MHD simulation. The intensitygram at 500 nm (left) and synthetic longitudinal magnetogram (right). The full horizontal extent of the simulation domain (92 Mm × 49 Mm) is shown. Figure reproduced from Cheung et al. (2010) by permission of the AAS.

the observations by *Hinode*/SOT. Cheung et al. (2010) modeled the rise of an axisymmetric, twisted flux tube with a shape of a semi-torus and reproduced a pair of sunspots (Figure 1.14). In this calculation, the rising flux extends sideways beneath the photosphere to make a "pancake-like" structure. Also, surface convection were found to make undulatory fields and eventually reconnect with each other (flux cancellation), which drains down the plasma from the surface layer. For other simulations, see, e.g., Fang et al. (2010) and Stein & Nordlund (2012).

1.3.7 Summary of this Section

In the convection zone, a magnetic flux tube in thermal equilibrium with the surrounding plasma has a magnetic buoyancy and tends to rise. The rising tube in the convection zone is resisted by the aerodynamic drag, reaching the terminal velocity of the order of Alfvén speed. Various TFT studies have inferred a super-equipartition field strength of 10^5 G for a flux tube at the bottom of the convective layer to explain the observed emergence latitude, active region tilt, asymmetry of the two polarities, etc. In order to prevent the tube's deformation, the twist component was found to be necessary for the flux tube.

Regarding the flux emergence from the surface layer, a number of numerical simulations have found that the magnetic buoyancy instability well explains the observational characteristics such as the formation of AFS, the supersonic downflows at the footpoints, and the resistive emergence process. The recent progress of the computational resources allows us to calculate the realistic flux emergence coupled with the thermal convection.

1.4 Motivation

Flux emergence and the resultant active region (AR) formation is one of the most interesting targets in solar physics. It plays an important role in the dynamo mechanism, carrying the flux and the helicity from the deep interior to the surface layer. Through magnetic

reconnection, mature ARs (presumably including sunspots) may produce flares and CMEs and affect the interplanetary space. Thus, a large number of solar phenomena are closely linked together via the flux emergence as an important node.

It is therefore natural that flux emergence has attracted many astronomers, both observers and theorists, for a long time. As seen in the previous sections, many authors have modeled the emergence by numerical calculations and successfully explained the observational characteristics. Due to the computational limitations, these numerical models have been divided into two groups: the emergence in the interior and in the atmosphere. The former is on the emergence inside the convection zone such as the thin-flux-tube (TFT) simulations. Here, the TFT approximation breaks down at a depth of ~ -20 Mm since the tube is no longer thin. The latter group is for the simulations from the photospheric layer to the corona. The initial depth is just beneath the photosphere (~ -2000 km). However, since the flux emergence is a seamless process from the convection zone to the corona through the photosphere, the entire process should be treated in a self-consistent manner as a coherent mechanism and, hence, the gap between the two kinds of simulations should be filled (see also Abbett & Fisher, 2003).

In this study, motivated by the above reasons, we first perform large-scale three-dimensional magnetohydrodynamic (3D MHD) simulations of the emerging magnetic flux from the deep convection zone to the corona. The aim of the simulations is to investigate the emergence in much larger scale, particularly the dynamics when the rising flux from the deep interior approaches the surface layer. For this purpose, the initial depth of the flux tubes is set to be -20 Mm, where the TFT approximation becomes inappropriate. We intend to start our simulations consistently with the series of global-scale calculations within the convection zone (e.g. Section 1.3.2).

Then, we analyze the observational data of the newly emerging flux regions and compare with the simulations, aiming to observationally examine the theory of the flux emergence based on the above simulations. By combining the theory and the observation, we may be

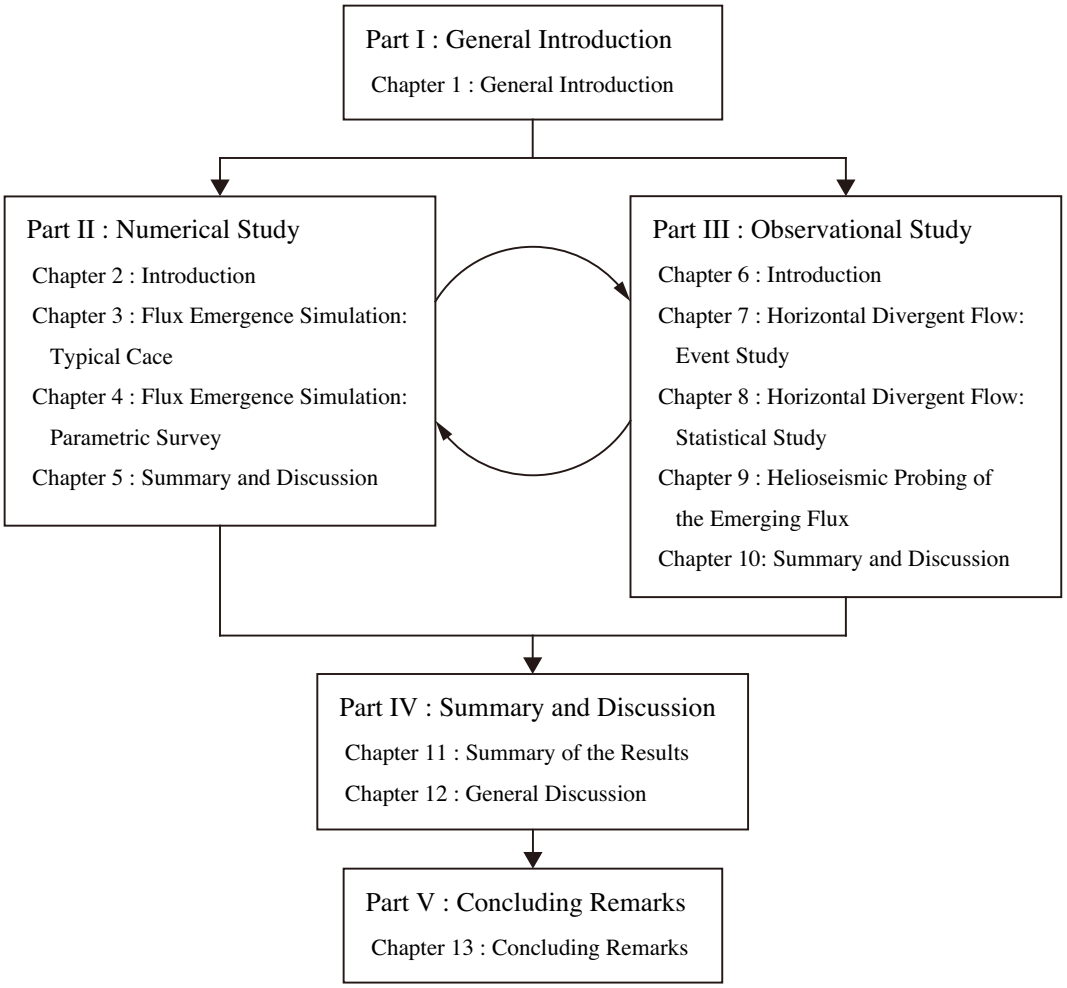

Figure 1.15: Flow chart of this thesis.

able to speculate the physical state of the emerging flux below the visible surface from the surficial observation.

The rest of this thesis proceeds as follows. In Part II, we show the MHD simulations of the emerging magnetic flux. We give basic setup, results, discussion, proposal of the flux emergence model, etc. in the chapters in that part. Then, in Part III, we report our observational works on newly emerging ARs. Summary of the numerical and observational results, general discussion, and the future prospects are given in Part IV. Finally, concluding remarks are given in Part V. Figure 1.15 shows the flow chart of this dissertation.

Part II

Numerical Study

Chapter 2

Introduction

In this chapter, we conduct three-dimensional magnetohydrodynamic (3D MHD) simulations of emerging magnetic flux tubes from the deeper convection zone at -20 Mm to the corona through the photosphere. The purpose of this study is to investigate the emergence process of a flux tube in a larger scale. In the preceding works, the emergence in the convection zone has been studied through various simulations using approximations (e.g., the thin-flux-tube approximation). However, such approximations become inappropriate in the top convection zone around -20 Mm. Regarding the emergence simulations from the photospheric layer, the initial depths of the magnetic fields were just beneath the surface at ~ -2000 km. Our initial depth of -20 Mm is intended to fill the gap between these two groups.

Although 2D simulations were previously carried out in Toriumi & Yokoyama (2010) and Toriumi & Yokoyama (2011), which are for the cross-sectional evolutions parallel and perpendicular to the tube's axis, respectively, it is still necessary to investigate the 3D evolution since multi-dimensionality may play an important role in the emergence process. For example, in 3D regime, the downward magnetic tension of the tube's axial field may pull down the emergence, which is not seen in the 2D cross-sectional evolution perpendicular to the axis.

In Chapter 3, we show a simulation of a typical case with an axial field strength of

2.0×10^4G. As a result, we find some interesting characteristics in the emergence process. On the basis of the simulation, we suggest a new theoretical picture of the flux emergence and the birth of an active region. Then, we conduct a parametric survey in Chapter 4, aiming to investigate the effects of the axial field strength, the twist, and the perturbation wavelength of the initial flux tube on the emergence process. In this chapter, we focus on the flow field that corresponds to the flux emergence. We also take an analytical approach to explain the mechanism of the flux tube emergence. Finally, in Chapter 5, the numerical results in this part are summarized and discussed. Also, a theoretical model for the flux emergence and the active region formation is newly proposed based on the simulations.

Chapter 3

Flux Emergence Simulation: Typical Case[1]

3.1 Introduction

In this chapter, we show the first results of the large-scale three-dimensional magnetohydrodynamic (3D MHD) simulation of the emergence of a twisted flux tube from the deep convection zone (-20 Mm) to the corona. The purpose is to study the emergence in a large scale by combining the convection zone, the photosphere, and the corona into a single simulation domain, which previously was not investigated.

In the next section, we describe a numerical setup of this study. Then, in Section 3.3, simulation results are shown in detail. After summarizing the results in Section 3.4, we compare the numerical results with previous active region (AR) observations by Strous et al. (1996) and Strous & Zwaan (1999) and suggest a new theoretical picture of the flux emergence and the birth of an AR in Section 3.5.

[1]Most part of this chapter was published in Astronomy & Astrophysics (Toriumi & Yokoyama, 2012)

3.2 Numerical Setup

The basic MHD equations in vector form are:

$$\frac{\partial \rho}{\partial t} + \boldsymbol{\nabla} \cdot (\rho \boldsymbol{V}) = 0, \tag{3.1}$$

$$\frac{\partial}{\partial t}(\rho \boldsymbol{V}) + \boldsymbol{\nabla} \cdot \left(\rho \boldsymbol{V}\boldsymbol{V} + p\boldsymbol{I} - \frac{\boldsymbol{B}\boldsymbol{B}}{4\pi} + \frac{\boldsymbol{B}^2}{8\pi}\boldsymbol{I} \right) - \rho \boldsymbol{g} = 0, \tag{3.2}$$

$$\frac{\partial \boldsymbol{B}}{\partial t} = \boldsymbol{\nabla} \times (\boldsymbol{V} \times \boldsymbol{B}), \tag{3.3}$$

$$\begin{aligned} &\frac{\partial}{\partial t}\left(\rho U + \frac{1}{2}\rho \boldsymbol{V}^2 + \frac{\boldsymbol{B}^2}{8\pi} \right) \\ &+ \boldsymbol{\nabla} \cdot \left[\left(\rho U + p + \frac{1}{2}\rho \boldsymbol{V}^2 \right) \boldsymbol{V} + \frac{c}{4\pi} \boldsymbol{E} \times \boldsymbol{B} \right] - \rho \boldsymbol{g} \cdot \boldsymbol{V} = 0, \end{aligned} \tag{3.4}$$

and

$$U = \frac{1}{\gamma - 1}\frac{p}{\rho}, \tag{3.5}$$

$$\boldsymbol{E} = -\frac{1}{c}\boldsymbol{V} \times \boldsymbol{B}, \tag{3.6}$$

$$p = \frac{k_{\mathrm{B}}}{m}\rho T, \tag{3.7}$$

where ρ denotes the gas density, $\boldsymbol{V}$ velocity vector, p pressure, $\boldsymbol{B}$ magnetic field, c the speed of light, $\boldsymbol{E}$ electric field, and T temperature, while U is the internal energy per unit mass, $\boldsymbol{I}$ the unit tensor, k_{B} the Boltzmann constant, $m\,(=\text{const.})$ the mean molecular mass, and $\boldsymbol{g}$

the uniform gravitational acceleration. We assume the medium to be an inviscid perfect gas with a specific heat ratio $\gamma = 5/3$. All the physical values are normalized by the pressure scale height $H_0 = 200$ km for length, the sound speed $C_{s0} = 8$ km s^{-1} for velocity, $\tau_0 \equiv H_0/C_{s0} = 25$ s for time, and $\rho_0 = 1.4 \times 10^{-7}$ g cm^{-3} for density, all of which are the typical values in the photosphere. The units for pressure, temperature, and magnetic field strength are normalized by the combinations of the units above: $p_0 = \rho_0 C_{s0}^2 = 9.0 \times 10^4$ dyn cm^{-2}, $T_0 = mC_{s0}^2/(\gamma H_0) = 4000$ K, and $B_0 = (\rho_0 C_{s0}^2)^{1/2} = 300$ G, respectively.

Here, 3D Cartesian coordinates (x, y, z) are used, where z is parallel to the gravitational acceleration vector, $\boldsymbol{g} = (0, 0, -g_0)$, and $g_0 = C_{s0}^2/(\gamma H_0)$ by definition. The simulation domain is $(-400, -200, -200) \leq (x/H_0, y/H_0, z/H_0) \leq (400, 200, 250)$, resolved by $1602 \times 256 \times 1024$ grids. In the x-direction, the mesh size is $\Delta x/H_0 = 0.5$ (uniform). In the y-direction (z-direction), the mesh size is $\Delta y/H_0 = 0.5$ ($\Delta z/H_0 = 0.2$) in the central area of the domain, which gradually increases for each direction. We assume periodic boundaries for both horizontal directions and symmetric boundaries for the vertical direction. A damping zone is attached near the top boundary to reduce the effects of reflected waves. To solve the equations numerically, we use the modified Lax-Wendroff scheme. The simulation code is developed based on the numerical package CANS (Coordinated Astronomical Numerical Software) maintained by Yokoyama et al.[2]

The background atmosphere consists of three different layers. From the bottom, the layers are the adiabatically stratified convection zone, the cool isothermal photosphere/chromosphere, and the hot isothermal corona. The stratification in the convection zone ($z/H_0 < 0$) is given as

$$T = T_{\rm ph} - z \left| \frac{dT}{dz} \right|_{\rm ad}, \tag{3.8}$$

[2]CANS (Coordinated Astronomical Numerical Software) is available online at `http://www-space.eps.s.u-tokyo.ac.jp/~yokoyama/etc/cans/`.

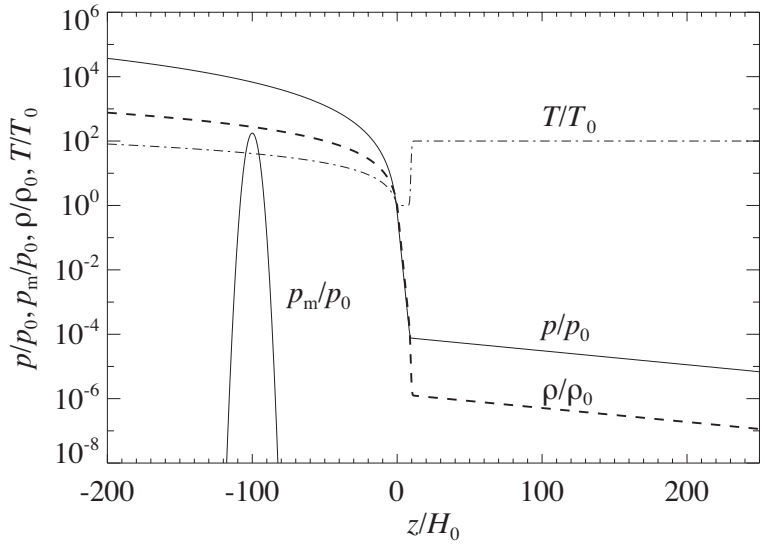

Figure 3.1: One-dimensional z-distributions of the initial background gas pressure (thick solid line), density (dashed line), and temperature (dash-dotted line). The magnetic pressure $p_{\rm m} = B^2/(8\pi)$ at $y/H_0 = 0$ is overplotted with a thin solid line. Figure reproduced from Toriumi & Yokoyama (2012).

where $T_{\rm ph}/T_0 = 1$ is the respective temperature in the photosphere/chromosphere and

$$\left|\frac{dT}{dz}\right|_{\rm ad} = \frac{\gamma - 1}{\gamma}\frac{mg_0}{k_{\rm B}} \tag{3.9}$$

is the adiabatic temperature gradient. The profile above the surface is

$$T(z) = T_{\rm ph} + \frac{1}{2}(T_{\rm cor} - T_{\rm ph})\left\{\tanh\left[\frac{z - z_{\rm cor}}{w_{\rm tr}}\right] + 1\right\}, \tag{3.10}$$

where $T_{\rm cor}/T_0 = 100$ is the temperature in the corona, $z_{\rm cor}/H_0 = 10$ is the base of the corona, and $w_{\rm tr}/H_0 = 0.5$ is the transition scale length. Based on the temperature distribution above, the pressure and density profiles are defined by the equation of static pressure balance

$$\frac{dp(z)}{dz} + \rho(z)g_0 = 0. \tag{3.11}$$

The initial flux tube is embedded in the convection zone at $z_{\rm tube}/H_0 = -100$, i.e., $z_{\rm tube} = -20$ Mm, of which the axial and azimuthal profiles are given as

$$\left\{ \begin{array}{lcl} B_x(r) & = & B_{\rm tube} \exp\left(-\dfrac{r^2}{R_{\rm tube}^2}\right) \\ B_\phi(r) & = & qrB_x(r) \end{array} \right. , \tag{3.12}$$

respectively, where $B_{\rm tube} = 67B_0 = 2.0\times10^4$ G is the axial field strength, r the radial distance from the tube's center $(y_{\rm tube}/H_0, z_{\rm tube}/H_0) = (0, -100)$, $R_{\rm tube} = 5H_0 = 1000$ km the typical radial size, and q the twist intensity which is set to be $0.1/H_0 = 5.0 \times 10^{-4}$ km^{-1} (stable against the kink instability: Linton et al., 1996). For the pressure balance between the field and the plasma, the pressure distribution inside the tube is defined as $p_{\rm i} = p(z) + \delta p_{\rm exc}$ (the subscript i denotes inside the tube), where the pressure excess $\delta p_{\rm exc}(< 0)$ is described as

$$\delta p_{\rm exc} = \frac{B_x^2(r)}{8\pi}\left[q^2\left(\frac{R_{\rm tube}^2}{2} - r^2\right) - 1\right]. \tag{3.13}$$

The density inside the tube is also defined as $\rho_{\rm i} = \rho(z) + \delta\rho_{\rm exc}$, where

$$\delta\rho_{\rm exc} = \rho(z)\frac{\delta p_{\rm exc}}{p(z)} \exp\left(-\frac{x^2}{\lambda^2}\right), \tag{3.14}$$

and $\lambda = 400H_0 = 80$ Mm is the perturbation wavelength. That is, the middle of the tube, $x/H_0 = 0$, is in thermal equilibrium with external media and is most buoyant. The buoyancy decreases as $|x|/H_0$ increases. The initial background distribution of gas pressure, density, and temperature, and the magnetic pressure are shown in Figure 3.1.

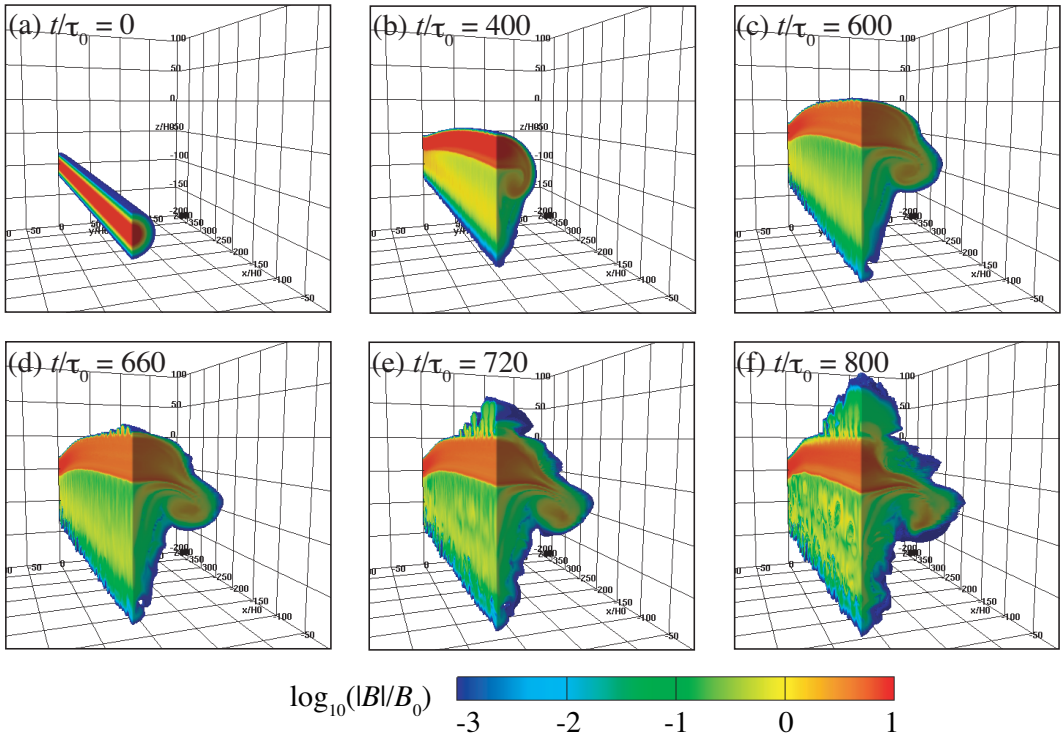

Figure 3.2: Time-evolution of the twisted emerging flux tube. Logarithmic field strength $\log_{10}(|B|/B_0)$ for six different times in a limited region ($x/H_0 < 0, y/H_0 > 0$) is shown. The solar surface ($z/H_0 = 0$) is shown by a horizontal line. Figure reproduced from Toriumi & Yokoyama (2012).

3.3 Results

3.3.1 General Evolution

Figure 3.2 shows the time evolution of the emerging twisted flux tube. Here, the logarithmic field strength $\log_{10}(|B|/B_0)$ only in the region $x/H_0 \leq 0$ and $y/H_0 \geq 0$ is plotted. Figure 3.3 shows the temporal evolution of the apex and the axis of the flux tube. Here, the apex is determined as the highest point of the grids whose total field intensities $|B|/B_0$ reach the critical value of 0.015, while the axis is selected as the location where $dB_x/dz = 0$ along $(x/H_0, y/H_0) = (0, 0)$. At $t/\tau_0 = 0$ as in Figure 3.2(a), the initial tube is placed at $z/H_0 = -100$. Due to the buoyancy of the tube itself, it rises through the convection zone ($t/\tau_0 = 400$, see Figure 3.2(b)). During the emergence, the tube expands as the external density decreases with height. While the plasma draining from the apex to both feet accelerates the rising tube, the aerodynamic drag decelerates the tube. Thus, the rise velocity levels off and reaches the terminal velocity of $\sim 0.18 C_{s0} = 1.4$ km s^{-1} (see also Section 1.3.1). The drag creates an external flow around the tube's cross-section, forming a wake behind the main tube. One can see a vortex roll at the flank of the rising tube and an elongated tail below. However, the azimuthal component (i.e., the twist) of the flux tube yields an inward curvature force to maintain the tube coherent. Due to the interchange-mode of the magnetic buoyancy instability (magnetic Rayleigh-Taylor instability), the upper surface of the rising tube becomes fluted. Figure 3.4 is a two-dimensional (x–z) slice of the rising flux tube, which shows the fluting at the top of the tube.

As the tube approaches the surface at $t/\tau_0 = 600$ as in Figure 3.2(c), it slows down and expands laterally in the y-direction to make a flat structure just beneath the photosphere (60 Mm $\times$ 20 Mm). The deceleration and the flattening occur because the unmagnetized plasma is trapped and compressed between the rising tube and the isothermally-stratified (i.e., convectively-stable) photosphere, which in turn suppresses the rising tube from below (see Section 3.3.2). Here, the outermost field lines of the flat tube (i.e., fields at the surface)

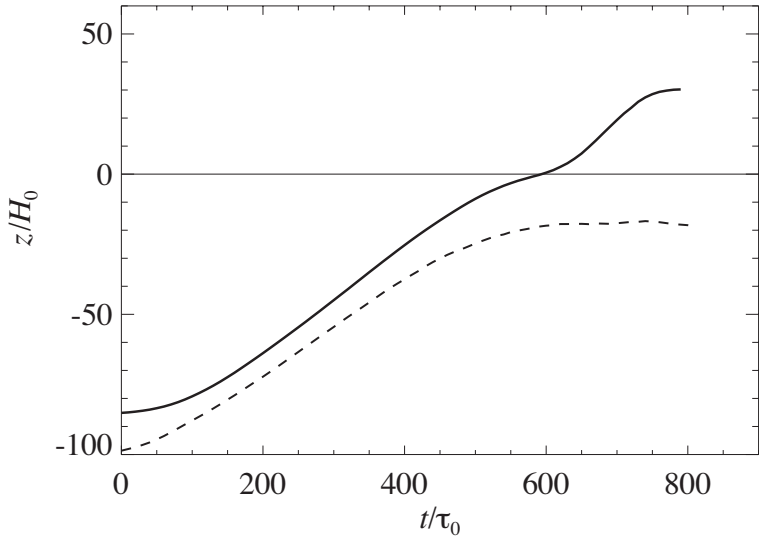

Figure 3.3: Height-time evolution of the apex (solid) and the axis (dashed) of the flux tube. The photospheric height $z/H_0 = 0$ is indicated with a horizontal line.

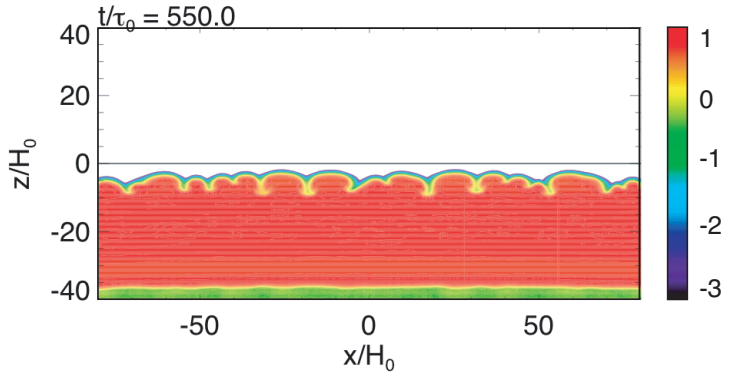

Figure 3.4: Two-dimensional (x–z) closeup of the rising flux tube at $t/\tau_0 = 550$. Logarithmic field strength $\log_{10}(|B|/B_0)$ is plotted, while the photospheric height $z/H_0 = 0$ is indicated by a horizontal line. Figure reproduced from Toriumi & Yokoyama (2012).

are mostly in the negative y-direction.

As the surficial field strength increases to satisfy the criterion for the magnetic buoyancy instability (Newcomb, 1961; Acheson, 1979), the secondary evolution to the upper atmosphere takes place at around $t/\tau_0 = 660$ as in Figure 3.2(d). We found that several magnetic domes have been built in the central area around $x/H_0 = y/H_0 = 0$ at this stage, aligned in the x-direction, each being directed in the y-direction. As the central domes develop, another several domes are newly created beside the central ones ($t/\tau_0 = 750$; Figure 3.2(e)). The domes continue growing and merge with each other in the corona. After $t/\tau_0 = 700$, the rising velocity declines again, and eventually the emerging flux reaches $z/H_0 \sim 30$ at $t/\tau_0 = 800$ (Figure 3.2(f)). The subsurface structure extends $-200 < x/H_0 < 200$ and $-40 < y/H_0 < 40$ around this time.

The whole evolution process from the convection zone to the corona is in a two-step way (see Figure 3.3). Because of the compressed material in front of the rising tube, the rise motion of the tube slows down in the top convection zone. As time goes on, the tube restarts emergence into the corona due to the magnetic buoyancy instability. Hereafter we call this process "two-step emergence."

3.3.2 Deceleration of the Flux Tube

In this section, we describe the deceleration of the rising flux tube in the convection zone, following the analysis in Toriumi & Yokoyama (2011).

According to Fan et al. (1998), the motion of the cylindrical tube rising by its magnetic buoyancy in 2D is described as

$$I\rho\frac{dV_z}{dt} = -\Delta\rho g - C_{\rm D}\frac{\rho|V_z|V_z}{\pi R}, \tag{3.15}$$

where I is the enhanced inertia factor (~ 2), $C_{\rm D}$ is the drag coefficient of order unity, and $\Delta\rho = \rho_{\rm i} - \rho$ is the density difference between the flux tube ($\rho_{\rm i}$) and the external media

($\rho_{\rm s}$). Therefore, this equation indicates that the tube's motion is determined by the upward magnetic buoyancy and the downward aerodynamic drag. This model is based on the thin-flux-tube (TFT) approximation. Namely, the tube is assumed to keep the cylindrical shape. From Equation (3.15), one can calculate the rising velocity of the tube $V_z(t)$ and its height at the center $z(t)$.

Now, let us introduce the effect of the plasma accumulation by replacing $\Delta\rho$ with

$$\begin{aligned} \Delta\rho' &= \Delta\rho + F\Delta\rho_{\rm acm} \\ &= \rho_{\rm i} - \rho_{\rm s} + F[\bar{\rho}_{\rm acm}(0) - \bar{\rho}_{\rm acm}(t)]. \end{aligned} \tag{3.16}$$

Here,

$$\bar{\rho}_{\rm acm}(0) = \frac{1}{z_{\rm ph} - z(0)} \int_{z(0)}^{z_{\rm ph}} \rho(\zeta) d\zeta \tag{3.17}$$

is the plasma on the flux tube in the initial state ($z_{\rm ph} = 0, z(0) = z_{\rm tube} = -100H_0$) and

$$\bar{\rho}_{\rm acm}(t) = \frac{1}{z_{\rm ph} - z(t)} \int_{z(t)}^{z_{\rm ph}} \rho(\zeta) d\zeta \tag{3.18}$$

is the background plasma at a given time. That is, $\Delta\rho_{\rm acm} = \bar{\rho}_{\rm acm}(0) - \bar{\rho}_{\rm acm}(t)$ corresponds to the density that would be swept by an ideal flux sheet extending horizontally, and, because of the tube's actual shape, we also consider the factor $F(< 1)$. In the present analysis, we assume F to be constant and vary this parameter to fit the analytic model to the simulation results. By replacing $\Delta\rho$ with $\Delta\rho'$, Equation (3.15) reduces to

$$I\frac{dV_z}{dt} = -\frac{\Delta\rho'}{\rho}g - \frac{C_{\rm D}}{\pi R}|V_z|V_z. \tag{3.19}$$

If the pressure balance, the mass and flux conservations, and the adiabatic evolution of the flux tube (in 2D) are all assumed, the buoyancy and the radius of the model tube can

be described by

$$-\frac{\Delta\rho'}{\rho}g = \left(-\frac{\Delta\rho}{\rho}g\right)_{z=z_{\rm tube}} \left[\frac{(\Gamma+1)-z/H_0}{(\Gamma+1)-z_{\rm tube}/H_0}\right]^{\Gamma-1} - F\frac{\Delta\rho_{\rm acm}}{\rho}g, \tag{3.20}$$

$$R(z) = R(z=z_{\rm tube})\left[\frac{(\Gamma+1)-z/H_0}{(\Gamma+1)-z_{\rm tube}/H_0}\right]^{-\Gamma/2}, \tag{3.21}$$

where $\Gamma = 1/(\gamma-1)$. Here, we use their initial values

$$\left(-\frac{\Delta\rho}{\rho}g\right)_{z=z_{\rm tube}} = \frac{\iint(-\Delta\rho/\rho)g\,B_x\,dy\,dz}{\iint B_x\,dy\,dz}, \tag{3.22}$$

and

$$R(z=z_{\rm tube}) = \left[\frac{\iint\left[(y-y_{\rm tube})^2+(z-z_{\rm tube})^2\right]B_x\,dy\,dz}{\iint B_x\,dy\,dz}\right]^{1/2} \tag{3.23}$$

(see Fan et al., 1998). Then, we can calculate the temporal evolution of the model tube, $V_z(t)$ and $z(t)$, by integrating Equation (3.19).

Figure 3.5(a) compares the vertical velocity of the simulated flux tube at the center and the analytic model. The dotted line is for the model by Fan et al. (1998) using $\Delta\rho$ (without plasma accumulation), while the solid line is our model using $\Delta\rho'$ (with plasma accumulation). The height-time evolutions of the tube center of the numerical and the analytic models are indicated in Figure 3.5(b). In this modeling, we use $C_{\rm D} = 2.5$ and $F = 0.002$. From this figure, one can see that the vertical velocity at the tube center levels off at $t/\tau_0 \sim 150$ because of the force balance between the buoyancy and the drag, which is explained by the simple TFT model (dotted line). The rising trend then turns into deceleration from around $t/\tau_0 = 350$ (at this time, $z_{\rm axis}/H_0 \sim -50$), which, however, cannot be reproduced by the TFT model. Therefore, in order to explain the deceleration of the tube, it is necessary to consider the effect of the plasma accumulation between the

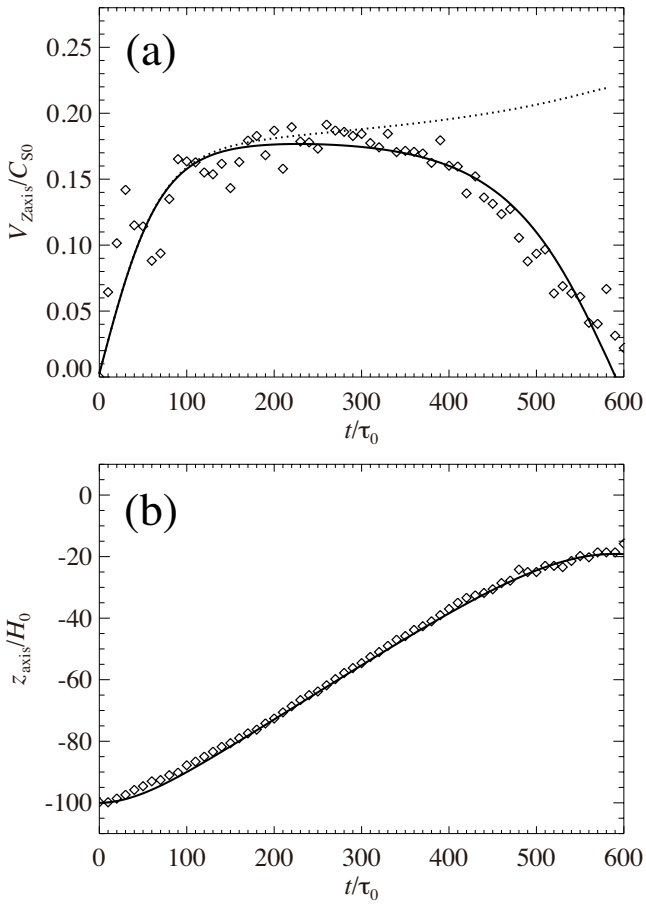

Figure 3.5: (a) Temporal variation of the vertical velocity of the rising flux tube (velocity of the axis). Diamonds indicate the simulation results, while the solid and the dotted lines are analytic models with and without considering the plasma accumulation, respectively. (b) Height-time relation of the numerical results (diamonds) and the analytic model with plasma accumulation (solid). Here, we use $C_D = 2.5$ and $F = 0.002$.

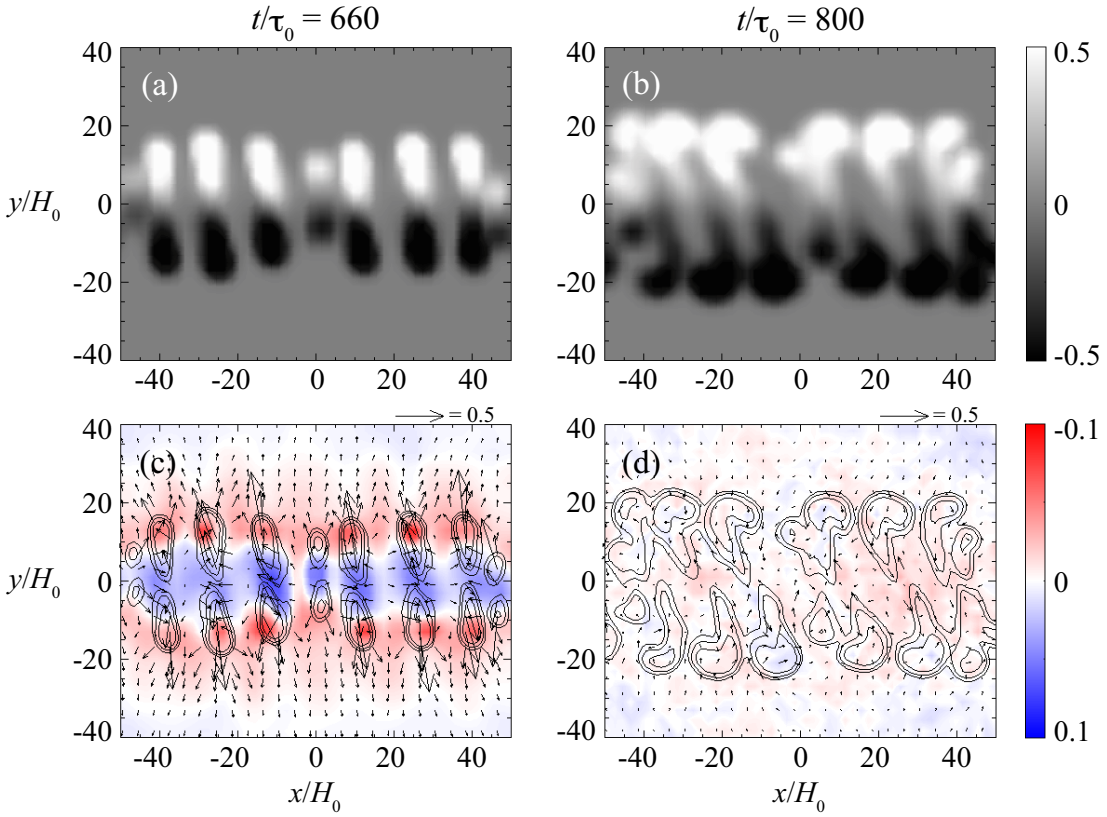

Figure 3.6: (*Top*) Time-evolution of vertical magnetic field strength B_z/B_0 at the surface $z/H_0 = 0$ (magnetogram). White (black) indicates the positive (negative) polarity. (*Bottom*) Corresponding velocity fields (Dopplergram). The vertical velocity V_z/C_{s0} (color; red is downward) and the horizontal velocity V_h/C_{s0} (arrows) are shown. Corresponding vertical field B_z/B_0 at the photosphere is over-plotted with contours. Figure reproduced from Toriumi & Yokoyama (2012).

expanding tube and the convectively-stable photosphere (solid line).

3.3.3 Magnetic Structures in the Photosphere

Figure 3.6 shows the vertical field strength (B_z/B_0; magnetogram) and the corresponding vertical velocity (V_z/C_{s0}; Dopplergram) with the horizontal velocity field (V_h/C_{s0}) at the surface $z/H_0 = 0$ at $t/\tau_0 = 660$ and 800. In the Dopplergram, red indicates a downward motion ($V_z/C_{s0} < 0$). At $t/\tau_0 \sim 610$, we observe that some blueshifts and divergent flows

appear before the flux emergence, which indicates that the compressed plasma between the rising tube and the photosphere escapes laterally at the surface (horizontal divergent flow: HDF).

At $t/\tau_0 = 660$ as in Figure 3.6(a), magnetic elements of positive and negative polarities emerge onto the surface. The absolute field strength of each polarity is more than a hundred Gauss. In Figure 3.6(c), one can find the blueshifts of a few km s^{-1} between each pair and the redshifts up to $0.12C_{\rm s0} = 1$ km s^{-1} in the core of each patch. At this time, the horizontal speed in the positive and negative polarities is at its peak (4–8 km s^{-1}), showing separative motions. These features indicate that the magnetic flux emerges upward, while the plasma drains downward to both footpoints along the field lines. Here, the surface field is mostly directed in the negative y-direction, and the wavelengths are $\lambda_\parallel \sim 20H_0$ and $\lambda_\perp \sim 15H_0$, respectively, where $\lambda_\parallel$ and $\lambda_\perp$ are the wavelengths parallel and perpendicular to the surface horizontal field. The parallel wavelength $\lambda_\parallel \sim 20H_0$ is the most unstable wavelength of the linear Parker instability at the photosphere (Appendix A).

We speculate that the wavelength perpendicular to the field $\lambda_\perp$ is determined by the wavelength of the interchange-mode instability of the flux tube before it reaches the surface. During its ascent within the convection zone, the surface of the flux tube is found to be fluted due to the interchange instability (see Figure 3.4). According to Chandrasekhar (1961, Chapter 10), when the density smoothly increases upward between the magnetized and the unmagnetized atmosphere, the growth rate of the interchange instability levels off as the wavenumber increases, and the typical wavenumber of this saturation is approximately an inverse of the density transition scale. Considering the original tube is assumed to have a Gaussian profile, i.e., $B_x(r) = B_{\rm tube}\exp\left(-r^2/R_{\rm tube}^2\right)$, and thus the density transition is also a function of $\exp\left(-r^2/R_{\rm tube}^2\right)$, the scale of this transition layer is $\sim R_{\rm tube}$. Therefore, the wavelength of this instability within the convection zone is approximately several times the original tube's radius ($R_{\rm tube} = 5H_0$), which results in the wavelength of the secondary emergence $\lambda_\perp \sim 15H_0$ at the photosphere.

At $t/\tau_0 = 800$ as in Figure 3.6(b), the magnetic pairs develop and the region extends $-120 < x/H_0 < 120$ and $-30 < y/H_0 < 30$, i.e., 48 Mm $\times$ 12 Mm. The direction of separations is found to be tilted. Here, each separated patch has formed a tadpole-like shape; $|B_z|$ up to 350 G. This configuration is formed because the newly emerged elements separate outward and catch up with the elements that emerged earlier, and stop at the edge of the region. Also, the heads of these tadpoles make two alignments at the edges, and they show shearing motion. The shearing is leftward where $y/H_0 > 0$, and rightward where $y/H_0 < 0$. In this phase, the total unsigned flux $\int_{z=0} |B_z|\, dx\, dy$ reaches up to $\sim 3.3 \times 10^{20}$ Mx. In Figure 3.6(d) the redshifts are no longer seen, which indicates that the emergence has stopped. To clarify the difference between the aligned large elements (tadpole-heads) and the tilted elements (tadpole-tails), we use the term "pores" for the heads of the tadpole-like features. Moreover, this term is used in the sense of the accumulated fields that do not reach the size of a sunspot.

Figure 3.7 shows the selected field lines plotted on the surficial magnetogram at $t/\tau_0 = 800$. Here, emerged field lines in the corona connect positive and negative polarities in the photosphere. The footpoints of coronal fields stop at the edge of the region, which is determined by the extension of the flat magnetic structure beneath the surface. That is, the size of the AR (48 Mm $\times$ 12 Mm in this case) depends on the subphotospheric flux tube (60 Mm $\times$ 20 Mm). The wavelength of the initial density deficit, λ in Equation (3.14), would be one of the parameters that determine the size of the subphotospheric structure. We also found that some field lines connect different patches deep under the surface (see Figure 3.8). Although such field lines are not undulating at around the surface, they are still reminiscent of a sea-serpent configuration and a corresponding resistive emergence process.

The tilt of magnetic elements in the central area is caused by the emergence of the inner field lines (kinematic effect). Here, the initial flux tube is uniformly twisted, and thus the pitch angle of inner fields are smaller. Therefore, the footpoints shift as the inner field lines rise. Also, the shearing of two aligned "pores" is due to the Lorentz force acting on the

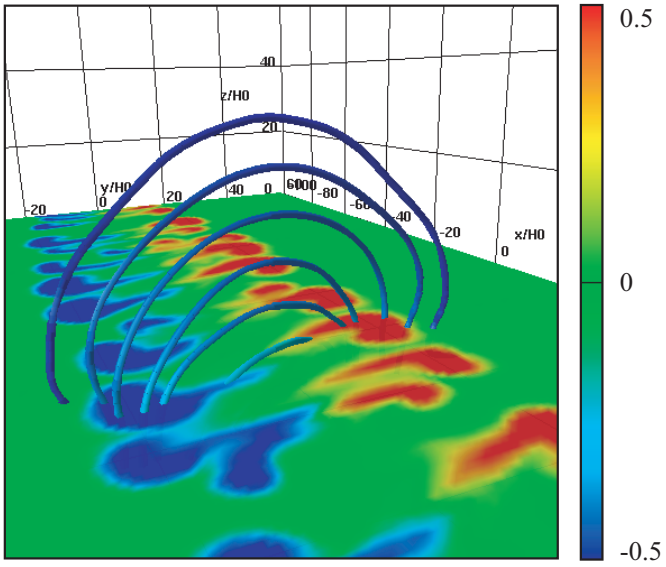

Figure 3.7: Perspective view of selected field lines that pass through the vertical axis $(x/H_0, y/H_0) = (26, 0)$ at $t/\tau_0 = 800$, plotted on the photospheric vertical field B_z/B_0. Figure reproduced from Toriumi & Yokoyama (2012).

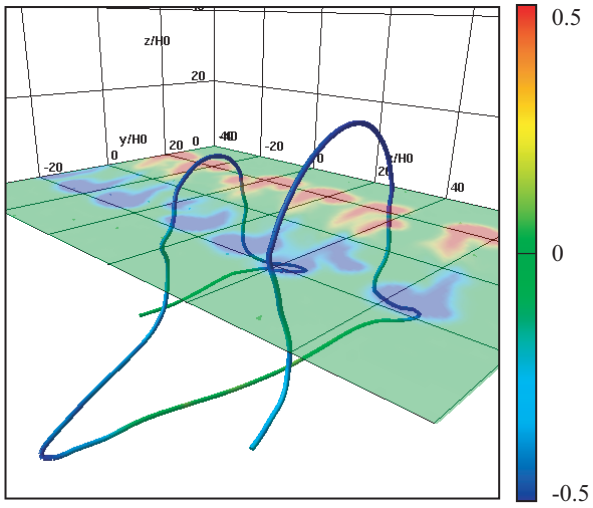

Figure 3.8: A single field line that connects different photospheric magnetic elements. Plotted is the photospheric vertical field B_z/B_0 at $t/\tau_0 = 800$, which is transparentized. Figure reproduced from Toriumi & Yokoyama (2012).

surface field (dynamic effect; see Manchester (2001) and Fan (2001)).

3.4 Summary

In this chapter, we performed a 3D MHD simulation of the emergence of a twisted flux tube. The initial tube at -20 Mm in the convection zone has a field strength of 2.0×10^4 G, a total flux of 6.3×10^{20} Mx, and a twist of 5.0×10^{-4} km^{-1}, which starts rising due to its own magnetic buoyancy. On reaching the surface after $t \sim 2.8$ hr, the tube decelerates and extends horizontally (60 Mm $\times$ 20 Mm) owing to the convectively stable photosphere ahead of the tube. As the surface field satisfies the criterion for the magnetic buoyancy instability, the field emerges again into the upper atmosphere after $t \sim 4.1$ hr. Eventually, several magnetic domes attain a height of ~ 6000 km at $t \sim 5.6$ hr. The size of the AR grows to 48 Mm $\times$ 12 Mm, and the photospheric flux amounts to 3.3×10^{20} Mx. The entire evolution can be described as the "two-step emergence" of a rising magnetic flux.

We also observed multiple separation events of the magnetic elements at the photosphere, posterior to the horizontal escaping flow of the compressed plasma. Such separating elements move apart from each other at the rate of 4–8 km s^{-1} and stop at the edges of the AR, which is determined by the extension of the subphotospheric field. The multiple separations are the results of the interchange-mode instability of the rising tube while in the convection zone. The magnetic elements then gather at the edges to make two alignments of the "pores" (tadpole-heads). The alignments show shearing motions at the rate of ~ 0.5 km s^{-1}, which is explained by the inner field emergence (kinematic effect) and the Lorentz force effect (dynamic effect). Upflows of a few km s^{-1} and downflows up to 1 km s^{-1} are observed in the emergent areas and in the cores of surface fields, respectively. As far as we know, we have never observed such photospheric features, especially the multiple separations, in previous 3D calculations applying flux tube as an initial condition (e.g., Fan, 2001; Archontis et al., 2004). Note that some calculations using flux sheets showed multiple separations via similar

instabilities (Isobe et al., 2005; Archontis & Hood, 2009).

3.5 Discussion

The features found in this calculation are strongly reminiscent of the observations of NOAA AR 5617 by Strous et al. (1996) and Strous & Zwaan (1999). They found that faculae of both polarities separate from each other toward the edges of the region, which is similar to our findings of multiple separations. Also, the shearing motions of the aligned tadpole-heads are consistent with the pores moving along the edges of the region toward the main sunspots. Figure 3.9 gives a comparison between Strous & Zwaan (1999)'s observation and our simulation. This figure clearly shows the consistency between the two. The difference of the tilt of magnetic elements between these two cases is caused by the twist direction. We assumed a right-handed tube in the initial state, which is favorable for the southern hemisphere (Pevtsov et al., 1995). AR 5617 appeared in the northern hemisphere, which yields a left-handed twist.

The summary of the comparison between our results and the observations by Strous et al. (1996) and Strous & Zwaan (1999) is presented in Table 3.1. The size of AR and the velocities are consistent between the two. As for the difference of separation speeds, note that Harvey & Martin (1973) observed that faculae of opposite polarities separate initially at the rate of > 2 km s^{-1}. The photospheric total flux is one digit smaller than the observed value, and we did not find any major sunspots in our AR. These differences may be because, in our calculation, the rising tube stops in 1.4 hours after it appears at the surface. The age of AR 5617 was estimated to be 6.5–7.5 hours old at the beginning of the observation and 8–9 hours old at the end. In the observation, emergence events showed undulatory structures with a typical wavelength of 8 Mm, while, in our case, each field line does not show undulation at around the surface. Such undulating features might be found in the more resolved calculations or in the calculations including thermal convection (Isobe et al., 2007;

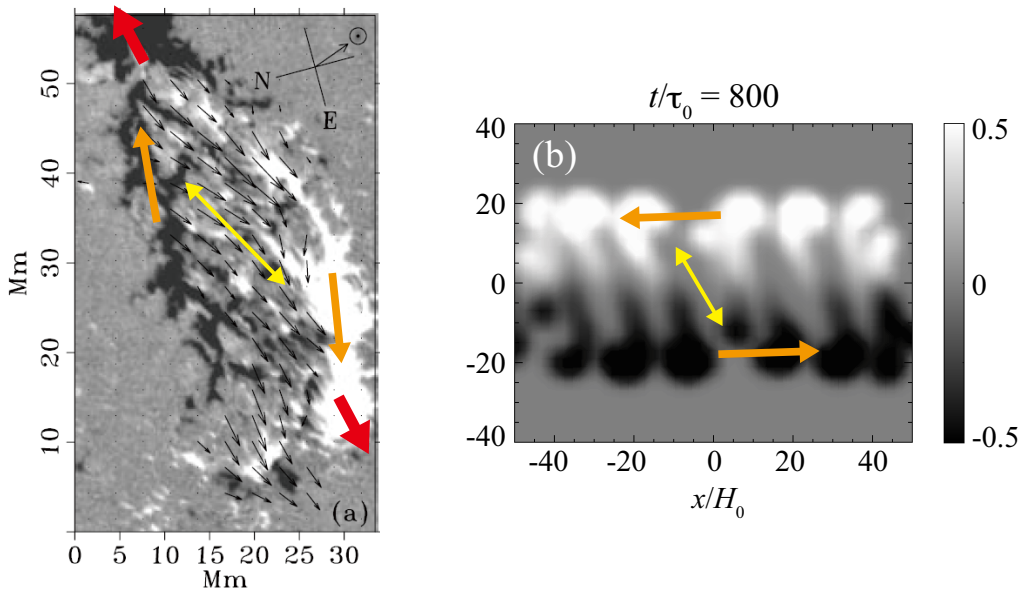

Figure 3.9: Comparison between the AR observation and the numerical results. (a) Photospheric magnetogram that shows the separation of faculae and shearing of pores. Figure reproduced from Strous & Zwaan (1999) by permission of the AAS. Color arrows are overlaid. (b) Photospheric magnetogram (B_z/B_0) in our simulation which also shows the separation and the shear motion. Figure reproduced from Toriumi & Yokoyama (2012). Color arrows are overlaid.

Table 3.1: Summary of comparison with AR 5617 (Toriumi & Yokoyama, 2012)

	Simulation results	AR 5617[a]
Size of the region	48 Mm × 12 Mm	50 Mm × 30 Mm
Vertical unsigned total flux	3.3×10^{20} Mx	4×10^{21} Mx
Age from the appearance	0–1.4 h	6.5–9 h
Separation speed	4–8 km s^{-1}	0.84 km s^{-1} [b]
Shearing speed	~ 0.5 km s^{-1}	0.73 km s^{-1} [c]
Upflow velocity	$\sim$ a few km s^{-1}	0.86 km s^{-1} [d]
Downflow velocity	$\lesssim 1$ km s^{-1}	1.26 km s^{-1} [e]
Wavelength of emergence pattern	-	~ 8 Mm

[a]Strous et al. (1996) and Strous & Zwaan (1999).
[b]Separation of facular elements.
[c]Separation of pores.
[d]Upflow in an emergent region.
[e]Downflow in a facula.

Cheung et al., 2010). Strous & Zwaan (1999) summarized their observations as a model in which each emergence event (separation) occurs in a single vertical sheet, which forms a series of sheets aligned in a parallel fashion (see Figure 1.6 in Chapter 1). From our results, the separations are explained as the consequence of the interchange-mode instability of the flattened flux tube beneath the surface (see e.g. Figure 3.4).

On the basis of the numerical results in this chapter, we suggest a theoretical picture of the flux emergence and the formation of an AR through the surface, which includes Strous & Zwaan (1999)'s model. Our model is schematically illustrated in Figure 3.10. (1) The flux tube rises through the convection zone due to magnetic buoyancy. On approaching the surface, the tube decelerates and becomes flattened because of the photosphere in front of the rising tube. The compressed unmagnetized plasma between the rising tube and the photosphere escapes horizontally around the surface layer before the tube appears at the visible surface. (2) When the photospheric field satisfies the criterion for the magnetic buoyancy instability, further evolution to the corona breaks out. Due to the interchange-mode instability, photospheric magnetogram shows multiple separation events. The separated elements

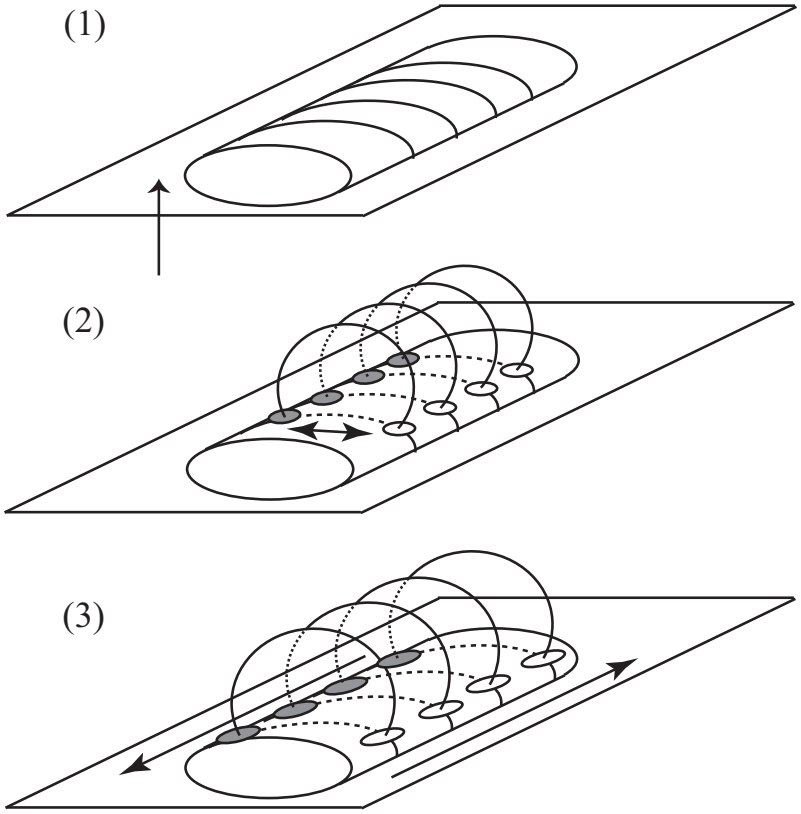

Figure 3.10: Picture of flux tube emergence and the formation of an AR derived from the calculation results in this chapter. Solar surface is indicated by a horizontal slice. (1) Flux tube rising through the convection zone decelerates to form a flat structure beneath the surface. (2) Magnetic elements of opposite polarities are observed to separate due to the interchange-mode instability. White and black ellipses indicate the positive and negative elements. These elements gather at the edges of the AR to make two alignments of pores. (3) Aligned pores show shearing motion when inner fields emerge. Figure reproduced from Toriumi & Yokoyama (2012).

reach the edges of the region, whose size is determined by the subsurface field. These elements then make two alignments of pores. Compare this panel with Figure 1.6 in Chapter 1. (3) As the emergence continues, inner fields of the flux tube rise and footpoints shift to show shearing motions. Lorentz force also drives the pores to shear.

The initial condition of the present experiment ($B_{\rm tube} = 67B_0 = 2.0 \times 10^4$ G, $R_{\rm tube} = 5H_0 = 1000$ km, and $q = 0.1/H_0 = 5.0 \times 10^{-4}$ km^{-1}) is the same as that of Case 5 of our 2D cross-sectional calculation in Toriumi & Yokoyama (2011). One of the basic differences between these two simulation results is the rising time from the initial depth of -20 Mm to the surface. In 2D calculation, the flux tube reached the surface in $t \sim 550\tau_0 = 3.8$ hr, while, in 3D case, it took $t \sim 600\tau_0 = 4.2$ hr. That is, the 3D tube rises slower. In 3D case, plasma in the tube apex drains down along the field lines to the both feet of the tube, which drives the tube more buoyant. At the same time, in the 3D regime, the magnetic curvature force pulls down the rising tube. The time difference between the two cases indicates that the curvature force dominates the draining effect in the present 3D experiment.

In the solar interior as well as in the photosphere, several classes of convection may affect the rise of magnetic flux. Recent observations by SOT on board *Hinode* satellite have revealed the convective nature of the surface field (Lites, 2009). Stronger pores ($>$ 1kG) or sunspots, which are not found in this calculation without convection, would be formed through the convective collapse process (Parker, 1978). Large-scale upflow supports the rising of the tube, and more flux could be transported to the surface (Fan et al., 2003). Surface convection creates undulating fields, and the cancellation of such fields removes the mass trapped in the U-loop (Isobe et al., 2007; Cheung et al., 2010). This process accelerates the density draining from the surface layer, which may be important to the spot formation. On the other hand, Stein et al. (2011) reported that flux of 20 kG in their convective experiment, the same as used in ours, is too strong, because it produces large, hot, bright granules at the surface, which are not seen in the Sun. This is an interesting difference between the two types of calculations. It should be noted that the initial settings are different in the

two cases; we used an initial horizontal flux tube in the marginally-unstable convection zone, while, in Stein et al. (2011)'s calculation, uniform horizontal fields are advected into the computational domain by the convective upflows from the bottom boundary. More theoretical and observational studies are needed on the effects of the convection in the whole flux emergence process.

Chapter 4

Flux Emergence Simulation: Parametric Survey[1]

4.1 Introduction

In the previous chapter, we carried out a three-dimensional magnetohydrodynamic (3D MHD) simulation of an emerging magnetic flux tube from the convection zone to the corona, aiming to investigate the flux emergence in a large scale. As a result, the initial flux placed at a depth of -20 Mm starts its emergence in the solar interior, which then slows down gradually in the uppermost convection zone. This is because the plasma pushed up by the emerging flux rises to the isothermally-stratified (i.e. convectively-stable) surface layer and is then trapped and compressed between them, which, in turn, suppresses the rising flux from below. Such compressed plasma will escape laterally around the photospheric layer from the rising flux as a horizontal divergent flow (HDF), just before the flux itself reaches the surface. Observational studies of the HDF will be shown later in Chapters 7 and 8.

In this chapter, we report the results of the parametric survey of the 3D MHD flux emergence simulation. The aims of this study are to investigate which force drives the

[1]Most part of this chapter was published in Astronomy & Astrophysics (Toriumi & Yokoyama, 2013)

Table 4.1: Summary of the simulation cases (Toriumi & Yokoyama, 2013)

Case[a]	Field strength $B_{\rm tube}/B_0$	Twist qH_0	Wavelength λ/H_0
A	67	0.1	400
B	133	0.1	400
C	33	0.1	400
D	67	0.2	400
E	67	0.05	400
F	67	0.1	100
G	67	0.1	25

[a]Case A is the same as that simulated in Chapter 3. Cases B and C are for different field strengths than that of case A, while D and E are for different twists, and F and G different wavelengths.

HDF and to observe the dependence of the HDF on the parameters in the simulation. One important feature of this HDF study is that it can be a probe for exploring the physical state of the magnetic field in the upper convection zone. That is, we may be able to obtain valuable information on the subsurface layers from the direct optical observation at the surface. Therefore, in this numerical study, we vary the parameters of the initial flux tube, and then check the characteristics of the consequent HDF seen at the surface layer.

In the next section we briefly mention the basic setup of the numerical calculation. In Section 4.3, we show the results of the parametric survey, and, in Section 4.4, we provide some analytic explanations of the results. We finally summarize this chapter in Section 4.5.

4.2 Numerical Setup

The basic MHD equations, normalizing units, computational domain size, grid spacings, boundary conditions, and background stratification are the same as those in Chapter 3.

In this study, we vary the parameters that define the initial flux tube. The initial tube

is given as

$$\begin{cases} B_x(r) &= B_{\rm tube} \exp\left(-\dfrac{r^2}{R_{\rm tube}^2}\right) \\ B_\phi(r) &= qrB_x(r) \end{cases}, \tag{4.1}$$

respectively, where $B_{\rm tube}$ is the axial field strength, r the radial distance from the tube's center, $R_{\rm tube}$ the typical radial size, and q the twist intensity. In order to instigate a buoyant emergence, the initial tube is endowed with a density deficit of a function of $\exp\left(-x^2/\lambda^2\right)$, where λ is the perturbation wavelength. The parameters we varied are the field strength $B_{\rm tube}$, the twist q, and the perturbation wavelength λ. Table 4.1 summarizes the cases in this study. The case simulated in Chapter 3 is named here as case A, while cases B–F are for different field strength, twist, and wavelength than those of A. Here we fixed the tube's radial size at $R_{\rm tube}/H_0 = 5$ for all the cases. It should be noted that the critical twist for the kink instability is $qH_0 = 0.2$ (Linton et al., 1996). Therefore, all the tubes examined here are stable or, at least, marginally stable against the instability at the beginning of the calculation.

4.3 Simulation Results

4.3.1 General Evolution

Figure 4.1 shows the temporal evolution of the apex of the rising tube, $z_{\rm top}(t)$. Also, in Figure 4.2, we plot the total field strength, $\log_{10}\left(|B|/B_0\right)$, of the initial condition for case A and the final states for all the cases. As can be seen in Figure 4.1(a), it is clear that the tubes with stronger field $B_{\rm tube}$ rise faster. The rising speed of each tube in the convection zone is in simple proportion to the initial field strength, which is well in accordance with Murray et al. (2006) and other previous studies. Case A, which has a middle field strength, shows deceleration just before it reaches the surface. This deceleration is the result of the plasma accumulation, which is caused by the trapping of material between the rising tube

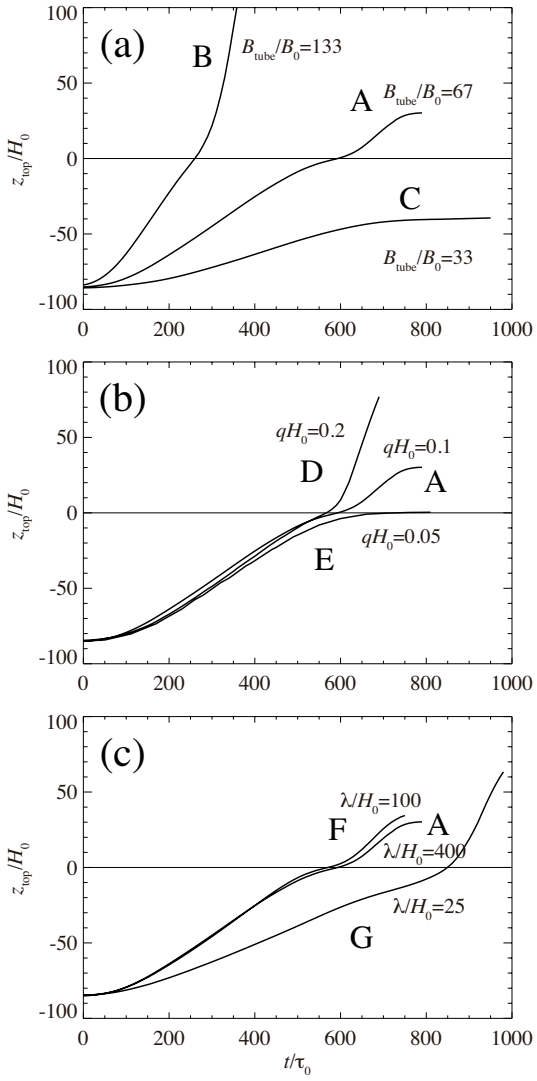

Figure 4.1: Height-time evolution of the flux tube. (a) Cases for different axial field strength $B_{\rm tube}$. (b) Cases for different twist intensity q. (c) Cases for different perturbation wavelength λ. Figure reproduced from Toriumi & Yokoyama (2013).

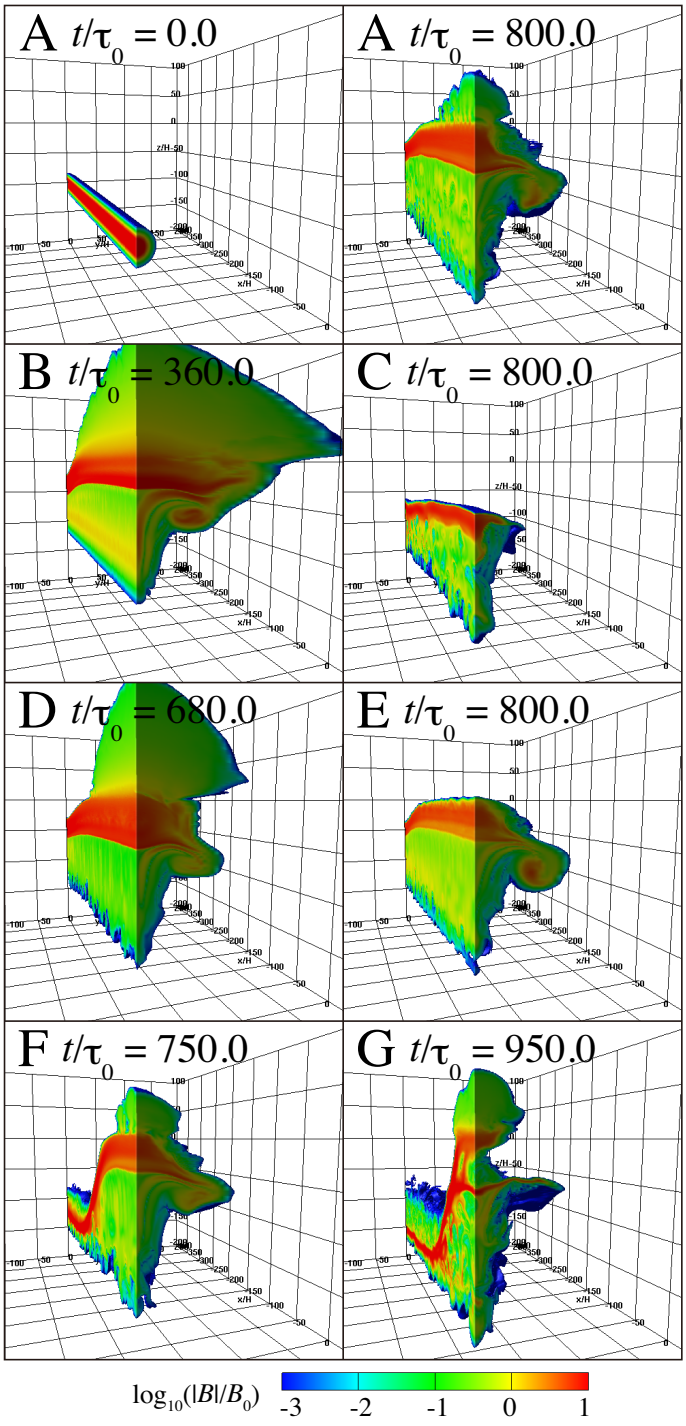

Figure 4.2: Total magnetic field strength of the initial condition for case A and the final states for cases A to G, plotted over the range $-400 \leq x/H_0 \leq 0$ and $0 \leq y/H_0 \leq 200$. Figure reproduced from Toriumi & Yokoyama (2013).

and the isothermally-stratified photosphere above the tube. After a while, the tube then starts further emergence into the atmosphere (see the top panels of Figure 4.2). As for the strongest case in B, the accumulation becomes less marked, and thus the tube almost directly passes through the surface layer and expands into the higher corona, without undergoing strong deceleration (Figure 4.2B). When the field is very weak, as in case C, the tube stops its emergence halfway to the surface, since the tube's buoyancy is not strong enough to continue its emergence (Figure 4.2C).

Figure 4.1(b) shows the evolution with different twist q. In this figure, all three tubes are seen to rise almost at the same rate in the convection zone, which is again consistent with previous studies (e.g. Murray et al., 2006). When the twist is weak and thus cannot hold the coherency (case E), the tube expands and suffers deformation by aerodynamic drag. As a result, the tube cannot maintain a strong enough magnetic field to continue its further emergence (Figure 4.2E).

Figure 4.1(c) compares three cases with different wavelengths of the initial perturbation. The initial wavelength is crucial for two factors: the curvature force (magnetic tension), which pulls down the rising tube, and the drainage of the internal media due to gravity, which encourages the emergence. When the wavelength is smaller, the curvature force is expected to be stronger, while the drainage becomes more effective. In Figure 4.1(c) the rising velocities of cases A and F are almost the same, which indicates that both effects cancel each other out. However, the shortest wavelength tube (case G) shows a much slower emergence rate in the convection zone, which indicates that the curvature force is more effective and slows down the emergence. As for the emergence above the surface layer, on the contrary, Figure 4.1(c) shows an exactly opposite trend that the rising is much faster when the wavelength is shortest (case G). One may find that, in Figure 4.2G, the main tube remains in the convection zone at around $z/H_0 = -50$, while the upper part has been detached from the main tube and has started further emergence into the atmosphere. The reason for the rapid ascent may be because, in the shortest wavelength case, namely, in the

highly curved loops, the draining of the plasma from the apex is more effective, which helps the faster emergence above the photosphere.

4.3.2 Driver of the HDF

Figure 4.3(a) is the cross-sectional distribution of the field strength of Case A. The plotted value is the logarithmic field strength $\log_{10}(|B|/B_0)$ averaged over $6.5 \leq x/H_0 \leq 13.5$, i.e., around $x/H_0 = 10$. The reason we choose this x-range is to select one folded structure at the tube's surface (see Figure 3.6 in Chapter 3). In Figure 4.3(a), there is a flow field in front of the rising flux tube, which is flowing from the apex to the flanks of the tube. One characteristic of this plasma layer is the horizontal divergent flow (HDF) that is seen at the solar surface just before the flux tube itself emerges.

To investigate which force drives the HDF, in Figures 4.3(b) and (c), we plot the horizontal flow velocity V_y, pressure gradient $-\partial p/\partial y$, and magnetic pressure gradient $-\partial p_{\rm m}/\partial y$, averaged over $6.5 \leq x/H_0 \leq 13.5$ and $-10 \leq z/H_0 \leq 0$, where $p_{\rm m} = B^2/(8\pi)$. Magnetic tension is not plotted here, since it is rather small compared to the two other forces. At $t/\tau_0 = 500$, before the tube reaches the uppermost convection zone, $z/H_0 > -10$, the horizontal flow is clearly driven only by the gas pressure, and, of course, the magnetic pressure gradient is zero. Therefore, we can conclude that the HDF prior to the flux appearance is caused by the pressure gradient. This is consistent with other numerical simulations including thermal convection (Cheung et al., 2010). At $t/\tau_0 = 600$, the shallow layer is covered by the rising tube and the gas pressure gradient reverses its sign. Instead, the magnetic pressure gradient becomes dominant enough to drive the flow.

4.3.3 Dependence of the HDF

In this subsection, we show the dependence of the HDF on the initial field strength $B_{\rm tube}$ and on the twist q. The investigated parameters are the duration of the HDF (from the HDF start to flux appearance), $\Delta t/\tau_0$, and the maximum HDF velocity, $\max(V_y)/C_{\rm s0}$, during this time

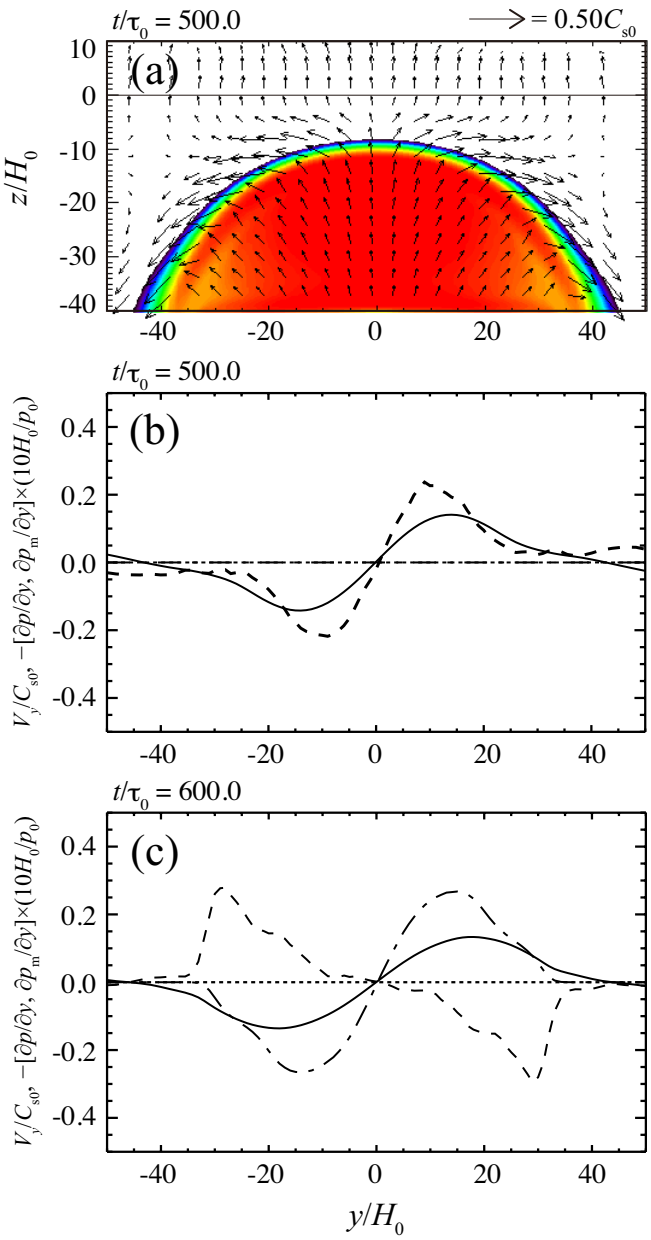

Figure 4.3: (a) Cross-sectional profile of the rising magnetic flux tube (case A). Plotted value is the logarithmic field strength $\log_{10}(|B|/B_0)$ averaged over $6.5 \leq x/H_0 \leq 13.5$, at the time $t/\tau_0 = 500$. The color saturates at $|B|/B_0 = 1.0$ (red) and -4.0 (purple). (b) Horizontal velocity V_y/C_{s0} (thick solid), pressure gradient $-\partial p/\partial y \times (10H_0/p_0)$ (dashed), and magnetic pressure gradient $-\partial p_m/\partial y \times (10H_0/p_0)$ (dash-dotted), at $t/\tau_0 = 500$. (c) Same as (b) but for $t/\tau_0 = 600$. Figure reproduced from Toriumi & Yokoyama (2013).

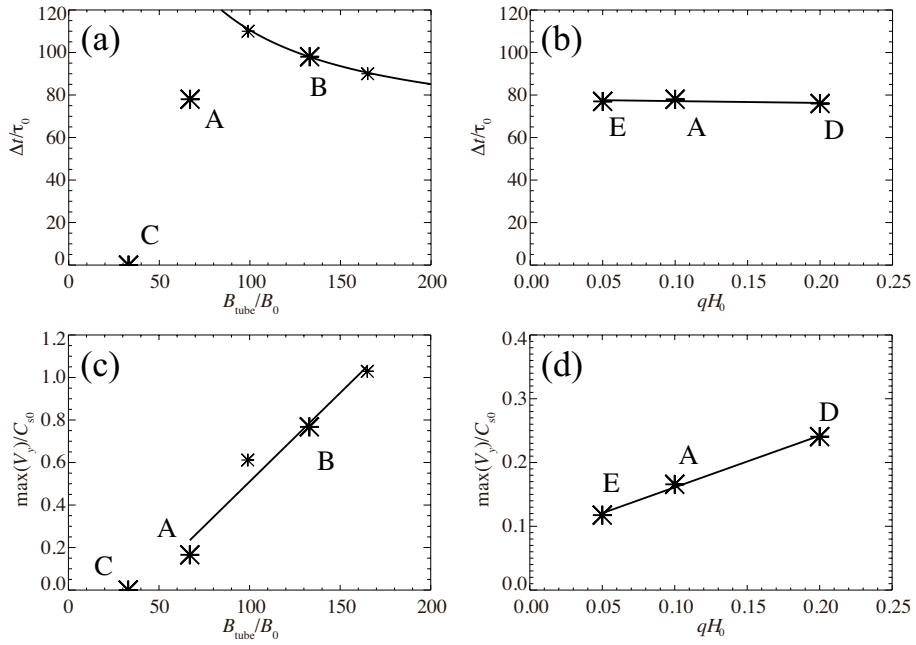

Figure 4.4: (a) Dependence of the HDF duration Δt on the field strength $B_{\rm tube}$, and (b) that on the twist q. (c) Dependence of of the maximum HDF speed $\max(V_y)$ on the field strength $B_{\rm tube}$, and (d) that on the twist q. In panels (a) and (c), we also plot other field strength cases, which are indicated by smaller asterisks. Solid lines are the fitted curves; (a) $\Delta t/\tau_0 = 5.08 \times 10^3/(B_{\rm tube}/B_0) + 5.97 \times 10$, (b) $\Delta t/\tau_0 = -8.57 \times (qH_0) + 7.80 \times 10$, (c) $\max(V_y)/C_{\rm s0} = 8.35 \times 10^{-3} \times (B_{\rm tube}/B_0) - 3.26 \times 10^{-1}$, (d) $\max(V_y)/C_{\rm s0} = 8.10 \times 10^{-1} \times (qH_0) + 8.02 \times 10^{-2}$. Figure reproduced from Toriumi & Yokoyama (2013).

period. Here we defined the start time of the HDF as "when the horizontal speed V_y in the horizontal range $-50 \leq y/H_0 \leq 50$, averaged over $6.5 \leq x/H_0 \leq 13.5$ and $-10 \leq z/H_0 \leq 0$, exceeds $0.06C_{\rm s}$ ($= 0.5$ km s^{-1})" and the flux appearance as "when the field strength $|B|$ in this range exceeds $0.67B_0$ ($= 200$ G)."

Figures 4.4(a) and (b) show the dependence of the duration on the field strength $B_{\rm tube}$ and the twist q. Panel (a) is the comparison among the different field strength cases. A comparison of cases A and B, the middle and stronger field tubes, shows that the time duration is longer for the stronger field. If other stronger cases are considered (here we also plot two stronger tube cases other than A, B, and C), however, it may be found that the duration decreases with field strength. Thus, we can divide these cases into two groups:

stronger cases that show a decreasing trend, which is fitted by a function of $B_{\rm tube}^{-1}$, and a middle case that deviates from the decreasing trend. The weakest tube, case C, did not reach the surface. That is why the duration is 0 for case C. In contrast, in panel (b), the duration is almost constant for the different twist cases.

Dependence of the maximum HDF speed, $\max(V_{\rm y})$, is shown in Figures 4.4(c) and (d). Panel (c) indicates the positive linear correlation with the field strength $B_{\rm tube}$. Again, the speed of case B is plotted as zero, since it did not reach the surface. Note that, in panel (a), we found a gap between the middle-field regime and the stronger-field regime. Thus the linear fitting in panel (c) might not reflect the actual trend. Nevertheless, the maximum speed basically increases with field strength. In panel (d), we can see that the maximum HDF velocity is clearly proportional to the initial twist q.

4.4 Analytic Explanation

In this section, the dependencies of the rising speed and of the HDF on the physical parameters obtained in Section 4.3 are analytically explained.

4.4.1 Rising Speed

In Section 4.3.1, we found that the rising speed of the flux tube is proportional to the field strength $B_{\rm tube}$ and the dependence on the twist q is significantly small. The curvature is effective for the flux tube with the shortest wavelength λ. Here we assume that the rising speed in the convection zone is given as a terminal velocity where the buoyancy of the tube equals the aerodynamic drag by the surrounding flow field (Parker, 1975; Moreno-Insertis & Emonet, 1996; see also Section 1.3.1) and the downward magnetic tension. Buoyancy, dynamic drag, and tension force acting on a unit cross-sectional area are written as

$$f_{\rm B} = \frac{B^2}{8\pi H_{\rm p}}, \tag{4.2}$$

$$f_{\rm D} = C_{\rm D}\frac{\rho V_z^2}{\pi R_{\rm tube}}, \tag{4.3}$$

and

$$f_{\rm T} = \frac{B^2}{4\pi R_{\rm c}}, \tag{4.4}$$

respectively, where $H_{\rm p} = H_0(T/T_0)$ denotes the local pressure scale height, V_z the tube's vertical speed, $C_{\rm D}$ the drag coefficient of order unity, and $R_{\rm c}$ is the radius of curvature. The mechanical balance $f_{\rm B} = f_{\rm D} + f_{\rm T}$ yields the terminal velocity

$$V_\infty^2 = \frac{R_{\rm tube}B^2}{4C_{\rm D}\rho}\left(\frac{1}{2H_{\rm p}} - \frac{1}{R_{\rm c}}\right). \tag{4.5}$$

First, let us discuss the curvature effect. In Equation (4.5), the tension force is negligible for $R_{\rm c} \to \infty$, while the tension becomes effective when $R_{\rm c} \sim 2H_{\rm p}$. The relationship between the curvature radius $R_{\rm c}$ and the perturbation wavelength λ is illustrated as Figure 4.5(a). Here, we write the tube's height as $\Delta z = z_{\rm top}(t) - z_{\rm tube}$. From this figure, we have

$$\begin{cases} R_{\rm c} - R_{\rm c}\cos\theta = \Delta z \\ R_{\rm c}\sin\theta = \lambda \end{cases}, \tag{4.6}$$

which gives

$$\lambda = \sqrt{2R_{\rm c}\Delta z - (\Delta z)^2}. \tag{4.7}$$

Thus, using the condition $R_{\rm c} \sim 2H_{\rm p}$, we obtain the critical wavelength for the tension to be effective:

$$\lambda_{\rm c} = \sqrt{4H_{\rm p}\Delta z - (\Delta z)^2}. \tag{4.8}$$

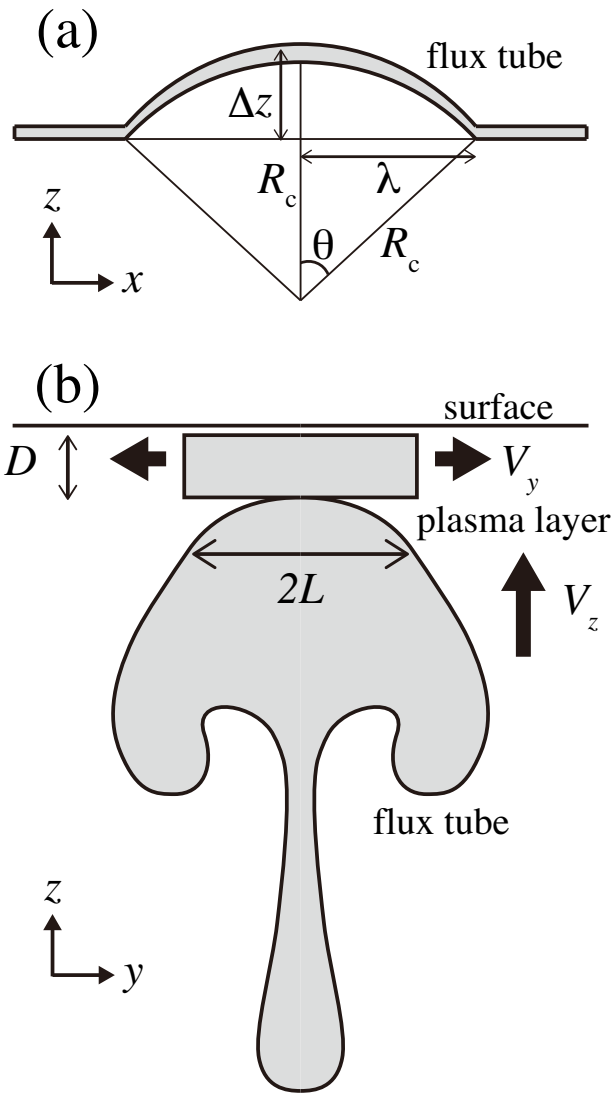

Figure 4.5: (a) Cross-section of the rising flux tube along the axis (in the $x - z$ plane). (b) Cross-section of the rising flux tube and the plasma layer ahead of the tube (in the $y - z$ plane). Figure reproduced from Toriumi & Yokoyama (2013).

For instance, when the tube is halfway to the surface, i.e., $z_{\rm top}/H_0 = -50$ and thus $\Delta z/H_0 = 50$, the local pressure scale height at this depth is $H_{\rm p}/H_0 \sim 21$. Therefore, the critical wavelength is evaluated to be $\lambda_{\rm c} \sim 41.2H_0$, and the flux tube with a wavelength smaller than this value will be resisted by the tension force, $\lambda \lesssim \lambda_{\rm c} \sim 41.2H_0$. In Figure 4.1(c), we found that only the tube with $\lambda = 25H_0$ shows slower emergence due to the effective curvature force, which satisfies the condition $\lambda \lesssim \lambda_{\rm c}$.

Next, let us go on to the dependencies on the field strength and the twist, by considering $R_{\rm c} \to \infty$. Now the equation of the terminal velocity, Equation (4.5), reduces to

$$\begin{aligned} V_\infty &= \sqrt{\frac{R_{\rm tube}}{8C_{\rm D}H_{\rm p}\rho}}\, B_{\rm tube}\sqrt{1+q^2r^2}\, \exp\left(-\frac{r^2}{R_{\rm tube}^2}\right) \\ &\sim \sqrt{\frac{e^{-2}R_{\rm tube}}{8C_{\rm D}H_{\rm p}\rho}}\, B_{\rm tube}\sqrt{1+q^2R_{\rm tube}^2}. \end{aligned} \tag{4.9}$$

Here, in the first line we use Equation (4.1) and in the second line we assume $r \sim R_{\rm tube}$. From this equation, we see that the rising velocity is in simple proportion to the initial field strength $B_{\rm tube}$ when q is constant. If we change q with considering $R_{\rm tube} = 5H_0$, for $qH_0 = [0.05, 0.1, 0.2]$, the third term in the right-hand-side of Equation (4.9) gives

$$\sqrt{1+q^2R_{\rm tube}^2} = \begin{cases} 1.03 \\ 1.12 \\ 1.4 \end{cases}. \tag{4.10}$$

That is, the third term has only a weak positive correlation to the value of q. Therefore, the rising velocity of the flux tube is proportional to the field strength, while it is almost independent of the initial twist. The trend of the rising speed found in Section 4.3.1 is thus explained.

Note here that, if we substitute $H_{\rm p} \sim 40H_0$, $\rho \sim 275\rho_0$ (values at $z_{\rm tube}$), $B_{\rm tube} = 67B_0$, $q = 0.1/H_0$, and $R_{\rm tube} = 5H_0$ (values for case A) and assume $C_{\rm D} \sim 1$ in Equation (4.9), we

obtain $V_\infty = 0.21 C_{s0}$, which is comparable to the simulation result $\sim 0.17 C_{s0}$ (Figure 4.1). This agreement indicates that Equation (4.9) is a rather reasonable estimation of the tube's rising speed (see also Parker, 1975; Moreno-Insertis & Emonet, 1996).

4.4.2 Dependence on the Twist

We found in Section 4.3.3 that when the twist q is varied while the field strength $B_{\rm tube}$ is kept constant, the duration of the HDF Δt is almost constant while the maximum horizontal speed $\max(V_y)$ is proportional to q.

This feature can be explained by considering a simple model illustrated as Figure 4.5(b). Here the flux tube with a head size of $2L$ is rising at V_z, which pushes the plasma layer with a thickness D. The thickness D is also described as $D \sim |z_{\rm top}(t)|$, where $z_{\rm top}(t) = z_{\rm tube} + \int_0^t V_z(t')dt'$. From the discussion in Section 4.4.1, V_z and thus D are independent of q, which indicates that the HDF duration $\Delta t \simeq D/V_z$ is also independent of q.

If we write the outflow speed as V_y, mass flux conservation can be written as

$$V_y = \frac{V_z}{D} L. \tag{4.11}$$

Here, V_z/D is independent of q. The head size of the tube L, however, depends on the twist q, since the aerodynamic drag peels away the tube's outer flux and its amount depends on the twist. The head size remains larger with q, which results in the stronger HDF; $V_y \propto L(q)$. Thus the maximum speed, $\max(V_y)$, will also depend on q.

It should be noted here that L and q are not always linearly correlated. According to Moreno-Insertis & Emonet (1996), the boundary of the expanded tube is well defined by the equipartition surface, where the kinetic energy density equals the magnetic energy density of the azimuthal field:

$$\frac{1}{2}\rho V^2 = \frac{B_\phi^2}{8\pi}. \tag{4.12}$$

On the basis of an analogy from Equation (4.1), the profile of the expanded tube at the equipartition surface, where the radial distance is r_1 (the subscript "1" indicates the expanded tube), is assumed to be written as

$$\begin{cases} B_x(r_1) &= B_{\rm tube1} \exp\left(-\dfrac{r_1^2}{R_{\rm tube1}^2}\right) \\ B_\phi(r_1) &= q r_1 B_x(r_1) \end{cases}, \tag{4.13}$$

where $B_{\rm tube1}$ and $R_{\rm tube1}$ are the axial field and the typical radius, respectively. Then, Equation (4.12) reduces to

$$\frac{r_1}{R_{\rm tube1}} \exp\left(-\frac{r_1^2}{R_{\rm tube1}^2}\right) = \left(\frac{4\pi\rho V^2}{B_{\rm tube1}^2}\right)^{1/2} \frac{1}{qR_{\rm tube1}}. \tag{4.14}$$

Here we assume that V is more or less approximate to V_z and thus V does not depend on q. Other values of $B_{\rm tube1}$, $R_{\rm tube1}$, and ρ are also assumed to be constant for different q. Here we introduce the notation $\mu \equiv r_1/R_{\rm tube1}$. Then Equation (4.14) reduces to

$$\mu \exp\left(-\mu^2\right) = 1/\hat{q}, \tag{4.15}$$

or,

$$\mu^2 - \ln \mu = \ln \hat{q}, \tag{4.16}$$

where $\hat{q} \equiv qR_{\rm tube1}[B_{\rm tube1}^2/(4\pi\rho V^2)]^{1/2}$. For a larger radial distance, $r_1 \gg R_{\rm tube1}$, i.e., $\mu \gg 1$,

$$\mu^2 \sim \ln \hat{q}. \tag{4.17}$$

Then we obtain

$$r_1 \sim R_{\rm tube1} \left[\ln\left(qR_{\rm tube1}\right) + \frac{1}{2} \ln\left(\frac{B_{\rm tube1}^2}{4\pi\rho V^2}\right)\right]^{1/2}. \tag{4.18}$$

Therefore, the effective size of the expanded tube $L \sim r_1$ is at least positively correlated to q, but not in a linear manner.

4.4.3 Dependence on the Field Strength

When the field strength at the tube's axis $B_{\rm tube}$ is varied while the twist q is fixed, the maximum HDF speed, $\max(V_y)$, is found to be roughly proportional to the field strength. From Equation (4.11), if we assume L/D is constant, the horizontal speed V_y and thus the maximum speed $\max(V_y)$ are proportional to the field strength $B_{\rm tube}$.

As for the HDF duration Δt, however, Figure 4.4(a) clearly shows two regimes: stronger field cases that show a decreasing trend, and a middle case that deviates from this trend. Thus we should take into account the difference between these regimes.

First, let us focus on the stronger field regime. Since the rising speed is proportional to the field strength, stronger tubes emerge faster. In this case, the accumulated plasma ahead of the tube does not drain down so much because of the short emergence period, and thus the thickness of the plasma layer becomes almost the same for these cases. That is, the thickness of the layer D is constant and is independent of the rising speed V_z. Since the rising speed is proportional to the field strength $B_{\rm tube}$, we have

$$\Delta t \simeq D/V_z \propto 1/B_{\rm tube}. \tag{4.19}$$

Hence, the HDF duration is inversely proportional to the field strength, which explains the trend in the stronger field regime of the fitted inverse function in Figure 4.4(a).

As for the middle strength case, the emergence takes longer and thus the drainage of the accumulated plasma becomes more effective, resulting in the much thinner layer D compared to the rising speed V_z. Therefore, the HDF duration $\Delta t \simeq D/V_z$ becomes shorter and thus deviates from the inverse trend in the stronger field cases.

4.5 Summary

In this parametric survey, we vary the axial field strength, twist, and perturbation wavelength of the initial flux tube. As a result, we found the following features.

The rising speed in the convection zone strongly depends on the initial field strength but its correlation with the twist is weak. The emergence is resisted by the curvature force only in the case when the perturbation wavelength is shortest. According to the analytic study, the rising rate (terminal velocity) is written as $V_\infty \propto B_{\rm tube}\sqrt{1+q^2R_{\rm tube}^2}$, which indicates a strong dependence on the field strength and a weak correlation with the twist.

As the flux tube approaches the surface, the accumulated plasma ahead of the tube escapes horizontally around the surface layer, which is called the HDF. The driver of the HDF is found to be the pressure gradient.

When the field strength increases, the maximum HDF speed becomes higher, because the rising speed mainly depends on the field strength. The HDF duration is divided into two groups. For the stronger tube regime ($B_{\rm tube} \gtrsim 100B_0$), the duration is in simple inverse proportion to the field strength, while the weaker field regime ($B_{\rm tube} \lesssim 100B_0$) deviates from the trend in the stronger tube regime because the fluid draining is more effective.

The duration of the HDF is found to have no relation with the tube's twist, since the rising speed is independent of the twist. However, the maximum HDF speed shows a positive correlation with the twist. This feature is explained by considering the head size of the main tube that remains after the aerodynamic drag peels away the tube's outer field. The head size remains larger with the twist, which results in the stronger HDF.

If we apply the above dependencies of the HDF to the actual observations, we may be able to obtain information on the magnetic field in the subsurface layer, which we cannot observe optically.

Chapter 5

Summary and Discussion

5.1 Summary

In this part, we conducted three-dimensional magnetohydrodynamic (3D MHD) simulations of the emerging magnetic flux tubes in a large scale. Initial depth of the flux tubes is set to be -20 Mm of the convection zone, which is 10 times deeper than most of the previous calculations focusing on the flux emergence from the uppermost convection zone (e.g., Shibata et al., 1989). This value is also comparable to the depth at which the thin-flux-tube (TFT) approximation breaks down (see Section 1.3.2). By conducting the simulations, we found that the evolution is illustrated as follows.

Phase 1: The initial tube rises through the convection zone due to its magnetic buoyancy, subject to aerodynamic drag due to the external flow. The mechanical balance between the buoyancy and the drag (and the downward curvature force) acting on the rising tube yields a terminal velocity, which is essentially of the order of Alfvén speed. In the convection zone, the tube expands with the decrease in the surrounding density and pressure. However, the tube maintains its coherency because of the twist component of the magnetic field.

Phase 2: When the flux tube approaches the photosphere and expands sufficiently, the

plasma on the rising tube accumulates to suppress the tube's emergence, since the photosphere above the plasma is isothermally-stratified, i.e., convectively-stable. Therefore, the flux decelerates and extends horizontally beneath the surface. The compressed unmagnetized plasma escapes horizontally around the surface layer as a horizontal divergent flow (HDF), before the flux appears at the visible surface. At this time, the upper surface of the expanded tube becomes folded because of the interchange instability of the tube's twist component.

Phase 3: After the flux reaches the photosphere, the magnetic pressure gradient increases around the surface, since the flux is continuously transported from below. Hence, the magnetic buoyancy instability is triggered locally and, as a result, the flux rises further into the upper atmosphere, forming magnetic domes.

In the photosphere, we observed small-scale magnetic elements of both polarities separating from each other at multiple locations. They stop at the outer edges of the AR. The separations are caused by the interchange instability of the rising tube while in the convection zone. Then, the magnetic elements gather and make two alignments of "pores" at the edges of the region. They show a shearing motion, which is explained by two independent mechanisms (kinematic and dynamic effects).

Focusing on the height-time evolution of the rising tube (e.g., Figure 3.3), one may find that the entire emergence from the convection zone to the upper atmosphere is in a two-step way. The rising speed in the convection zone strongly depends on the initial field strength, while its correlation with the twist is weak. The emergence is resisted by the downward curvature force only when the perturbation wavelength is shortest. The deceleration of the rising tube within the solar interior is due to the unmagnetized plasma between the flux tube and the photosphere. It can be observed as an HDF, of which the driving force was found to be the pressure gradient.

By conducting the parametric survey, we also investigated the dependence of the HDF duration and the maximum HDF speed on the field strength and the twist of the initial flux tube.

- The maximum HDF speed increases with the field strength. The HDF duration is inversely proportional to the field strength when the field is strong. The duration deviates from this trend in the weak field case.

- The HDF duration has no relation with the tube's twist, while the maximum HDF speed shows a positive correlation with the twist.

5.2 Discussion

5.2.1 Combination of Different Layers

From the numerical simulations, we found many interesting features that are summarized in the previous section. These findings, particularly the dynamics when the tube approaches the surface layer (deceleration of the tube, horizontal divergent flow, etc.), entirely owe to the large-scale simulation, which simultaneously calculates the dynamics within the interior as well as around and above the surface. That is, the effects of the convection zone, the photosphere, and the corona are altogether important for the emergence process.

In the TFT simulation of Figure 1.10 in Chapter 1, as the flux tube rises through the convection zone, it expands due to the decreasing external pressure and the tube's radius a exceeds the local pressure scale height $H_{\rm p}$ at ~ -20 Mm (panel d) and, naturally at this height, the approximation breaks down. In our simulation, when the tube expands, it becomes much deformed by the aerodynamic drag. Also, the accumulation of the plasma becomes more effective and, hence, the rising tube starts deceleration, which is not seen in the TFT simulation. In Figure 1.10(a), the rise velocity V_r continuously increases after passing the depth of -20 Mm.

The temporal deceleration of the rising flux tube was also found in the previous simulations about the emergence from the surface layer. For example, Magara (2001) found that the rising speed slows down when the tube enters the photosphere (see Figure 3 of his paper). However, the deceleration mechanism is different from our model. In his model, the deceleration occurs because the flux tube itself penetrates into the the convectively-stable photosphere, which inhibits the rising motion of the material. The radius of the flux tubes in his simulation is typically 600 km and they are initially embedded just beneath the photosphere at -1800 km. However, in our case, the deceleration is due to the unmagnetized plasma trapped between the flux tube and the photosphere. In our models, the initial radius is 1000 km, while the initial depth is as deep as $-20,000$ km. Therefore, the compression of the material becomes more effective before the tube reaches the surface, and this difference of the size scales is essential for the "two-step emergence" found in our simulations.

5.2.2 Effect of the Radiative Cooling and Thermal Convection

Although the effect of the radiative cooling and the resultant thermal convection on the emergence process is beyond the scope of the present study, it is still worth discussing. As was introduced in Section 1.3.6, some recent simulations now deal with the flux emergence in the "convective" convection zone. Large-scale upflows may support the emergence of the magnetic flux in the convection zone (Fan et al., 2003). Cheung et al. (2010) reported that, in the further emergence process from the photosphere, the local flux cancellation due to the convection drains down the mass from the surface layer. Stronger pores or sunspots of > 1 kG, which are not seen in our simulations, may be formed through the convective collapse process (Parker, 1978). Another explanation for the spot formation is the radiative cooling (e.g., Rempel et al., 2009). Because of the radiation, the surficial plasma becomes cooler and heavier, and, hence, the plasma sinks deeper down into the convection zone. Therefore, the field strength of the vertical flux increases, resulting in the spot formation.

In our simulation, a large amount of the flux tube remains below the photosphere (see

e.g. Figure 3.2(f)). For the typical case in Chapter 3, the fraction of the magnetic flux that emerges above the surface, measured over the vertical plane $x/H_0 = 0$ at $t/\tau_0 = 800$, is

$$\frac{\int_{z\geq 0} B_x|_{x=0}\, dy\, dz}{\int B_x|_{x=0}\, dy\, dz} = 4.8 \times 10^{-3}, \tag{5.1}$$

namely, about 0.5%. Although it is still unknown if there remains a magnetic flux below a mature AR in the actual Sun, the emergence of the entire flux tube helps to enhance the total unsigned flux in the photosphere. Apart from the aforementioned radiative cooling process and the resultant thermal convection, Hood et al. (2009) suggested to use a toroidal tube with an arch-like shape, instead of a horizontal tube. Since the drainage of the material works more effectively, axial field of the toroidal loop emerges fully into the corona.

5.2.3 Parameter Dependence and Emergence in the Actual Sun

In the parametric study in Chapter 4, we found that, when the initial twist is too weak, the tube stops around the surface and fails to emerge further into the upper atmosphere. It is because the smaller magnetic curvature force cannot hold the coherency and thus the tube cannot maintain the strong enough field strength to continue its ascent. If this is the case in the actual Sun, we can speculate that the magnetic flux of "failed" emerging tubes stays around the surface layer. Convections (granulation and supergranulation) may locally enhance the strength of such a flux and, in some cases, the flux may appear as ephemeral ARs.

Another interesting parameter in the emergence process is the initial perturbation wavelength. In the dynamo simulation by Nelson et al. (2013), buoyant emerging loops are generated from the toroidal magnetic wreaths in the lower convection zone. Here, the scale of the emerging loops is basically determined by the size of large-scale convection cells (A.S. Brun, private communication). Therefore, it may be possible to infer the emergence in the actual

Sun from the simulation results by comparing the size of local convection in the Sun and the perturbation wavelength in the simulation.

The parameters also affect the resultant magnetic structure in the photosphere. As seen in Figure 4.2, the size of the rising portion that appears at the surface depends on the parameters. For example, in case G, the magnetic region extends only around the center of the simulation domain, which is caused by the shortest perturbation wavelength. Interestingly, in this case, the photospheric magnetogram shows only a single pair of positive and negative polarities instead of multiple pairs as in Figure 3.6. It is because the upper part is detached from the original rising tube and restarts emergence from the shallower convection zone. That is, the situation is closer to the emergence simulation from just below the surface layer (e.g., Fan, 2001), which typically shows a single bipole in the photosphere.

5.3 Suggestion of Theoretical Model

Based on the simulation results in this part, we suggest the "two-step" model of the flux emergence and AR formation. The bottom of Figure 5.1 illustrates the previous view by Zwaan (1985), while the upper panels are for our "two-step emergence" model. Here, (1) the rising tube expands at the top convection zone due to the external pressure stratification, and the tube pushes up the unmagnetized plasma. (2) The plasma compressed between the rising flux and the photosphere escapes horizontally around the surface layer as an HDF, before the flux appears at the visible surface. (3) The flux restarts emergence further into the upper atmosphere after a sufficient amount of magnetic flux accumulates. In our simulation, the second-step emergence is due to the magnetic buoyancy instability. (4) As the fields continuously emerge into the corona, the magnetic elements of both polarities gather and form pores at the photosphere, which eventually grow up to be sunspots. In this way, an AR is built on the solar surface.

Compared to the classical model by Zwaan (1985; see the bottom of Figure 5.1), the

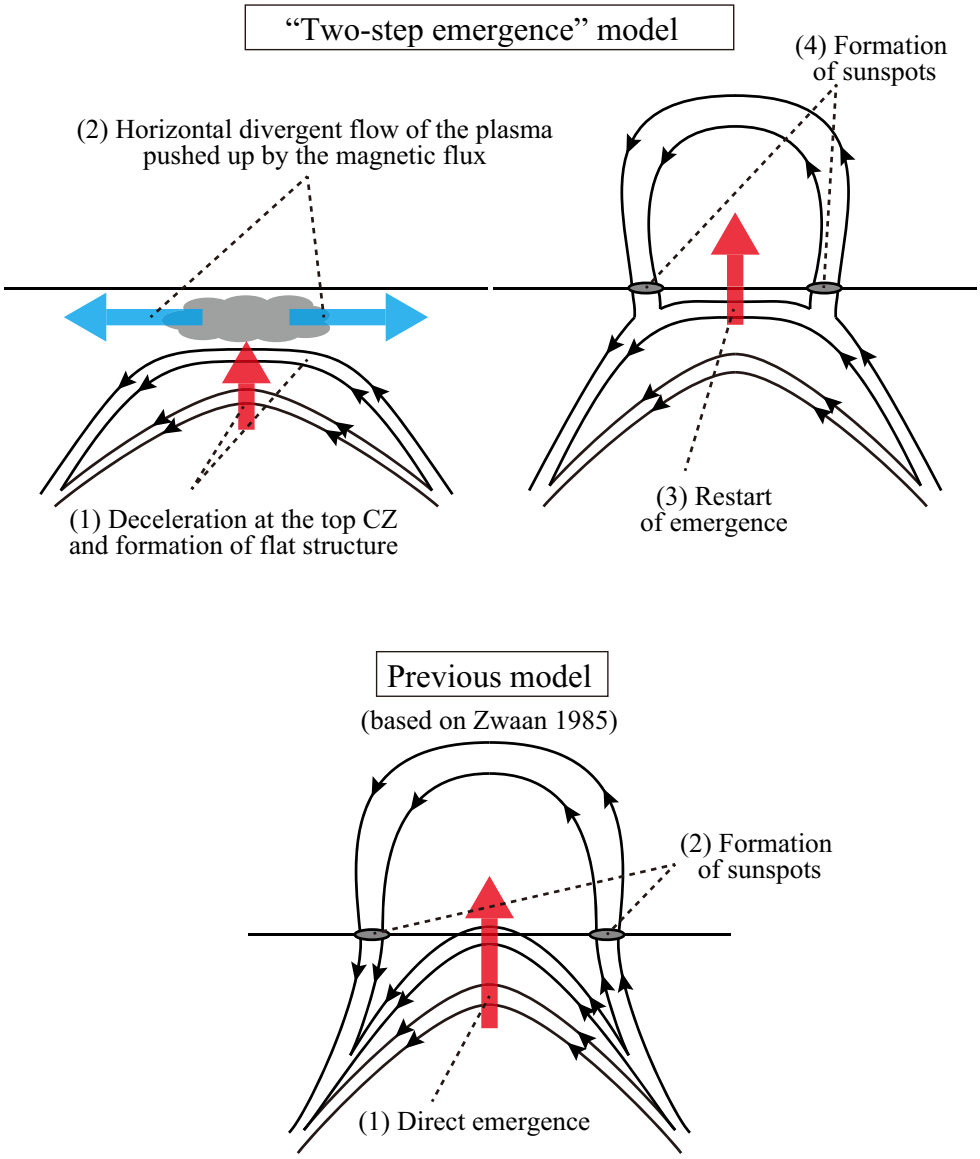

Figure 5.1: (Top) "Two-step" model of the flux emergence and the AR formation. The flux decelerates at the top convection zone (CZ), and the flux becomes flat. Then, the compressed plasma escapes horizontally around the surface (HDF) before the flux appears the visible surface. The photospheric flux restarts emergence into the corona, and, eventually, sunspots are formed. (Bottom) Classical model by Zwaan (1985).

present model takes account more of the effects of the upper convection zone and the photospheric layer, which were not investigated from direct optical observations. In particular, the deceleration of the rising flux and the horizontal flow of the compressed material (HDF) can be the targets of the observational studies in the next part.

Part III

Observational Study

Chapter 6

Introduction

In this part, we analyze observational data of newly emerging active regions (ARs) and compare the results with numerical simulations conducted in Part II. The primal aim of this part is to observationally examine the theoretical "two-step emergence" model (Figure 5.1). For this purpose, we here observe (1) the horizontal divergent flow (HDF) of a compressed unmagnetized plasma around the photospheric layer and (2) the rising motion of the emerging magnetic flux in the top convection zone, both of which were previously predicted in the simulations.

For observing these targets, we first generate original ideas and then develop them into practical observation methods. Also, for investigating the births of emerging ARs, we use the magnetograms and Dopplergrams obtained by the Michelson Doppler Imager (MDI: Scherrer et al., 1995) aboard the *Solar and Heliospheric Observatory* (*SOHO*) and the Helioseismic and Magnetic Imager (HMI: Schou et al., 2012) aboard the *Solar Dynamics Observatory* (*SDO*). Their continuous full-disk observations allow us to investigate the earliest phase of, or even before the start of the flux emergence.

In this part, we first report the HDF detection in one AR in Chapter 7 and, then, the statistical analysis of the HDF in Chapter 8. We develop and apply a new helioseismic technique for probing the emerging magnetic flux in the top convection zone in Chapter 9.

Finally, in Chapter 10, we summarize this part and discuss future prospects.

Chapter 7

Horizontal Divergent Flow: Event Study[1]

7.1 Introduction

In the large-scale flux emergence simulations in Part II, we found that the unmagnetized plasma, which is pushed up by the rising flux, escapes laterally around the surface. The appearance of the divergent outflow at the photosphere was found to be earlier than that of magnetic flux, and, at this moment, the outflow is mainly horizontal. Here we call this preceding outflow as a horizontal divergent flow (HDF). A similar flow is also reported by Cheung et al. (2010). However, to our knowledge, the HDF prior to the flux emergence has not been confirmed clearly in previous observations (Kosovichev, 2009). Here, we use the term "horizontal" to indicate the direction parallel to the solar surface.

The aim of this study is to investigate the HDF and the evolving magnetic field at an early phase of the flux emergence. For this purpose, we use the Dopplergrams and magnetograms of the Helioseismic and Magnetic Imager (HMI) on board the *Solar Dynamics Observatory* (*SDO*), since their continuous observations of the whole solar disk make it possible to achieve

[1]Most part of this chapter was published in Astrophysical Journal (Toriumi et al., 2012)

information at the very moment of, or even before the flux emergence at the surface.

Our numerical result indicates that, if the newly emerging region is located away from the disk center, if a pair of positive and negative Doppler patterns is detected just before the flux emergence, and if the positive (negative) pattern is limbward (disk-centerward), the observed Doppler velocity is mainly horizontal rather than vertical. Therefore, we can evaluate the horizontal velocity of the escaping plasma from the Doppler velocity, by considering the heliocentric angle of the active region (AR) from the disk center. One advantage of this method over the ordinal local correlation-tracking method (November & Simon, 1988) is that the horizontal velocity of the plasma can be evaluated independently of the apparent motion of magnetic elements at the photosphere. After the flux has emerged, we cannot obtain the horizontal speed from the Doppler velocity, since it may contain a vertical motion such as rising of magnetic fields or a downflow in the convective collapse process.

In this chapter, we report the first determination of the HDF prior to the flux appearance, using *SDO*/HMI Dopplergrams and magnetograms. We also studied the chromospheric reaction to the flux emergence in the photosphere by using Hα images taken by the Solar Magnetic Activity Research Telescope (SMART) at Hida Observatory. In Section 7.2, we will introduce the observations and the method of data reduction. Analysis and the results will appear in Section 7.3. Then, in Section 7.4, we will discuss the observational results. Finally, we will summarize the chapter in Section 7.5.

7.2 Observation and Data Reduction

In this chapter, we studied NOAA AR 11081 formed in 2010 June, in the northwest of the solar disk. To measure the Doppler shift and line-of-sight (LoS) magnetic field in the photosphere, we used Dopplergrams and magnetograms taken by *SDO*/HMI. Also, to study the chromospheric response to the flux emergence, we used Hα images taken by SMART at Hida Observatory.

7.2.1 *SDO*/HMI Dopplergram and Magnetogram

SDO/HMI continuously observes the whole solar disk at the 6173 Å Fe I line, which is resolved by 4096^2 pixels (Schou et al., 2012). To obtain the tracked data cubes of the birth of AR 11081, we used `mtrack` module[2]. The data cubes of the Doppler velocity and the LoS magnetogram have a spatial resolution of 0.5 arcsec (1 pixel corresponds to ~ 360 km) with 512^2 pixel field-of-view (FoV), and a temporal resolution of 45 s with a duration of 36 hr, starting at 12:00 UT on 2010 June 10. In the initial state, the center of the 512^2 FoV is located at N22° W25.6°, or $(+392, +383)$ arcsecs in solar disk coordinates. Here, we applied Postel's projection, that is, both Doppler and magnetic maps are projected as if seen from directly above. Then, to eliminate the effects of the rotation of the Sun and the orbital motion of the satellite, and to determine the zero point of the LoS velocity, we reduced the mean velocity from each Dopplergram. Also, a 30-min (40-frame) moving average was applied to the Dopplergrams and magnetograms. The noise level of original HMI data (precision and zero-point accuracy) is estimated in Appendix B.1.

Figure 7.1 is the HMI magnetogram of NOAA AR 11081 taken at 06:00 UT, 2010 June 11, that is, after the emergence started. Here, white and black indicate the positive and negative polarities, respectively. The diagonal line in this figure is the slit for the time-sliced diagram in Section 7.3.1. The slit angle is chosen to fit the first separating motion of both polarities. The square indicates the region analyzed in Section 7.3.2 to measure the distributions of the Doppler velocity and the LoS field strength.

7.2.2 SMART Hα Images

SMART at Hida Observatory, Kyoto University, consists of four different telescopes, which are T1, T2, T3 and T4, respectively (UeNo et al., 2004). They are placed on a tower with a height of 16 m. T1 obtains Hα full solar disk images at high temporal and spatial resolution. For studying the chromospheric reaction to the photospheric flux emergence, we analyzed

[2]http://hmi.stanford.edu/teams/rings/mod_mtrack.html

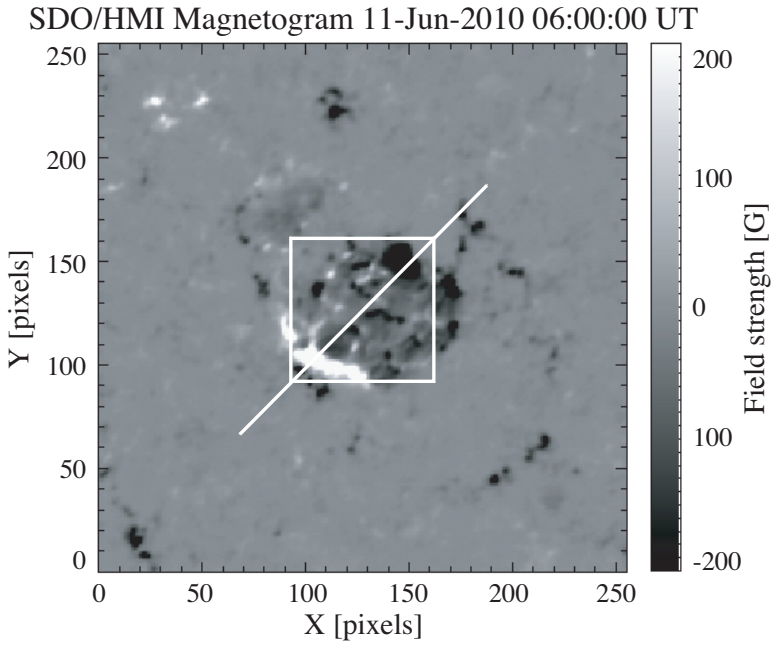

Figure 7.1: *SDO*/HMI magnetogram of NOAA AR 11081 taken at 06:00 UT on 2010 June 11. Positive and negative polarities are indicated by white and black, respectively. One pixel corresponds to $\sim$ 360 km. The diagonal line is the slit for time-sliced diagram (see Section 7.3.1). The square indicates the field in which temporal evolution of the Doppler velocity and the magnetic field strength (see Section 7.3.2) are analyzed. Figure reproduced from Toriumi et al. (2012) by permission of the AAS.

the Hα data of 01:00–05:00 UT, 2010 June 11, which resolves the full solar disk with 4096^2 pixels (1 pixel corresponds to ~ 0.56 arcsec) and has a maximum temporal resolution of 2 minutes.

In this study, we only used Hα line core images (wavelength at 6562.8 Å). First, dark-current subtraction and flat fielding were performed on the obtained SMART data. Then, by taking a cross-correlation of the two consecutive images to fix the position of the target emerging AR, we made a data cube of Hα images. Note that Hα image is a simple zoom-up of the full disk image, while Postel's projection is applied to the HMI images.

7.3 Data Analysis and Results

Figure 7.2 shows the temporal evolution of the Dopplergram and the magnetogram for 12 hours from 18:00 UT, 2010 June 10. In the Dopplergram, the motion toward and away from the observer are shown in blue and red, respectively. At first, during 18:00–00:00 UT, the surface is relatively quiet with some preceding magnetic elements of both positive and negative polarities. An area with strong blue shift (< -1 km s^{-1}) appears in the middle of the FoV at 01:00 UT on 11 June, which is gradually growing in size. After 03:00 UT, the strong red shift (> 1 km s^{-1}) appears and magnetic field emergence takes place. Both positive and negative polarities move apart from each other. Here, the separation of the magnetic elements is almost along the slit, which is indicated as a diagonal line. Finally, at 06:00 UT, the red and blue areas become faint. The separated magnetic elements stop and gather to form pores at the boundary of the emerging region.

In this section, we first introduce the results of time-slices of the Dopplergrams and magnetograms in Section 7.3.1. Then, in Section 7.3.2, we will clarify the occurrence times of the HDF and the flux emergence, and evaluate the horizontal speed of the HDF. Section 7.3.3 is dedicated to showing the chromospheric studies.

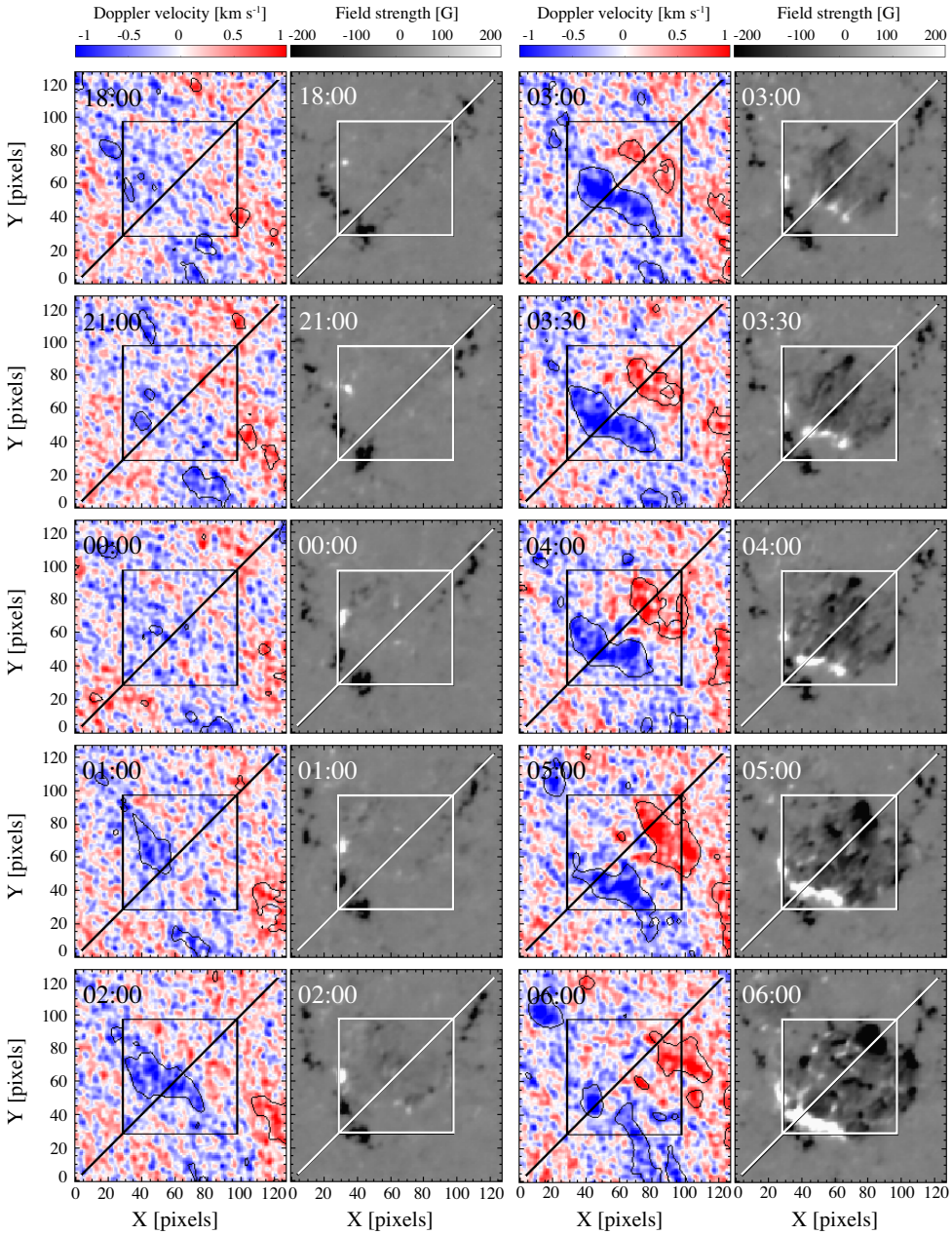

Figure 7.2: Temporal evolutions of the Dopplergram (red-blue map) and the magnetogram (white-black map) for 12 hours from 18:00 UT, 2010 June 10 to 06:00 UT, June 11. The diagonal line and the square in each panel are the slit for time-sliced diagrams (Section 7.3.1) and the field-of-view in which histograms are made (Section 7.3.2), respectively. In the Doppler maps, the motion toward and away from the observer are indicated in blue and red, respectively, and contours indicate the smoothed isolines of ± 1 km s^{-1}. In the magnetograms, positive and negative polarities are shown with white and black, respectively. Figure reproduced from Toriumi et al. (2012) by permission of the AAS.

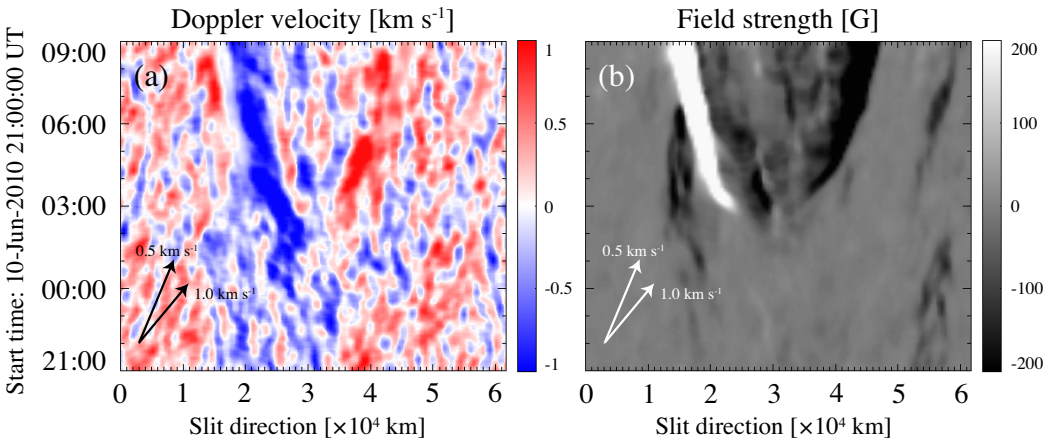

Figure 7.3: Time-slice diagram of (a) Dopplergram and (b) magnetogram along the slit shown in Figures 7.1 and 7.2. Slit direction is selected limbward, i.e., the distance from the disk center increases with the horizontal axis. The duration of the time-slice is 12 hours, starting from 21:00 UT on 2010 June 10. In the Doppler time-slice (a), the motion toward (away from) the observer is indicated by blue (red) color. In the magnetogram time-slice (b), positive (negative) polarity is shown as white (black). Arrows give the apparent velocity. Figure reproduced from Toriumi et al. (2012) by permission of the AAS.

7.3.1 Time-sliced Diagram

To examine the motion of the magnetic elements of positive and negative polarities and the corresponding LoS velocity, we made time-sliced diagrams of HMI Dopplergrams and magnetograms. The spatial slit is indicated as a diagonal line in Figures 7.1 and 7.2, which is placed parallel to the separation of both polarities.

Figure 7.3 is the time-sliced diagram of the Dopplergram and the magnetogram along the slit. From the time-slice of the magnetogram, Figure 7.3(b), we can see that both positive and negative polarities move apart from each other from around 03:00 UT on June 11. The speed of each element is estimated to be ~ 1.2 km s^{-1}, which then drops to ~ 0.4 km s^{-1}. Thus, the separation speed is 0.8–2.4 km s^{-1}. This deceleration of the separated polarities may reflect that the polarities are reaching the boundary of the AR (see Figure 3.10, panel (2), in Chapter 3). These elements then gathered to create stronger pores, of which the

absolute LoS field intensity is greater than 200 G. One would find that weak and small elements of both polarities appear between the main separating pores during 03:00–09:00 UT on June 11. Also, the main positive pore collides with the preexisting negative polarity, and they cancel each other out.

In the Doppler slice, Figure 7.3(a), a pair of red and blue patterns emerged at around 02:00 UT, June 11, slightly earlier than the appearance of the magnetic elements in Figure 7.3(b). The red and blue shift patterns immediately started to separate, and the propagation speed of the patterns (the slope of the patterns) is about 0.4 km s^{-1}. Here, we note that the blue (red) pattern is located disk-centerward (limbward), which indicates that the flow is divergent. Moreover, from the fact that the divergent outflow came before the flux emergence, we can assume that the outflow during this period is caused by the plasma escaping from the rising magnetic flux. It should be noted that the trend of the Doppler pattern coming before the flux emergence does not change when we vary the thickness of the slit.

However, the determination of the appearance time of the Doppler pattern associated with the flux emergence is difficult, because the Doppler pattern, especially the blue shift, appeared at the location where the supergranulation showed blue shift (21:00–01:00 UT). The definition of the flux emergence and the appearance of the related Doppler pattern is dealt with in the next subsection (Section 7.3.2).

7.3.2 Appearance times of the HDF and the flux emergence, and the velocity of the HDF

It is not easy to determine the timings of the appearance of the HDF and the associated flux emergence from Figures 7.2 and 7.3. In particular, we have to distinguish the outflow related to the flux emergence from the preexisting convective motions of the quiet Sun (e.g., granulations and supergranulations). To clarify with significance when the HDF occurred and when the magnetic flux emerged, we studied the temporal changes of the Doppler and magnetic patterns from those before the emergence, namely, patterns of the quiet Sun. Also,

in this subsection, we describe how we evaluate the horizontal speed of the HDF.

First, we plotted the histograms of the Doppler velocity and the absolute LoS field strength inside the square of Figure 7.1 for each frame. The size of the square is 70×70 pixels ($\sim 25 \times 25$ Mm^2), which is selected to include the emergence region. As for the Dopplergram, the apex of the histogram was shifted to fit the zero point. Then, considering the photospheric condition in the 3 hours from 21:00 UT of June 10 to be sufficiently quiet, we averaged up each 240 histograms of the Dopplergrams and the magnetograms in this period, and regarded these averages as reference quiet-Sun profiles.

In the left column of Figure 7.4, we show histograms of the Doppler velocity at five different times of June 11, plotted over the reference quiet-Sun profile. Here we note that the quiet-Sun profile obtained is similar to a Gaussian distribution. The shade indicates the standard deviation above and below the reference. As time goes by, the profile becomes deviated from the reference, because the number of pixels of which the absolute Doppler velocity is greater than 0.5 km s^{-1} increases. The right column of Figure 7.4 is the residual of the Doppler histogram from the reference. One standard deviation is also shown as a shaded area. At first, the residual is below one standard deviation level for most of the velocity range. From 02:00 UT, however, the residual exceeds the deviation.

Figure 7.5 is the same as Figure 7.4, but for the absolute field strength of the LoS magnetograms. Here, the quiet-Sun profile consists of a distribution with a width of ~ 10 G (i.e., about the precision of the HMI magnetogram; see Appendix B.1) and some preexisting pores within the FoV. Thus, the profile is different from a Gaussian distribution. The residual in the range of > 200 G further exceeds one standard deviation level from 04:00 UT. After this time, the residual of > 200 G becomes well over the standard deviation, because more and more flux is emerged and stronger pores are created.

For the significance of the measurement, we define the start time of the HDF and the flux emergence as the time when each residual of the Dopplergrams and the magnetograms exceeded one standard deviation level. To know these times, we show in Figure 7.6 each time-

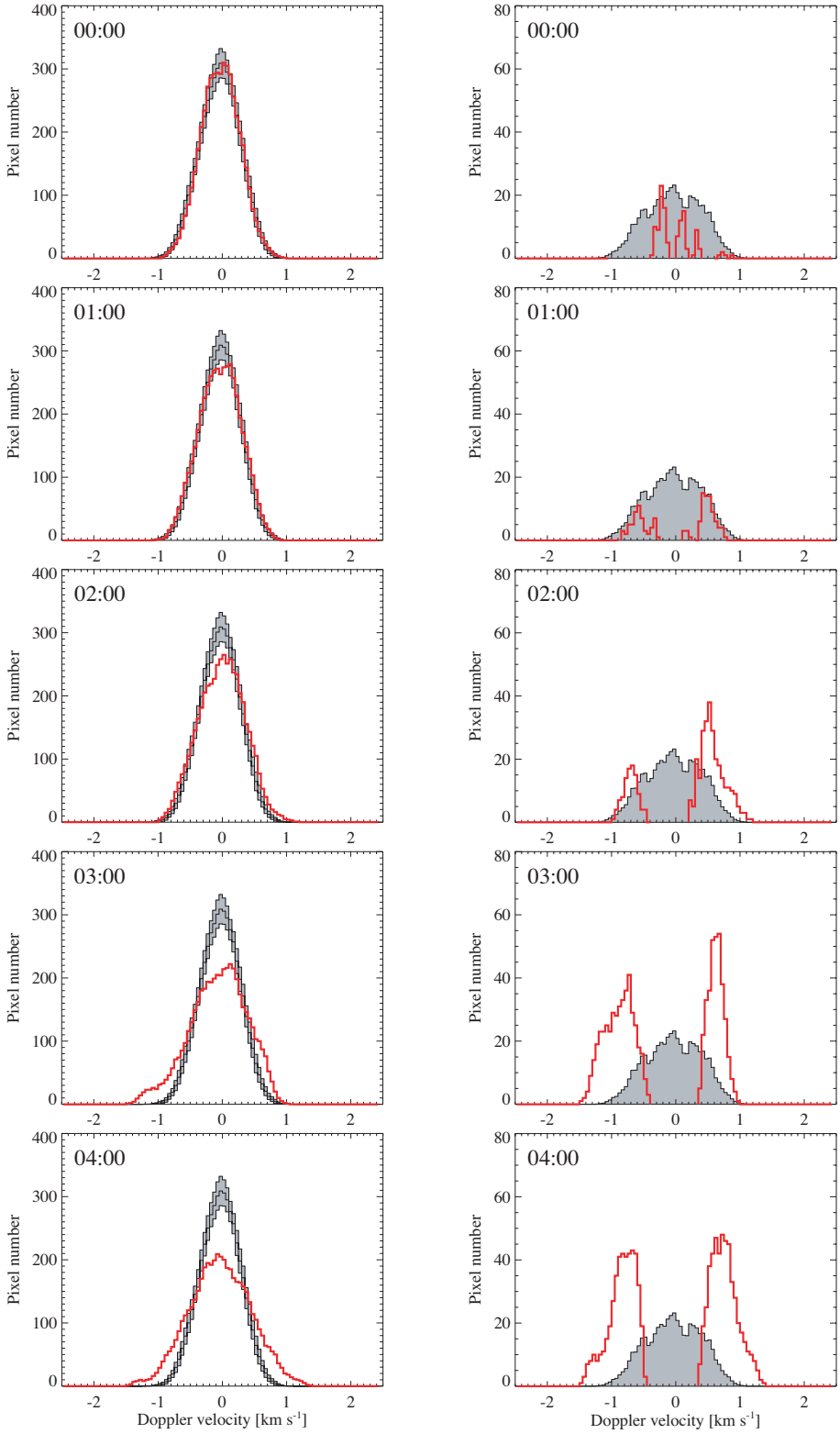

Figure 7.4: (*Left*) The histogram of the Doppler maps at five different times of 2010 June 11, indicated by red line, plotted over the quiet-Sun reference profile (middle black line). Shade indicates the standard deviation above and below the reference. (*Right*) The residual of the histogram from the reference, indicated by red line. Shade is one standard deviation level. Figure reproduced from Toriumi et al. (2012) by permission of the AAS.

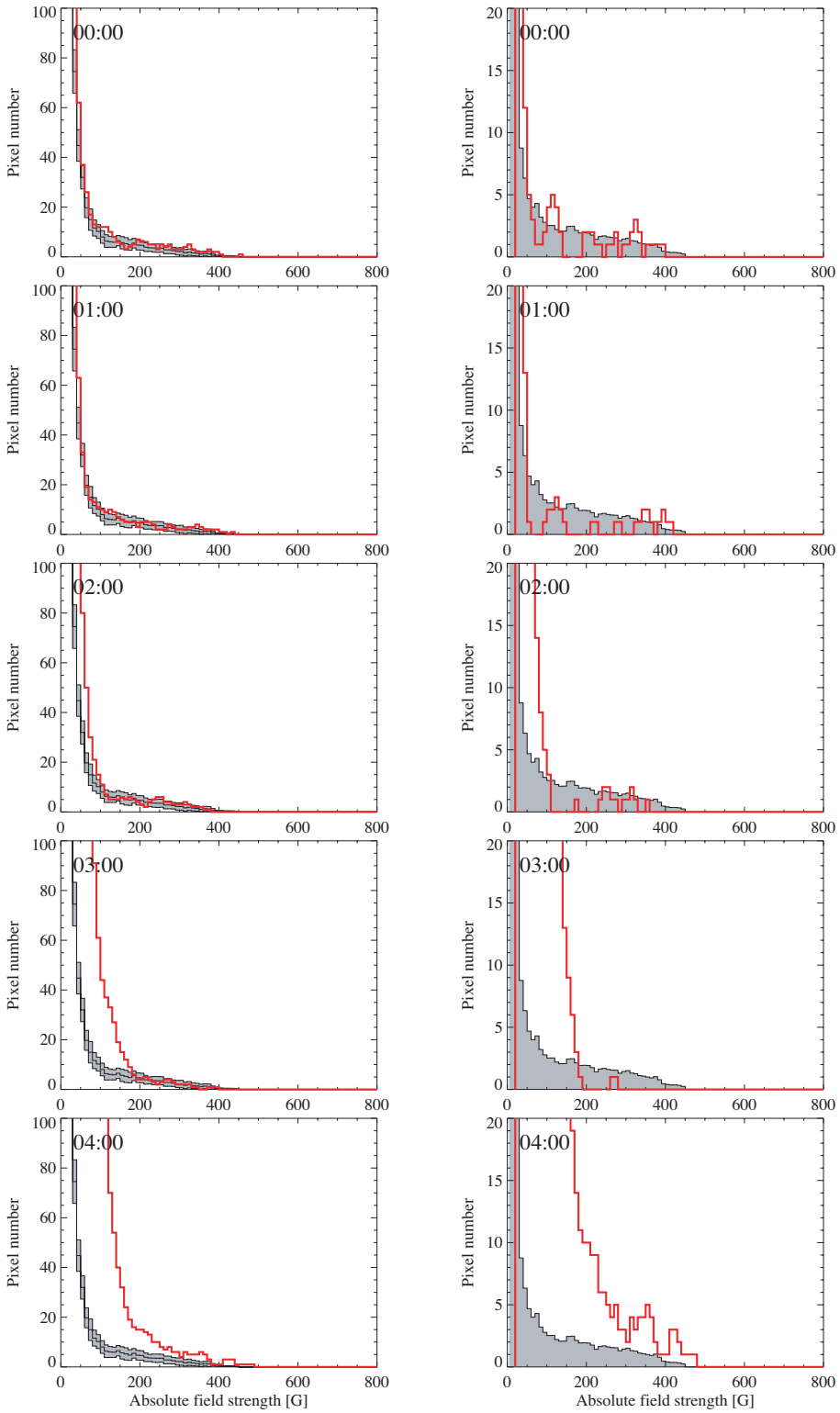

Figure 7.5: Same as Figure 7.4, but for the absolute field strength of the LoS magnetograms. Figure reproduced from Toriumi et al. (2012) by permission of the AAS.

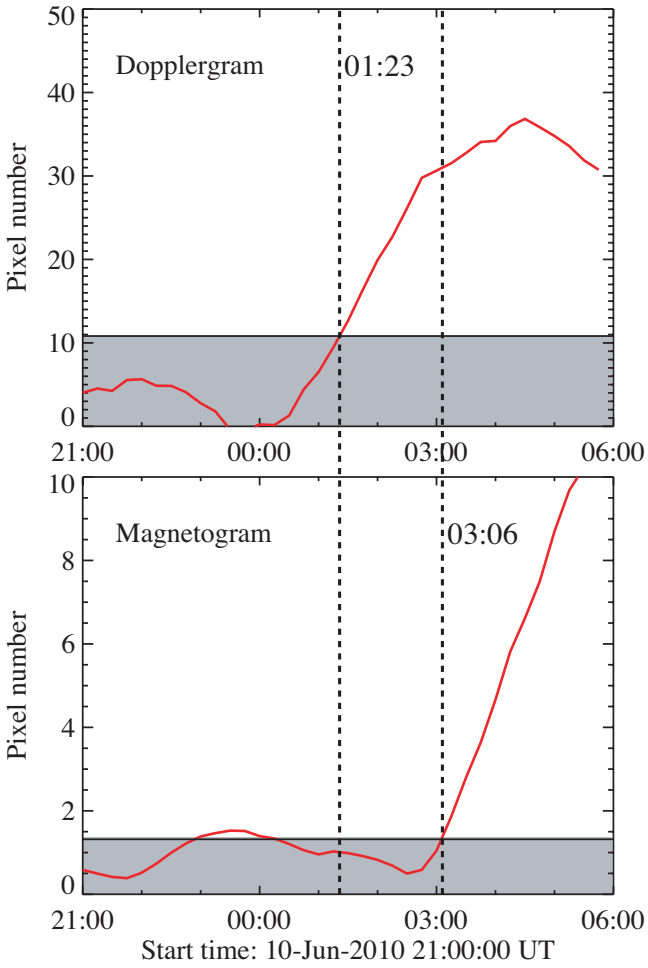

Figure 7.6: (*Top*) Time-evolution of the residual of the Doppler histogram (Figure 7.4), averaged over the range of $[-0.8\ \mathrm{km\ s^{-1}}, -0.4\ \mathrm{km\ s^{-1}}]$ and $[0.4\ \mathrm{km\ s^{-1}}, 0.8\ \mathrm{km\ s^{-1}}]$, starting from 21:00 UT, 2010 June 10. The shaded area is one standard deviation level. The residual exceeds the standard deviation level at 01:23 UT on June 11. (*Bottom*) The same for the magnetogram (Figure 7.5) over the range of $[200\ \mathrm{G}, 300\ \mathrm{G}]$. The residual exceeds at 03:06 UT. Figure reproduced from Toriumi et al. (2012) by permission of the AAS.

Table 7.1: Dependence of the field-strength range (Toriumi et al., 2012)

Field-strength range (G)	Start of flux emergence
0–50	$\cdots$ UT[a]
50–100	01:25 UT
100–200	02:15 UT
200–300[b]	03:06 UT
300–400	03:20 UT
400–500	03:25 UT
500–600	$\cdots$ UT[c]

[a]Residual is always below one standard deviation level.
[b]Used in this study.
[c]One standard deviation level is not defined.

evolution of the residuals (taken from and averaged over the range $[-0.8\ \mathrm{km\ s^{-1}}, -0.4\ \mathrm{km\ s^{-1}}]$ and $[0.4\ \mathrm{km\ s^{-1}}, 0.8\ \mathrm{km\ s^{-1}}]$ for Dopplergram, and the range $[200\ \mathrm{G}, 300\ \mathrm{G}]$ for magnetogram), plotted over one standard deviation. In this figure, the residual of the Dopplergram becomes over the standard deviation at 01:23 UT on 11 June, while that of the magnetogram exceeds the level at 03:06 UT. That is, the appearance of the HDF came before the flux emergence by 103 minutes.

During this period, it is expected that the flow is mainly horizontal and a vertical component is less dominant. Thus, we can calculate the horizontal velocity from the residual distribution of the Doppler velocity (Figure 7.4), by considering the geometric effect. The relation between the horizontal velocity V_h and the Doppler velocity V_D is $V_\mathrm{h} = V_\mathrm{D}/\sin\theta$, where θ is the heliocentric angle of the emerging region measured from the disk center. From 01:23 to 03:06 UT, the Doppler velocity range where the residual exceeds the one standard deviation is typically 0.4–1.0 km s^{-1}, which is up to 1.5 km s^{-1}, and the heliocentric angle is $\sim 40°$. Therefore, the horizontal velocity is calculated to be 0.6–1.5 km s^{-1}, and the maximum is 2.3 km s^{-1}.

Here, we comment on the selection of the field-strength range ($[200\ \mathrm{G}, 300\ \mathrm{G}]$) and its

Table 7.2: Dependence of the square size (Toriumi et al., 2012)

Square size (pixels)	HDF appearance	Start of flux emergence	Time difference (minutes)
50×50	01:00 UT	02:35 UT	95
60×60	01:25 UT	03:00 UT	115
70×70^a	01:23 UT	03:06 UT	103
80×80	01:35 UT	03:15 UT	100
90×90	01:25 UT	03:20 UT	115
100×100	01:35 UT	03:20 UT	105
110×110	01:45 UT	03:05 UT	80
120×120	01:50 UT	03:05 UT	75

[a]Used in this study.

dependence on the start time of the flux emergence. If we use the lower strength range, for example [50 G, 100 G] or [100 G, 200 G], at which the residual exceeds one standard deviation level faster (Figure 7.5, right column), the start time of the flux emergence is calculated to be much earlier. In the present analysis, however, the strength range [200 G, 300 G] is used, since the number of the pixels of > 200 G is so small in the quiet Sun that the flux emergence is easily detected when it occurs. We confirmed this fact by applying the same analysis on the quiet-Sun data. As for the dependence of the strength range on the observation results, we tested the analysis with various ranges, which is summarized in Table 7.1. From this table one can see that the start time does not change much for [200 G, 300 G], [300 G, 400 G], and [400 G, 500 G] cases. In the numerical simulations in Part II, it is rather easy to determine the start of the flux emergence, since there is no pre-existing field in the photosphere before the emergence. However, in the actual Sun, there exist magnetized pixels with a field strength of 100 G or even 200 G in the "quiet" regions, which makes it difficult to determine the start times. This is one of the critical differences between the modeled and the actual Sun in the point of the HDF study.

We also checked the dependence of the size of the square where the histograms are made (Figure 7.1), which is summarized in Table 7.2. Here, the time difference is almost constant

for various square sizes and is about 100 min. With increasing square size, the ratio of high-speed or strong pixels in the square reduces. At the same time, the quiet-Sun reference profile becomes more accurate and one standard deviation level decreases. Therefore, in total, the time difference remains constant.

7.3.3 Chromospheric Response

In this subsection, we investigate the time-evolution of the Hα intensity to examine the relation between the chromosphere and the photosphere in this studied event. Figure 7.7(a) is a sample image of the SMART Hα data. The color and contours indicate the relative Hα intensity. In this figure, there are two bright regions (plages) in the middle of the FoV. Then, along the slit of Figure 7.7(a), we made a time-sliced diagram for 4 hours starting at 01:00 UT, 11 June, which is shown as Figure 7.7(b). Note that the slit in Figure 7.7(a) is not exactly the same as that in Figure 7.1, since the Hα data is a simple closeup view of the full disk image, while Postel's projection is applied to the HMI data. Thus, from this study, we can only determine the appearance time of the chromospheric brightening.

In Figure 7.7(b), the first bright source at the slit location of 5×10^4 km starts at 02:40 UT. However, it was found that this brightening is due to the activity among the preexisting quiet-Sun pores of both polarities, which later collide with positive patches of the newly emerging flux (see Section 7.3.1). It is difficult to separate this bright source into activity of the preexisting pores and that of the newly emerged positive pores. The second source located at 7×10^4 km starts at 03:20 UT, and there was no preceding pore in this region. Therefore, we consider that the second source is entirely due to the newly emerged negative pores, and determine that the chromospheric reaction starts at this time (03:20 UT; indicated by a dashed line in Figure 7.7(b)). The two chromospheric sources are located just over the positive and negative polarities in the photosphere.

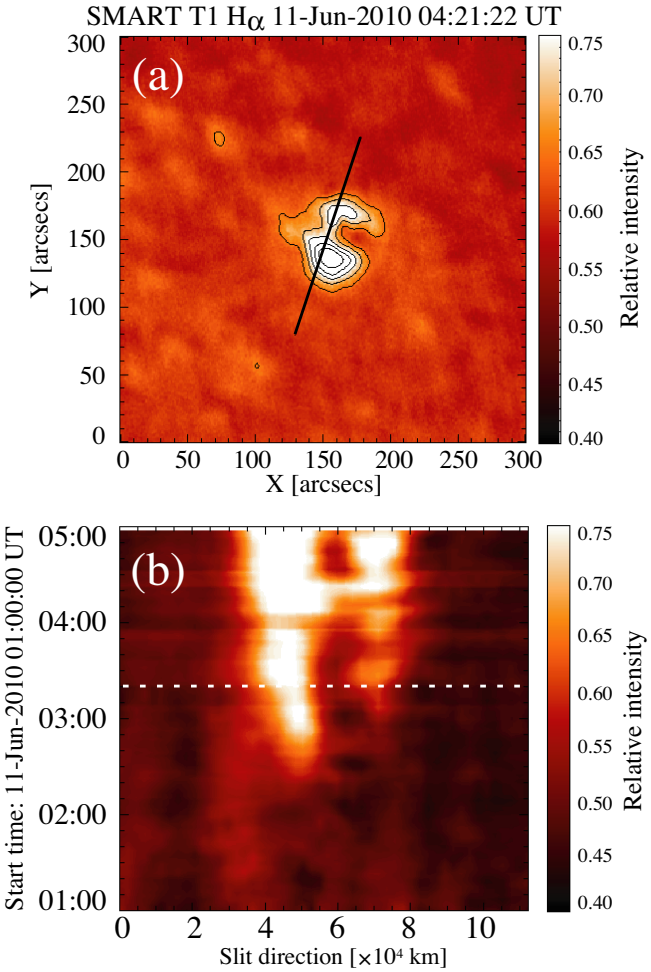

Figure 7.7: (a) A sample image of SMART chromospheric Hα data. The color and contours indicate the relative Hα intensity. Contour levels are 0.65, 0.70, 0.75, 0.80, and 0.85, respectively. The slit in the middle of the panel is used to make a time-sliced diagram. (b) Time-sliced diagram of Hα image for 4 hours from 01:00 UT, 2010 June 11. Color is the relative intensity. Slit direction (horizontal axis) starts from the bottom left of the slit in Panel (a). The dashed line indicates the time 03:20 UT (see text for details). Figure reproduced from Toriumi et al. (2012) by permission of the AAS.

7.4 Discussion

7.4.1 Mechanism of the Time Difference

In this chapter, we analyze the newly emerging AR and find that there is a time difference between the appearance of the HDF and the corresponding flux emergence; the HDF appears prior to the flux emergence by about 100 minutes.

According to the thin-flux-tube simulation (Fan, 2009), the rising speed of the flux tube accelerates from the top few tens of Mm of the convection zone. However, at the same time, the flux tube expands as the external density (pressure) decreases with height. The radius of the tube eventually exceeds the local pressure scale height at a depth of $\sim$ 20 Mm and the thin-flux-tube approximation breaks out. In Part II, our numerical simulations using the fully compressible MHD, including the convection zone, the photosphere, and the corona in a single computational box, have revealed that the rising flux tube decelerates in the uppermost convection zone. It is because the plasma on the flux tube piles up between the apex of the tube and the subadiabatically stratified photosphere ahead, and the plasma inhibits the rising motion of the flux tube. Then, the accumulated plasma in turn extends the tube laterally. This accumulation becomes effective from the depth where the apex of the tube becomes "flat". This critical depth is also considered as being where the tube's radius exceeds the local pressure scale height (depth ~ -20 Mm). The lateral expansion of the flux tube appears similar to those found by Magara (2001) and Archontis et al. (2004). However, their expansions occur because the tubes themselves move into the subadiabatic photosphere.

As the rising tube approaches the photosphere, the accumulated plasma on the rising tube escapes horizontally around the surface and is observed as an HDF, while the tube stops beneath the surface. Since the flux is continuously transported from below, the magnetic pressure gradient at the photosphere enhances and the further emergence to the upper atmosphere starts due to the magnetic buoyancy instability. When the flux resumes rising,

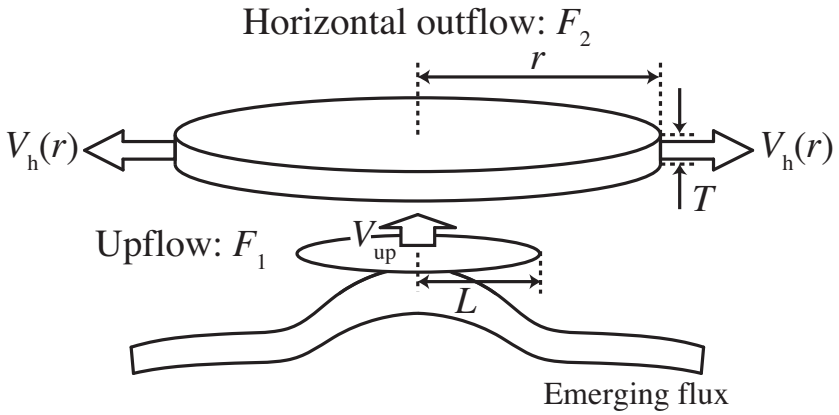

Figure 7.8: Schematic illustration of the model of flux emergence and the HDF. When the magnetic flux is emerged from the deeper convection zone, an upflow region with a size of L and a velocity of $V_{\rm up}$ is formed above the magnetic flux. At the photospheric level, the plasma is pushed away to create an HDF with a thickness of T. Here, r is the radial distance from the center of the emerging region and $V_{\rm h}(r)$ is the horizontal velocity at r. F_1 and F_2 are the mass fluxes of the upflow and the HDF, respectively. Figure reproduced from Toriumi et al. (2012) by permission of the AAS.

it can be observed as a "flux emergence" at the photospheric level. Therefore, the time difference detected in this study implies the period of latency during which the flux tube reaching the photosphere develops the magnetic buoyancy instability. The growth time of the instability is, however, complicated and may be related to many parameters of the rising flux tube such as field strength, total flux, twist, etc.[3]

7.4.2 Depth of the Magnetic Flux

To describe the relation between the HDF and the contributing upflow below the surface, we make a simple model, which is schematically illustrated as Figure 7.8. When the magnetic flux tube has emerged from the deeper convection zone, an upflow region is formed in front of the flux tube. If the typical size of this region is L and the velocity is $V_{\rm up}$, the mass flux

[3]This dependency was studied in the numerical simulations in Chapter 4.

passing through the area of πL^2 can be described as

$$F_1 = \rho_1 V_{\rm up} \pi L^2, \tag{7.1}$$

where ρ_1 is the plasma density. Next, the photospheric plasma that escapes from the upflow propagates the surface as an HDF. If we write the horizontal velocity at the radial distance r as $V_{\rm h}(r)$, the thickness as T, and the density as ρ_2, the mass flux passing through $2\pi rT$ is

$$F_2 = 2\pi r \rho_2 T V_{\rm h}(r). \tag{7.2}$$

These fluxes, F_1 and F_2, are assumed to be conserved. Therefore, from Equations (7.1) and (7.2), the upflow velocity is

$$V_{\rm up} = \frac{2\rho_2}{\rho_1} \frac{rTV_{\rm h}(r)}{L^2}. \tag{7.3}$$

As a result of the observational study, the horizontal speed is $V_{\rm h} \sim 1$ km s^{-1} at $r = 5000$ km. Here we assume that (1) plasma density is almost uniform around the photosphere, i.e., $\rho_1 \sim \rho_2$; (2) the thickness is about the local pressure scale height, $T \sim 200$ km; and (3) the size of the upflow is 4000 km (the smallest distance between the blue and red patterns in Figure 7.3), $L \sim 2000$ km. Under these assumptions, Equation (7.3) reduces to $V_{\rm up} = 0.5$ km s^{-1}. The time gap between the HDF appearance and the flux emergence was observed to be 100 min. Therefore, the depth that the apex of the magnetic flux transited across after it decelerated, is estimated to be ~ 3000 km, if the flux tube rises at the same rate as the upflow.

In this section, for simplicity, we assumed that the apex of the rising flux is circular, and that the outflow velocity $V_{\rm h}$ is only a function of r. From Figure 7.2, however, it seems that the HDF is not axisymmetric and is stronger in the direction of flux emergence (the northwest-southeast slit in this figure). This property is consistent with our preceding

numerical results; the photospheric plasma flow is found to be along the direction of flux emergence (see Figure 3.6 of Chapter 3). Moreover, in that simulation, the twist of the rising flux tube is stronger and the magnetic field at the tube's surface is almost perpendicular to the axis of the tube. In the later phase of the target AR of this study, the separation of positive and negative polarities shifted into the northeast-southwest direction, i.e., perpendicular to the diagonal line in Figure 7.2. Taking into account the previous numerical results, and considering that the observed NE-SW direction indicates the axis of the flux tube that forms this AR, we can think that the twist of this flux tube is tight, and therefore the flow is in the NW-SE direction.

7.4.3 Relations with Recent Observations: HDF as a Precursor

Using *SOHO*/MDI, Grigor'ev et al. (2007) observed NOAA AR 10488 and found that upflows of matter with a high velocity ($\gtrsim 0.4$ km s^{-1}) preceded flux emergences by 8 and 13 min. Thus, the last ~ 10 min of the divergent Doppler pattern observed in our study that remained for 100 min may contain the upward motion. However, for most of the period, the flow is expected to remain horizontal. Note that the upflow velocity of $\gtrsim 0.4$ km s^{-1} reported by Grigor'ev et al. (2007) may be the speed of a magnetic flux rising in the photosphere. As for the estimated velocity ($V_{\rm up} = 0.5$ km s^{-1}) in Section 7.4.2, this value indicates the emergence speed of a magnetic flux in the uppermost convection zone.

By means of time-distance helioseismology, Ilonidis et al. (2011) detected strong acoustic travel-time anomalies as deep as 65 Mm, 1 to 2 days before the flux rate reaches its peak, and (in most cases) a few hours before the start of the flux appearance at the surface (see also Kosovichev & Duvall, 2008; Kosovichev, 2009). These anomalies are considered as signs of the rising magnetic flux. Taking account of our numerical simulations in Part II, it is consistent to interpret this helioseismic anomaly as a result of the effect similar to the plasma accumulation; external media may be perturbed or compressed by the rising motion of the magnetic flux. The importance of the helioseismic anomaly in Ilonidis et al. (2011)

and the HDF in our study is that these phenomena occur prior to the flux emergence at the photosphere. That is, these are the precursors of the flux emergence. By combining two types of observations, sunspot appearances may be predicted in the near future.

7.4.4 Further Emergence to the Upper Atmosphere

In Section 7.3.3, we found that the Hα brightenings (plages) were located over the positive and negative pores in the photosphere. This indicates that the brightenings are caused by the plasma flowing down along magnetic loops that connect the photospheric magnetic elements (see Figure 10 of Shibata et al., 1989). The appearance of the chromospheric source was at 03:20 UT on June 11, while the flux emergence was at 03:06 UT. If we assume the Hα formation height as 2000 km, the rise velocity of the magnetic field is ~ 2.5 km s^{-1}. This value is smaller than the observed speed of the chromospheric arch filament system (AFS) of ~ 20 km s^{-1} (e.g. Bruzek, 1967), which implies that the actual rise speed is faster than 2.5 km s^{-1} and it takes some time to create Hα plage after the flux reaches the chromospheric height.

7.5 Summary

In this chapter, we have observed the horizontal divergent flow (HDF) prior to the flux emergence by using *SDO*/HMI Dopplergram and magnetogram. The presence of the HDF was predicted by our preceding numerical simulations in Part II. The HMI's continuous observation of the whole solar disk provides the means to analyze the earlier stage of the flux emergence. The summary of the observation is given as Table 7.3.

First, we made time-slices of Dopplergram and LoS magnetogram of NOAA AR 11081. From the magnetic slice, we found that the magnetic elements of positive and negative polarities separated from each other. The apparent speed of a single element was, at first, 1.2 km s^{-1}. The speed then dropped to 0.4 km s^{-1} and the elements gathered to create

Table 7.3: Summary of the AR 11081 observation (Toriumi et al., 2012)

Physical value	Observational results
Field strength	< 500 G
Unsigned total flux	$\sim 10^{21}$ Mx
Region area	1.2×10^9 km^2
Appearance of horizontal outflow	01:23 UT[a]
Start of flux emergence	03:06 UT[a]
Start of chromospheric response	03:20 UT[a]
Time difference[b]	~ 100 min
Apparent speed[c]	$1.2 \rightarrow 0.4$ km s^{-1}
Horizontal velocity[d]	0.6–1.5 km s^{-1} (max 2.3 km s^{-1})

[a]On 11 June, 2010.
[b]Time difference between the appearance of the horizontal outflow and the flux emergence.
[c]Apparent speed of the magnetic elements.
[d]Horizontal velocity of the surface plasma prior to the flux emergence.

stronger pores of > 200 G. In the Doppler slice, a pair of blue and red pattern was observed to separate, slightly earlier than the flux emergence, and the blue (red) pattern was located disk-centerward (limbward). This indicates that the HDF appeared prior to the flux emergence. According to our previous numerical experiments, the outflow is mainly horizontal during the period from the appearance of the outflow to the emergence of the magnetic flux.

Secondly, we evaluated the times of the HDF appearance and the flux emergence. To determine these times with significance, we studied the temporal changes of the Doppler and magnetic patterns from those of the quiet Sun, and defined them as the times when each profile exceeded one standard deviation of its quiet-Sun profile. As a result, the Doppler profile was found to deviate from the quiet-Sun profile at 01:23 UT, 2010 June 11, while the magnetic profile deviated at 03:06 UT. Therefore, the time difference was about 100 minutes. Also, by considering the heliocentric angle, the horizontal speed of the HDF in this time gap was estimated to be 0.6–1.5 km s^{-1}, up to 2.3 km s^{-1}.

The creation of the HDF is due to the density accumulated on the apex of the flux tube during its ascent in the convection zone. This accumulation occurs between the flattened

apex of the rising flux tube and the subadiabatically stratified photosphere. The compressed plasma escapes horizontally around the photosphere, which was observed in this study. After the magnetic flux is sufficiently intensified, the magnetic buoyancy instability is triggered and the magnetic field restarts into the upper atmosphere, which was also seen as a flux emergence in this study. Therefore, the time difference of ~ 100 min may reflect the latency during which the flux is waiting for the instability onset.

Applying a simple model of the horizontal flow and the corresponding upflow beneath the surface, we speculated that the depth of the magnetic flux is about 3000 km. Previously, *SOHO*/MDI found that an upflow preceded the flux emergence by about 10 minutes (Grigor'ev et al., 2007). This implies that the last ~ 10 min of the divergent outflow may include the upward motion. Even so, for most of the period, the outflow remains horizontal.

Moreover, using Hα images taken by SMART, we studied chromospheric response to the flux emergence at the photosphere. The time-slice showed a pair of Hα plages, which started from 03:20 UT, that is, ~ 14 min after the flux emergence. The location of these brightenings were just over the photospheric pores. Therefore, we speculated that these brightenings are caused by the plasma precipitating along the magnetic fields that connect photospheric pores of both polarities.

In this chapter, we observed the HDF in the actual Sun, which was predicted in our previous numerical simulations, and, in this way, we were able to observationally support the theoretical "two-step emergence" model (Figure 5.1). As for the observational study, the statistical analysis on HDFs would be the next target. Another importance of observing HDF is that this phenomenon can be considered as a precursor, which may allow us to predict sunspot formation that occurs in several hours.

Chapter 8

Horizontal Divergent Flow: Statistical Study

8.1 Introduction

In Chapter 7, we analyzed the observational data of NOAA active region (AR) 11081 and detected the horizontal divergent flow (HDF) of the plasma that appears at the visible surface before the magnetic flux emerges to the photosphere. The duration of the HDF, i.e., the time gap from the start of the HDF to that of the flux emergence, was about 100 minutes. Also, the flow speed of the HDF was 0.6–1.5 km s^{-1}, up to 2.3 km s^{-1}.

Although the previous detection of the HDF was a promising result which supports the "two-step emergence" model (Figure 5.1) based on the numerical studies, we only observed the HDF in just a single emergence event. Therefore, we need to repeat our analysis in many more events to further support this theory. Also, the properties of the HDF, such as the duration and the maximum velocity, may depend on the parameters of the subsurface magnetic field that pushes up the plasma. By conducting numerical simulations of large-scale flux tube emergence in Chapter 4, we found that these properties actually depend on the field strength and the twist intensity of the initial flux tube. Therefore, by analyzing HDFs

in larger ensemble of emergence events, we may be able to investigate the physical aspects of the subsurface flux such as the rising speed.

In this chapter, we report the statistical analysis of the HDFs in 23 flux emergence events. The aims of this study are to detect HDFs in larger ensemble of AR data and investigate the commonness of the HDF and, if possible, to derive any physical properties of rising magnetic fields in the solar interior.

The rest of this chapter is organized as follows. In the next section, we provide the data selection and reduction. In Section 8.3, we analyze the data and show the results. Section 8.4 is dedicated to discussing the results and to deriving the physical properties of rising flux tubes in the convection zone. Finally, in Section 8.5, we summarize this chapter.

8.2 Data Selection and Reduction

8.2.1 Data Selection

In this study, we used observational data taken by the Helioseismic and Magnetic Imager (HMI: Schou et al., 2012) on board the *Solar Dynamics Observatory* (*SDO*). We searched for flux emergence events that occurred during the period from May 2010 to June 2011 (14 months), which is the solar minimum between Solar Cycles 23 and 24 after the launch of the *SDO* spacecraft in February 2010. The reason of choosing this period is to obtain "clear" events, that is, a flux emergence into a quiet region with less preexisting magnetic fields. As the Sun steps into the active phase, it may become difficult to distinguish magnetic flux of the newly emerged fields from that of the preexisting fields, which may be the remnant of previously emerged fields. During this period, we selected emergence events in the area with a heliocentric angle $\theta \leq 60^\circ$ to keep the quality of the HMI data. Also, we picked up events only in the eastern hemisphere of the solar disk in order to monitor the AR evolution as long as possible from their births. After all, 23 emerging events in 21 ARs including 2 ephemeral ARs (Harvey & Martin, 1973) were obtained.

8.2.2 Data Reduction

For each target AR, we made tracked data cubes of the Doppler velocity and the line-of-sight (LoS) magnetogram, both having a pixel size of 0.03 heliographic degree ($\simeq$ 0.5 arcsec $\simeq$ 360 km) with a 512×512 pixel field-of-view (FoV), and a 12 minute cadence with a 7 day duration. Also, for each emergence event, we made tracked data cubes of Dopplergram and LoS magnetogram with the same resolution and FoV but with a cadence of 45 s and a duration of 36 hr. For each data cube, we applied Postel projection. The noise levels of the original magnetograms and Dopplergrams are shown in Appendix B.1.

In order to eliminate the effects of the rotation of the Sun and the orbital motion of the *SDO* spacecraft, and to reduce the east-west trend (due to the spherical geometry of the Sun) from the Dopplergram, we constructed additional background data and subtracted the background from each Doppler frame. The reduction procedure is as follows (see also Grigor'ev et al., 2007).

1. We first averaged ten upper and ten lower rows of the FoV of each frame, and linearly smoothed the both rows, obtaining additional background data only with upper and lower rows of smoothed data.

2. Then, we performed a linear interpolation between the upper and lower pixels of the columns to produce full background data.

3. Finally, by subtracting the background data from each frame, we obtained trend-free Doppler data.

In addition, a 10 minute running average was applied to the 36 hr Dopplergrams and magnetograms to smooth out rapid fluctuations that may not be related to the HDF (5-min oscillation, surface gravity wave, etc.).

8.3 Data Analysis

8.3.1 Properties of ARs

In this subsection, we analyze the properties of ARs. For each 7-day magnetogram of the target AR, we measured the maximum total unsigned flux, the maximum unsigned flux growth rate, and the maximum footpoint separation. In the magnetogram, we first set a box surrounding the emerging region, and measured the total unsigned flux $\Phi = \int_S |B|\, dS$ and its time derivative $d\Phi/dt$, where B is the magnetic field strength of each pixel, S is the box size, dS is the area of a pixel element, and t is the time. We applied 120 and 240 minute smoothings for Φ and $d\Phi/dt$, respectively, and recorded their maximum values, $\max(\Phi)$ and $\max(d\Phi/dt)$. Also, within the box in each frame, we measured the flux-weighted center of each polarity

$$(x_\pm, y_\pm) = \left(\frac{\sum x B_\pm}{\sum B_\pm}, \frac{\sum y B_\pm}{\sum B_\pm} \right), \tag{8.1}$$

and evaluated the footpoint separation between both centers,

$$d_{\rm foot} = \sqrt{(x_- - x_+)^2 + (y_- - y_+)^2}. \tag{8.2}$$

Here, in evaluating the flux-weighted centers, we only used the pixels with $|B| \geq 200$ G to keep the data quality. Then, we recorded the maximum separation, $\max(d_{\rm foot})$.

Figure 8.1 is an example of AR data. In panel (a), the HMI magnetogram of NOAA AR 11130 (event #7) is shown, and the flux-weighted center of each polarity is indicated with a cross. Panels (b) and (c) are for the temporal evolutions of the total unsigned flux, the flux rate, and the footpoint separation. The maximum total flux, the maximum flux rate, and the maximum separation of this AR are 1.1×10^{22} Mx, 7.3×10^{16} Mx s^{-1}, and 61.1 Mm, respectively. The corresponding figures of all the analyzed ARs are listed in Appendix B.2.

The obtained properties of the target regions are summarized in Table 8.1. As can be

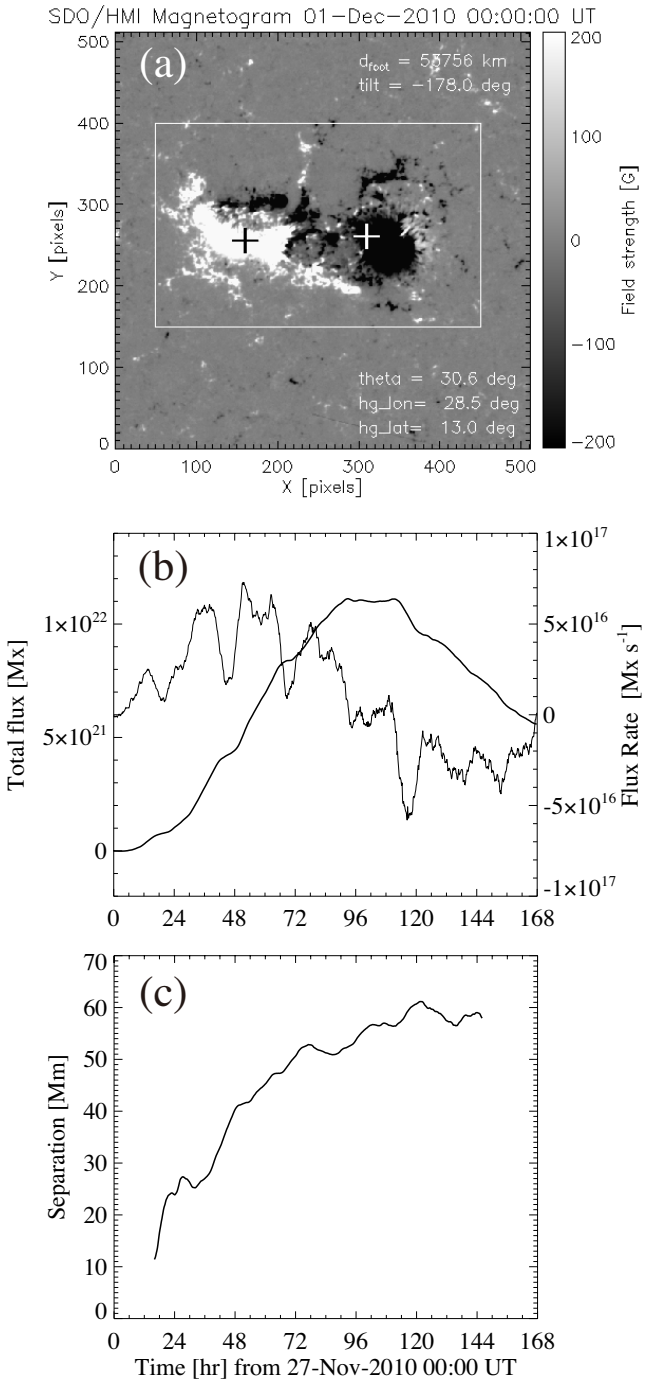

Figure 8.1: An example of AR data from the list in Appendix B.2. (a) HMI magnetogram of NOAA AR 11130 (event #7). Black and white crosses are the flux-weighted centers of positive and negative polarities, respectively, which are calculated inside the rectangular box. (b) Temporal evolutions of the total unsigned flux (thick) and its time derivative (thin). (c) Temporal evolution of the footpoint separation.

Table 8.1: Newly emerging ARs analyzed in this study.

Event #	NOAA AR	Year	Date	$\max(\Phi)$ (Mx)	$\max(d\Phi/dt)$ (Mx s^{-1})	$\max(d_{\rm foot})$ (Mm)
1	11066	2010	May 1	2.1×10^{21}	5.1×10^{16}	57.1
2[a]	"		May 2	"	"	"
3	11072		May 20	7.1×10^{21}	6.0×10^{16}	50.1
4	11075		May 27	1.8×10^{21}	3.3×10^{16}	38.0
5	11076		May 30	7.7×10^{21}	7.5×10^{16}	52.9
6	11098		Aug 10	2.4×10^{21}	4.7×10^{16}	57.9
7	11130		Nov 27	1.1×10^{22}	7.3×10^{16}	61.1
8	ephemeral		Dec 10	1.2×10^{21}	2.6×10^{16}	32.6
9	11137		Dec 24	1.8×10^{21}	3.9×10^{16}	68.3
10	11138		Dec 26	3.1×10^{21}	4.4×10^{16}	61.4
11	11141		Dec 29	4.3×10^{21}	6.1×10^{16}	64.8
12[b]	"		Dec 30	"	"	"
13	11152	2011	Feb 1	2.4×10^{21}	3.8×10^{16}	75.7
14	11153		Feb 2	7.7×10^{21}	1.1×10^{17}	66.8
15	11156		Feb 7	4.8×10^{21}	4.2×10^{16}	89.3
16	11158		Feb 10	2.3×10^{22}	1.7×10^{17}	59.6
17	11162		Feb 17	7.5×10^{21}	1.1×10^{17}	60.1
18	11179		Mar 20	1.9×10^{21}	3.1×10^{16}	38.2
19	11184		Apr 2	8.2×10^{21}	8.7×10^{16}	72.8
20	11192		Apr 12	1.6×10^{21}	3.6×10^{16}	59.8
21	ephemeral		Apr 18	5.6×10^{20}	1.3×10^{16}	20.5
22[c]	11214		May 13	–	–	–
23[c]	11217		May 15	–	–	–

[a]Region is the same as event #1.
[b]Region is the same as event #11.
[c]Magnetic fields of events #22 and #23 are difficult to separate from each other.

seen in the table, the total flux ranges from 5.6×10^{20} to 2.3×10^{22} Mx, while the flux rate is from 1.3×10^{16} to 1.7×10^{17} Mx s^{-1} and the footpoint separation is from 20.5 to 89.3 Mm. Note that, in order to keep the data quality, the physical values of each AR in this table are measured under the condition that the heliocentric angle is $\theta \leq 60°$. We should also take care of the fact that, because of the diffusion of the sunspots, footpoint separations of some ARs may become larger even after the ARs become mature. Regarding quadrupolar regions such as NOAA AR 11158 (event #16), we measure the separation not between the most distant footpoints but between the two representative flux-weighted centers simply calculated from the entire AR.

8.3.2 Detection of the HDF

First, for each 36 hr data of the 23 emergence events, we measured the start of the HDF in the Dopplergram (HDF start: $t_{\rm HDF}$) and the start of the flux emergence in the magnetogram (emergence start: $t_{\rm FE}$) by using the method developed in Chapter 7. If $t_{\rm HDF}$ was defined by this method, we then calculated the time gap between these two times (HDF duration: $\Delta t = t_{\rm FE} - t_{\rm HDF}$). If $\Delta t > 0$, we double-checked the Doppler images by visual inspection and determined if the HDF was "clear" or not. If $\Delta t \leq 0$, we defined that the HDF detection was failed. If $t_{\rm HDF}$ was not defined by the previous method, or if the result of the double-check was negative, we determined $t_{\rm HDF}$ by visual inspection. Then, again, if $\Delta t = t_{\rm FE} - t_{\rm HDF} > 0$, we determined that the HDF was detected. If $t_{\rm HDF}$ was still not defined, or if $\Delta t \leq 0$, we concluded that the detection was failed.

The result of the detection is shown as Table 8.2. In 6 events out of the entire 23 events, we observed clear HDFs, that is, $t_{\rm HDF}$ was detected by the method in Chapter 7 and $\Delta t > 0$. The temporal evolutions of the Dopplergram and magnetogram for the 6 clear events, along with the corresponding continuum images, are shown as Figure B.4 in Appendix B.3. Another 4 events indicated with asterisks are the cases that $t_{\rm HDF}$ was detected not by the previous method but by visual inspection, and that $\Delta t > 0$. Events indicated with daggers are that

Table 8.2: Results of the HDF detection.

Event #	NOAA AR	Year	Date	t_{HDF}[a]	t_{FE}[b]	Δt[c] (min)	HDF[d]	θ (°)
1	11066	2010	May 1	07:24	08:11	47	Y	46.5
2	”		May 2	19:25	20:30	65	Y	30.1
3	11072		May 20	13:05	14:51	106	Y	40.6
4	11075		May 27	–	05:59	–	N	45.7
5	11076		May 30	17:08	16:31	−37	N	35.7
6	11098		Aug 10	18:40*	19:36	56	Y*	45.4
7	11130		Nov 27	–	06:54	–	N	28.0
8	ephemeral		Dec 10	–	11:00	–	N	17.2
9	11137		Dec 24	21:02	22:42	100	Y	33.6
10	11138		Dec 26	10:21	07:49	−152	N	29.7
11	11141		Dec 29	–	13:44	–	N	41.3
12	”		Dec 30	19:15*	20:08	53	Y*	36.7
13	11152	2011	Feb 1	16:41*	16:58	52	Y†	32.7
14	11153		Feb 2	21:38*	21:36	33	Y†	35.7
15	11156		Feb 7	18:27	18:32	5	Y	58.2
16	11158		Feb 10	21:21	22:04	43	Y	47.4
17	11162		Feb 17	14:15*	15:04	49	Y*	29.2
18	11179		Mar 20	–	22:02	–	N	29.6
19	11184		Apr 2	00:40*	02:21	101	Y*	36.7
20	11192		Apr 12	02:48	01:19	−89	N	19.9
21	ephemeral		Apr 18	–	02:13	–	N	49.0
22	11214		May 13	13:00*	14:26	77	Y†	43.6
23	11217		May 15	–	07:29	–	N	25.7

[a]Start of the HDF. Values determined by visual inspection are indicated with asterisks.

[b]Start of the flux emergence.

[c]Duration of the HDF: $\Delta t = t_{\mathrm{FE}} - t_{\mathrm{HDF}}$.

[d]Yes/No. Events that t_{HDF} is determined by eye and that $\Delta t > 0$ are indicated with asterisks. Events that results of the double-check are negative but that t_{HDF} are defined by eye and $\Delta t > 0$ are indicated with daggers.

Table 8.3: Clear HDF events.

Event #	Δt (min)	θ (°)	max($\lvert V_\mathrm{D}\rvert$) (km s^{-1})	max($\lvert V_\mathrm{h}\rvert$) (km s^{-1})	max($d\Phi/dt$) (Mx s^{-1})
1	47	46.5	2.8	3.9	1.4×10^{16}
2	65	30.1	2.2	4.4	2.1×10^{16}
3	106	40.6	2.4	3.7	1.1×10^{16}
9	100	33.6	1.7	3.1	9.4×10^{15}
15	5	58.2	1.5	1.8	1.2×10^{16}
16	43	47.4	1.5	2.0	3.0×10^{15}

the t_HDF was defined by the previous method but was rejected in the double-check process. These three cases were then checked visually and, in every case, t_HDF was determined. Since $\Delta t > 0$ in all three cases, we concluded that they have HDFs. Thus, in total, the HDFs were found in 13 events, or, 56.5% of all the analyzed events.

In the 6 clear events, the HDF duration Δt ranges from 5 to 106 minutes (the average being 61.0 minutes and the median 56.0 minutes). For these events, we also evaluated the maximum horizontal speed from the maximum Doppler velocity, max (V_D). During Δt, we applied a slit with a thickness of 5 pixels to the Dopplergrams and averaged over 5 pixels, and measured the largest absolute Doppler velocity. Here, the slit is parallel to the separation of both magnetic polarities, centered at the middle of the emergent region. Using the heliocentric angle θ, the maximum horizontal velocity can be obtained by

$$\max\left(|V_\mathrm{h}|\right) = \frac{\max\left(|V_\mathrm{D}|\right)}{\sin\theta}. \tag{8.3}$$

Table 8.3 shows the results of the analysis. The maximum HDF speed ranges from 1.8 to 4.4 km s^{-1} (the average being 3.1 km s^{-1} and the median 3.4 km s^{-1}). The obtained durations and the horizontal speeds will be discussed later in Section 8.4.2.

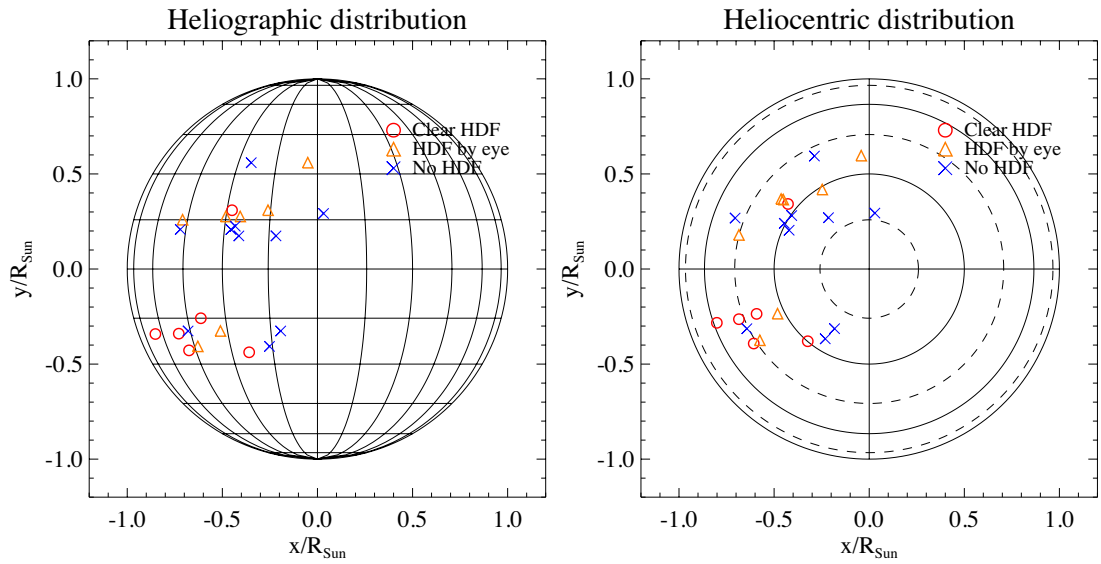

Figure 8.2: Distribution of the flux emergence events. (Left) Heliographic coordinates, where the Sun's rotation axis is fixed onto the x–y plane. (Right) Heliocentric coordinates, where the LoS is perpendicular to the x–y plane. (z-axis is toward the Earth.)

8.4 Discussion

8.4.1 HDF Detection

In the previous section, we analyzed 23 flux emergence events and detected 6 clear HDFs. We also found another 7 HDFs by visual inspection. Figure 8.2 shows the distribution of the events in heliographic and heliocentric coordinates. From the heliographic map, one may find that newly emerging ARs are distributed in the mid-latitude bands of both hemispheres (latitude ranging from $\sim 15°$ to $\sim 30°$). Also, from the heliocentric map, one can see that all clear HDFs are detected in the range of $\theta > 30°$.

In the remaining 10 events, we did not find HDFs, which can be divided into two groups: the cases that the HDF was not detected nor found even by eye, and the cases that the emergence start came before the HDF start ($\Delta t < 0$). The possible reasons for the failed detections are as follows.

- If the flux emergence occurs at the location too close to the disk center, the HDF will not appear in the Dopplergrams because of the projection. In fact, all 6 clear events are located away from the disk center ($\theta > 30°$), while 7 out of 10 failed events are closer to the disk center ($\theta \leq 30°$).

- The HDF may be stronger in the direction of the separation of the positive and negative polarities (see Figure 3.6 in Chapter 3). When the footpoint separation on the solar disk is perpendicular to the axis from the disk center to the AR, the HDF may not be seen, since it has less LoS component. This effect seems to be responsible for the failed detection in event #11.

- The smaller ARs may not have coherency or energy enough to push up the sufficient amount of plasma that can be observed as HDF. For the two ephemeral ARs (#8 and #21), we did not observe HDFs in both cases.

- If the flux emerges into a preexisting field, it is difficult to separate the HDF from the Doppler component caused by the preexisting field (#23).

8.4.2 Physical Properties of the HDF

For the 6 clear HDF events, we observed that the HDF duration is on average 61 minutes. This value is comparable to the duration of 103 minutes observed in Chapter 7. This value is also comparable to 30–45 minutes obtained from a parameter survey of the flux emergence simulations in Chapter 4. The physical explanation of this HDF duration is, according to the simulations, the elapse time from the deceleration of the rising flux at the top convection zone to the start of the further emergence into the upper atmosphere from the surface layer. In other words, the time gap of 61 minutes indicates the waiting time for the secondary emergence in the "two-step emergence" model. Note that, in the actual Sun, thermal convection is continuously excited around the surface layer and thus the situation may be more complex.

The maximum HDF speed of the 6 clear events is on average 3.1 km s^{-1}, which is again comparable to 2.3 km s^{-1} observed in the previous study. According to our simulation in Chapter 4, the HDF is driven by the pressure gradient and the velocity is a fraction of the local sound speed ($\sim$ 10 km s^{-1} in the photospheric layer), which agrees with the observation results (see also Cheung et al., 2010).

8.4.3 Investigation of the Subsurface Magnetic Flux

In this section, we investigate the subsurface rising magnetic fields that push up the unmagnetized plasma, which is observed as an HDF.

First, we consider a simple two-dimensional model of the emerging magnetic flux as illustrated in Figure 8.3; see also Figure 4.3(a). Here, we assume that the rising speed of the magnetic flux V_z is of the order of Alfvén speed $V_{\rm A}$ (see Section 1.3; Parker, 1975), namely,

$$V_z = \alpha V_{\rm A} = \alpha \frac{B}{\sqrt{4\pi\rho}}, \tag{8.4}$$

where B and ρ are the field strength and the plasma density. For simplicity, we here assume the factor α to be unity. From the mass conservation of the HDF, we obtain

$$V_{\rm h} = \frac{L}{D} V_z = \frac{L}{D} \frac{B}{\sqrt{4\pi\rho}}, \tag{8.5}$$

where $V_{\rm h}$, L, and D, are the horizontal speed, the lateral extension, and the thickness of the HDF, respectively. Also, the flux growth rate when the flux appears at the surface can be written as:

$$\frac{d\Phi}{dt} = 2LV_zB = 2L\frac{B^2}{\sqrt{4\pi\rho}}, \tag{8.6}$$

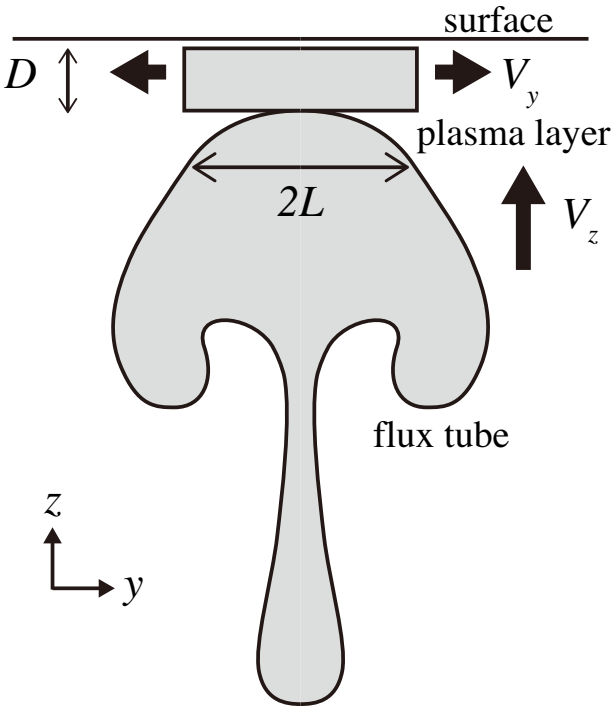

Figure 8.3: Two-dimensional model of the rising magnetic field and the plasma. Same as Figure 4.5(b).

where Φ is the magnetic flux. Combining Equations (8.5) and (8.6), we get

$$V_{\rm h} = \frac{(L/2)^{1/2}}{D(4\pi\rho)^{1/4}} \left[\frac{d\Phi}{dt}\right]^{1/2}. \tag{8.7}$$

In this equation, the horizontal speed $V_{\rm h}$ and the flux growth rate $d\Phi/dt$ can be measured from the observational data, which are summarized in Table 8.3.

In Figure 8.4(a), we plot $\max(d\Phi/dt)$ and $\max(V_{\rm h})$, measured during Δt, for the 6 clear HDF events. Here, we fit a function $\max(V_{\rm h}) = C_1 \times [\max(d\Phi/dt)]^{1/2}$ in the diagram. The obtained constant C_1 is comparable to the coefficient in Equation (8.7). The result of the fitting is

$$C_1 = \frac{(L/2)^{1/2}}{D(4\pi\rho)^{1/4}} = 2.3 \times 10^{-3}. \tag{8.8}$$

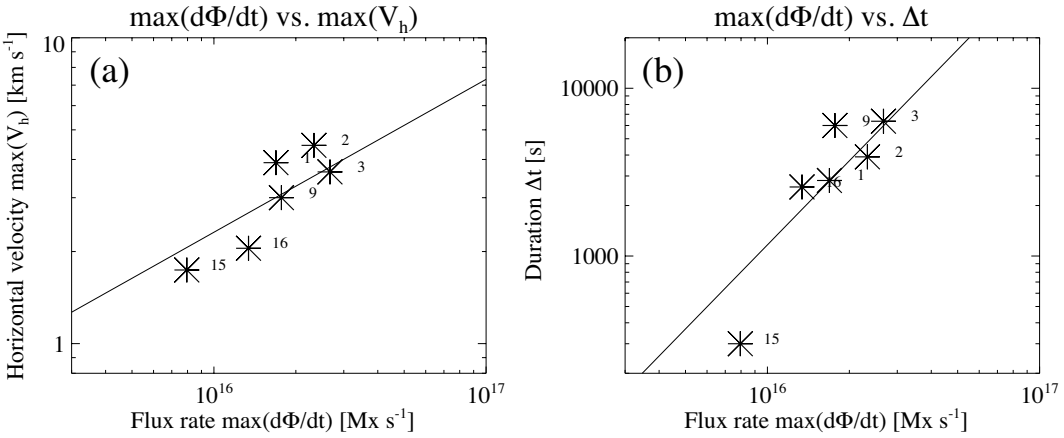

Figure 8.4: (a) Maximum flux growth rate and maximum horizontal speed for 6 clear HDF events. The solid linear line is the fitted function $\max(V_{\rm h}) = C_1 \times [\max(d\Phi/dt)]^{1/2}$. (b) Maximum flux growth rate and HDF duration for 6 clear HDF events. The solid liner line is the fitted function $\Delta t = C_2 \times [\max(d\Phi/dt)]^{C_3}$. In both panels, the number right to each asterisk denotes the event number.

Note that, in the fitting process, $V_{\rm h}$ is measured in the unit of cm s^{-1}. From Equation (8.7), by assuming $L = 5$ Mm and $\rho = 2.5 \times 10^{-7}$ g cm^{-3}, we obtain the thickness of the HDF: $D = 1.6$ Mm.

Finally, by inserting $D = 1.6$ Mm into Equation (8.5), the rising speed of the magnetic flux, V_z, can be evaluated for each HDF event, which is summarized in Table 8.4. The rising speed of the magnetic flux ranges from 0.6–1.4 km s^{-1}. This value is comparable to the simulation results of ~ 1 km s^{-1} in Part II and other simulation results (e.g., Fan, 2009). This rising speed is also comparable with the seismic studies (e.g., Ilonidis et al., 2011; also the result in Chapter 9)

Figure 8.4(b) shows the relation between the maximum flux growth rate, $\max(d\Phi/dt)$, and the HDF duration, Δt. According to Equation (8.6), $d\Phi/dt$ is proportional to the square of B. The linear line of Figure 8.4(b) is the fitted function $\Delta t = C_2 \times [\max(d\Phi/dt)]^{C_3}$ and the best fitting parameters are $C_2 = 2.7 \times 10^{-24}$ and $C_3 = 1.7$. Thus, the observation indicates $\Delta t \propto B^{3.4}$. In the parameter survey of the flux emergence simulations in Chapter

Table 8.4: Rising velocity of the magnetic flux for the 6 clear HDF events.

Event #	V_z (km s^{-1})
1	1.3
2	1.4
3	1.2
9	1.0
15	0.6
16	0.7

4 (see Figure 4.4), we found that, when the initial tube is stronger (field strength $\gtrsim 30$ kG), the HDF duration Δt is inversely proportional to the field strength $B_{\rm tube}$ of the initial flux tube. On the other hand, when the tube is weaker (field strength $\lesssim 30$ kG), it deviates from the inverse-square law and has a positive correlation with the field strength. Therefore, the observed positive correlation of $\Delta t \propto B^{3.4}$ hints that the field strength of the rising flux in the deep convection zone (~ -20 Mm) has a field strength of $\lesssim 30$ kG.

8.4.4 Correlation with AR Parameters

Figure 8.5 summarizes the correlations between HDF parameters (HDF duration, Δt, and maximum HDF speed, $\max(V_{\rm h})$) and AR parameters (maximum total unsigned flux, $\max(\Phi)$, maximum flux rate, $\max(d\Phi/dt)$, and maximum footpoint separation, $\max(d_{\rm foot})$) for 6 clear HDF events. Note that the AR parameters including $\max(d\Phi/dt)$ were measured not during the HDF duration (Δt) but during the entire AR evolution using 7 day magnetogram, under the condition of $\theta \leq 60^\circ$ (see Section 8.3.1).

In this figure, the best correlation is -0.7 of panel (f), the correlation between the maximum footpoint separation, $\max(d_{\rm foot})$, and the maximum HDF speed, $\max(V_{\rm h})$. According to the simulation results in Chapter 4, the maximum HDF speed, $\max(V_y)$, is proportional to the initial field strength, $B_{\rm tube}$; see Figure 4.4(c). On the other hand, when the field $B_{\rm tube}$ is stronger, the total flux is expected to be larger, and thus the AR size, or, the footpoint

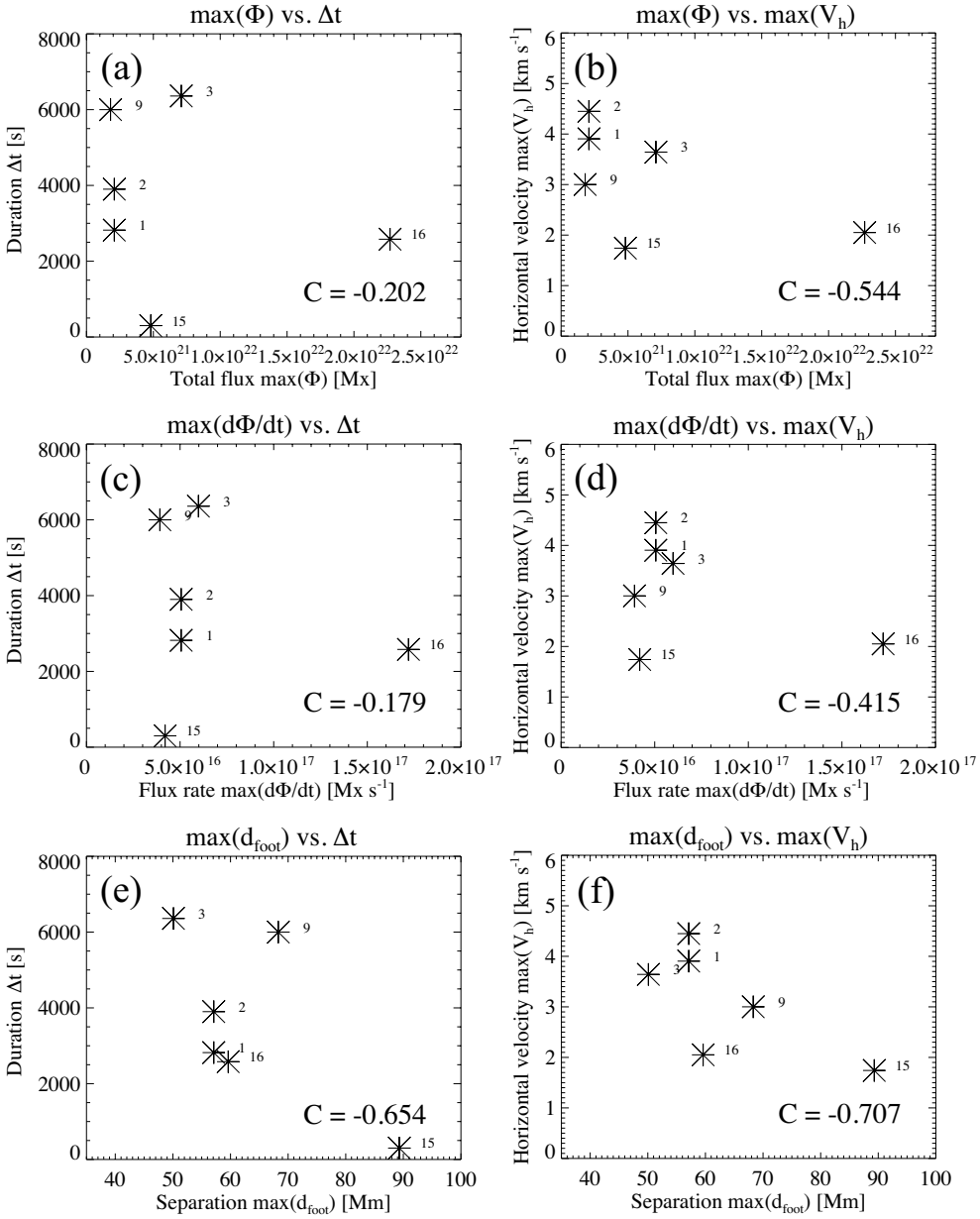

Figure 8.5: Correlations between HDF parameters (HDF duration, Δt, and maximum HDF speed, $\max(V_{\rm h})$) and AR parameters (maximum total unsigned flux, $\max(\Phi)$, maximum flux rate, $\max(d\Phi/dt)$, and maximum footpoint separation, $\max(d_{\rm foot})$). Correlation coefficient C is indicated in the bottom right of each panel. Note that these parameters are measured from the 7 day magnetograms, under the condition that the heliocentric angle θ is $\leq 60°$.

separation $d_{\rm foot}$ may also become larger. Therefore, the separation $\max(d_{\rm foot})$ and the horizontal speed $\max(V_{\rm h})$ are expected to have a positive correlation, which is opposite from the observational result of panel (f). The absolute correlation coefficients of other panels are at most, or less than 0.6. The AR parameters here represent the global structure of emerging magnetic flux that eventually forms the AR, and, since the HDF appears only in the very initial phase of the flux emergence, they might be independent of the HDF parameters.

8.4.5 HDF and Elongated Granules

In continuum, the granulation pattern in an emerging flux region is known to appear different from that in quiet region. In the early phase of flux emergence, the transient dark alignments, or the darkened intergranular lanes, appear in the center of the emerging region, aligned roughly in parallel with the axis connecting the two main polarities (Brants & Steenbeek, 1985; Zwaan, 1985; Strous & Zwaan, 1999). It is thought that the dark lanes are created by the horizontal magnetic fields at the apex of the rising flux tube from the convection zone (Zwaan, 1985). Numerical simulations also support this scenario (e.g., Cheung et al., 2007)

In event #1 in Figure B.4, for example, the granulation pattern in the continuum image looks mostly circular at first at 07:15 UT and also at 07:30 UT, namely, after the HDF started ($t_{\rm HDF}$ = 07:24 UT). However, at 08:00 UT, the pattern in the central region shows a slight elongation to the direction of the red and blue Doppler pair. Although the flux emergence is not detected yet at this moment ($t_{\rm FE}$ = 08:11 UT), the magnetogram shows a faint positive (white) pattern, which may be the horizontal magnetic fields reflected because of the projection (this emerging AR is located 46.5° away from the disk center). However, at 08:15 UT, namely, after the significant line-of-sight flux is detected at 08:11 UT, the elongated pattern is not seen in the continuum. This transient elongation (after the HDF appearance, $t_{\rm HDF}$, and just before the magnetic detection, $t_{\rm FE}$) reminds us of the concept that the HDF is pushed up by the horizontal magnetic fields at the apex of the large-scale rising flux transported from the deeper convection zone. Therefore, this scenario agrees well

with the "two-step emergence" scenario (Figure 5.1).

8.4.6 Flux Emergence and Supergranulation

Another interesting topic may be the appearance of the emerging flux in the supergranulation pattern. Bruzek (1969) pointed out a *striking coincidence* between the size of the arch filament system (AFS: Figure 1.3) and the Ca network (referred to as supergranulation) and suggested that an AFS may cover a supergranule. Also, based on the observation, Frazier (1972) suggested an empirical model in which a supergranule brings the magnetic fields to the surface and transports horizontally to the vertices of the cell. However, Harvey & Martin (1973) found that the locations of emerging ephemeral ARs are not associated with the distribution of the existing network fields.

Judging from the Doppler patterns in Figure B.4, the emergence events #1 and 2 appear at the boundaries between the pre-existing blue and red regions. These events (NOAA AR 11066) took place to the southeast of the disk center and, thus, the blue (red) signal in upper right (lower left) indicates that the pre-existing flow fields are divergent. Therefore, we can at least speculate that these emergence events occur at the centers of the supergranules. However, it is not sufficient to determine whether these fluxes are transported to the surface by the convective cells. Regarding the other 4 events, it is difficult to determine the locations of the supergranules.

8.5 Summary

In this chapter, we have shown a statistical analysis of the HDF, which was suggested to appear at the visible surface of the Sun just before the flux emergence. We picked up 23 flux emergence events in 21 ARs, total unsigned flux ranging from 5.6×10^{20} to 2.3×10^{22} Mx, and detected 6 clear HDFs using the method developed in Chapter 7. In another 7 emergence events, we found HDFs by visual inspection. In total, the HDFs were observed in 56.6% of

all events. If we exclude the emergence events closer to the disk center ($\theta \leq 30°$), which are supposed to have less Doppler components, the detection rate increases up to more than 80%.

In the 6 clear events, the HDF duration from the HDF appearance to the flux emergence was on average 61 minutes, which is comparable to 103 minutes observed in the previous study in Chapter 7. The physical meaning of this time gap is the waiting time after the rising magnetic flux slows down in the top convection zone before it restarts emergence into the upper atmosphere. Compared with the duration of 30–45 minutes observed in the numerical simulations in Chapter 4, the obtained 61 minutes is a reasonable value. The maximum horizontal speed of the HDF is on average 3.1 km s^{-1}, which is also comparable to 2.3 km s^{-1} observed in the previous detection in Chapter 7 and several km s^{-1} in our simulations in Chapter 4.

From a simple two-dimensional model, we estimated the rising speed of the subsurface magnetic flux, which we cannot observe from direct optical observations. The estimated rising speed was 0.6–1.4 km s^{-1}, which is comparable with our simulations in Chapter 4, previous calculations for the solar interior, and other seismic studies (including our result in Chapter 9). By comparing with our simulation results, we also speculated that the rising flux tubes have a field strength of less than 30 kG in the deep convection zone.

In this chapter, we statistically analyzed the HDFs in many more regions. We here conclude that the HDF is rather a common feature and, thus, it further supports the "two-step emergence" model, which was proposed based on the numerical studies in Part II. We also found that the HDF observation provides us with a tool to investigate the physical states of the subsurface magnetic fields.

Chapter 9

Helioseismic Probing of the Emerging Flux[1]

9.1 Introduction

In the "two-step emergence" model (Figure 5.1), the rising magnetic flux in the top convection zone slows down because of the strongly-stratified uppermost convection zone and the convectively-stable photosphere. However, we cannot investigate the physical state (e.g., rising speed) of the subsurface magnetic flux from direct optical observations. One possible way to overcome this problem is helioseismology. In this chapter, we present the first detection of the "rising motion" corresponding to the emerging magnetic flux, by using a newly-developed seismic technique. First, in this section, we briefly introduce helioseismology and show the idea behind this study. Then, we analyze the observation data in Section 9.2 and show the results in Section 9.3. Finally, in Section 9.4, we discuss the results and summarize this chapter.

[1]Most part of this chapter was published in Astrophysical Journal (Toriumi et al., 2013)

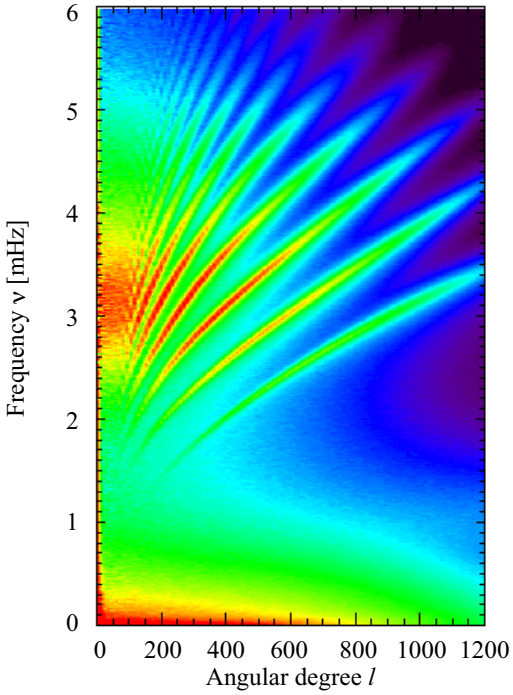

Figure 9.1: An example of the oscillation power spectrum of the Sun shown in (l, ν) plane (so-called "k–ω diagram"). Color represents the power in logarithmic scaling.

9.1.1 Helioseismology

The Sun is continuously oscillating due to the waves generated by the turbulence in the top convection zone. Since the aspects of the oscillation (frequency, wavenumber, etc.) are determined by the structure of the oscillating body (i.e., the Sun), we can investigate the inner structure and dynamics of the Sun by observing the wave field, particularly of acoustic pressure waves, at the visible surface. This is the technique of helioseismology.

Figure 9.1 is an example of the oscillation power spectrum of the Sun known as $k_{\rm h}$–ω diagram (commonly called "k–ω diagram"), where $k_{\rm h}$ denotes the horizontal wavenumber ($k_{\rm h} = \sqrt{k_x^2 + k_y^2}$) and ω the frequency. In this figure, instead of $k_{\rm h}$ and ω, we use angular degree l of spherical harmonic functions for wavenumber, where $l = k_{\rm h} R_\odot$ and $R_\odot \simeq 700$ Mm is the solar radius, and ν for frequency. Here, one may find several ridges, which are the

global standing waves, or, normal modes. The lowest ridge is the f-mode (fundamental mode: surface gravity waves) and the others are the p-mode (pressure mode: acoustic waves), while g-mode (gravity mode: gravity waves) is thought to be trapped in the deeper interior and is not seen in this diagram. One may also find that the power of the p-modes (standing acoustic waves) is strongest around 3 mHz, i.e., 5 minutes. This is the so-called "5-min oscillation" and was first discovered by Leighton et al. (1962). The power enhancement at the bottom of the figure is due to the local convection (granulation and supergranulation).

While the global structure of the Sun has widely been revealed by global helioseismology (e.g., the differential rotation: Schou et al., 1998), new technique called local helioseismology has also been developed to locally probe subsurface structures and flow fields. For example, the meridional circulation was investigated using local seismology (Giles et al., 1997; Schou & Bogart, 1998).

Instead of using eigenfrequencies of solar oscillations, local helioseismology deals with the way acoustic waves propagate in the solar interior. In time-distance method (Duvall et al., 1993), one of the major techniques of local helioseismology, oscillation signals at two selected locations on the solar surface are measured and, by cross-correlating the two signals, travel times of the acoustic waves between the two locations are evaluated. These travel times are then inverted to obtain the distribution of the sound speed, flow field, etc. in the interior. In this method, acoustic waves are assumed to propagate through the solar interior in accordance with the background stratification. Since the temperature and thus the sound speed become higher for larger depth, each acoustic wave generated near the solar surface reaches a certain depth and refracts back to the surface. Using a solar model (e.g., model S by Christensen-Dalsgaard et al., 1996) and applying Snell's law, we can calculate this ray path of each acoustic wave (ray theory). The estimation of the returning depth and travel distance of the ray is given in Appendix C.

9.1.2 Idea behind this Study

Local helioseismology is now opening a door to the investigation of a rising magnetic flux in the convection zone, although previously it was thought to be difficult to detect any significant seismic signatures associated with the emerging flux before it appears at the surface because of the fast emergence and low signal-to-noise ratio (S/N; Kosovichev, 2009). Recent observation by Ilonidis et al. (2011), however, detected strong acoustic travel-time anomalies 1–2 days before the photospheric flux attains its peak flux emergence rate (see Figure 1.8 in Chapter 1). They estimated the flux rising speed from -65 Mm of the convection zone to the surface to be 0.3–0.6 km s^{-1}. Hartlep et al. (2011) focused on the surficial acoustic oscillation power (time-averaged squared velocity) and found that a reduction in acoustic power in the frequency range of 3–4 mHz can be seen about 1 hr before the start of the flux appearance (see Figure 1.9). Their interpretation was that the acoustic power is reduced by the subsurface magnetic field.

In this study, we develop a new method to detect the rising motion that corresponds to the subsurface flux emergence, by using acoustic power measurement at the surface. The idea behind this study is as follows: It is possible to apply a Fourier filter to the Doppler data, to extract acoustic waves penetrating to a particular range of depths. A scheme similar to deep focusing (Duvall, 2003), with annuli set up around the surface points above the targets, can also be applied to integrate the signal from that depth range. The acoustic power of such a filtered wave field, then, must be influenced by the acoustic power in this depth range. That is, if the acoustic power is reduced in a certain region in the solar interior by a power-reducing agent such as magnetic field[2], the acoustic power observed in the surface regions which are connected to this region through rays corresponding to the observed wave components may also be reduced. Therefore, in this study, to the Doppler data in an emerging AR, we apply six different filters that have primary sensitivities to six different depths according

[2]Here we assume that waves may be locally damped, or scattered off their original paths, by such an agent, resulting in surface power reduction. Therefore, for simplicity, we use the term "power-reducing agent."

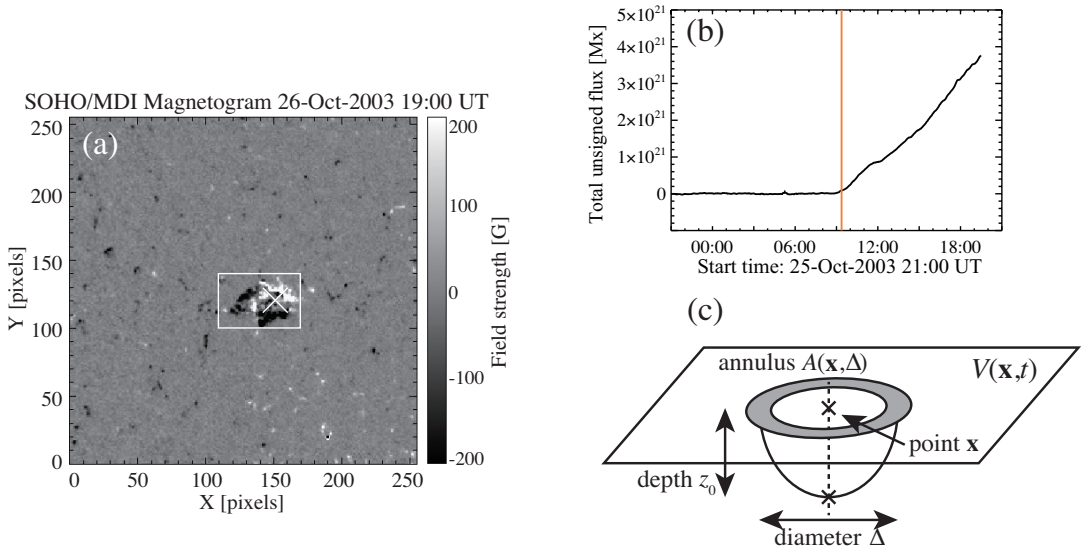

Figure 9.2: (a) Magnetogram of NOAA AR 10488. The field of view is the same as Doppler data used in this analysis. The center of X indicates the emergence location $\boldsymbol{x}_1$. (b) Time-evolution of the total unsigned flux calculated in the white window in panel (a). The vertical line shows the start of the flux emergence measured by the method in Chapter 7. (c) Schematic illustration of calculating the acoustic power from the filtered Doppler velocity data. See text for details. Figure adapted from Toriumi et al. (2013) by permission of the AAS.

to ray theory, and see the temporal evolutions of acoustic power that may correspond to those depths. If the power reduction starts from the deeper layer, we can speculate that the power-reducing agent is rising in the interior. In this analysis, we focus on the uppermost convection zone just before the flux emergence at the visible surface.

9.2 Data Analysis

Doppler observations of NOAA AR 10488 (Figure 9.2(a)) from Michelson Doppler Imager (MDI; Scherrer et al., 1995) on board the *Solar and Heliospheric Observatory* (*SOHO*) are used in this work. Time-evolution of the total unsigned magnetic flux in this AR is plotted as Figure 9.2(b). The tracked Doppler data set (AR data) has a cadence of 1 min with a duration of 24 hr from 19:30 UT, 2003 October 25 (about 14 hr before the flux appearance)

Table 9.1: Filtering parameters used in this study (Toriumi et al., 2013)

Filter	Target depth z_0 (Mm)	Phase speed $V_{\rm ph}$ (km s^{-1})	Annulus range Δ (Mm)
Phase-speed filter[a]			
1	-2.2 ± 0.8	14.9 ± 2.2	6.6–9.5
2	-3.2 ± 0.8	17.6 ± 2.2	9.5–12.4
3	-4.6 ± 0.9	21.5 ± 2.7	13.1–16.0
Ridge filter[b]			
1	-4.4 ± 2.2	21.0 ± 6.0	7.1–15.5
2	-7.7 ± 2.4	31.0 ± 7.0	13.7–24.3
3	-14.2 ± 4.9	46.0 ± 10.0	22.0–46.2

[a]The phase speed and annulus range are cited from Zhao et al. (2012), while the target depth is calculated from the model S of Christensen-Dalsgaard et al. (1996).

[b]After the filtering, the effective phase speed is evaluated, then the depth and annulus range are calculated from the model S.

and a size of 256×256 pixels with a pixel size of 0.12 degree in the heliographical coordinates. For comparison we also use the Doppler data at the same disk location but 17 days later when there was no active region (QS data). Here it should be noted that each data set has some temporal gaps (periods of no observation) in the whole 24 hr data[3]. According to Hartlep et al. (2011), the gaps may cause significant variations in the power. Therefore, in the 24 hr data, we discuss the power evolution only between 06:00–12:00 UT, during which there is no temporal gap, to avoid the effect of the gap.

First we eliminate the signal below 1.5 mHz and above 5.5 mHz from Fourier-transformed data both in AR and QS, using a box-car filter in the frequency domain with a hyperbolic-tangent roll-off. To eliminate the contribution of the f-mode, we also apply a high-pass filter with a Gaussian roll-off. Then we consider two types of Fourier filters, one of which is applied to the both data sets. The first type of filters is a series of phase-speed filters constructed based on the parameters used in Zhao et al. (2012). The second type is ridge filters which extract the power of p1, p2, and p3-modes. The ridge filters are constructed by

[3]AR data: 19:53–20:01 UT on October 25th and 05:11–05:19 UT on 26th. QS data: 02:57–03:05 UT and 13:12–13:26 UT on November 12th.

approximating the location of each ridge and have a box-car shape in the frequency domain with hyperbolic-tangent roll-offs. The properties of the filters are listed in Table 9.1. Also, in Appendix C, we summarize the characteristics of the two filters.

To determine the depth to which each filter is most sensitive, we examined how the filtered power is distributed over the phase speed $V_{\rm ph} = \omega/k_{\rm h}$, by constructing a histogram indicating the power, for each phase-speed bin, summed over the corresponding $k_{\rm h}$–ω bins. We identify the mode of this distribution as the effective phase speed, and then find the target depth z_0 as the asymptotic inner turning point corresponding to this phase speed, using the model S of Christensen-Dalsgaard et al. (1996). The target depth z_0 and its error, which is determined from the width of the histogram, are shown in Table 9.1. Here, ω and $k_{\rm h}$ are the angular frequency and horizontal wavenumber of a sound wave, respectively.

Finally, we produce the acoustic power maps from the filtered Doppler velocity data. In order to increase the S/N ratio, the acoustic power at the point $\boldsymbol{x}$ at the time t, $P(\boldsymbol{x}, t)$, is given as the squared velocity averaged over an annulus of a diameter of one travel distance Δ centered at $\boldsymbol{x}$, $\mathcal{A}(\boldsymbol{x}, \Delta)$:

$$P(\boldsymbol{x}, t) = \frac{\displaystyle\sum_{\boldsymbol{x}' \in \mathcal{A}} \Big[V(\boldsymbol{x}', t)\Big]^2}{\displaystyle\sum_{\boldsymbol{x}' \in \mathcal{A}} \delta S(\boldsymbol{x}')}, \tag{9.1}$$

where $V(\boldsymbol{x}, t)$ is the filtered velocity and $\delta S(\boldsymbol{x})$ is the area of a pixel element. The schematic illustration of the power calculation is shown as Figure 9.2(c). If the acoustic wave is affected by the power-reducing agent at the bottom of the ray path, the observed acoustic power in the annulus will be reduced. For a higher S/N, the thickness of the annulus is made twice as broad as shown in Table 9.1. The obtained maps show the temporal and two-dimensional evolution of acoustic powers at six different depths. See Appendix C.3 for the obtained acoustic power maps.

9.3 Results

Figure 9.3 shows the temporal evolutions of acoustic power that correspond to six different depth ranges by phase-speed filters (a–c) and ridge filters (d–f). In each panel, the plotted curve is the acoustic power from AR data at the location of flux emergence $\boldsymbol{x}_1$, normalized by the power at the same location but from QS data: $P_{\rm AR}(\boldsymbol{x}_1, t)/P_{\rm QS}(\boldsymbol{x}_1, t)$. We apply 60-min running average ($\pm$30-min from the target time) to smooth measurements, both in AR and QS, to reduce rapid fluctuations that may not correspond to the subsurface magnetic field. The horizontal lines are the mean, $\pm1\sigma$, and $\pm2\sigma$ levels calculated from the quiet regions surrounding the emerging AR. Here, one can see that the acoustic powers, which are more or less unity before 08:00 UT, fall below -2σ level around 10:00 UT. Considering that the flux of AR 10488 appears at around 09:20 UT by the method introduced in Chapter 7, the power reduction seems to be highly related to the magnetic field of this emerging AR. The amount of the reduction is basically larger for shallower filters. The shallowest filter, in panel (a), reveals the reduction up to 65%.

To see the timing of the power reduction in Figure 9.3, we fit a linear trend to the curve and measure the "mean-crossing" (reduction start) and "-1σ-crossing" (significant reduction) times. The start of the fitting interval is the last peak greater than the mean level that comes before the reduction slope and the end is the point where the slope becomes flattened below the -2σ level. It is easily seen that the mean-crossing times are before 09:00 UT, namely, before the flux appearance at the photosphere, and that the mean-crossing time becomes earlier with depth. Here, the deepest filter, in panel (f), shows the earliest reduction, which is more than 2 hr before the flux appearance.

Figure 9.4 shows the depth-time evolution of the "mean-crossing" and "-1σ-crossing" of each filter for (a) phase-speed filter, (b) ridge filter, and (c) both. Here, the mean-crossings in panels (a) and (b) show upward trends from deeper to shallower with time. In this figure, we also plot the occurrence of the horizontal divergent flow (HDF), which is the manifestation of the plasma escaping from the rising magnetic field, and the flux emergence at the surface,

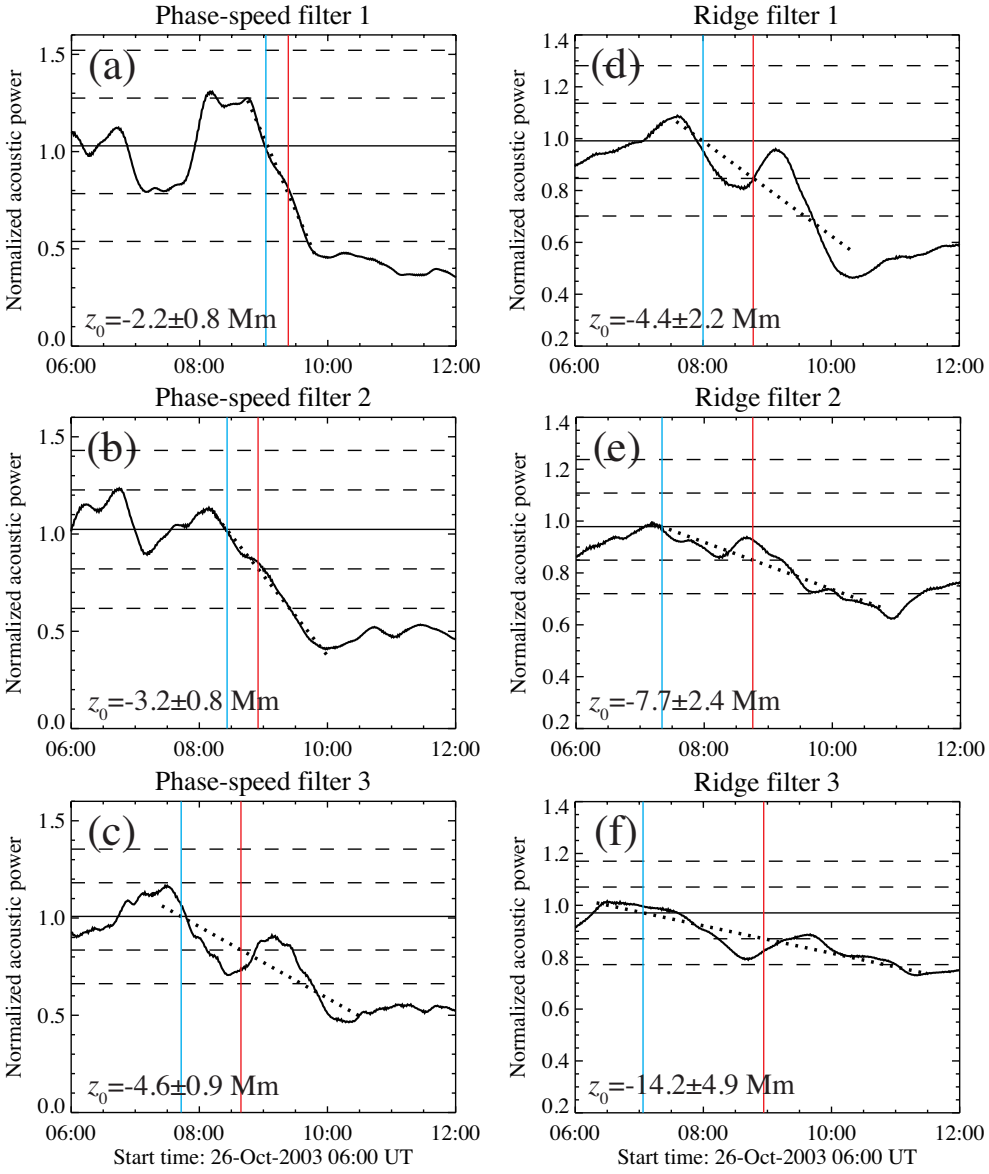

Figure 9.3: Acoustic power of the emerging AR 10488 normalized by the quiet-Sun power for (a)–(c) phase-speed filters and (d)–(f) ridge filters. The horizontal lines (solid and dashed) are the mean, $\pm 1\sigma$, and $\pm 2\sigma$ power levels calculated from the surrounding region data. The dotted line is a fitted linear trend representing the power reduction, while blue and red vertical lines are the "mean-crossing" and "-1σ-crossing" times of the dotted line, respectively. The target depth z_0 is indicated in the bottom left of each panel. Figure reproduced from Toriumi et al. (2013) by permission of the AAS.

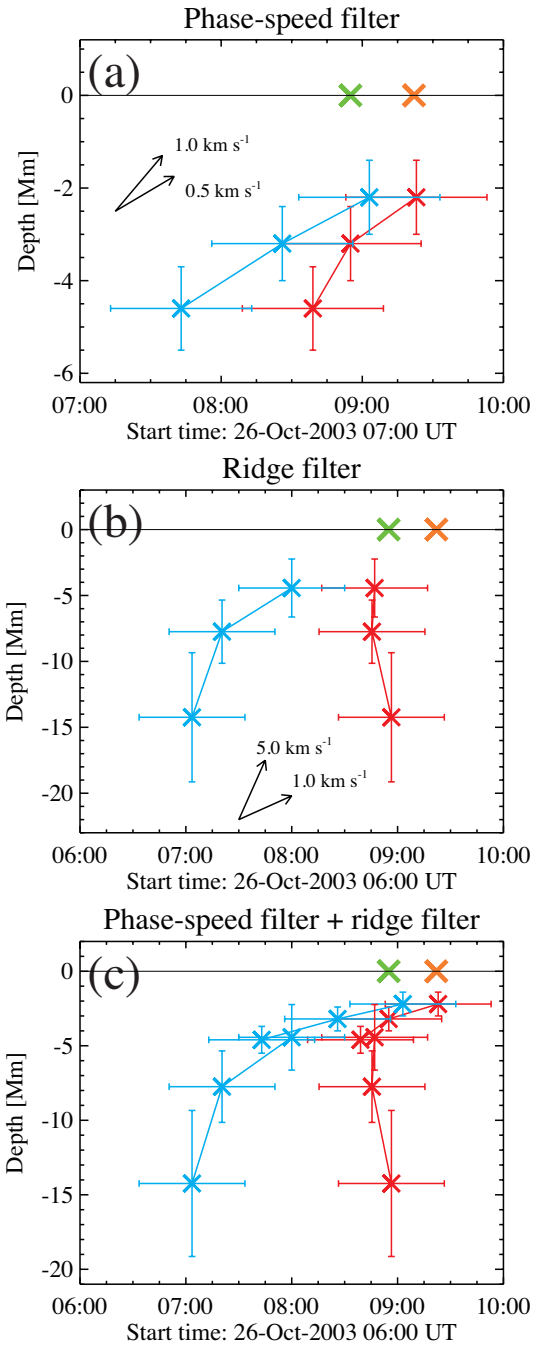

Figure 9.4: Depth-time evolution of the "mean-crossing" (reduction start; blue) and "-1σ-crossing" (significant reduction; red) for (a) phase-speed filters, (b) ridge filters, and (c) both. The vertical and horizontal error bars indicate the uncertainty in the effective target depth of each filter and 60-min smoothing average, respectively. Green and orange X's are the occurrence time of horizontal divergence flow (HDF) and the flux appearance measured by the method in Chapter 7. Figure reproduced from Toriumi et al. (2013) by permission of the AAS.

using the method developed in Chapter 7. Therefore, this figure indicates that the rising patterns come before the flux emergence, or even before the HDF appearance at the visible surface. The mean-crossing of the ridge filters (-14 to -4.4 Mm) show a fast rising pattern first at the rate of several km s^{-1}, then at ~ 1.5 km s^{-1}, while that of the phase-speed filters (-4.6 to -2.2 Mm) show the slower rate of ~ 0.5 km s^{-1}. In Figure 9.4(c), one can clearly see the decelerating trend of the mean-crossing times, which will be discussed in detail in Section 9.4. We confirmed that even if we expand the fitting intervals in Figure 9.3 by 40 minutes, at the cost of increased degree of misfit, the mean- and -1σ-crossing times shift by less than 15 minutes (within the horizontal error bars in Figure 9.4c) and thus the rising speed does not change much.

9.3.1 Effect of the Surface Field

It is known that the acoustic power is suppressed in the surface magnetic fields. Vertical fields may cause mode conversion of the acoustic waves into down-going slow mode waves, leading to power reduction. Other reduction mechanisms include energy conversion into thermal energy, enhanced leakage to atmosphere due to changes in cut-off frequency, emissivity reduction, local suppression, etc. (see Chou et al., 2009). Numerous observations and theoretical works have widely been carried out in this field (e.g., Braun et al. 1987 for sunspots, Jain et al. 2009 for plage regions, and Chitta et al. 2012 for small magnetic elements in quiet region).

In order to examine the effect of the surface field, at least the direct and local effects, we compare the acoustic power calculated with and without masking the strong surface field in the averaging annulus. Figure 9.5(a) shows the temporal evolution of the normalized acoustic power for the shallowest filter (here we call "without masking"), which is the same as Figure 9.3(a). To reduce the effect of the field, we also calculated the power by excluding the pixels with field strength greater than 100 G from the averaging annulus ("with masking"), which is shown as Figure 9.5(b). Here, the fitted (dotted) line is found to be just the same as that

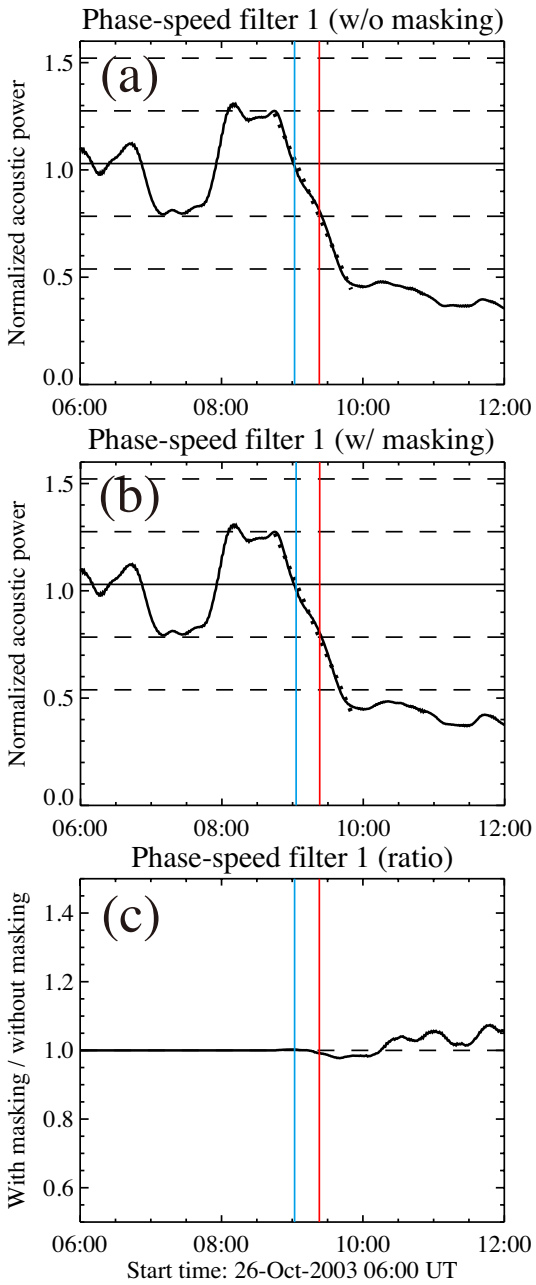

Figure 9.5: Normalized acoustic power for the shallowest filter, calculated (a) without masking and (b) with masking the pixels with field strength greater than 100 G in the averaging annulus. (c) The ratio of the power (b) over (a). Figure reproduced from Toriumi et al. (2013) by permission of the AAS.

in panel (a), and thus the mean-crossing and -1σ-crossing times do not change. Panel (c) shows the ratio of the power (b) with masking over (a) without masking. Here, the ratio is deviated from unity in the later time, which indicates that in fact we see the effect of the surface field. However, when the flux first appears at 09:20 UT, the difference is less than 5%, which increases afterward but remains less than 10%. It is because the fraction of magnetized pixels to the total number of pixels in the annulus is small (of the order of a few percent). As for the other five deeper filters, the difference is much smaller and the mean- and -1σ-crossing times do not change at all. Therefore, we can conclude that, although the emergence starts at 09:20 UT and the temporal power-smoothing has a $\pm$30-min window from the target time, the effect of the surface field on the power reduction at around and before 08:50 UT is fairly negligible.

Note that this masking method does not remove the surface field effect perfectly, since weaker pixels (field strength $\leq$ 100 G) may also be affected by the surrounding fields and unresolved kG strength flux tubes may exist in such pixels. Thus, wave absorption or mode conversion by surface fields (maybe associated with the rising flux) may play a role in the observed acoustic power reduction, particularly after the emergence of the flux. To measure to which extent the surface field affects our measurements, we need to repeat our analysis on many more regions, e.g., regions with similar flux distributions but without emerging ARs, or with other ARs.

9.4 Discussion and Conclusions

As is evident in Figure 9.4, before the emerging flux appears at the visible surface, the onset of the acoustic power reduction starts from the deeper layers, and the speed of the rising trend gradually changes from several to less than 1 km s^{-1} in the shallower convection zone (> -20 Mm), suggesting the deceleration of the power-reducing agent. If we assume that this is actually a magnetic field, Figure 9.4 means that the magnetic flux shows the rising motion,

first at the rate of 6 km s^{-1} in the 15–10 Mm depth range, then at the rate of 1.5 km s^{-1} in 10–5 Mm, finally at 0.5 km s^{-1} in 5–2 Mm. This gradual deceleration of the emerging magnetic flux is well in line with the theoretical "two-step emergence" model (Figure 5.1). In this model, the emerging flux in the uppermost convection zone is decelerated because of the photospheric layer ahead of the flux, which then triggers the magnetic buoyancy instability to penetrate the photosphere, and eventually restart rising into the solar atmosphere, leaving an HDF just before the flux appearance at the visible surface. The deceleration may be more effective in the shallower layer above -20 Mm, since, at around -20 Mm, the radius of the rising flux tube exceeds the local pressure scale height (Fan, 2009), which encourages the mass accumulation and the resultant deceleration. By considering this model, we can speculate that the deceleration in the shallower layer and the flux appearance at the surface shown in Figure 9.4 are the manifestation of the two-step emergence model.

In Ilonidis et al. (2011), the average emergence speed of the magnetic flux in AR 10488 from -65 Mm to the surface is estimated to be 0.6 km s^{-1}, while, in Ilonidis (2012), the speed from -70 to -50 Mm is estimated to be ~ 1 km s^{-1}. Also, from the thin-flux-tube simulation, the rising speed is about 1 km s^{-1} at -10 Mm (Fan, 2009). In the present study, the rising speed between 0.5 and 1.5 km s^{-1} (namely, of the order of 1 km s^{-1}), measured from the five filters in the upper 10 Mm, are consistent with previous studies. In addition, we find that the flux went through in the upper ~ 15 Mm within ~ 2 hours, which is also in agreement with previous helioseismic studies (Kosovichev, 2009).

One important factor we should take into account is the difference of the sensitivity to the power reduction between the two types of the filters (phase-speed filters and ridge filters), or even among the filters of the same group but for different depths. Here we expect that the measurements of the power-reduction due to rising magnetic fields will be less sensitive when the fields are at larger depths, since (1) large depths are probed by acoustic waves with large horizontal wavelengths and, for large wavelengths, the absorption may be less effective, and (2) the conversion of acoustic waves into slow MHD waves, one of the main

power-reduction mechanisms (Cally et al., 2003), is probably less effective at large depths, where the gas pressure dominates over the magnetic pressure. It was also shown that, in the case of sunspot fields, the absorption coefficient drops to almost zero at depths of about 15–20 Mm (Ilonidis & Zhao, 2011), which is the target depth of the deepest filter. Here the rising speed is simply calculated from the difference of target depths of two filters over the detection time difference. If the deepest filter is less sensitive, the detection time by this filter might be later than the actual time and thus the rising speed might be overestimated at 6 km s^{-1}.

These uncertainties make it difficult to directly compare the power reduction events in Figure 9.4. Therefore, a clear identification of the power-reducing agent requires much work, which we shall leave for future research. Nevertheless, we find a rising motion which is related to the flux emergence, prior to the flux appearance at the photosphere.

In this chapter, we apply a set of phase-speed filters and ridge filters to the *SOHO*/MDI Dopplergrams of the emerging AR 10488 to see the acoustic power reduction at different depths. In summary, our results show the following:

1. All of the investigated acoustic powers show reductions, up to more than 2 hr before the flux appearance at the photosphere.

2. In both filter groups, the start times of the power reduction show a rising trend and a gradual deceleration. The trend speed is first 6 km s^{-1} in the 15–10 Mm depth range, then 1.5 km s^{-1} in 10–5 Mm, finally 0.5 km s^{-1} in 5–2 Mm.

3. If we assume that the power reduction is caused by a magnetic field corresponding to AR 10488, the detected deceleration is well in accordance with the two-step emergence model of the emerging magnetic field. This study observationally supports the theoretical two-step model.

4. The estimated emerging speeds of about 1 km s^{-1} are highly consistent with other observations and numerical simulations. The speed at larger depths, however, may be

overestimated with this method. We should examine and improve the present analysis method and investigate how sensitive each filter is to the target region, and what the detected object actually is.

Although this work shows a promising result, here we just analyzed one particular set of AR and QS. Therefore, we need to repeat our measurements on many more regions.

Chapter 10

Summary and Discussion

10.1 Summary

In this part, we analyzed observational data of newly emerging active regions (ARs) to study the observational features related to the flux emergence. The primal aim of this part is to observationally examine the theoretical "two-step emergence" model, which is constructed based on the numerical studies in Part II. Motivated by the above scientific interest, we here observed (1) the horizontal divergent flow (HDF) that appears at the visible surface of the Sun prior to the flux emergence and (2) the rising speed of subsurface emerging fields. For each observation, we suggested a new approach and then applied it to the observational data set.

10.1.1 Detection of the Horizontal Divergent Flow

First, we detected the HDF in NOAA AR 11081, by using Dopplergram and line-of-sight (LoS) magnetogram obtained by *SDO*/HMI. Our idea in this study was that the HDF can be seen as a Doppler pattern when the AR emerges away from the Sun's disk center. Perhaps it is similar to the observation of supergranules in the Sun. The horizontal velocity can also be evaluated from the Doppler velocity by considering the heliocentric angle between the disk

center and the AR.

We focused on how different the velocity and magnetic distributions are, with significance, from those of the reference state before the flux emergence. As a result, the HDF duration, namely, the time gap from the start of the HDF to that of the LoS flux emergence, was measured to be 103 minutes. The HDF speed, i.e., the horizontal velocity of the HDF evaluated from the Doppler velocity, was typically 0.6–1.5 km s^{-1}, up to 2.3 km s^{-1}. These values were consistent with the simulation results and hence reasonable. Also, we analyzed the corresponding Hα images and estimated that the chromosphere responds about 14 minutes after the start of the flux emergence in the photosphere.

Then, we picked up 23 ARs, emerging onto the eastern hemisphere and the total flux being from 5.6×10^{20} to 2.3×10^{22} Mx, and detected 6 clear HDFs by the method constructed above. We also found another 7 HDFs by visual inspection. Therefore, in total, we observed the HDFs in 56.5% of the entire data set. Here, the emergence events closer to the disk center are expected to have less Doppler components. If we leave such events out of count, the detection rate becomes more than 80%, which leads us to the conclusion that the HDF is a common feature in the newly emerging flux region.

The HDF duration and the maximum HDF speed of the 6 clear events were, on average, 61 minutes and 3.1 km s^{-1}, respectively, both being consistent with the observed values in the above study and in the numerical simulations in Part II. The physical explanation of the HDF duration is, according to the numerical study, the time gap after the flux decelerates in the top convection zone due to the accumulated plasma before it restarts further emergence into the upper atmosphere. By assuming a simple model, we also estimated the rising speed of the subsurface magnetic fields, which cannot be observed from direct optical observations. The estimated value was 0.6–1.4 km s^{-1}, again being consistent with our simulations and previous seismic studies.

10.1.2 Helioseismic Probing of the Subsurface Magnetic Fields

We also developed a new method of observing the rising speed of emerging magnetic fields using helioseismology, the unique way to investigate the solar interior. It is known that the acoustic oscillation power measured at the visible surface starts reduction, up to 1 hr before the start of the flux emergence, since the rising subsurface magnetic field reduces the power of acoustic waves propagating through the convection zone. Therefore, we thought it may be possible to investigate the rising speed of the magnetic flux by comparing 6 different power maps that correspond to 6 different subsurface layers. We applied this idea to Dopplergram of NOAA AR 10488, taken by *SOHO*/MDI.

As a result, we found that the power reduction starts from the deeper filters, more than 2 hours before the flux emergence, first at a rate of a few km s^{-1} in the depth range of 15–10 Mm, then at 1.5 km s^{-1} in 10–5 Mm, finally at 0.5 km s^{-1} in 5–2 Mm. If we assume that the power-reducing agent here is actually the magnetic field, this result indicates that the flux rises through the uppermost convection zone with showing a gradual deceleration. The observed speed and the decelerating nature of the rising flux are well in line with our simulations in Part II, previous emergence simulations focusing on the convection zone, and other seismic studies.

10.2 Discussion

Figure 10.1 summarizes the observed physical values plotted on the "two-step emergence" model. Throughout the observational study, we found a number of consistencies between the theoretical model and the actual observations, as was mentioned above in Section 10.1. These consistencies strongly lend support to our "two-step" model.

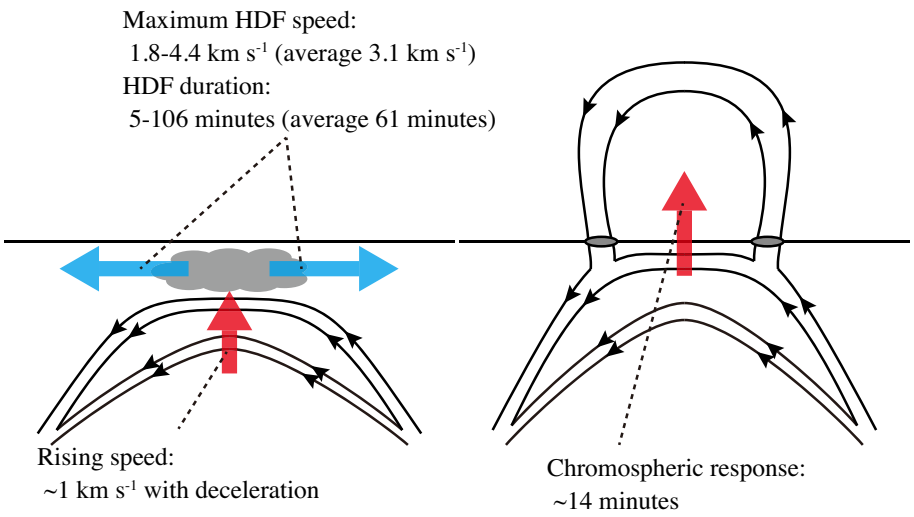

Figure 10.1: Observed values in the "two-step emergence" model (Figure 5.1).

10.2.1 Observations Prior to the Flux Emergence

One of the most important points in the present observations is that they are the observations prior to the flux emergence. Thanks to the continuous full-disk observations by *SOHO* and *SDO*, now we can observe the Sun at the very moment of, or even before the start of the flux emergence. Although the resolutions are not so high as the Solar Optical Telescope (SOT: Tsuneta et al., 2008) aboard the *Hinode* satellite, *SOHO*/MDI and *SDO*/HMI provide the means to investigate the AR emergence at the photosphere.

As we found in Chapter 9, the acoustic power reductions of deeper filters begin more than 2 hours before the start of the flux emergence. However, the reductions of these filters are by far smaller than those of shallower filters. Moreover, helioseismology requires a Fourier transformation for time domain. The required time window for the transformation is typically at least 6 to 8 hours. Therefore, it may be difficult to predict the emergence by this technique.

Regarding the HDF detection method developed in Chapter 7, the start of the HDF is about 1 hour before that of the flux emergence and, thus, the HDF can be considered as

a precursor of the emergence, although the successful detection is possible only when the AR emerges away from the disk center (heliocentric angle $\theta > 30^\circ$). However, this method has an advantage over the seismic technique; the HDF can be observed in real time. While seismology requires a certain time window for a Fourier transformation, the HDF detection only compares the property of the current velocity field with that of the reference state, i.e., the quiet Sun. Therefore, by observing the whole solar disk and tracking the temporal residual from the reference, we may find a start of flux emergence *a priori* as an HDF.

10.2.2 Future Work

In this chapter, we developed two new methods for investigating the flux emergence. Although we successfully observed the HDF and the rising subsurface field, future works may offer opportunities to improve our techniques.

As for the HDF detection, the successful detections were only for ARs away from the disk center ($\theta > 30^\circ$). Since the horizontal motion at the disk center is not reflected in the Doppler velocity, we were not able to observe the HDFs of the emergence events closer to the disk center ($\theta \leq 30^\circ$). However, this disadvantage may be overcome by applying local correlation tracking (LCT) to the Dopplergram or the intensitygram of the central region. If the divergent motion is observed before the flux emergence, it may also support the existence of the HDF.

Regarding the seismic probing technique, the physical origin of the acoustic power reduction is not yet well known and we should examine what the detected object actually is. One possible way to solve this problem is to apply seismology to the flux emergence simulation with thermal convection (see also Braun et al., 2012). In the simulations in Part II, we neglected thermal convection and, thus, there was no continuous excitation of acoustic waves around the surface layer. We could apply the seismic technique to the simulation that deals with the emergence and the convection together at the same time, and examine the cause of the reduction and the sensitivity of each filter. It may also help to examine the effect of

the surface magnetic field. For example, there may be small fragmental precursor magnetic fields appearing before the emergence of the main flux. We could check where such fields appear and compare with the size of annuli to examine the effects on the filters.

Another interesting topic for the seismic probing is to investigate the structure of the subsurface emerging flux. One way is to change the method of spatial averaging of the acoustic power. Instead of averaging the signal over the annulus (see Section 9.2; see also Figure 9.2(c)), we can use an arc (a divided annulus) to investigate the anisotropy of the power reduction. For instance, by dividing the annulus into four to make two arc pairs (north-south and east-west) and averaging over each pair, we may observe a difference of the power reductions between the north-south and east-west pairs, which may hint the direction of the magnetic field of the emerging flux (except the polarity of the field).

In addition to the above-mentioned methodology, we could also take into account the time gap of the acoustic rays from the passing of the target point to the arrival at the surface. It may decrease the fast rising speed of 6 km s^{-1}, which is estimated from the deepest filter.

Part IV

Summary and Discussion

Chapter 11

Summary of the Results

In this thesis, we have carried out numerical and observational studies, aiming to investigate the solar flux emergence when the flux approaches the surface layer. We here summarize the numerical and observational results in this study.

11.1 Numerical Study

It has long been believed that ARs are created by emerging magnetic fields from the deeper convection zone (Parker, 1955). Although the flux emergence from the convection zone to the corona is a seamless process, the series of previous global simulations within the convection zone applying the assumptions (e.g., the thin-flux-tube approximation) have an upper limit of about -20 Mm. Therefore, in this thesis, we first performed a series of three-dimensional magnetohydrodynamic (3D MHD) flux emergence simulations in a large scale from -20 Mm to the upper atmosphere through the photosphere, intending to start the simulations consistently with the previous studies. Based on the simulation results, we suggested a theoretical "two-step emergence" model.

11.1.1 Typical Case

First, we carried out a 3D MHD simulation of a rising flux tube from -20 Mm of the convection zone in Chapter 3, aiming to investigate the large-scale flux emergence and its initial appearance at the photosphere.

In the initial state, the flux tube of 6.3×10^{20} Mx, embedded in the convection zone at -20 Mm, is endowed with a density deficit with respect to the surroundings and, thus, starts its ascent. Because of the stratification, the tube expands as it rises, while, at the same time, the aerodynamic drag becomes larger. As a result, the rising velocity levels off and reaches the terminal velocity of ~ 1.4 km s^{-1}. The upper surface of the tube becomes fluted because of the interchange mode instability (magnetic Rayleigh-Taylor instability: Appendix A). As the tube approaches the surface after about 4.2 hours, it slows down and becomes flat. The deceleration and the flattening occur because the unmagnetized plasma is trapped and compressed between the rising tube and the isothermally-stratified (i.e., convectively-stable) photosphere. As the surficial field intensifies and satisfies the criterion for the magnetic buoyancy instability, further emergence from the surface layer to the corona takes place. We found that, at first, several magnetic domes appear above the surface and, then, they merge with each other in the corona. The rising flux slows down when the apex reaches a height of 6000 km after about 5.5 hours.

At the photosphere, horizontal divergent flow (HDF) of unmagnetized plasma appears prior to the magnetic flux. Then, the flux of positive and negative polarities (> 100 G) emerge onto the surface. Between the photospheric patches, we found upflows of a few km s^{-1}, while, in the cores of the photospheric patches, downflows up to 1 km s^{-1} were observed. Both polarities move at 4–8 km s^{-1}, showing separative motions from each other. As time goes on, the separated photospheric patches show a shearing motion, which is reminiscent of the AR observations by Strous et al. (1996) and Strous & Zwaan (1999).

The entire process, namely, the initial tube's emergence in the convection zone, the deceleration and the horizontal expansion just beneath the surface, the appearance of the

HDF, and the further evolution into the corona, can be described as the "two-step emergence" model.

11.1.2 Parametric Survey

Then, in Chapter 4, we conducted parametric survey of the flux emergence simulation. While the basic conditions were kept the same as those in Chapter 3, we varied the axial field strength, the twist, and the perturbation wavelength of the initial tube.

As a result of the survey, we found that the tube rises faster with a stronger axial field, since the magnetic buoyancy depends on the square of the field strength. When the tube is too weak, it remains in the convection zone, never to appear at the surface. The rise speed within the convection zone is almost the same for different twist cases. However, the secondary emergence from the surface layer was found to depend on the twist intensity. In the weak twist case, the tube stops at the surface, since it cannot hold the coherency of the tube that is enough to trigger the magnetic buoyancy instability for the further emergence. When the perturbation wavelength of the initial tube is too short, the ascent in the interior is slower, because the downward magnetic tension holds back the rising tube. However, the secondary emergence of this case is faster than the other cases. It may be because the drainage of the material, which drives the Parker instability, is more effective in this case.

We also analyzed the properties of the HDF, the escaping flow of the plasma trapped between the expanded tube and the photospheric layer. The driving force of the HDF was found to be the pressure gradient. The HDF duration is typically from 30 to 45 minutes. When the field is very strong ($\gtrsim$ 30 kG), the HDF duration is in simple inverse proportion to the field strength, while the weaker field regime ($\lesssim$ 30 kG) deviates from this inverse trend. The duration was found to have no relation with the tube's twist, since the rising speed is independent of the twist. The maximum HDF speed is 1.6–8 km s^{-1}, basically a fraction of the photospheric sound speed. The maximum speed becomes faster when the field strength increases, because the tube's rise speed mainly depends on the field strength. The maximum

speed also showed a positive correlation with the twist.

11.2 Observational Study

In order to observationally examine the "two-step emergence" model, we then investigated the HDF and the rising speed of the subsurface emerging flux, both of which are predicted in the theoretical model. For the observation, we proposed our original ideas and developed them into practical methods. The obtained physical values of the HDF and the rising flux were well in line with the simulation results, which strongly assists the theoretical model.

11.2.1 HDF Detection

We observed the HDF prior to the flux emergence by using *SDO*/HMI Dopplergram and line-of-sight (LoS) magnetogram. Thanks to the continuous full-disk observation by *SDO*, we are able to analyze the earlier stage of the flux emergence. The idea behind this observation is to detect the Doppler pattern of the newly emerging AR that appears away from the disk center.

First, we made time-sliced LoS magnetogram and Dopplergram of NOAA AR 11081. A pair of blue and red pattern in the Doppler slice was found to start slightly earlier than the appearance of the flux in the magnetic slice. The blue (red) pattern was located disk-centerward (limbward), which indicates that the flow is divergent.

Second, we evaluated the start times of the LoS magnetic and Doppler patterns. To determine the times with significance, we studied the temporal change of the magnetic and Doppler patterns from their references without emerging flux, namely, the profiles of the quiet Sun. As a result, the Doppler signal was found to deviate from the quiet-Sun profile at 01:23 UT on 2010 June 11, while the magnetic signal deviated at 03:06 UT of that day. Therefore, we concluded that the HDF appeared 103 minutes before the start of the flux emergence in the LoS magnetogram. According to the numerical work, the duration here

is the time gap from the flux deceleration in the top convection zone to the restart of the flux emergence evolving into the upper atmosphere. The horizontal speed of the HDF was estimated to be 0.6–1.5 km s^{-1}, up to 2.3 km s^{-1}. These values are consistent with the numerical results.

We also studied the chromospheric response to the photospheric flux emergence by using Hα images taken by SMART. The time-slice showed that the Hα plages started to brighten at 03:20 UT, that is, 14 minutes after the start of the flux emergence in the HMI magnetogram.

11.2.2 Statistical Analysis of the HDF

Aiming to repeat the HDF detection in many more ARs and to investigate the physical property of the subsurface emerging flux, we then conducted a statistical analysis of the HDF. We picked up 23 emergence events in 21 ARs, which emerged on the eastern hemisphere of the Sun from May 2010 to June 2011, total unsigned flux being 5.6×10^{20} to 2.3×10^{22} Mx. We detected 6 clear HDFs by the previously developed method. Plus, we found 7 additional HDFs by visual inspection. In total, HDFs were observed in more than 50% of the entire data set. If we exclude the emergence events around the disk center (heliocentric angle $\leq 30°$), which are supposed to have less LoS velocity components, the detection rate increases up to more than 80%. From this result, we concluded that the HDF is a common feature in an emerging AR.

In the 6 clear events, the HDF duration was on average 61 minutes, which is consistent with 103 minutes in the previous detection in NOAA AR 11081 and with 30–45 minutes in the numerical simulations. The maximum HDF speed was on average 3.1 km s^{-1}, which is also comparable to 2.3 km s^{-1} in the previous study and 1.6–8 km s^{-1} in the simulations. By assuming a simple two-dimensional model, we estimated the rising speed of the subsurface flux to be 0.6–1.4 km s^{-1}, which is again comparable to the simulation results.

11.2.3 Helioseismic Probing of the Subsurface Magnetic Flux

With a view to detect the rising motion of a subsurface magnetic flux that forms an AR, we then developed a new helioseismic technique that measures acoustic oscillation powers. The idea is to make 6 power maps that correspond to the 6 different subsurface layers and investigate the start times of the power reductions. We applied this method to the *SOHO*/MDI Dopplergram of NOAA AR 10488 and found that the reduction starts from the powers of deeper filters, up to 2 hours before the start of the flux emergence at the visible surface. The rising trend was first at the rate of a few km s^{-1} in the depth range of 15–10 Mm, then at 1.5 km s^{-1} in 10–5 Mm, finally at 0.5 km s^{-1} in 5–2 Mm. If we assume that the power reduction is in fact caused by the magnetic flux, our detection, i.e., the rising speed and its decelerating nature, is consistent with the simulation results, previous simulations focusing on the convection zone, and other seismic studies.

Chapter 12

General Discussion

In this chapter, we first discuss the consistencies between the numerical and observational results of this thesis. We then summarize the "two-step emergence" model of a rising magnetic flux, the main result of this thesis, with emphasizing the importance of the surface layer to the large-scale transportation of the magnetic flux in the Sun. Finally, we discuss perspectives for future works.

12.1 Discussion

12.1.1 Consistencies between the Numerical and Observational Studies

Figure 12.1 compares the height-time evolutions of rising magnetic flux of the numerical simulation in Chapter 3 and of the helioseismic detection in Chapter 9. Here, one can easily find the clear consistency between the two panels. Both rising trends (highlighted with red arrows) show the "two-step emergence" that a rising magnetic flux slows down at the top convection zone and restarts emergence further into the upper atmosphere. Moreover, the start of the horizontal divergent flow (HDF) indicated with green X in panel (b) suggests the existence of a plasma layer accumulated on the top of the rising flux, which is also in line with the numerical results.

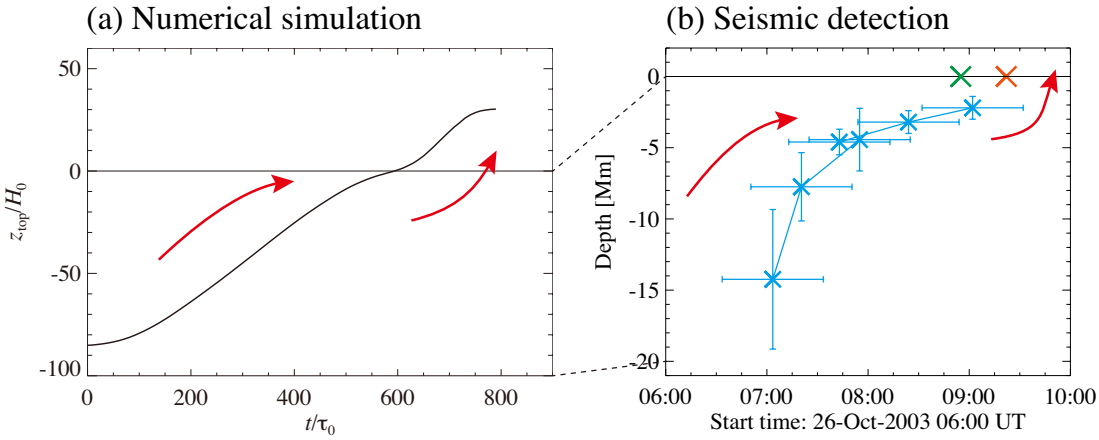

Figure 12.1: Comparison between the numerical and observational results. (a) Same as Figure 3.3. Height-time evolution of the rising flux tube in the numerical simulation in Chapter 3. (b) Same as Figure 9.4(c). Start times of the power reduction for 6 different filters ("mean-crossing" times: blue X's) obtained from the seismic detection in Chapter 9. Green and orange X's indicate the start of the horizontal divergence flow (HDF) and the flux appearance at the visible surface, respectively. The red arrows emphasize the "two-step" trend, while dashed lines compare the surface and the depth of -20 Mm.

In Part III, we obtained several physical parameters of the emerging flux. For example, in the statistical analysis of the HDF (Chapter 8), we found that the HDF duration is on average 61 minutes and the maximum HDF speed is 3.1 km s^{-1}. Assuming a simple model, we estimated the rising speed of the subsurface flux to be 0.6–1.4 km s^{-1}. The seismic probing (Chapter 9) also yields the rising speed to be of the order of 1 km s^{-1} with a gradual deceleration. These values are in good agreement with the simulation results in Part II.

12.1.2 Two-step Emergence Model

The clear consistencies between the theoretical and observational works strongly support the "two-step emergence" model. Figure 12.2 illustrates the essence of this model.

The toroidal flux at the bottom of the convection zone generated through the dynamo mechanism starts emergence and approaches the surface layer. In the uppermost convection

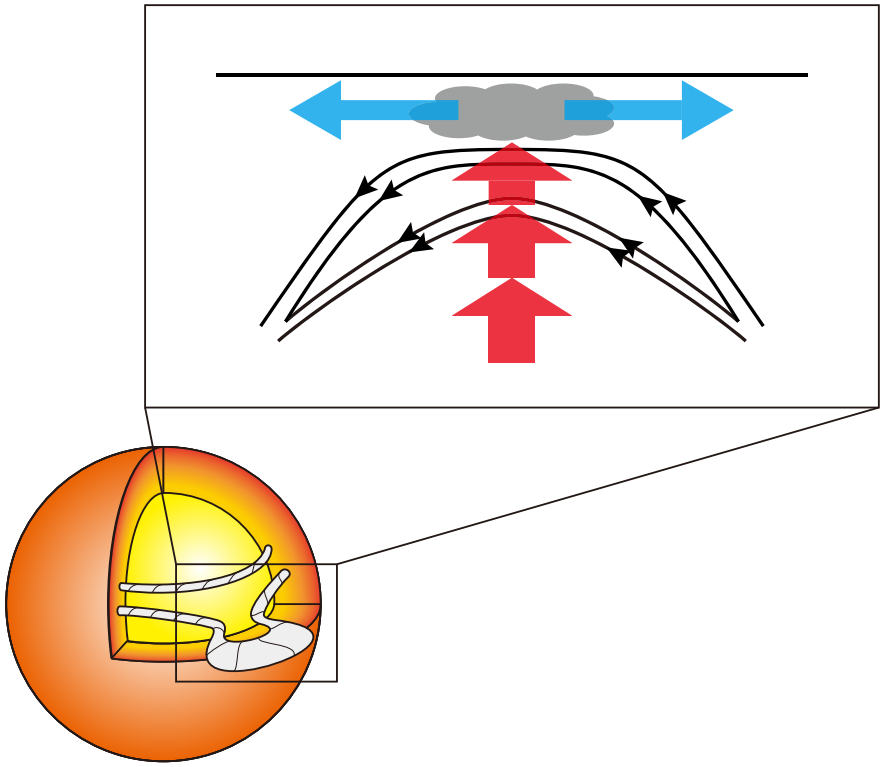

Figure 12.2: The essential part of the "two-step emergence" model of the rising magnetic flux. The toroidal flux at the bottom of the convection zone partly starts its ascent and approaches the visible surface. The flux decelerates (red arrows) because the unmagnetized plasma becomes trapped between the flux and the surface layer. The plasma escapes horizontally around the surface as an HDF (blue arrows).

zone ($\gtrsim -20$ Mm), the external density and pressure decrease drastically (Figure C.2), causing the expansion of the flux tube. Since the cross-sectional size exceeds the local pressure scale height around this depth (Figure 1.10(d)), the tube becomes no longer "thin." On the top of the expanded tube, the plasma becomes accumulated and trapped between the tube and the isothermally-stratified (i.e., convectively-stable) photosphere, which, in turn, pushes down the rising tube. This effect may be negligible in much deeper convection zone, since such a perturbation may be instantly eliminated by the fast sound wave. However, now that the local sound speed falls below the convective velocity, it becomes more effective. Finally, the tube slows down just below the photosphere (red arrows) and the compressed plasma escapes horizontally around the surface layer as an HDF (blue arrows).

In the simulation, because of the continuous accumulation of the surface magnetic flux, the magnetic buoyancy instability is triggered and thus the tube restarts emergence further into the upper atmosphere. In the actual Sun, the flux eventually build an active region (AR).

12.1.3 Surface Layer as a Magnetic "Transition Region"

From the point of view of the "two-step" model, or the magnetic flux transportation in a large scale, the surface layer can be considered as a "transition region" for the emerging magnetic fields. Because of the following reasons;

- The density and the pressure drastically decrease in the upper convection zone.
- The sound speed becomes slower as the temperature decreases.
- The convectively-stable photosphere inhibits the vertical motion of a gas.

the properties of a rising flux substantially change around this layer;

- The tube expands and exceeds the local pressure scale height, eventually having a sheet-like structure.

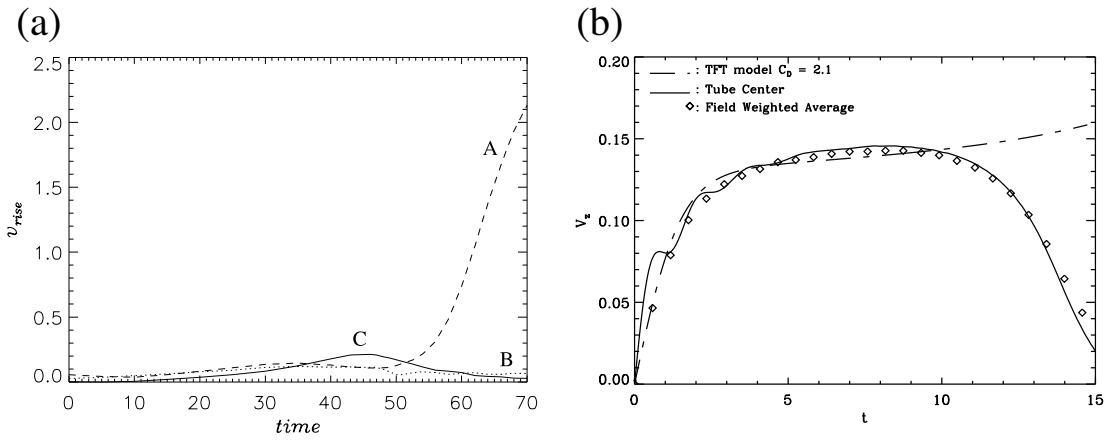

Figure 12.3: (a) Temporal evolution of the rise velocities at the top (A), the center (B), and the bottom (C) of the flux tube. Figure reproduced from Magara (2001) by permission of the AAS. (b) Rise velocity of the flux tube. The solid line is the velocity of the center, while the diamonds correspond to the field-weighted average of the vertical velocity over the tube. Dash-dotted line is a prediction by the thin-flux-tube model. Compare these figures with Figure 3.5(a). Figure reproduced from Fan et al. (1998) by permission of the AAS.

- The rising motion turns into deceleration.

- As the flux passes through the surface, the plasma-β falls below unity.

Here, the surface layer is not a simple open boundary nor a closed boundary. Therefore, when considering a large-scale flux emergence, we should simultaneously treat the interior, the surface layer, and the upper atmosphere in a consistent manner.

It should be noted that the deceleration of a rising flux was found in the previous studies. Magara (2001) simulated the buoyant rise of flux tubes from just below the photosphere at -1800 km in 2D and found that the tube slows down when it enters the photosphere. Figure 12.3(a) shows the rise motion in Magara (2001)'s calculation. After $t = 35$, the vertical velocity at the tube's top (A: dashed line) turns into deceleration. According to Magara (2001), *the continuous rise motion generated in the convection zone cannot persist through the photosphere because the photosphere is a convectively stable layer.* That is, the deceleration occurs because the magnetic flux itself goes into the photosphere. Similar results

have also been obtained in 3D simulations by, e.g., Fan (2001) and Murray et al. (2006). Such decelerations may depend on the numerical condition that the tube is initially located just below the photosphere.

Contrary to this, the tube's deceleration we found in this thesis occurs not at the surface but at much deeper location around -10 Mm in the convection zone (see Figure 3.5(a) in Chapter 3). Also, the deceleration occurs not because the tube itself enters the photosphere, but because unmagnetized material is trapped between the expanded tube and the convectively-stable photosphere. Perhaps this deceleration in the deeper convection zone is similar to those reported by Fan et al. (1998) and Cheung et al. (2006). They calculated the flux tube emergence within the convection zone in 2D. Figure 12.3(b) is the rise velocity of a flux tube in Fan et al. (1998), in which the tube slows down in the later phase (solid line and diamonds). This is due to the closed top boundary in the simulation box; their calculations do not include the convectively-stable photosphere. Considering our numerical results, in terms of the tube's deceleration, the closed boundary is rather a reasonable approximation. However, the surface layer and the upper atmosphere are still required for the second-step emergence from the photosphere and the resultant AR formation.

12.2 Future Prospects

In this section, we list up what we should study as a next step. We believe that, by developing numerical and observational methods, the transportation mechanism of magnetic flux in the Sun will be revealed further in the future.

12.2.1 Methodology

Numerical Simulation: Our magnetohydrodynamic (MHD) simulations in Part II revealed the dynamics of the emerging magnetic flux from the deeper convection zone to the corona through the photosphere. However, there still remain some important

processes which we neglected in this study: radiation, thermal convection, and partial ionization. As we discussed in Chapter 5, the radiative cooling and the resultant thermal convection may have several effects on the emergence process. For example, a large-scale updraft in the interior may help the flux emergence, whereas a downdraft may suppress the flux tube (Fan et al., 2003). By the assistance of flux cancellation due to the surface convection, photospheric flux may rise further into the upper atmosphere (Cheung et al., 2010). Therefore, the simulation including other physical processes may guide us further understanding of the nature of flux emergence.

HDF Detection: In the observational study in Chapters 7 and 8, we succeeded in detecting the HDFs of the escaping unmagnetized material, prior to the flux emergence at the visible surface. By visual inspection, the HDF is rather easy to distinguish from other convections such as granulation and supergranulation. It is because, although the typical size of the HDF is of the supergranulation ($\sim$ 10–20 Mm), the horizontal speed is faster than that of the supergranulation (HDF $\sim$ 1.5 km s^{-1}; supergranulation $\sim$ a few 100 m s^{-1}). Also, although the HDF velocity is rather comparable to the granulation speed (0.5–1.5 km s^{-1}), the scale size is by far different (granulation $\sim$ 0.5–2 Mm). In the present method, however, we only use the information of the velocity, by plotting the Doppler histograms. Therefore, it may help to increase the successful detection if we also take into account the structure, for instance, the cluster property of the HDF. Automatic detection of the HDF using the full-disk Dopplergram may allow us to predict the flux emergence in advance. Local correlation tracking (LCT) method can also be used to detect HDFs closer to the disk center.

Helioseismic Probing: Seismic technique in Chapter 9 is in fact a promising method for probing the solar interior. However, the physical origin of the acoustic power reduction is not yet well understood. Also, the sensitivity of each filter needs further study. One possible way is to apply seismology to the flux emergence simulation with thermal

convection and examine the cause of the reduction and the sensitivity of the filters. For investigating the amount of the power reduction by magnetic fields, it is also possible to generate sound wave around the surface layer of the simulation results in Part II as a post-process and monitor the power of the sound wave that refracts back to the surface.

12.2.2 Scientific Objectives

Properties of the Subsurface Magnetic Fields: Through the seismic probing, we evaluated the rising speed of the subsurface magnetic fields that eventually formed NOAA AR 10488. Other physical properties of the subsurface fields, namely, the geometrical structure, the scale size, the direction of the magnetic fields, the total flux, the field strength, the twist, etc. are also interesting objectives. We may be able to observe such parameters by developing the seismological method. For example, instead of averaging the signal over the annulus, we can use an arc (a divided annulus) to investigate the anisotropy of the power reduction, which may be related to the direction of the magnetic fields.

Emergence of the Flux Tube Axis: In the numerical simulation in Chapter 3, we found that a large amount of the original flux tube remained below the photosphere (see Figures 3.2(f) and 3.3). One reason of this may be that, because of the initially twisted flux tube, the plasma is entrained in the dipped (concave) field line, which inhibits the emergence of the entire flux tube. Hood et al. (2009) suggested to use a toroidal flux tube as an initial condition, instead of using a horizontal tube. The axial field of the toroidal tube was found to emerge above the photosphere, since the drainage of the material works more effectively. Also, Cheung et al. (2010) found that the thermal convection driven by the radiative cooling helps the reconnection of the surface field and thus the further emergence. In their model, due to the convective flows, undulating fields are created around the surface and mass is entrained in the

downflow region (dipped field). When the reconnection occurs, the undulating fields cancel each other and form longer loops above the photosphere, which rise further into the upper atmosphere. Because of the reconnection, the entrained mass is removed downward from the surface layer. This drainage of the material from the surface magnetic fields through reconnection supports the emergence of the entire flux tube. It is therefore of interest to probe the subsurface layer of ARs, particularly between two mature sunspots of both polarities, to investigate if there remains a magnetic flux.

Formation of Flaring ARs: Another interesting topic is the formation of flaring ARs. It is well known that solar flares and coronal mass ejections take place around the polarity inversion lines (PILs) in the ARs, particularly with a strong magnetic shear (see, e.g., Hagyard et al., 1984). It is also known that the so-called δ-sunspots produce stronger flares (Sammis et al., 2000). Such magnetic structures may be created during the emergence within the convection zone. Thus, for a thorough understanding of the triggering process of solar flares, the large-scale flux emergence including the process within the interior should be taken into account. By conducting flux emergence simulations with varying the parameters of a flux tube, perturbation function, etc. to reproduce flaring ARs, we may find the large-scale emergence process and the subsurface structure that initiate the flaring activity.

Part V

Concluding Remarks

Chapter 13

Concluding Remarks

Since Parker (1955) suggested the buoyant rise of a magnetic flux in the solar convection zone, a great advance has been made in the theoretical field of flux emergence studies. Thanks to the development of instruments, a lot of progress has also been made in the observational field. In this thesis, motivated by a scientific curiosity to understand the nature of the flux emergence in the Sun, we have carried out numerical and observational studies. Here, we summarize this dissertation as follows.

13.1 Numerical Study

We conducted three-dimensional magnetohydrodynamic (3D MHD) simulations of the flux tube emergence from the depth of -20 Mm in the convection zone. As a result of the simulation, we found that the magnetic flux tube rising in the convection zone slows down when it approaches the photosphere. In the meanwhile, unmagnetized plasma is trapped between the rising tube and the photosphere and, eventually, escapes horizontally around the surface layer as a horizontal divergent flow (HDF). When the field strength of the flux tube increases at the surface, it restarts emergence into the corona. From the numerical results, we derived a theoretical "two-step emergence" model of the rising magnetic flux.

We also conducted a parametric survey, varying the field strength, the twist, and the perturbation wavelength of the initial tube, with a view to investigate the relation between these parameters and the properties of the flux emergence. As a result, we succeeded in obtaining the parameter dependencies of the flux evolution and of the HDF. An analytical approach was also taken to explain the numerical results. The conclusions of the parameter survey are referred and used later in the observational part.

13.2 Observational Study

First, we observed the HDF of the unmagnetized plasma, which is supposed to appear at the visible surface prior to the flux emergence. We investigated the temporal evolution of the Dopplergram and line-of-sight (LoS) magnetogram of NOAA AR 11081, finding that the HDF appears about 100 minutes earlier than the start of the LoS magnetic flux. The HDF duration and its speed were comparable to the simulation results. We repeated our measurement in 23 additional emergence events, aiming at the statistical analysis. As a result, we found HDFs in more than half the entire data set. The averaged HDF duration and maximum HDF speed were in line with the event study and the numerical results. The estimated rising speed of the subsurface magnetic flux was again comparable to the simulation results.

Second, we developed a helioseismic technique to probe the subsurface rising magnetic fields, measuring acoustic oscillation signals. We applied this technique to the Doppler data of NOAA AR 10488. The obtained power reductions showed a rising trend with a gradual deceleration, which is consistent with the numerical results.

13.3 Conclusion

The results of the observational studies, the HDF detection and the helioseismic probing, were in support of the theoretical "two-step emergence" model, which was suggested based on

the numerical study. Therefore, we here conclude that the surface layer plays an important role in the large-scale flux emergence, changing the properties of the rising magnetic fields such as the structure, the rising speed, the plasma-β, etc. In addition, our study provides the means to investigate the physical state of the subsurface magnetic flux, even before the flux appears at the visible surface. By developing numerical and observational methods, we may be able to further investigate the transportation mechanism of magnetic flux in the Sun.

Appendices

Appendix A

Magnetic Buoyancy Instability

As we introduced in Chapter 1, Parker (1955) showed that an isolated horizontal flux tube in thermal equilibrium with surrounding media has a buoyancy and tends to rise (magnetic buoyancy). To make a system in a mechanical equilibrium, as well as in a thermal equilibrium, one can consider a horizontal magnetic sheet as in Figure A.1(a), instead of a flux tube. However, the sheet also becomes unstable depending on the profile of the density and the field, and eventually it partially starts emergence. This instability is called the magnetic buoyancy instability.

There are several modes in this instability and, here, we focus on two particular modes. One is the interchange mode that the wavenumber of the perturbation is perpendicular to the magnetic field ($\boldsymbol{k} \perp \boldsymbol{B}$, where $\boldsymbol{k}$ and $\boldsymbol{B}$ denote the perturbation wavenumber and the field vector, respectively), as illustrated in Figure A.1(b). This mode is also known as the magnetic Rayleigh-Taylor instability. The other is the undular mode instability ($\boldsymbol{k} \parallel \boldsymbol{B}$; Figure A.1(c)), known as the Parker instability after his pioneering work on the interstellar gas and the magnetic field (Parker, 1966).

Here, we consider a horizontal flux sheet $\boldsymbol{B} = (B, 0, 0)$ with pressure p and density ρ in a downward gravitation $\boldsymbol{g} = (0, 0, -g)$ as in Figure A.1(a). According to Newcomb (1961),

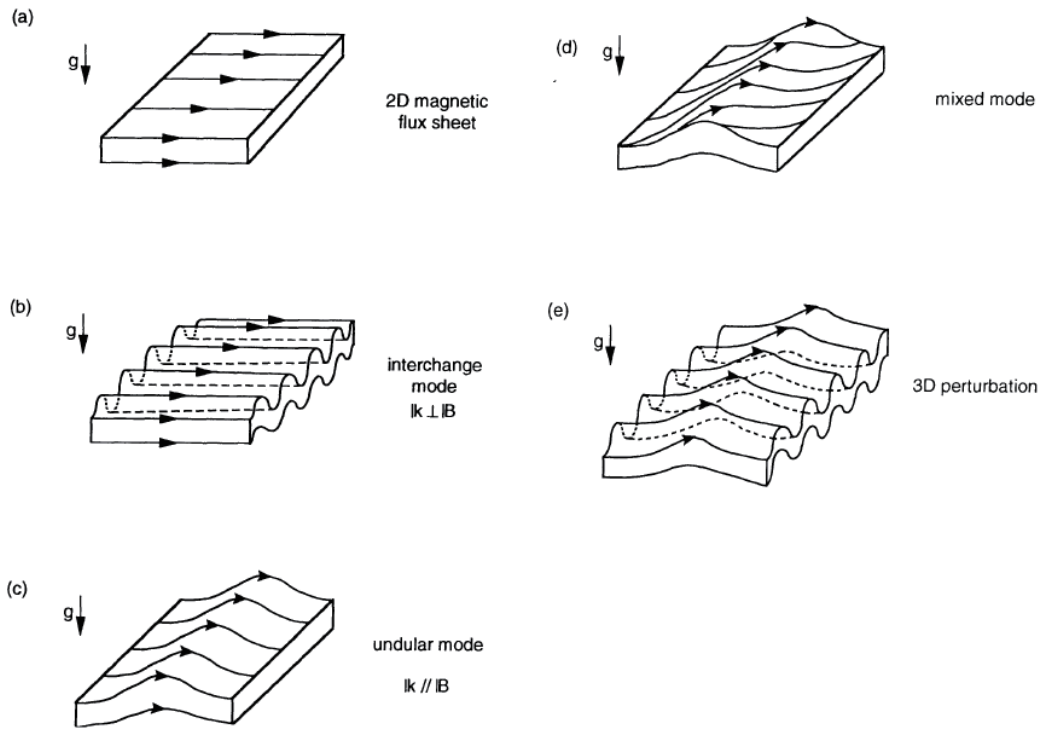

Figure A.1: Schematic illustration of the magnetic buoyancy instability in a horizontal flux sheet. Figure reproduced from Matsumoto et al. (1993).

the necessary and sufficient condition for the (pure) interchange instability is

$$\frac{d\rho}{dz} > -\frac{\rho^2 g}{\gamma p + B^2/(4\pi)}, \tag{A.1}$$

where γ is the ratio of specific heats. Acheson (1979) rewrote this relation as

$$\frac{d}{dz}\ln\left(\frac{B}{\rho}\right) < -\frac{N^2}{g}\frac{C_{\rm s}^2}{V_{\rm A}^2}, \tag{A.2}$$

where N is the Brunt-Väisälä frequency, or, the buoyancy frequency

$$N^2 = \frac{g}{\gamma}\frac{d}{dz}\ln\left(\frac{p}{\rho^\gamma}\right), \tag{A.3}$$

and $C_{\rm s} = \sqrt{\gamma p/\rho}$ and $V_{\rm A} = B/\sqrt{4\pi\rho}$ are the sound speed and the Alfvén velocity, respectively.

On the other hand, the necessary and sufficient condition for the general undular perturbation ($k_x \neq 0$, $k_y \neq 0$; Figure A.1(e)) by Newcomb (1961) is

$$\frac{d\rho}{dz} > -\frac{\rho^2 g}{\gamma p}, \tag{A.4}$$

which can be rewritten by Acheson (1979) as

$$\frac{d}{dz}\ln B < -\frac{N^2}{g}\frac{C_{\rm s}^2}{V_{\rm A}^2}. \tag{A.5}$$

If $k_y = 0$, or if the system is in a two-dimensional scheme (x, z), this relation gives the condition for the Parker instability (Figure A.1(c)).

Comparing Equations (A.1) and (A.4), or Equations (A.2) and (A.5), one may find that the condition for the (pure) interchange mode is more stringent than that for the (general) undular mode. However, there is a typical (most-unstable) wavelength in the Parker instability: $\lambda_{\rm Parker} = (10\text{–}20)H_{\rm p}$, where $H_{\rm p}$ is the local pressure scale height. It is

because, if the perturbation wavelength is too short, the downward magnetic tension of the undulating field exceeds the upward magnetic buoyancy and suppresses the instability, while, if the wavelength is too long, the downdraft of the plasma along the field lines takes so long that the instability does not develop.

Appendix B

HMI Data Analyzed in the HDF Studies

In Chapters 7 and 8, we conducted studies of the horizontal divergent flows (HDFs) in the emerging active regions (ARs). In this appendix, we show the precision and the accuracy of *SDO*/HMI data and the list of ARs analyzed in the statistical study.

B.1 Precision and Accuracy of HMI Data

The HMI instrument measures line-of-sight (LoS) magnetic flux density and Doppler velocity of the full solar disk and the units of the data are 1 Mx cm^{-2} (= 1 G) and 1 m s^{-1}, respectively. Table B.1 shows the specifications of HMI[1]. The precision and the zero-point accuracy of the magnetogram are 10 G and 0.05 G, respectively. In order to check the actual values, we here picked up 23 different full-disk HMI magnetograms for the 23 flux emergence events in Chapter 8 and estimated the noise levels, following the analysis by Hagenaar (2001).

In Figure B.1, we plot the distribution function of flux densities, $f(\phi)$, of each magnetogram, where ϕ denotes the flux density. To keep the data quality, we only use the pixels

[1] `http://hmi.stanford.edu/Description/hmi-overview/hmi-overview.html`

Table B.1: HMI Specifications

Doppler Velocity	
Cadence	45 s
Precision	13 m/s
Zero point accuracy	0.05 m/s
Dynamic range	±6.5 km/s
Line-of-Sight Magnetic Flux	
Cadence	45 s
Precision	10 G
Zero point accuracy	0.05 G
Dynamic range	±4 kG
Continuum Intensity	
Cadence	45 s
Precision	0.3%
Accuracy pixel to pixel	0.1%

with the heliocentric angle less than or equal to 60°. The central part of the distribution function is attributed to noise and thus can be described by a Gaussian

$$f(\phi) = f_{\max} \exp\left[-\frac{(\phi - \phi_{\max})^2}{2\sigma^2}\right], \tag{B.1}$$

where $\phi_{\max}$ indicates the position of the maximum and 2σ is the full width at half maximum (FWHM). The parabolic curve in this figure is a Gaussian fit. From this figure, one can see that the noise level (σ) is about 10 Mx cm^{-2} (= 10 G) and the zero-point ($|\phi_{\max}|$) ranges around 0.05 Mx cm^{-2} (= 0.05 G). Therefore, in this thesis, we adopt the precision of 10 G and the zero-point accuracy of 0.05 G, i.e., the values in Table B.1, for the original HMI LoS magnetograms. Similarly, for the original Dopplergrams, we take the precision of 13 m s^{-1} and the zero-point accuracy of 0.05 m s^{-1}.

In the analysis of Chapters 7 and 8, we made tracked magnetic and Doppler data cubes. We applied Postel's projection for making the data cubes.

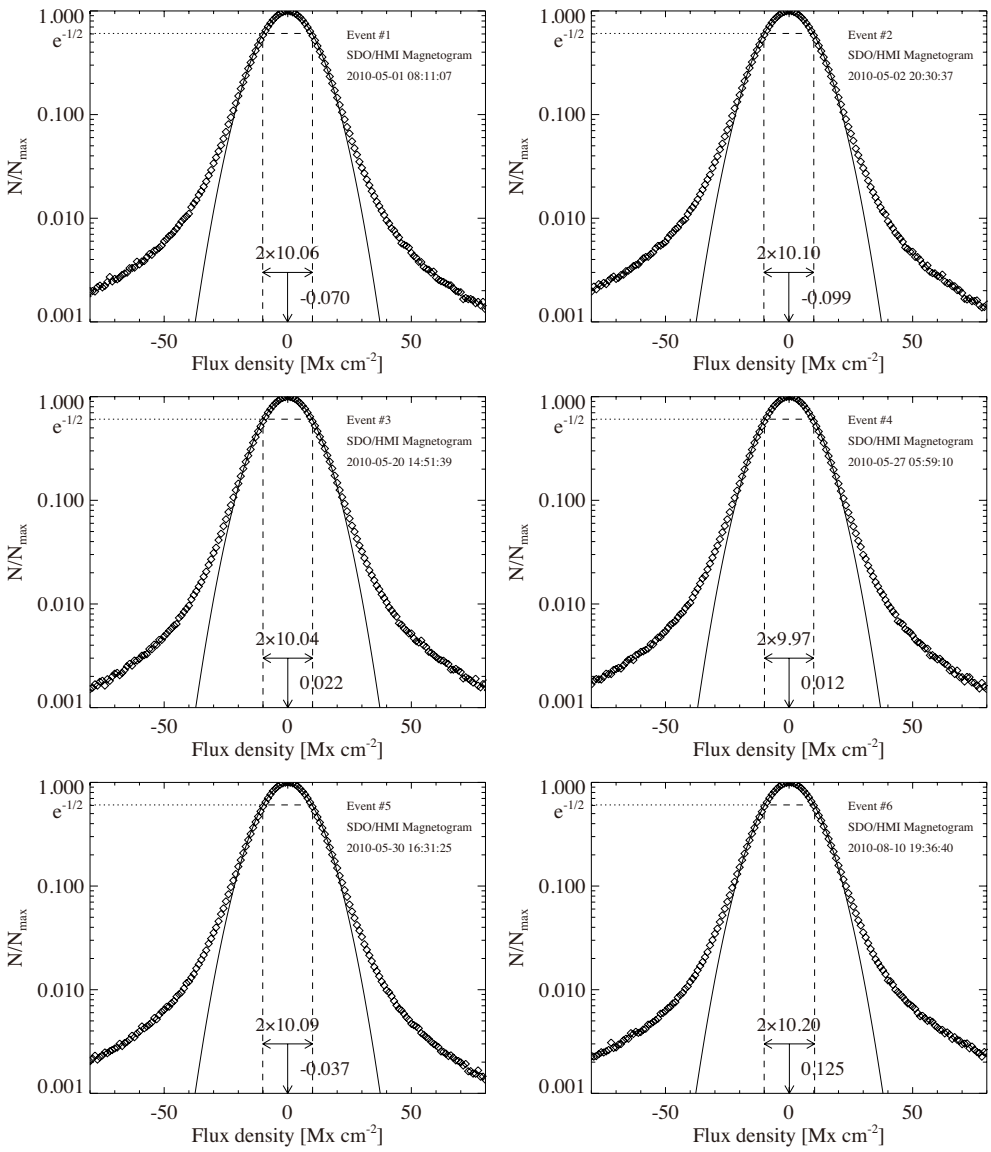

Figure B.1: Distribution function $f(\phi)$ of single HMI magnetogram (diamonds) of each emergence event. Here, N and $N_{\max}$ denote the pixel numbers of each bin (bin size: 1 Mx cm^{-2}) and of the maximum distribution, respectively. The solid line is a Gaussian fit to the function $f(\phi) = f_{\max} e^{-(\phi-\phi_{\max})^2/2\sigma^2}$. The horizontal arrow indicates the FWHM ($= 2\sigma$) and the vertical arrow shows the position of the maximum ($= \phi_{\max}$).

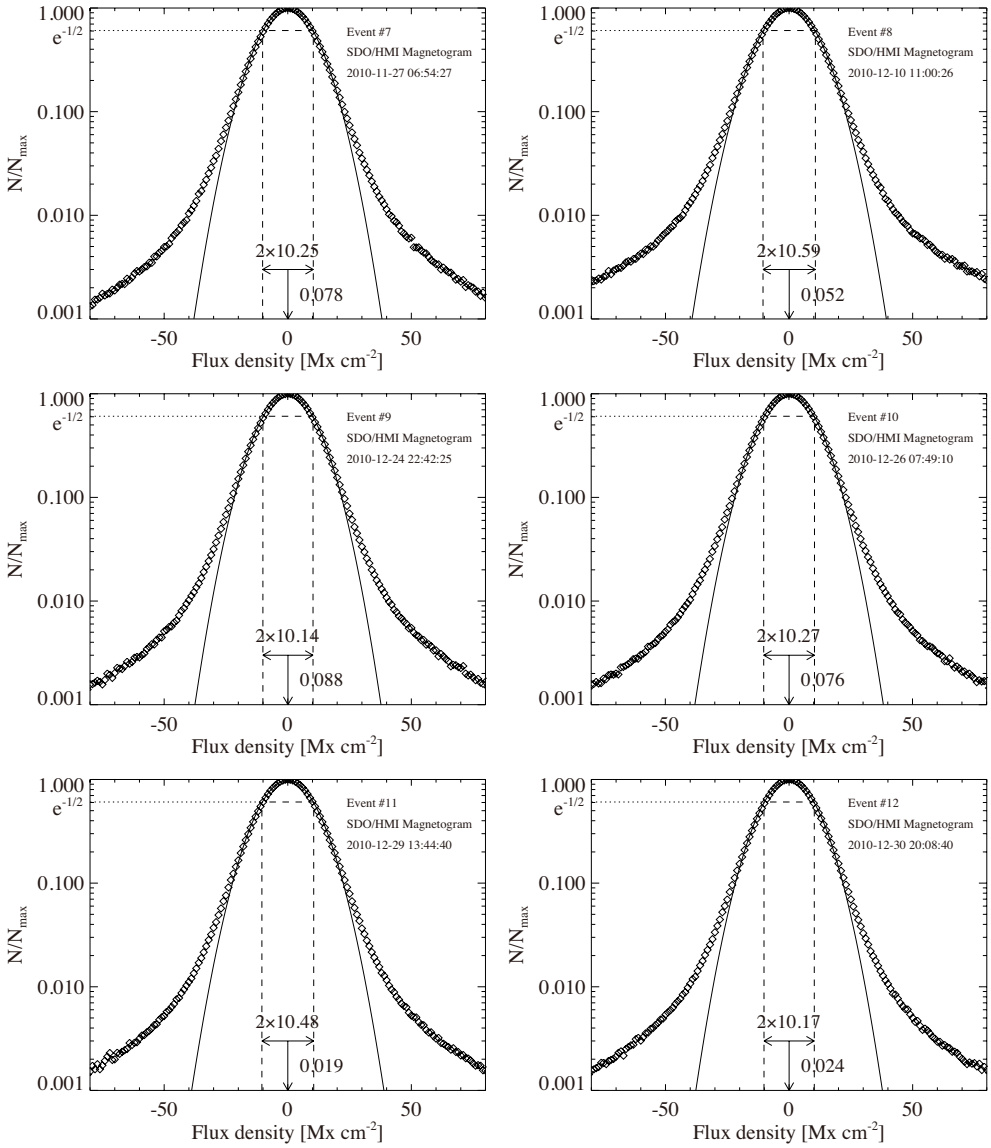

Figure B.1: *Continued.*

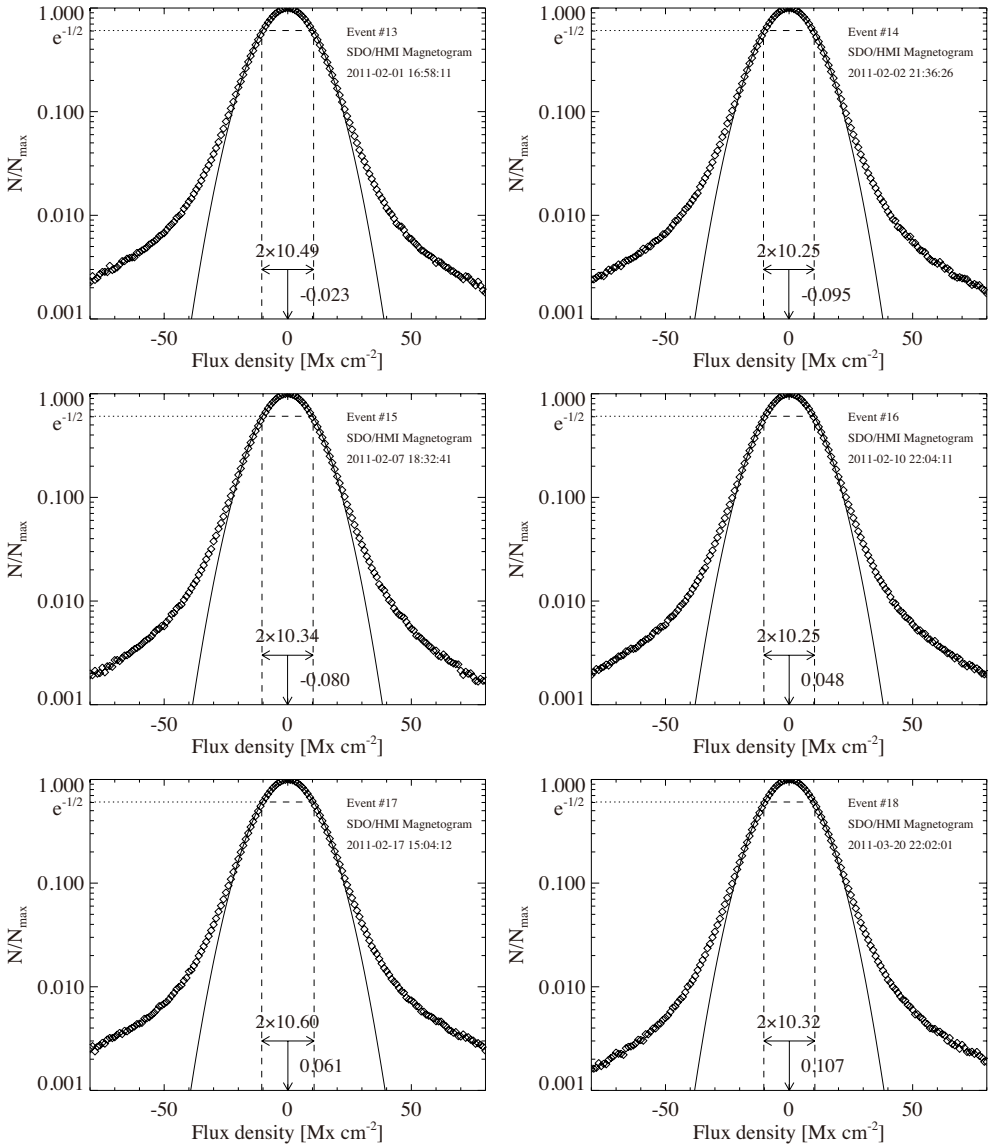

Figure B.1: *Continued.*

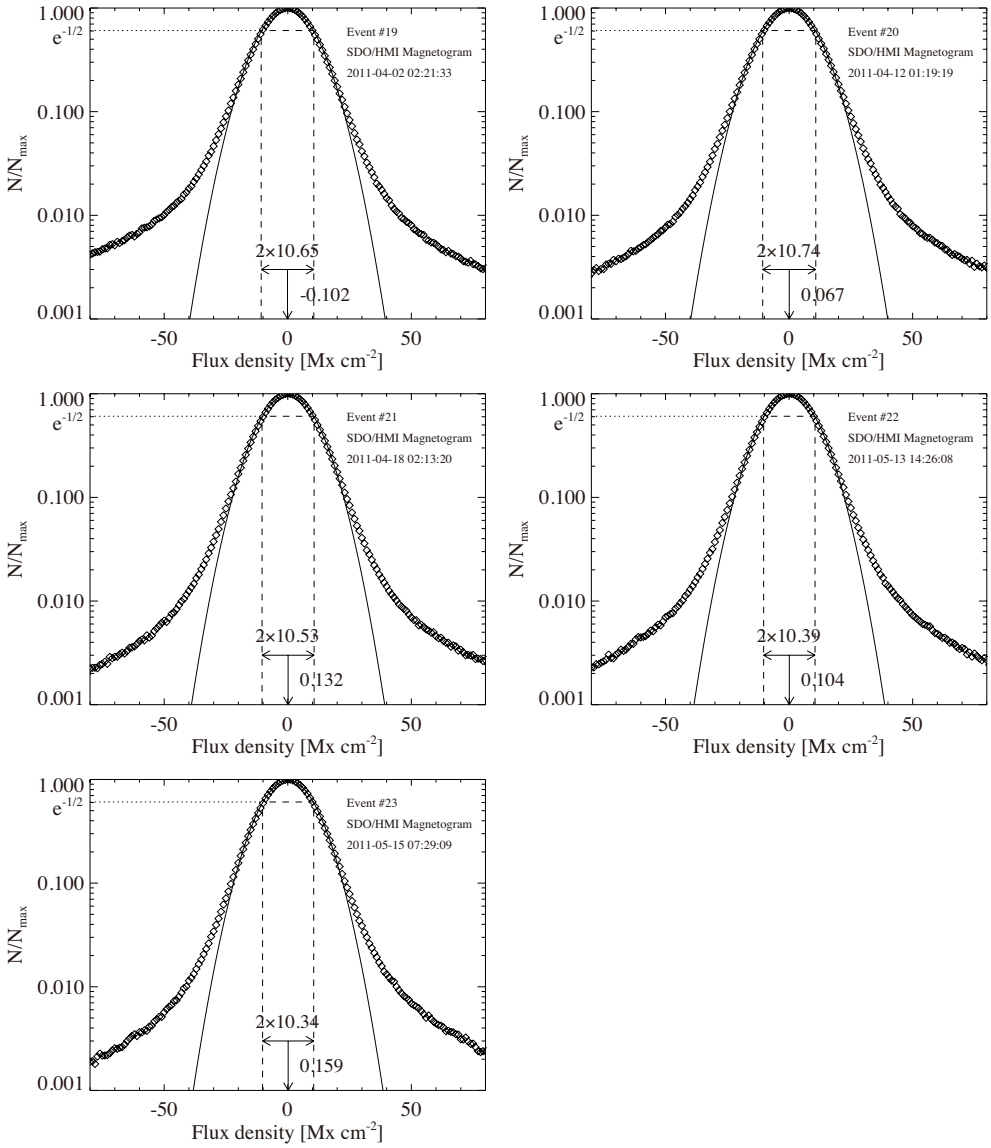

Figure B.1: *Continued.*

B.2 List of ARs Analyzed in the Statistical Study

Figure B.2 is the list of target ARs analyzed in the statistical study in Chapter 8. Here, we show the HMI magnetogram, the temporal evolutions of the total unsigned flux and its time derivative, and the footpoint separation and the tilt angle of both polarities. Note that the magnetic fields of events #22 and #23 are difficult to separate from each other and thus they are not listed.

Within the box plotted over each magnetogram, we measured the total unsigned flux and its time derivative. We also measured the flux-weighted center of each polarity

$$(x_{\pm}, y_{\pm}) = \left(\frac{\sum x B_{\pm}}{\sum B_{\pm}}, \frac{\sum y B_{\pm}}{\sum B_{\pm}} \right), \tag{B.2}$$

only using the pixels with the absolute field strength ≥ 200 G, and evaluated the footpoint separation between both centers,

$$d_{\rm foot} = \sqrt{(x_- - x_+)^2 + (y_- - y_+)^2}. \tag{B.3}$$

In addition, we calculated the tilt angle ψ between both polarities. The leading polarity of Solar Cycle 24 is negative (positive) in the northern (southern) hemisphere. As shown in Figure B.3, we put the expected leading polarity to the origin of the coordinate and define the angle of the vector from the origin to the expected following polarity to be the tilt angle ψ. For the northern hemisphere,

$$\psi = \arctan \left(\frac{y_+ - y_-}{x_+ - x_-} \right) \tag{B.4}$$

and, for the southern hemisphere,

$$\psi = \arctan \left(\frac{y_- - y_+}{x_- - x_+} \right). \tag{B.5}$$

Therefore, the tilt of $90^\circ < \psi < 180^\circ$ ($-90^\circ > \psi > -180^\circ$) agrees with the Hale's law in the northern (southern) hemisphere.

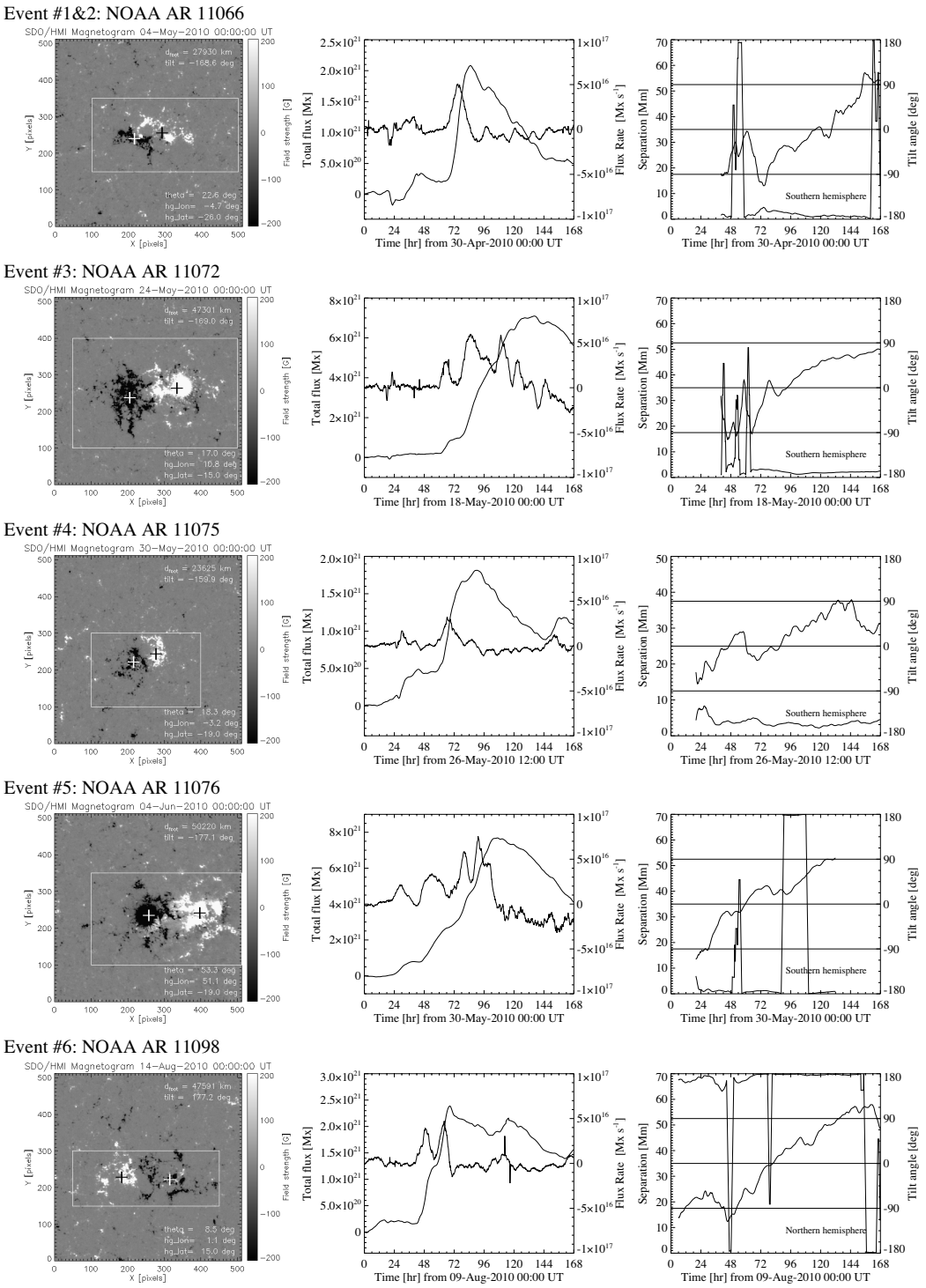

Figure B.2: ARs analyzed in the statistical study of the HDF. (Left) *SDO*/HMI magnetogram. Footpoint separation $d_{\rm foot}$, tilt angle ψ, heliocentric angle θ, heliographic latitude and longitude at the shown time are indicated. Black and white crosses denote the flux-weighted centers of the positive and negative polarities, respectively, which is measured within the box. (Middle) Temporal evolution of the total unsigned flux (thick) and its time derivative (thin). (Right) Footpoint separation (thick) and the tilt (thin).

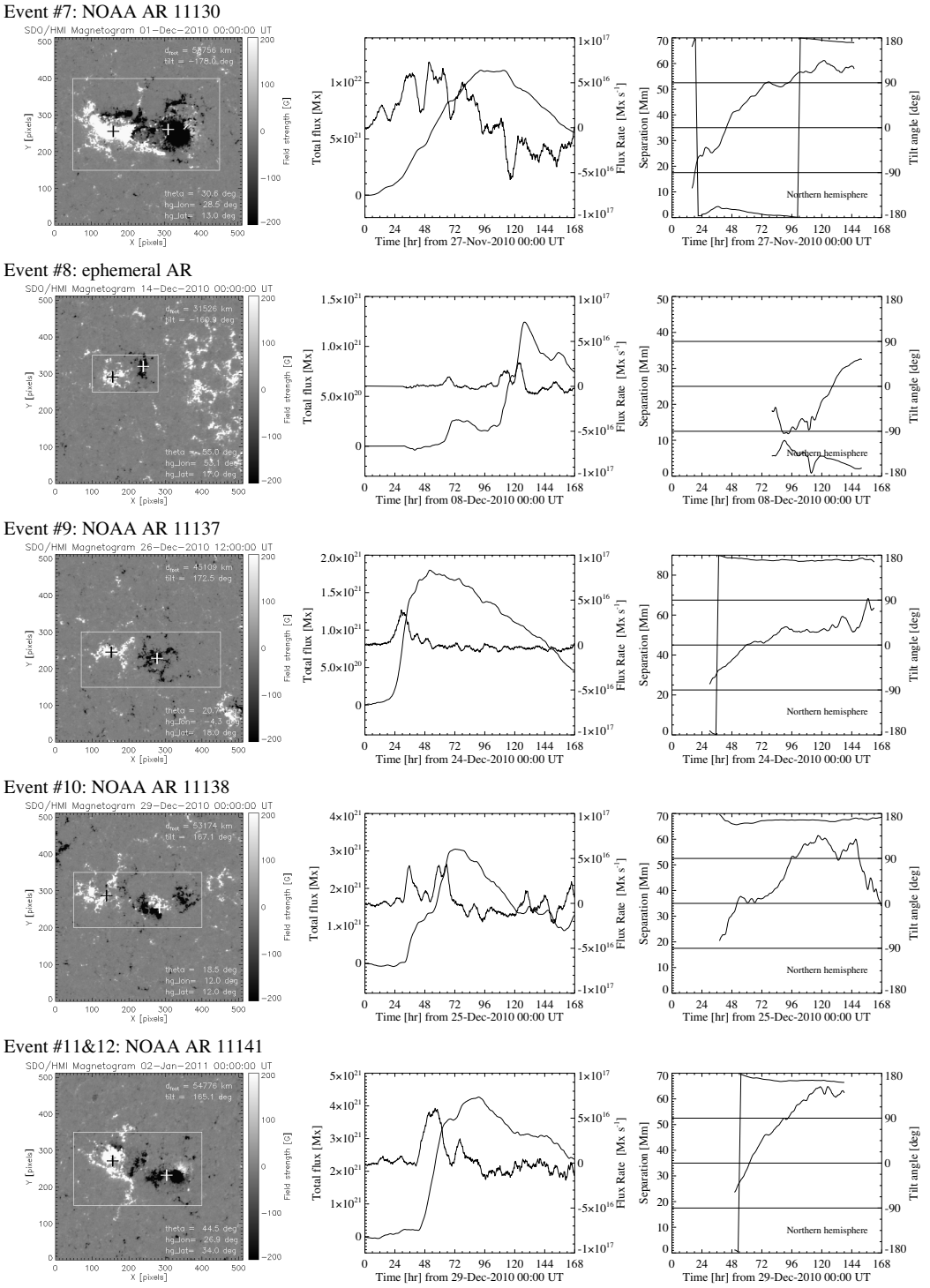

Figure B.2: *Continued.*

Event #13: NOAA AR 11152

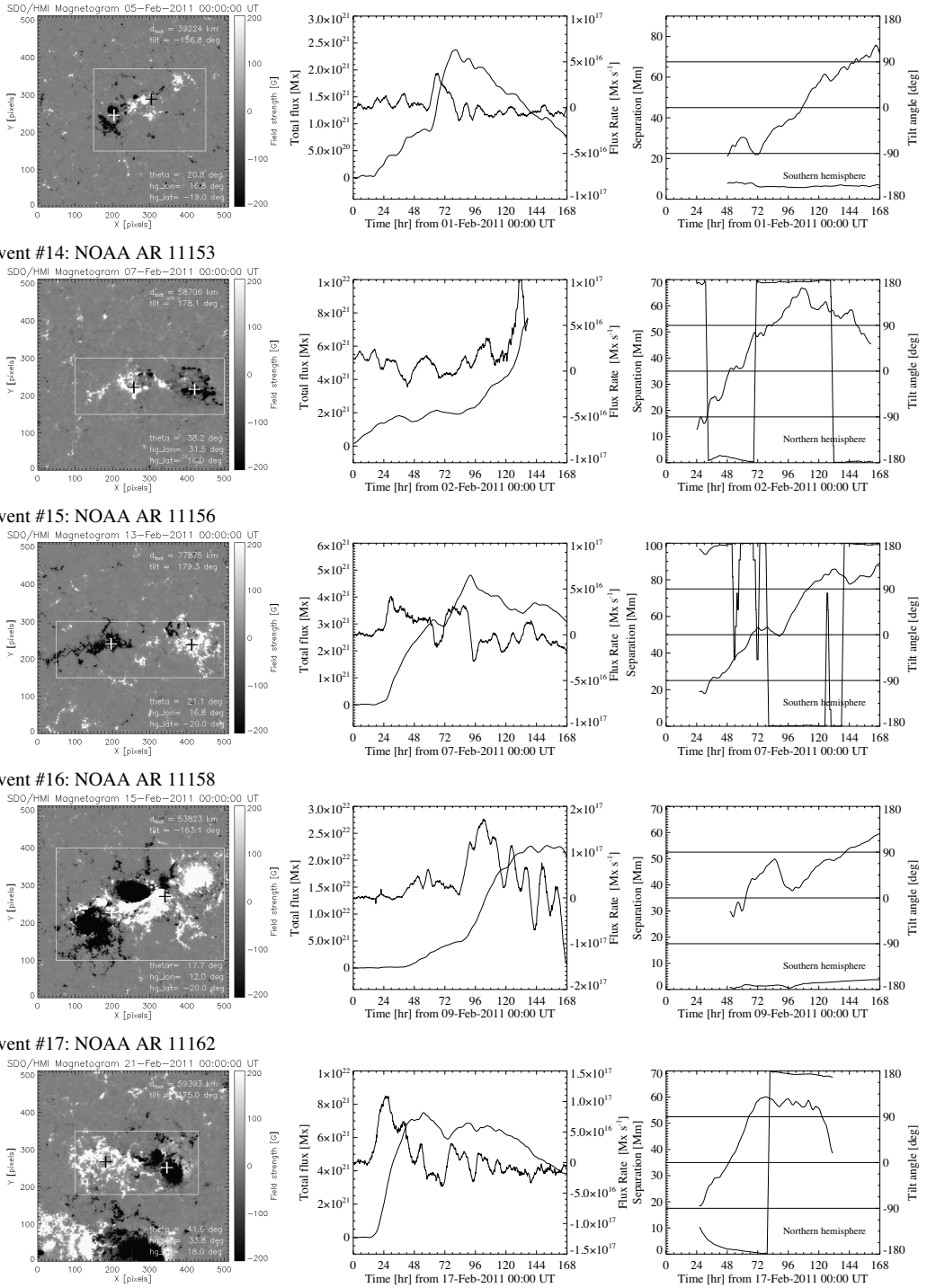

Event #14: NOAA AR 11153

Event #15: NOAA AR 11156

Event #16: NOAA AR 11158

Event #17: NOAA AR 11162

Figure B.2: *Continued.*

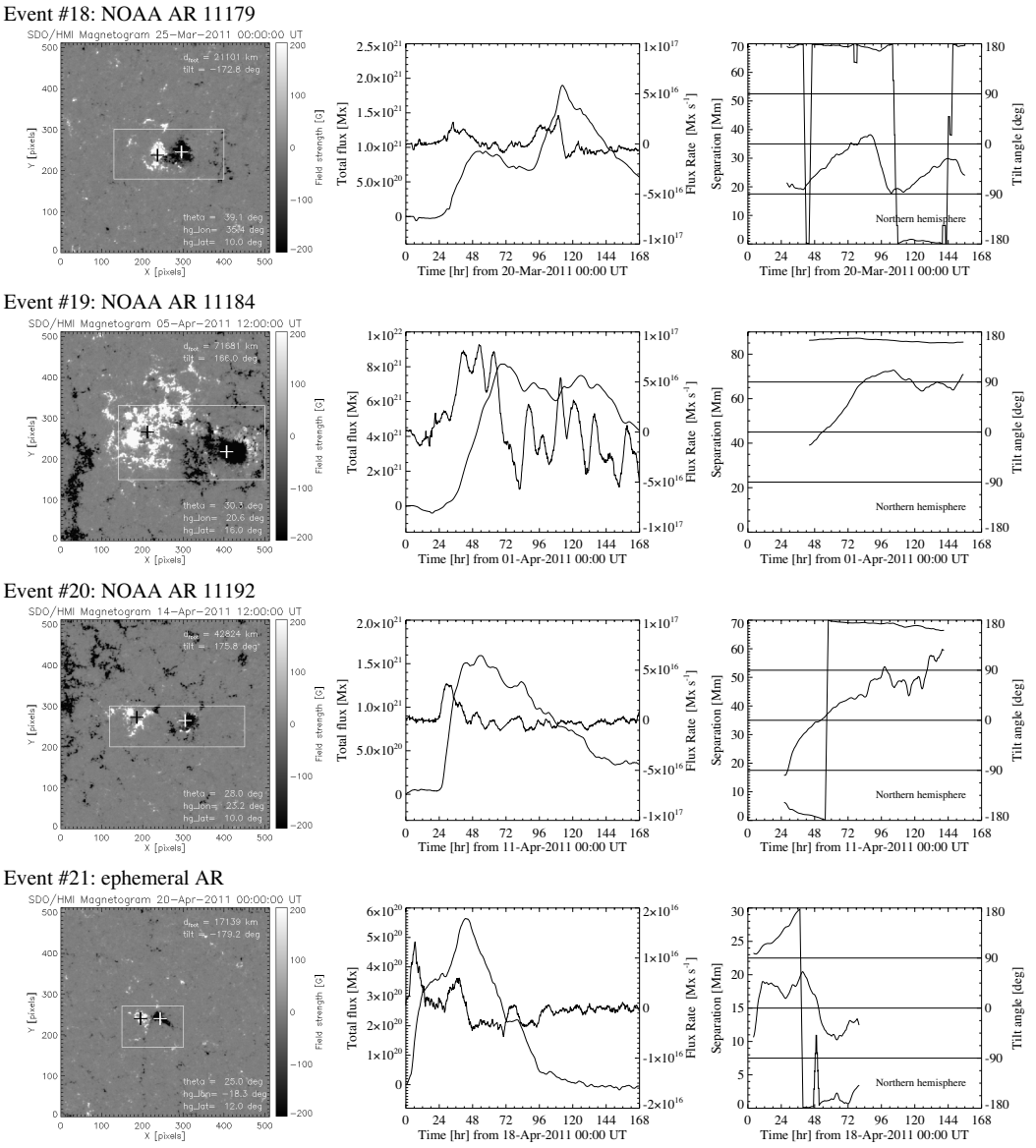

Figure B.2: *Continued.*

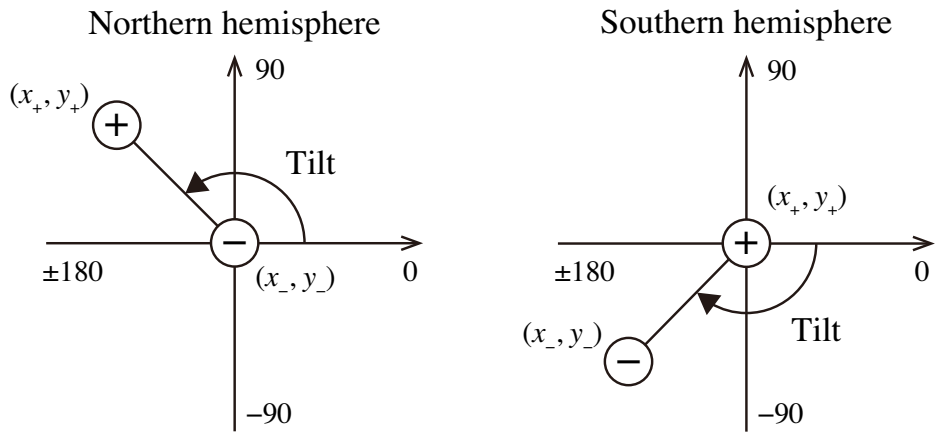

Figure B.3: Definition of the tilt angle.

B.3 Clear HDF Events

Figure B.4 shows the temporal evolution of 6 clear HDF events (events #1, 2, 3, 9, 15, and 16). Each column shows the continuum image, Dopplergram, and magnetogram taken by *SDO*/HMI. The overlaid box indicates the area we plot the histogram for the determination of the HDF start and flux emergence.

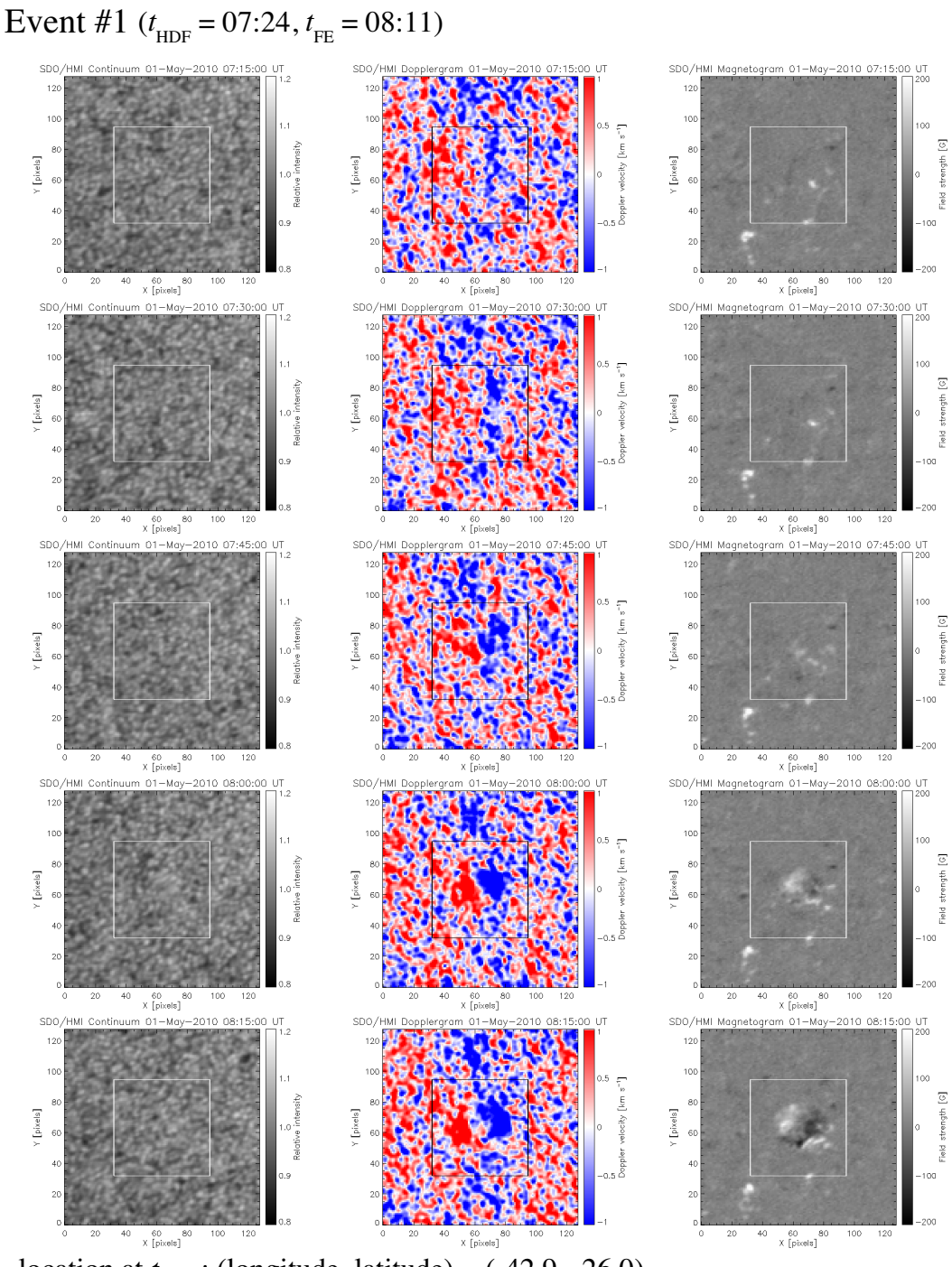

Figure B.4: Clear HDF events. Left, middle, and right columns show the evolutions of the continuum image, Dopplergram, and magnetogram, respectively. The box indicates the area we plot the histogram for the determination of the HDF start and flux emergence.

Event #2 (t_{HDF} = 19:25, t_{FE} = 20:30)

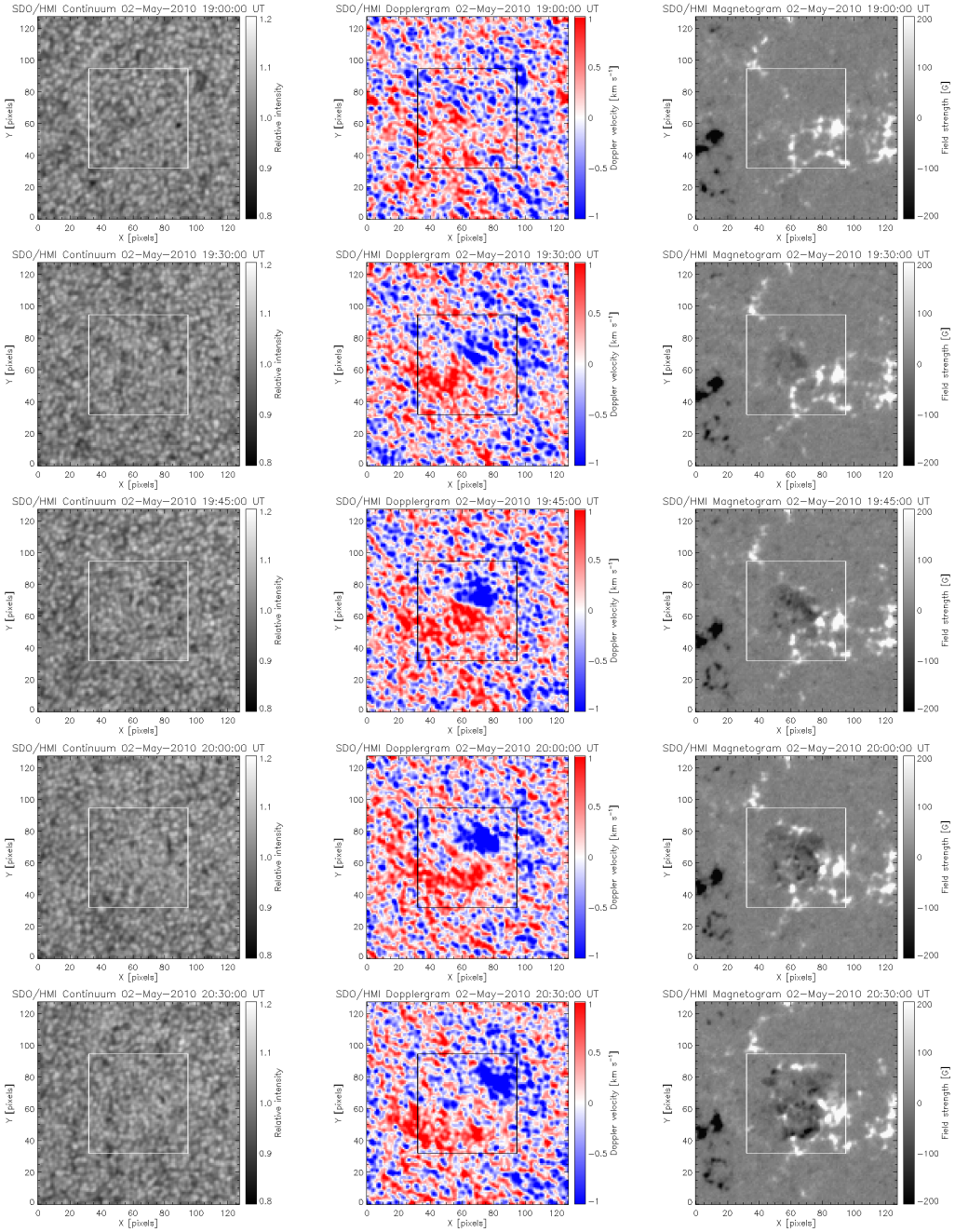

location at t_{HDF} : (longitude, latitude) = (-21.6, -26.0)

Figure B.4: *Continued.*

Event #3 (t_{HDF} = 13:05, t_{FE} = 14:51)

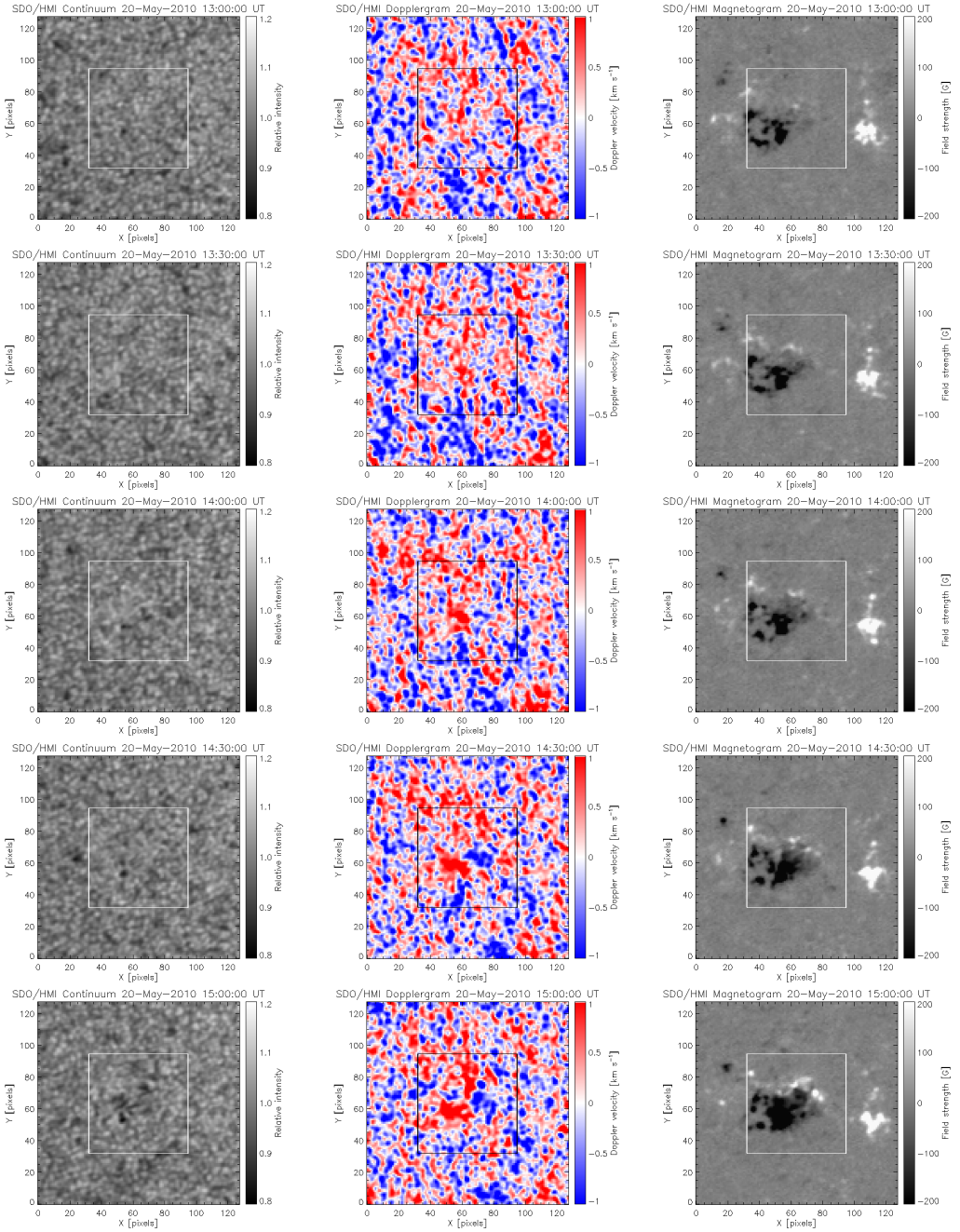

location at t_{HDF} : (longitude, latitude) = (-39.5, -15.0)

Figure B.4: *Continued.*

Event #9 (t_{HDF} = 21:02, t_{FE} = 22:42)

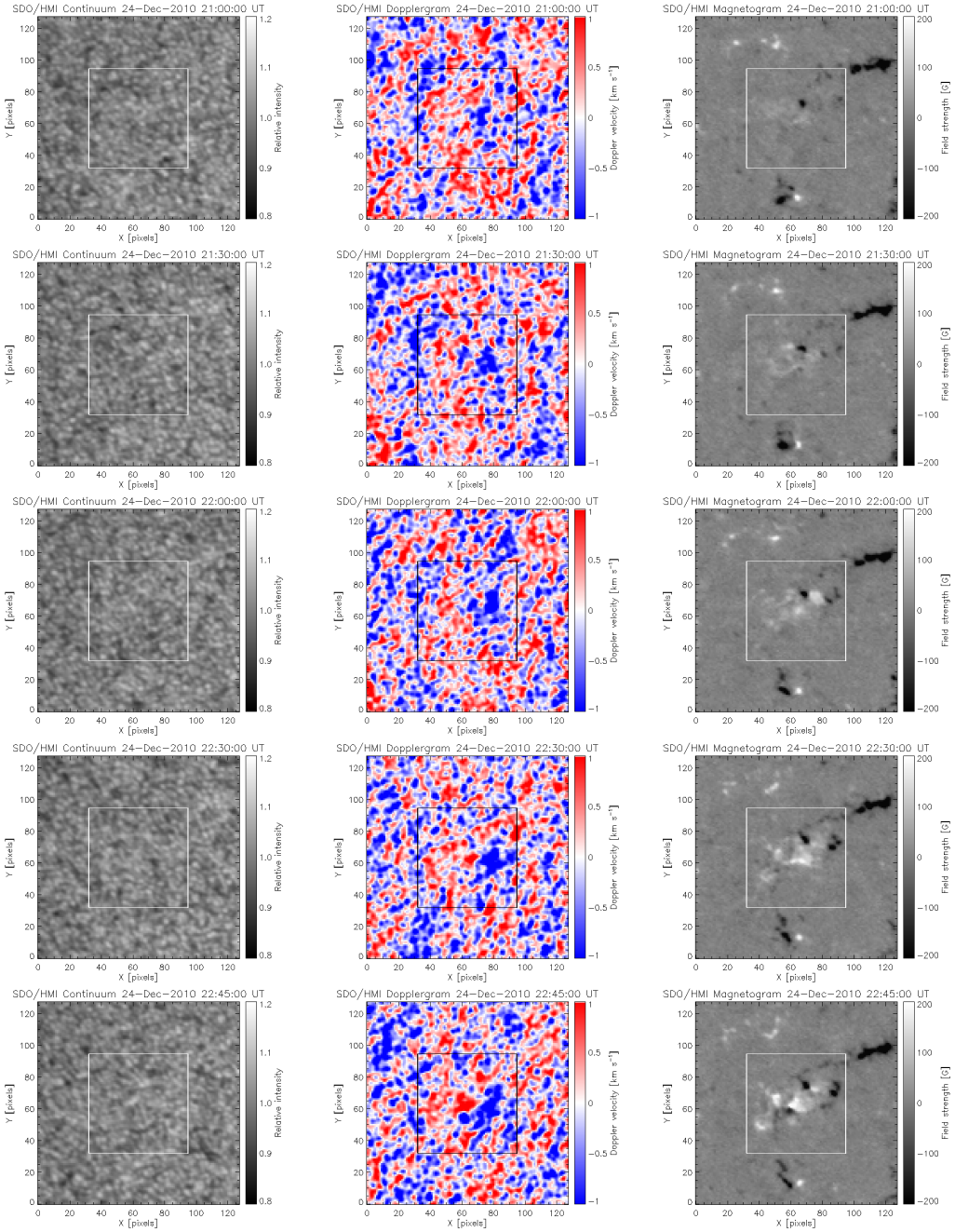

location at t_{HDF} : (longitude, latitude) = (-27.8, -18.0)

Figure B.4: *Continued.*

Event #15 (t_{HDF} = 18:27, t_{FE} = 18:32)

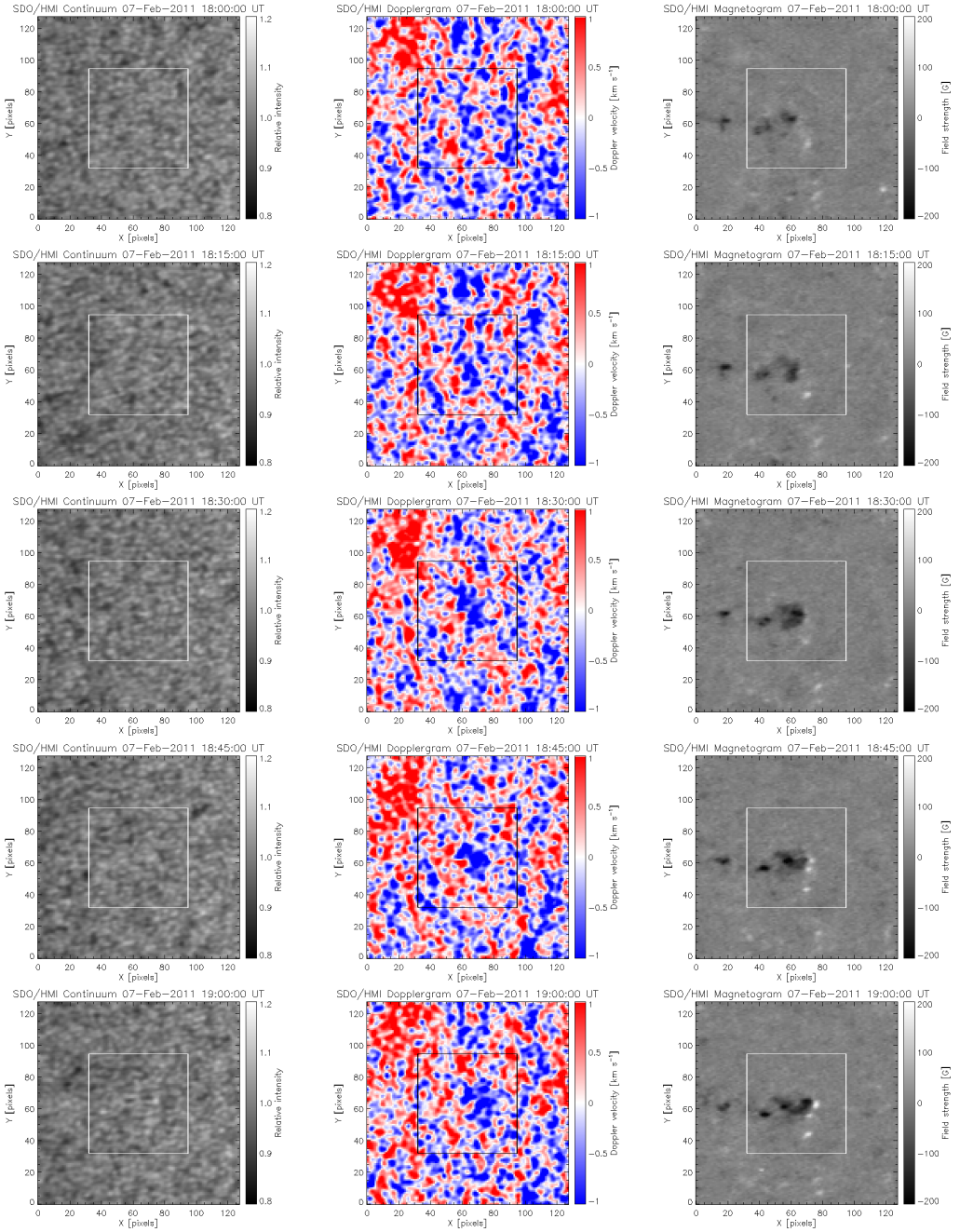

location at t_{HDF} : (longitude, latitude) = (-58.6, -20.0)

Figure B.4: *Continued.*

Event #16 (t_{HDF} = 21:21, t_{FE} = 22:04)

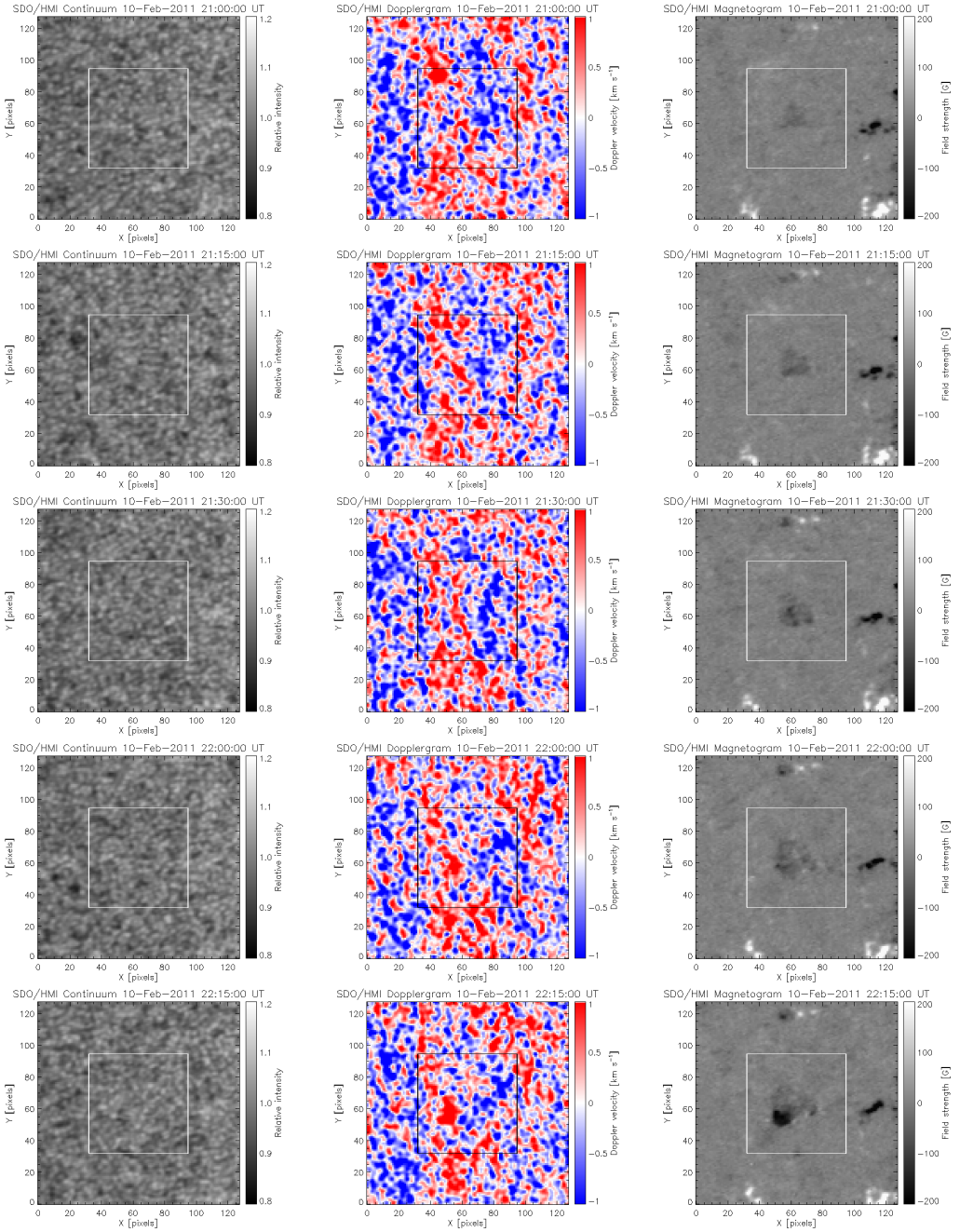

location at t_{HDF} : (longitude, latitude) = (-47.2, -20.0)

Figure B.4: *Continued.*

Appendix C

Acoustic Waves in the Ray Theory

In Chapter 9, we used the ray theory in which each acoustic wave propagates through the solar interior in accordance with the background stratification. In this appendix, we show the evaluation of the depth of the inner turning point (target depth), z_0, and the travel distance (skip distance), Δ, of acoustic waves. We also summarize the characteristics of the two filters we used in Chapter 9, both of which are based on the ray theory.

C.1 The Depth of the Inner Turning Point and the Travel Distance

The local dispersion relation of a sound wave is given as

$$\omega = C_{\rm s} k = C_{\rm s} \sqrt{k_r^2 + k_{\rm h}^2}, \tag{C.1}$$

where $C_{\rm s}$ is the local sound speed and k_r and $k_{\rm h}$ are the wavenumbers parallel and perpendicular to the radial axis of the Sun, respectively. Since the temperature in the Sun increases with depth, the sound speed also increases. And, according to Snell's law, the acoustic wave generated close to the solar surface reaches a certain depth and refracts back to the surface.

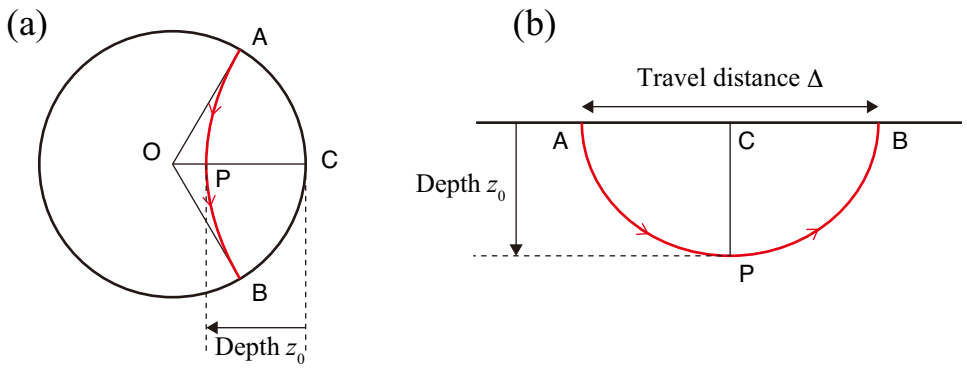

Figure C.1: Schematic depiction of an acoustic ray path in the actual Sun (a) and with the plane-parallel approximation (b). The ray starts at the point A on the solar surface, reaches the inner turning point P, and refracts back to the point B. The point O denotes the solar center. The turning depth z_0 is CP.

Figure C.1(a) shows the ray path from the surficial point A to B. As the ray approaches the inner turning point P, the radial wavenumber drops to zero ($k_r \to 0$), since the oscillation of the acoustic wave is parallel to the ray. Thus, at this point, Equation C.1 reduces to

$$\frac{k_r}{\omega} = \sqrt{\frac{1}{C_{\rm s}^2(r)} - \frac{k_{\rm h}^2}{\omega^2}} = 0, \tag{C.2}$$

and, therefore, we get

$$V_{\rm ph} = C_{\rm s}(r), \tag{C.3}$$

where $V_{\rm ph} = \omega/k_{\rm h}$ is the horizontal phase velocity of the acoustic wave.

Then, we use a solar model to find the depth where the phase velocity $V_{\rm ph}$ equals to the local sound speed $C_{\rm s}(r)$; $V_{\rm ph} = C_{\rm s}(r_0)$. Figure C.2 is the model S of Christensen-Dalsgaard et al. (1996). From the sound speed profile, we can determine the radial distance r_0 (OP in Figure C.1(a)) and the depth (CP); $z_0 = R_\odot - r_0$.

The travel distance (skip distance) Δ, over which one acoustic wave propagates through the interior, is also evaluated from the model S. In the analysis of Chapter 9, we used the

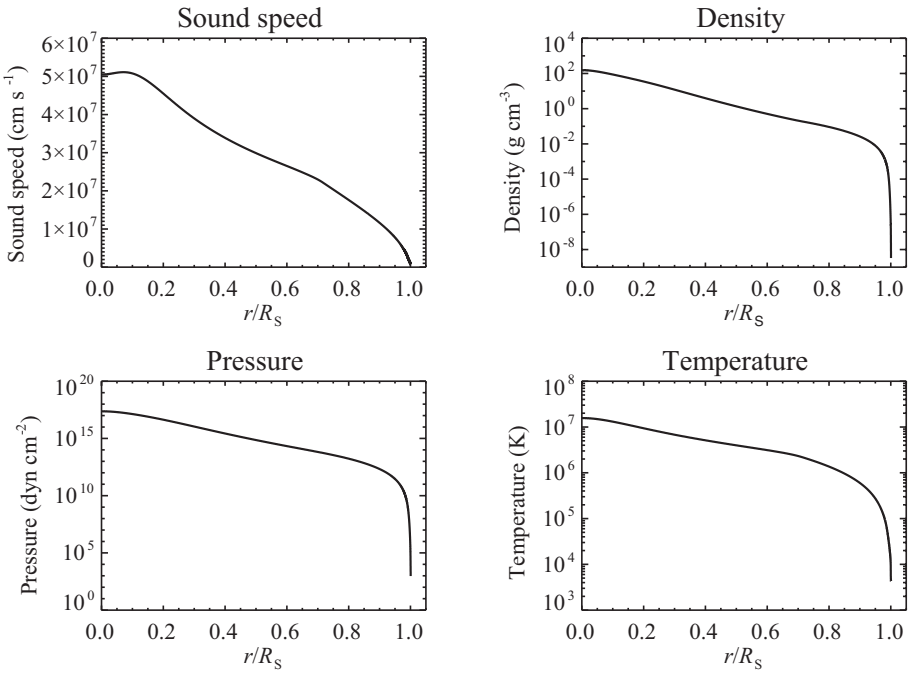

Figure C.2: The solar model S by Christensen-Dalsgaard et al. (1996). R_S indicates the solar radius.

plane-parallel approximation for the stratified atmosphere as in Figure C.1(b), since the target depth (up to ~ -20 Mm) is much smaller than the solar radius ($R_\odot \simeq 700$ Mm).

This is the way in which the phase-speed filter, one of the filtering methods we used in Chapter 9, extracts only the wave fields of the same turning depth and the travel distance.

C.2 Phase-speed Filter and Ridge Filter

In Chapter 9, we used two different types of filters. One is the phase-speed filter, which determines one specific phase speed $V_{\rm ph}$ and extracts the waves that reach the exact target depth z_0. Here, the phase speed may be selected with a certain width in order to increase the signal-to-noise ratio (S/N). Now that the depth z_0 has a certain width, we then consider that the travel distance Δ also has a width. This is why the squared velocity was integrated over the annulus, not the ring, in Section 9.2.

The other group is the ridge filter, which extracts the signal of the p-mode ridges. One merit of this filter is that we can accumulate the signals. However, in this case, the filter extends over a wide phase speed $V_{\rm ph}$ and thus we have to determine the representative target depth z_0. At the same time, the ridge filter has a wider sensitive depth compared to the phase-speed filter.

We can summarize the characteristics of the filters as follows: The phase-speed filter only selects the waves of the same phase speed (with a certain width) and is thus simpler. However, the S/N is not necessarily good, particularly for deeper waves. The ridge filter, on the contrary, is more sensitive since the filter extracts the signals of standing acoustic waves. At the same time, the phase speed of the ridge filter ranges much wider than that of the phase-speed filter. Therefore, we use ridge filters to improve S/N of the deeper waves, in spite of wider target depths.

C.3 Acoustic Power Maps

Figure C.3 shows the magnetogram and acoustic power maps obtained in Chapter 9. Here, panel (a) is the magnetogram of NOAA AR 10488 taken at 19:00 UT on 2003 October 26 and panel (b) is the corresponding Dopplergram. Panel (c) shows the filtered Dopplergram, $V(\boldsymbol{x}, t)$, (d) the annulus-averaged power, $P_{\rm AR}(\boldsymbol{x}, t)$, of which the target depth is -2.2 Mm, (e) the normalized power, $P_{\rm AR}(\boldsymbol{x}, t)/P_{\rm QS}(\boldsymbol{x}, t)$, and (f) its 60-min average. Panel (g) gives the vertical stack of the magnetogram and obtained 6 power maps, whose area is shown as a box in panels (a) and (f).

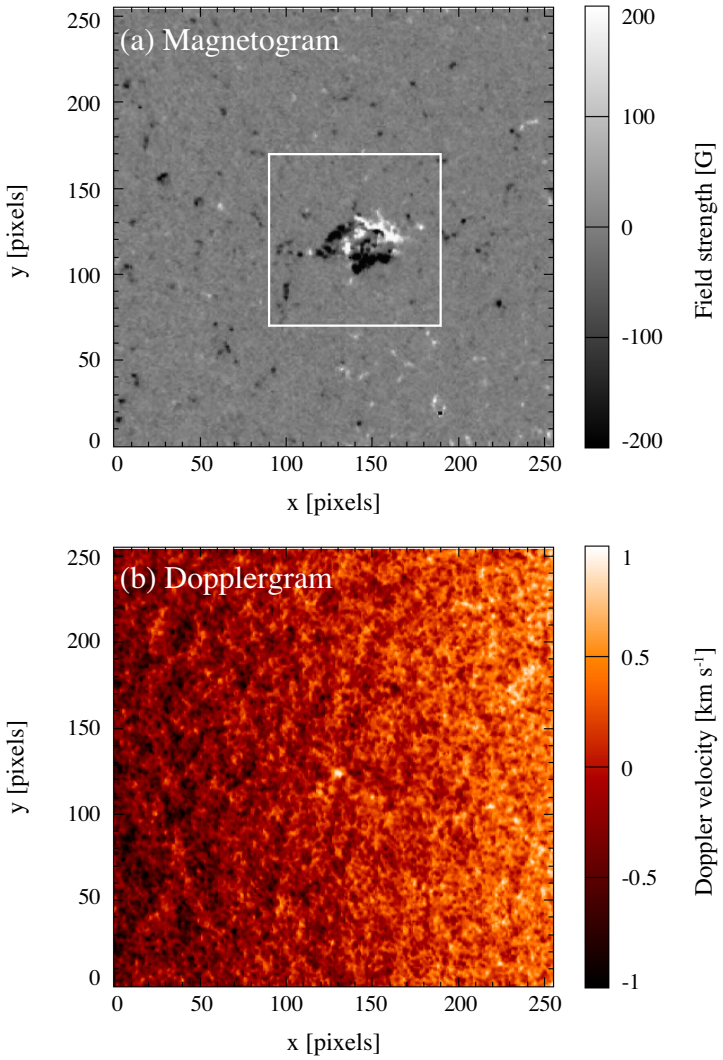

Figure C.3: (a) Magnetogram of NOAA AR 10488 taken at 19:00 UT on 2003 October 26. (b–f) Production process of the acoustic power map (target depth: −2.2 Mm) from the corresponding Dopplergram. (g) Vertical stack of the magnetogram and power maps of 6 layers. The box in panels (a) and (f) indicates the area for producing panel (g). See text for details.

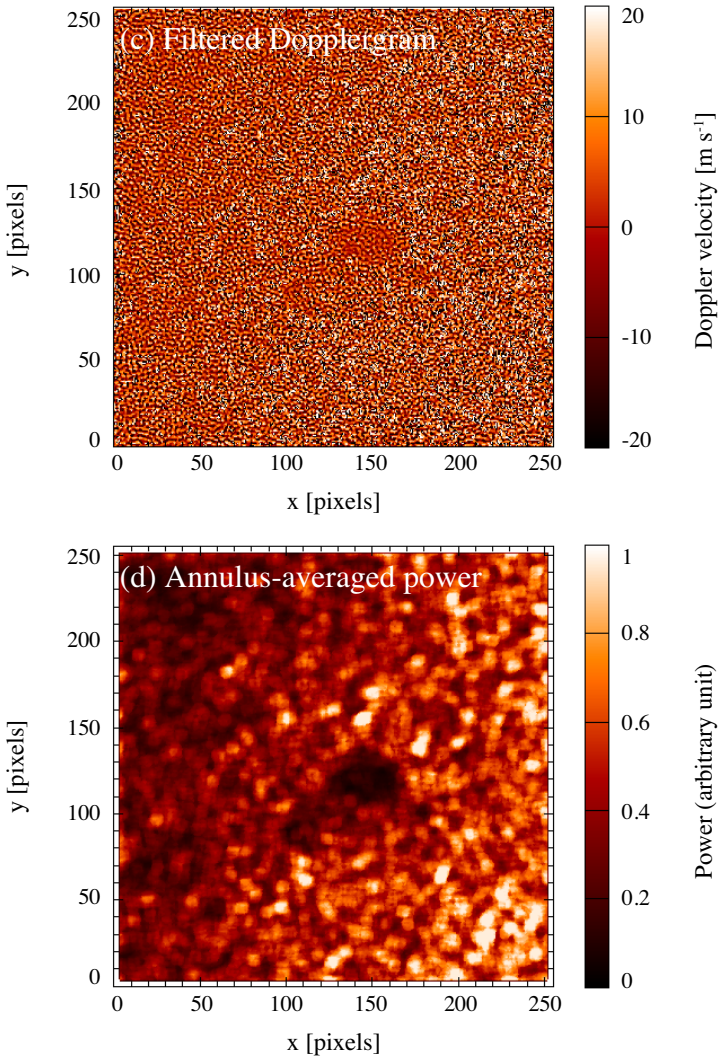

Figure C.3: *Continued.*

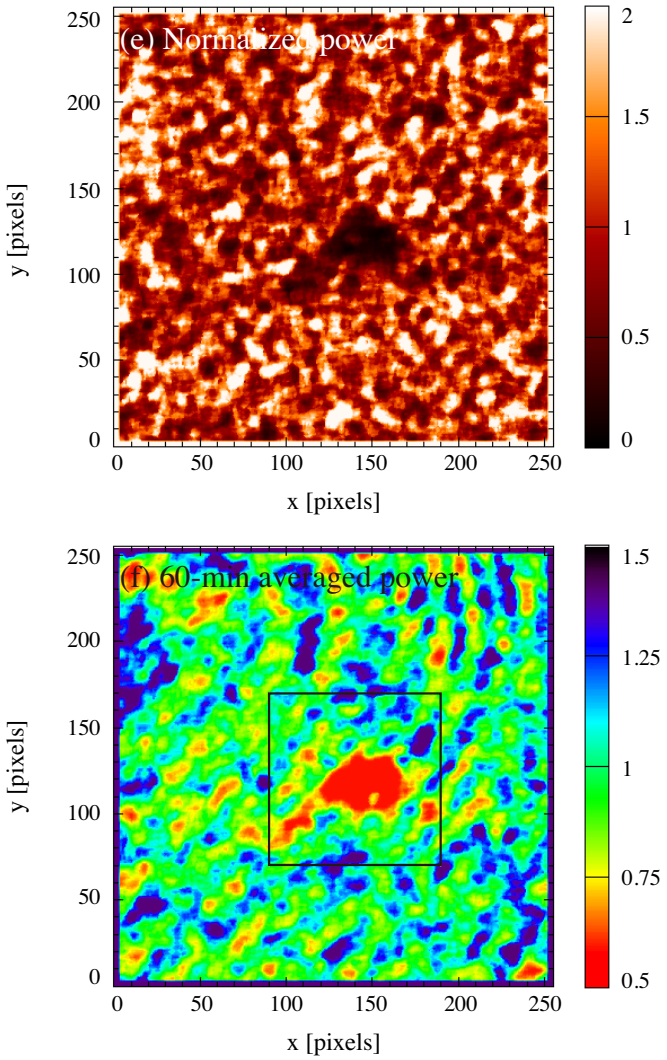

Figure C.3: *Continued.*

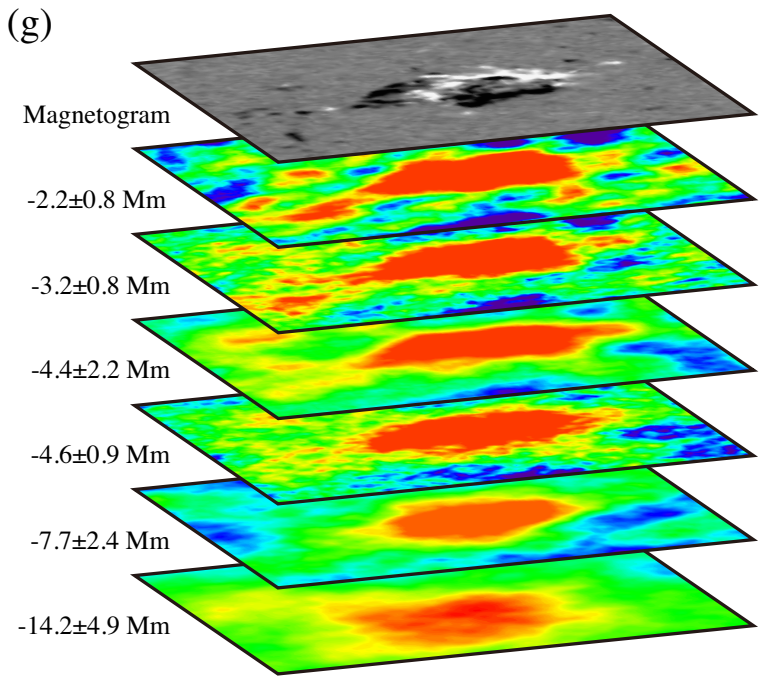

Figure C.3: *Continued.*

References

Abbett, W. P., & Fisher, G. H. 2003, ApJ, 582, 475

Acheson, D. J. 1979, Sol. Phys., 62, 23

Archontis, V., & Hood, A. W. 2009, A&A, 508, 1469

Archontis, V., Moreno-Insertis, F., Galsgaard, K., Hood, A., & O'Shea, E. 2004, A&A, 426, 1047

Bernasconi, P. N., Rust, D. M., Georgoulis, M. K., & Labonte, B. J. 2002, Sol. Phys., 209, 119

Birch, A. C., Braun, D. C., Leka, K. D., Barnes, G., & Javornik, B. 2013, ApJ, 762, 131

Brants, J. J., & Steenbeek, J. C. M. 1985, Sol. Phys., 96, 229

Braun, D. C., Birch, A. C., Rempel, M., & Duvall, T. L. 2012, ApJ, 744, 77

Braun, D. C., Duvall, Jr., T. L., & Labonte, B. J. 1987, ApJL, 319, L27

Bruzek, A. 1967, Sol. Phys., 2, 451

—. 1969, Sol. Phys., 8, 29

Caligari, P., Moreno-Insertis, F., & Schüssler, M. 1995, ApJ, 441, 886

Cally, P. S., Crouch, A. D., & Braun, D. C. 2003, MNRAS, 346, 381

Chandrasekhar, S. 1961, Hydrodynamic and hydromagnetic stability

Cheung, M. C. M., Moreno-Insertis, F., & Schüssler, M. 2006, A&A, 451, 303

Cheung, M. C. M., Rempel, M., Title, A. M., & Schüssler, M. 2010, ApJ, 720, 233

Cheung, M. C. M., Schüssler, M., & Moreno-Insertis, F. 2007, A&A, 467, 703

Cheung, M. C. M., Schüssler, M., Tarbell, T. D., & Title, A. M. 2008, ApJ, 687, 1373

Chitta, L. P., Jain, R., Kariyappa, R., & Jefferies, S. M. 2012, ApJ, 744, 98

Chou, D.-Y., Liang, Z.-C., Yang, M.-H., & Sun, M.-T. 2009, Sol. Phys., 255, 39

Choudhuri, A. R., & Gilman, P. A. 1987, ApJ, 316, 788

Christensen-Dalsgaard, J., et al. 1996, Science, 272, 1286

D'Silva, S., & Choudhuri, A. R. 1993, A&A, 272, 621

Duvall, Jr., T. L. 2003, in ESA Special Publication, Vol. 517, GONG+ 2002. Local and Global Helioseismology: the Present and Future, ed. H. Sawaya-Lacoste, 259–262

Duvall, Jr., T. L., Jefferies, S. M., Harvey, J. W., & Pomerantz, M. A. 1993, Nature, 362, 430

Ellerman, F. 1917, ApJ, 46, 298

Emonet, T., & Moreno-Insertis, F. 1998, ApJ, 492, 804

Fan, Y. 2001, ApJL, 554, L111

—. 2008, ApJ, 676, 680

—. 2009, Living Reviews in Solar Physics, 6, 4

Fan, Y., Abbett, W. P., & Fisher, G. H. 2003, ApJ, 582, 1206

Fan, Y., Fisher, G. H., & Deluca, E. E. 1993, ApJ, 405, 390

Fan, Y., Zweibel, E. G., & Lantz, S. R. 1998, ApJ, 493, 480

Fang, F., Manchester, W., Abbett, W. P., & van der Holst, B. 2010, ApJ, 714, 1649

Fox, P. 1908, ApJ, 28, 253

Frazier, E. N. 1972, Sol. Phys., 26, 130

Georgoulis, M. K., Rust, D. M., Bernasconi, P. N., & Schmieder, B. 2002, ApJ, 575, 506

Giles, P. M., Duvall, T. L., Scherrer, P. H., & Bogart, R. S. 1997, Nature, 390, 52

Gough, D. O. 1969, Journal of Atmospheric Sciences, 26, 448

Grigor'ev, V. M., Ermakova, L. V., & Khlystova, A. I. 2007, Astron. Lett., 33, 766

Hagenaar, H. J. 2001, ApJ, 555, 448

Hagyard, M. J., Teuber, D., West, E. A., & Smith, J. B. 1984, Sol. Phys., 91, 115

Hale, G. E., Ellerman, F., Nicholson, S. B., & Joy, A. H. 1919, ApJ, 49, 153

Hanawa, T., Matsumoto, R., & Shibata, K. 1992, ApJL, 393, L71

Hartlep, T., Kosovichev, A. G., Zhao, J., & Mansour, N. N. 2011, Sol. Phys., 268, 321

Harvey, K. L., & Martin, S. F. 1973, Sol. Phys., 32, 389

Hill, F. 1988, ApJ, 333, 996

Hood, A. W., Archontis, V., Galsgaard, K., & Moreno-Insertis, F. 2009, A&A, 503, 999

Ilonidis, S. 2012, PhD thesis, Stanford Univ.

Ilonidis, S., & Zhao, J. 2011, Sol. Phys., 268, 377

Ilonidis, S., Zhao, J., & Kosovichev, A. 2011, Science, 333, 993

Isobe, H., Miyagoshi, T., Shibata, K., & Yokoyama, T. 2005, Nature, 434, 478

Isobe, H., Tripathi, D., & Archontis, V. 2007, ApJL, 657, L53

Jain, R., Hindman, B. W., Braun, D. C., & Birch, A. C. 2009, ApJ, 695, 325

Jouve, L., & Brun, A. S. 2009, ApJ, 701, 1300

Komm, R., Morita, S., Howe, R., & Hill, F. 2008, ApJ, 672, 1254

Kosovichev, A. G. 2009, Space Sci. Rev., 144, 175

Kosovichev, A. G., & Duvall, Jr., T. L. 2008, in Astronomical Society of the Pacific Conference Series, Vol. 383, Subsurface and Atmospheric Influences on Solar Activity, ed. R. Howe, R. W. Komm, K. S. Balasubramaniam, & G. J. D. Petrie, 59

Kosugi, T., et al. 2007, Sol. Phys., 243, 3

Kusano, K., Moriyama, K., & Miyoshi, T. 1998, Physics of Plasmas, 5, 2582

Leighton, R. B., Noyes, R. W., & Simon, G. W. 1962, ApJ, 135, 474

Linton, M. G., Longcope, D. W., & Fisher, G. H. 1996, ApJ, 469, 954

Lites, B. W. 2009, Space Sci. Rev., 144, 197

Longcope, D. W., Fisher, G. H., & Arendt, S. 1996, ApJ, 464, 999

Longcope, D. W., & Klapper, I. 1997, ApJ, 488, 443

Magara, T. 2001, ApJ, 549, 608

Manchester, IV, W. 2001, ApJ, 547, 503

Matsumoto, R., & Shibata, K. 1992, PASJ, 44, 167

Matsumoto, R., Tajima, T., Chou, W., Okubo, A., & Shibata, K. 1998, ApJL, 493, L43

Matsumoto, R., Tajima, T., Shibata, K., & Kaisig, M. 1993, ApJ, 414, 357

Moreno-Insertis, F., Caligari, P., & Schüssler, M. 1995, ApJ, 452, 894

Moreno-Insertis, F., & Emonet, T. 1996, ApJL, 472, L53

Murray, M. J., Hood, A. W., Moreno-Insertis, F., Galsgaard, K., & Archontis, V. 2006, A&A, 460, 909

Nelson, N. J., Brown, B. P., Brun, A. S., Miesch, M. S., & Toomre, J. 2013, ApJ, 762, 73

Newcomb, W. A. 1961, Phys. of Fluids, 4, 391

November, L. J., & Simon, G. W. 1988, ApJ, 333, 427

Nozawa, S. 2005, PASJ, 57, 995

Nozawa, S., Shibata, K., Matsumoto, R., Sterling, A. C., Tajima, T., Uchida, Y., Ferrari, A., & Rosner, R. 1992, ApJS, 78, 267

Otsuji, K., Kitai, R., Matsumoto, T., Ichimoto, K., Ueno, S., Nagata, S., Isobe, H., & Shibata, K. 2010, PASJ, 62, 893

Pariat, E., Aulanier, G., Schmieder, B., Georgoulis, M. K., Rust, D. M., & Bernasconi, P. N. 2004, ApJ, 614, 1099

Parker, E. N. 1955, ApJ, 121, 491

—. 1966, ApJ, 145, 811

—. 1975, ApJ, 198, 205

—. 1978, ApJ, 221, 368

—. 1979, Cosmical magnetic fields: Their origin and their activity

Pevtsov, A. A., Canfield, R. C., & Metcalf, T. R. 1995, ApJL, 440, L109

Rempel, M., Schüssler, M., Cameron, R. H., & Knölker, M. 2009, Science, 325, 171

Sammis, I., Tang, F., & Zirin, H. 2000, ApJ, 540, 583

Scherrer, P. H., et al. 1995, Sol. Phys., 162, 129

Schou, J., & Bogart, R. S. 1998, ApJL, 504, L131

Schou, J., et al. 1998, ApJ, 505, 390

—. 2012, Sol. Phys., 275, 229

Schüssler, M. 1977, A&A, 56, 439

—. 1979, A&A, 71, 79

Sheeley, Jr., N. R. 1969, Sol. Phys., 9, 347

Shibata, K., Tajima, T., Steinolfson, R. S., & Matsumoto, R. 1989, ApJ, 345, 584

Spruit, H. C. 1981, A&A, 98, 155

Stein, R. F., Lagerfjärd, A., Nordlund, Å., & Georgobiani, D. 2011, Sol. Phys., 268, 271

Stein, R. F., & Nordlund, Å. 2012, ApJL, 753, L13

Stix, M. 1989, The Sun. an Introduction

Strous, L. H., Scharmer, G., Tarbell, T. D., Title, A. M., & Zwaan, C. 1996, A&A, 306, 947

Strous, L. H., & Zwaan, C. 1999, ApJ, 527, 435

Toriumi, S., Hayashi, K., & Yokoyama, T. 2012, ApJ, 751, 154

Toriumi, S., Ilonidis, S., Sekii, T., & Yokoyama, T. 2013, ApJL, 770, L11

Toriumi, S., & Yokoyama, T. 2010, ApJ, 714, 505

—. 2011, ApJ, 735, 126

—. 2012, A&A, 539, A22

—. 2013, A&A, 553, A55

Tsinganos, K. C. 1980, ApJ, 239, 746

Tsuneta, S., et al. 2008, Sol. Phys., 249, 167

UeNo, S., Nagata, S.-i., Kitai, R., Kurokawa, H., & Ichimoto, K. 2004, Proc. SPIE, 5492, 958

Yokoyama, T., & Shibata, K. 1995, Nature, 375, 42

—. 1996, PASJ, 48, 353

Zhao, J., et al. 2012, Sol. Phys., 275, 375

Zharkov, S., & Thompson, M. J. 2008, Sol. Phys., 251, 369

Zirin, H. 1972, Sol. Phys., 22, 34

Zwaan, C. 1978, Sol. Phys., 60, 213

—. 1985, Sol. Phys., 100, 397

—. 1987, ARAA, 25, 83